Implicit Large-Eddy Simulation of Low-Speed Separated Flows Using High-Resolution Methods

Marco Hahn

Submitted for the Degree of Ph.D.

Department of Aerospace Sciences
Cranfield University
Cranfield, UK

2008

Cranfield University

School of Engineering

PhD

Academic Year: 2007-2008

Marco Hahn

Implicit Large-Eddy Simulation of Low-Speed Separated Flows Using High-Resolution Methods

Supervisor: Dimitris Drikakis

March 27, 2008

Abstract

MOST flows of practical importance are governed by viscous near-wall phenomena leading to separation and subsequent transition to a turbulent state. This type of problem currently poses one of the greatest challenges for computational methods because its characteristics covers a wide range of physical processes that often place contradictory requirements on the numerics employed.

This thesis seeks to investigate the physics of complex, separated flows pertinent to aeronautical engineering and to assess the performance of variants of the Implicit Large-Eddy Simulation approach in predicting this type of problem realistically. For this purpose, different numerical solution strategies based on high-resolution methods, distinguished by their order of accuracy, are used in precursor simulations and one selected approach is applied to a fully three-dimensional wing flow.

In order to isolate the development from laminar to turbulent flow after separation has occurred, the prototype Taylor-Green Vortex is considered. Here, the behaviour of the numerical schemes during the linear, non-linear and fully turbulent stages in the flow evolution is tested for different grid sizes. It is found that the resolution power and the likelihood of symmetry breaking is increasing with the order of accuracy of the numerical method. These two properties allow the flow to develop more realistically on coarse grids if higher order schemes are employed.

In the next step, flow separation from a gently curved surface is included. The fundamental study of a statistically two-dimensional channel flow with hill-type constrictions demonstrates the basic applicability of ILES to problems featuring massive separation. Without specific wall-treatment, high-resolution methods can improve prediction of the detachment location when compared to classical Large-Eddy Simulations.

Finally, an ILES simulation of three-dimensional flow over a swept wing geometry at moderate angle of incidence is presented. The results are in excellent agreement with experiment in the fully separated and turbulent region and they are more accurate than a classical hybrid RANS/LES approach, using a grid twice the size, over the majority of the wing. This outcome will probably settle the dispute that has erupted in the past over the applicability of ILES to complex, wall-bounded flows.

Acknowledgements

FIRST and foremost I would like to sincerely thank my supervisor Professor Dimitris Drikakis for his guidance throughout the years and the freedom he granted me to pursue my own ideas. Above all, however, I have to express my gratitude not only for being a source of advice, but also a friend.

The fruitful discussions about physics and numerics with Ning Li, Shanying Zhang, Lionel Temmerman, Ben Thornber, Sanjay Patel and Evgeniy Shapiro are greatly appreciated. This work would have been impossible without you and the insightful comments provided truly shaped this thesis!

Thanks must also go to my former flatmates Adam and Ed for the great time we had living together and the fantastic people I had the privilege to share an office with: Sanj for keeping me company during the breaks, Marco for reminding me of our German heritage, Steve for making the best coffee in the world, Jason for his irrepressible good spirit, Ian for introducing me to the best pubs in Bedford, Simon for teaching me about golf, Sunil for the occasional great save, John for his left hammer and Ben for being the driving force behind so many "extra-curricular activities". Of course, Dr. Dim and all my friends in Germany, who I would have attempted to name if not for fear of accidentally leaving someone out, will not be forgotten!

Finally, I am deeply indebted to my parents and sisters plus families for their love, unwavering support and always being there when I need them most. My gratitude cannot be expressed in simple words!

Marco Hahn

Contents

List of Figures

List of Tables

Nomenclature

Acronyms

CFL	Courant-Friedrichs-Lewy number
DNS	Direct Numerical Simulation
ENO	Essentially Non-Oscillatory Scheme
FP	Focus Point
ILES	Implicit Large-Eddy Simulation
LDA	Laser Doppler Anemometry
LES	Large-Eddy Simulation
LEV	Leading Edge Vortex
MEA	Modified Equation Analysis
MILES	Monotonically Integrated Large-Eddy Simulation
MUSCL	Monotonic Upwind Scheme for Scalar Conservation Laws
VR	Vortex Reattachment
RANS	Reynolds-Averaged Numerical Simulation
SA	Saddle
SGS	Subgrid scale
SP	Stagnation Point
TVD	Total Variation Diminishing
TES	Trailing Edge Separation
URANS	Unsteady Reynolds-Averaged Numerical Simulation
WENO	Weighted Essentially Non-Oscillatory Scheme

Greek Symbols

ϵ	Dissipation rate
γ	Ratio of specific heats
η	Kolmogorov length-scale
κ	Thermal conductivity coefficient
λ	Eigenvalue
λ_b	Bulk viscosity coefficient
λ_T	Taylor micro-scale
$\mathbf{\Lambda}$	Diagonal matrix of the eigenvalues
μ	Dynamic viscosity coefficient
ν	Kinematic viscosity
ω	Vorticity magnitude
ϕ	Limiter function
ψ	Upwinding coefficient
ρ	Density
τ_w	Wall shear-stress
τ_η	Kolmogorov time-scale
τ_{ij}	Viscous stresses

Latin Symbols

$\mathbf{A}$	Flux Jacobian
$\mathbf{a}$	Weighting function
a	Speed of sound
$\mathbf{C}$	Cross stress term
c_p	Specific heat at constant pressure
c_v	Specific heat at constant volume
$\mathbf{E}$	Inviscid flux vector
e	Total energy per unit volume

e_i	Internal energy
$\mathbf{F}$	Inviscid flux vector
$\mathbf{G}$	Inviscid flux vector
H	Total enthalpy
$\mathbf{I}$	Identity tensor
k	Wavenumber
ℓ	Integral length-scale
$\mathbf{L}$	Leonard stress term
$\mathbf{L}$	Viscous flux vector
l_c	Characteristic reference length
$\mathbf{M}$	Viscous flux vector
$\mathbf{m}$	Commutation error term
μ_c	Characteristic reference viscosity
Ma	Mach number
$\mathbf{N}$	Viscous flux vector
$\mathbf{P}$	Convex combination of polynomials
$\mathbf{p}$	Polynomial reconstruction
p	Pressure
Pr	Prandtl number
$\mathbf{Q}$	Matrix of the right eigenvectors
$\mathbf{q}$	Heat flux
$\mathbf{Q}^{-1}$	Matrix of the left eigenvectors
Q	Second invariant of the velocity gradient tensor
$\mathbf{R}$	Reynolds stress term
ρ_c	Characteristic reference density
R	Gas constant
r	Ratio of the slopes of conserved variables

Re	Reynolds number
$\mathbf{S}$	Stress tensor
S	Strain-rate
s	Shock speed
$S_{0,1}$	Stencils for the WENO reconstruction
$\boldsymbol{\tau}$	Truncation error term
Δt	Time step
$\mathbf{T}$	Subgrid scale stress tensor
T	Temperature
T_c	Characteristic reference temperature
$\overline{\mathbf{U}}$	Array of characteristics-based variables
$\mathbf{U}$	Array of conservative variables
$\mathbf{u}$	Velocity vector
u	Flow velocity
$u_\perp$	Normal velocity component
u_η	Kolmogorov velocity-scale
u_τ	Friction velocity
$u_\parallel$	Parallel velocity component
u_c	Characteristic reference velocity
$\mathbf{V}$	Array of characteristic variables
$\mathbf{W}$	Array of primitive variables

CHAPTER 1

Introduction

THIS thesis is concerned with low-speed, separated flows of a turbulent nature. Flow separation is one of the most heavily studied phenomena in fluid mechanics because it is a major loss mechanism and thus usually undesirable in many engineering applications. It is a highly non-linear and inherently unsteady process, most often leading to zones dominated by turbulent, vortical structures. Therefore, the accurate representation of turbulence plays an essential role in predicting separated flows and the main focus of this work is to improve the understanding of numerical simulation techniques for turbulent flows.

The existence of turbulence has been well-established for centuries. Not only since Leonardo da Vinci's famous study of water flow[1] in 1510 A.D. has this subject attracted a great deal of attention. Its ubiquitous character and the importance to our everyday lives led many artists, scientists, researchers or other curious minds to busy themselves with one of the most forbidding and elusive topics in fluid mechanics. Turbulence is notoriously difficult to measure in a natural environment or in a laboratory experiment and, despite great efforts, a unified theory has yet to emerge. With the rapid development of computer power, numerical simulations have gained significance and are currently used as a tool to shed some light onto the unsolved mysteries of turbulence. Although major improvements have been made in the past decades, adequate simulations become prohibitively expensive with increasing Reynolds number and will still be beyond the scope of possibility in the years to come.

This chapter will briefly illustrate the physics behind flow separation from solid walls, as well as the omnipresent nature and the characteristic features of turbulence. More details can be found in several excellent textbooks, e.g. Anderson [2], Davidson [21], Pope [90], Tennekes and Lumley [113], that also inspired the schematic illustrations presented here. Furthermore, an overview of state-of-the-art numerical techniques will be given and their particular advantages and disadvantages will be elucidated.

[1] *"The water forms whirling eddies, one part following the impetus of the chief current, and the other following the incidental motion and return flow"*, original in The Royal Collection.

1.1 The Separation Process

Most flows of practical importance belong to the group of wall-bounded flows and can be divided into internal and external flows. Internal, wall-bounded flows are confined by one or more outer surfaces, such as a circular pipe or a plane channel, and external flows are predominantly defined by one or more closed surfaces forming an obstacle in an open stream, e.g. the flow around aircrafts and ships. The presence of a wall and the associated boundary-layer have a severe impact on the fluid flow, regardless if it is of internal or external type.

Viscosity. The flow of a fluid over a solid surface is dominated by viscosity and the associated friction forces affect both the fluid in the vicinity of the surface and the surface itself. The surface experiences a tangential force trying to drag it in the down-stream direction and, vice versa, an equally strong force acts on the fluid trying to decelerate it. This viscous shear force leads to a zero flow velocity at the wall.

Pressure Gradient. In most aerodynamic problems in engineering the shape of the body under consideration is aligned with the free-stream, e.g. a wing or a fuselage. A close-up view of the surface reveals that it exhibits a convex curvature, hence the static pressure is no longer constant in the streamwise direction as it rises due to the conservation of total energy. This situation is sketched in Figure 1.1(a). At location ℓ_1, a typical velocity profile in the boundary layer of a viscous, wall-bounded flow is shown. As the flow advances in the down-stream direction, it has to overcome an adverse pressure gradient, i.e. $p_1 < p_2 < p_3$. Consequently, kinetic energy has to be transformed into internal energy and the flow near the surface is further retarded. In addition to this retarding force, the viscous shear continuously slows the fluid down as it progresses along the surface until, ultimately, the slope of the velocity profile becomes zero, see location ℓ_2. Under the perpetual influence of the adverse pressure gradient the flow begins to reverse its direction and separates from the surface. This phenomena is inherently unstable, hence no well-defined point of separation can be accounted for. It results in a separation area with a down-stream recirculation zone, see location ℓ_3. The separation process largely depends on the character of the upstream boundary layer, i.e. whether it is laminar or turbulent. A turbulent boundary layer is less likely to separate compared to a laminar boundary layer because the agitated motion normal to the surface feeds the fluid near the wall with kinetic energy, thus it can overcome a higher pressure gradient.

Wake Region. Modelling of the separation process is not part of this thesis, however. The main focus is on predicting the recirculating flow after separation occurred. Figure 1.1(b) shows experimental evidence for the existence of an unsteady free shear-layer between the main-stream and the separated boundary layer. The shear-layer rolls up into Kelvin-Helmholtz-type vortices that transfer momentum between the free-flow and the recirculation zone. The instability of this unsteady system manifests itself in the breakdown of the Kelvin-Helmholtz structures. Thus, a highly turbulent wake region dominated by small-scale dynamics of the developing secondary vortices can be observed further down-stream.

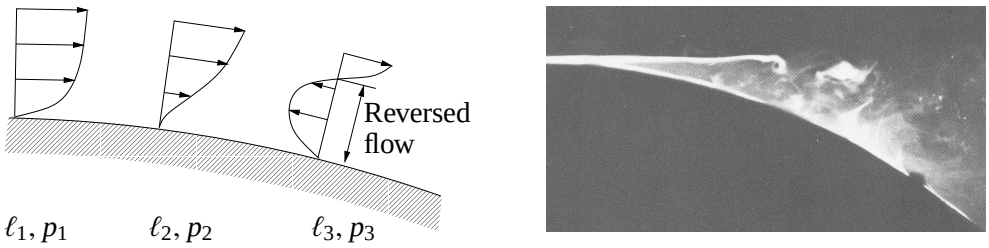

(a) Velocity profiles. (b) Separation from a convex surface.

Figure 1.1: Separation induced by an adverse pressure gradient along a curved surface (Picture (b) from van Dyke [118]).

As mentioned above, the adequate numerical representation of the turbulent wake is of prime importance to the current research. Not only is this a challenging problem for any turbulence modelling effort, it is also of great interest in many practical applications. As illustrated in Figure 1.2, separated wakes are characteristic for aerofoils at high incidence or the flow around bluff bodies. Bluff body flow is a very vague term comprising any flow over sharp geometrical discontinuities, e.g. a backward facing step, an apartment building, a weapons bay, etc. This definition already suggests the existence of a broad spectrum of applications for numerical simulation of separated, turbulent flows. In order to underline the importance of turbulence, more examples are presented in Section 1.2.

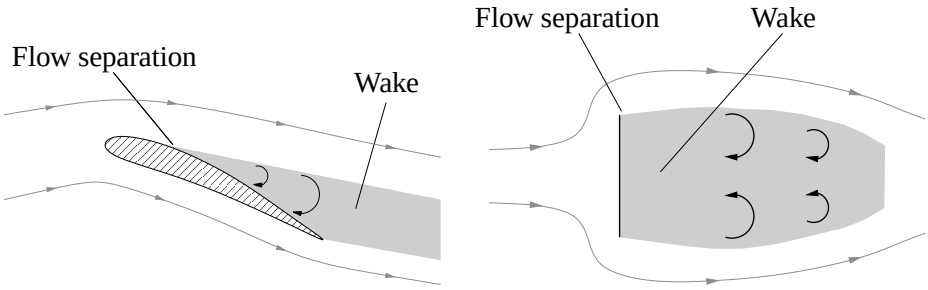

(a) Aerofoil. (b) Bluff body.

Figure 1.2: Examples of separated flow.

1.2 The Nature of Turbulence

Almost all flows, natural or man-made, are turbulent and can be observed in our everyday surroundings. They are not restricted to a specific type of fluid or environment and can appear in all sizes, extending from the minuscule scales to truly gigantic dimensions. Nevertheless, they all have certain unique features in common.

1.2.1 Turbulent Flows in Nature

Nature itself provides probably the most intriguing phenomena that motivate the current interest. For instance, the flow of water around obstacles like rocks in a river or

steps in the riverbed exhibits seemingly random, highly chaotic motions commonly known as rapids or waterfalls, see Figure 1.3(a). Less obvious, often the more treacherous peril, however, lurks beneath the surface. Immensely vast and powerful underwater currents can be turbulent, with the Gulf Stream being one of its most prominent representatives (Figure 1.3(b)).

(a) Rapids in a Welsh river.

(b) Gulf Stream separating from the coast of North Carolina, USA.

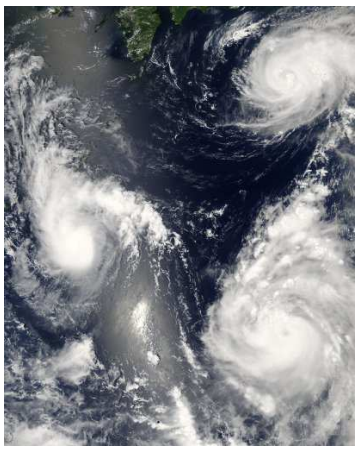

(c) Typhoons over the western Pacific Ocean.

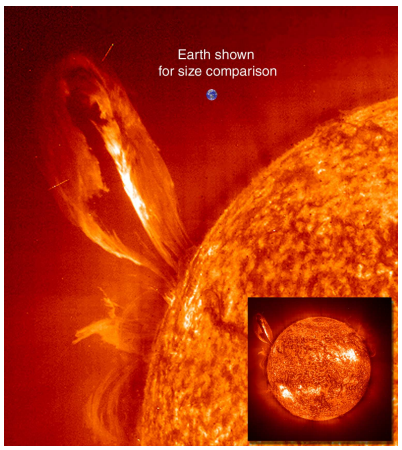

(d) Solar prominence with the Earth shown for comparison.

Figure 1.3: Turbulence observed in nature (Photographs (b) – (d) from `http://www.nasa.gov`).

Another example of meso-scale phenomena can be found in meteorology. Figure 1.3(c) is an interesting illustration of the formation of tropical storms systems. It shows a photograph of several typhoons spinning over the western Pacific Ocean that were predicted to hit China and Japan in 2006. One of the most spectacular and at the same time one of the largest manifestations of turbulence is at the origin of the Northern Lights. Eruptive prominences extending a distance equivalent to several tens of Earth diameters from the Sun eject solar mass, see Figure 1.3(d). This mass is transported by the solar wind, eventually breaches the Earth's magnetosphere and causes not only the remarkable displays in the northern night skies, but can also affect communications

and navigations systems.

1.2.2 Turbulent Flows in Engineering Applications

Practically all flows of interest to engineers and scientists are turbulent and in many engineering applications turbulence plays an important role in the planning, design and manufacturing process.

(a) Trailing wake of a Boeing B-747.

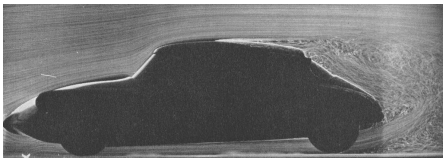

(b) Wake of an automobile.

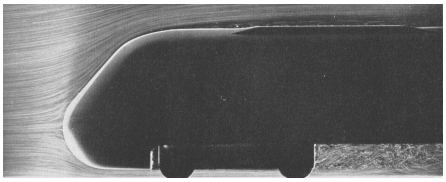

(c) Undercarriage of a train.

(d) Smoke from a chimney.

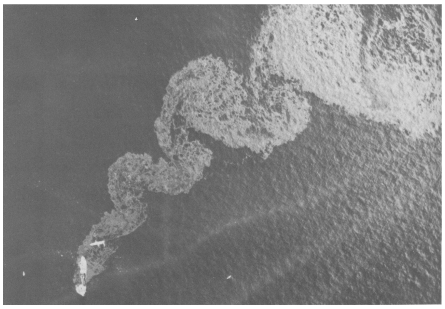

(e) Spill from an oil-tanker.

Figure 1.4: Turbulence observed in engineering applications (Photograph (a) from `http://www.nasa.gov`, Pictures (b) and (c) from Werle [125], Photograph (d) from `http://www.climatechangeinstitute.com`, Picture (e) from van Dyke [118]).

For instance, the reduction of aerodynamic drag due to turbulence is a major concern in the transport industry, be it for the manufacturers of aeroplanes, automobiles, trains or ships, see Figures 1.4(a) – 1.4(c). The prospect of cutting operational costs and the foreseeable shortage of natural resources also stimulate the current efforts to improve the fuel efficiency of engines, a domain where detailed knowledge of turbulent mixing of the fuel and gases is required. Apart from the economical consideration, an equally important ecological aspect can be argued for: increasing the efficiency of the current transport system is inevitably linked to lowering emissions. Thus, it lessens the impact on the anthroposphere and aids preserving the environment.

Turbulence has also a strong influence on the dispersion of air contaminants in urban areas. A source of pollution, for example, is the smoke from a chimney as shown in Figure 1.4(d). Moreover, there are other severely hazardous possible scenarios caused by the accidental or deliberate release of chemical or biological substances. Environmental disasters and life threatening agents are propagated not only by means of airflow: turbulent transport and turbulent mixing also occurs on the open sea. Photograph 1.4(e) was taken in 1976 when the oil leaking from the grounded tank-ship *Argo Merchant* endangered the surrounding marine life. Today, the effective containment of the consequences of such catastrophes still poses a challenge and a solid grasp of turbulence can be critical.

The list of examples is not exhaustive and could be extended further, also including internal turbulent flows such as pipe flows or natural convection in buildings. In fact, almost any engineering application concerned with fluid flows falls in this category because turbulence is the rule, not the exception in fluid dynamics.

1.2.3 Characteristics of Turbulence

The range of applications presented in the previous sections seems overwhelming and exposes one important fact. Turbulence is not coupled with a specific fluid, but it is a feature of fluid flow. Its dynamics is independent of the type of fluid and the characteristics of turbulent flows are not affected by the molecular properties of the liquid or gas under consideration. Thus, turbulent flow is an aspect of continuum mechanics, more precisely fluid mechanics, and the common characteristics serve as criteria for distinguishing between a laminar and a turbulent regime.

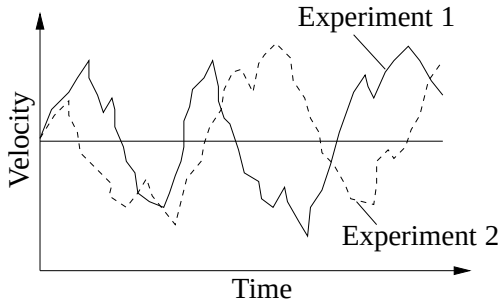

Figure 1.5: Two typical velocity histories obtained under identical experimental conditions (after Davidson [21]).

Randomness. No clear line can be drawn, however, because every turbulent flow has, in addition to the common characteristics, certain unique characteristics associated with its initial and boundary conditions. This point is illustrated in Figure 1.5, showing a typical velocity measurement obtained in an experiment. Although the measurement can be repeated under seemingly identical conditions, the velocity history does not match the previous experiment because of minuscule variations during the execution. Yet, both realisations exhibit a common feature: the time-averaged values of the signals

acquired are identical. The random character of the unsteady, irregular motion in space and time is probably the most cited attribute of turbulence. Its randomness is the reason why much of the research has to rely on statistical methods and no general solution, e.g. through a deterministic approach, can be found.

Vorticity and Dissipation. In addition to the chaotic motions, organised motions occur at random locations and different points in time. These well-defined regions of strong coherent structures are rotational and offer a high level of fluctuating vorticity. Therefore, vortex dynamics, an inherently three-dimensional phenomenon, plays an important role in the investigation and prediction of turbulent flows. The large vortices are continually forming and breaking down into smaller ones, which break down into yet smaller vortices until they dissipate into heat. This process is depicted in Figure 1.6(a) and the associated energy spectrum is shown in Figure1.6(b). All turbulent flows are essentially dissipative and transfer energy over a broad range of scales, i.e. from the large eddies to the small eddies. Hence, the large vortices need a continuous supply of energy from the surrounding fluid or they will simply decay.

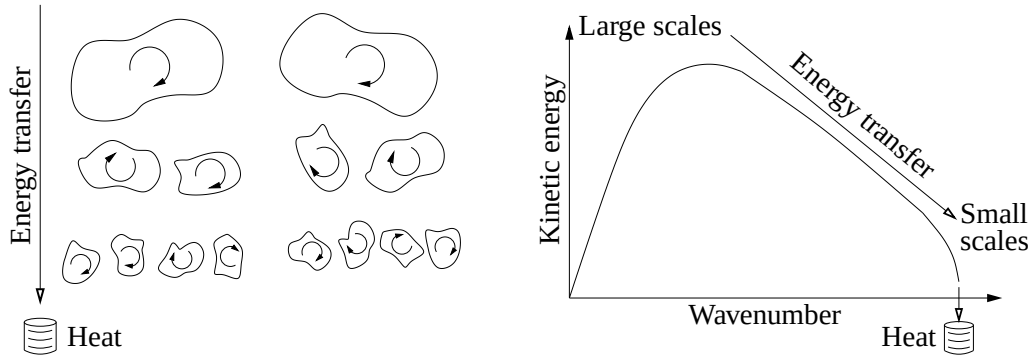

(a) Transfer of kinetic energy in physical space.

(b) Logarithmic scale of the kinetic energy distribution in spectral space.

Figure 1.6: Schematic representation of the energy transfer from large to small scales (after Davidson [21]).

Diffusivity and Mixing. Another aspect is directly related to the agitation induced by the various scales observed in turbulent flows: the transport of mass, momentum and energy is greatly enhanced due to convective effects. Consequently, the surrounding fluid will be entrained and the velocity fluctuations spread in space. This is the basis of the large mixing capacity and rapid dispersion in turbulent flows.

Determinism. Turbulence is often referred to as the most complex problem remaining in classical physics and despite decades of research the prospect of a general solution still seems distant, if not impossible. The difficulty lies in the interference of high-level random background motions with the unsteady coherent structures. This combination leads to inherently non-linear and non-equilibrium phenomena that cannot be tackled by currently available analytical methods. Hence, a simplified view of the problem has emerged, decomposing the flow-field into mean velocity and fluctuating velocity. This concept has been proven useful in developing theoretical and

numerical models, but it should be noted that it is by no means an exact representation of reality.

1.2.4 Scales of Turbulence

As discussed above, turbulent flow is characterised by a distribution of coherent vortical structures of various sizes and the vortex dynamics associated with the respective scales of the eddies. Assuming turbulence is composed of eddies of different sizes, the physical behaviour illustrated in Figure 1.6 can be described by *Richardson's hypothesis* of an energy cascade, see Richardson [95]. Although the concept of an energy cascade cannot be formally proven, it is a self-consistent theory that has been verified by numerous experimental investigations.

Richardson's Hypothesis. From Richardson's point of view, the velocity and the size of the largest eddies present in the flow are comparable to the global scales of the mean flow. The Reynolds number for the largest scales is therefore comparable to the global Reynolds number, i.e. $Re >> 1$, and viscous forces have a negligible effect. The large eddies are generally anisotropic and their shape is dependent on the boundary conditions. Since the surrounding fluid constantly feeds energy to the large scales and no dissipation can take place here because of the high Reynolds number, the energy must be transferred to a smaller scale. The rate of energy transfer and thus the rate of energy production can be estimated on the grounds of dimensional arguments. The energy contained in the large scale is of order u^2 and the lifespan can be expected to be of the order of one eddy turnover time $\tau = \ell/u$, where u and ℓ are the characteristic velocity- and length-scale of the eddy, respectively. Consequently, the rate at which energy is passed on to the smaller scales can be assumed to be of the order $u^2/\tau = u^3/\ell$. This energy transfer is often illustrated in physical space as eddy break-up, where the inherently unstable coherent structures deform and evolve into eddies of smaller size, see Figure 1.6(a). The smaller eddies pass through the same process again and the energy is transferred to progressively smaller and smaller scales — hence the name energy cascade. The cascade is driven purely by inertial forces until the Reynolds number becomes sufficiently small for viscous effects to interfere. At a Reynolds number of order unity, the molecular viscosity takes an active part and the kinetic energy is dissipated. As the intermediate scales of the flow only forward kinetic energy, dissipation occurs only at the smallest scale at a rate ϵ dictated by the energy production at the largest scale, i.e. ϵ is independent of the molecular viscosity and is of order u^3/ℓ.

Kolmogorov's Hypotheses. In order to obtain a more quantitative picture, the idea of an energy cascade has been developed further by Kolmogorov [64]. The assumptions on the physical behaviour of the eddies made in *Kolmogorov's hypotheses*[2] provide the framework for assessing the energy transfer rate and the scales involved in high Reynolds number, turbulent flows.

[2] *"At sufficiently high Reynolds numbers there is a range of high wavenumbers where the turbulence is statistically in equilibrium and uniquely determined ... this state of equilibrium is universal."*

Kolmogorov stated that the anisotropy, induced on the large scales by the boundary conditions, is gradually lost as the energy is transferred to progressively smaller eddies. The flow eventually becomes locally isotropic for the smallest scales of motion away from the boundaries and flow singularities; thus the small eddies have a statistically universal character common to all turbulent flows. The statistics mainly depend on the energy budget composed of the energy flux from the larger scales and viscous dissipation. Provided the small scales have a relatively short lifespan compared to the global time-scale, they are able to adapt quickly to the amount of energy received from the larger eddies and a dynamically balanced budget can be maintained.

As a consequence, the energy transfer rate is approximately equal to the heat dissipation rate ϵ and the viscous dissipation can be determined using the molecular viscosity ν. These are the two dominant parameters characterising the smallest scales in the flow, also known as the Kolmogorov scales. Dimensional reasoning leads to the following estimates for the Kolmogorov length-, velocity- and time-scales

$$\begin{aligned} \eta &\sim (\nu^3/\epsilon)^{1/4} , \\ u_\eta &\sim (\nu\epsilon)^{1/4} , \\ \tau_\eta &\sim (\nu/\epsilon)^{1/2} . \end{aligned}$$

The consistency of these relations with Richardson's Hypothesis can be verified by forming the Reynolds number based on the Kolmogorov scales. According to Richardson dissipation takes place only at the smallest scales, hence Re_η has to be of order unity because the molecular viscosity plays an active part in the physical process involved and the inertial forces no longer prevail.

The Kolmogorov scales can now be related to the largest scales present in the flow by recalling the scaling law for the viscous dissipation, i.e. $\epsilon \sim u^3/\ell$, yielding

$$\begin{aligned} \eta/\ell &\sim Re^{-3/4} , \\ u_\eta/u &\sim Re^{-1/4} , \\ \tau_\eta/\tau &\sim Re^{-1/2} , \end{aligned}$$

where Re is the flow Reynolds number. Since these ratios are always less than 1 for practical, turbulent flows, the velocity- and time-scales of the smallest eddies are always small compared to the corresponding scales of the largest eddies, as stated a priori.

Furthermore, the disparity between the largest and the smallest scales becomes more and more significant with increasing Reynolds number. As a consequence, there is a range of length-scales that are both small compared to ℓ and large compared to η. In this range the Reynolds number is sufficiently high that viscous effects can be neglected and the eddies only transfer energy from the larger to the smaller scales. Therefore, the statistics in this region are governed by a single parameter only, the dissipation rate ϵ, and no universal length-, velocity- or time-scales can be formed. It is often convenient, however, to characterise the intermediate range by defining a length-scale that is much smaller then the ℓ and much larger than η. This length-scale, commonly known as

the *Taylor micro-scale*, describes the mean spatial extent of the velocity gradients and is not related to any scales where dissipation takes an active part. Analysis of the energy budget composed of the energy transfer rate from the anisotropic, large scales and the viscous dissipation rate at the isotropic, small scales confirms that the Taylor micro-scale is indeed an intermediate length-scale given by

$$\begin{aligned} \lambda_T/\ell &\sim Re^{-1/2}\,, \\ \lambda_T/\eta &\sim Re^{1/4}\,. \end{aligned}$$

According to the idea of the energy cascade the energy flux has to remain constant over the range of intermediate length-scales because no energy is added by the mean flow and no energy is lost through viscous dissipation. The energy transfer rate for any given eddy-size is determined by the ratio of its characteristic velocity squared to its characteristic length, hence the velocity-scale, as well as the time-scale, decreases for progressively smaller length-scales.

Energy Spectrum. The distribution of kinetic energy over the scales observed in turbulent flows is usually described in spectral space. Here, the different length-scales are represented by their reciprocal value, the wavenumber k, and the velocity field is decomposed into a Fourier series. The energy contained in a specific length-scale in Fourier space, $E(k)$, is simply the product of the corresponding velocity, $u(k)$, with its complex conjugate. For this reason, the spectral analysis gives a clear picture of the distribution of energy over the whole range of length-scales.

In the kinetic energy spectrum, two main categories can be distinguished: the energy-containing range comprising the anisotropic large-scales (small wavenumbers) carrying most of the energy and responsible for the energy production process; and the universal equilibrium range containing the isotropic small-scales (higher wavenumbers). More precisely, the equilibrium range is subdivided into the dissipation range at the lower end of the scale (highest wavenumbers) where the Kolmogorov scales are located and essentially all of the viscous dissipation occurs; and the inertial subrange where neither production or dissipation of energy play an important role and the motions are dominated by inertial forces.

Figure 1.7 shows a schematic of a typical kinetic energy spectrum for turbulent flows, note that a logarithmic scaling has been employed. In the energy-containing range, turbulence accumulates kinetic energy at the very largest scales until the spectrum peaks at a characteristic length-scale of approximately the integral scale ℓ, a measure of the longest connection between two correlated velocities at different points in the flow. After the peak, the energy is then passed on to successively smaller scales by the cascading process. The shape of the spectrum in the production range is determined by the energy flux from mean to turbulent flow, i.e. the work of deformation of the mean motion by the turbulence shear stresses, and the energy transfer from large to smaller scales, i.e. the dissipation through the turbulent motion. Thus, the significant parameters here are the diffusivity of the mean flow, characterised by the strain rate S, and the dissipation rate ϵ. This definition of the energy production at the largest scales

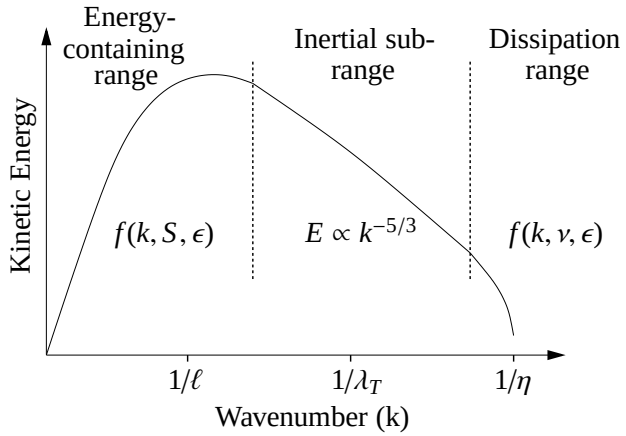

Figure 1.7: Schematic of a typical turbulent kinetic energy spectrum for turbulent flows plotted with logarithmic scales.

is not unique, however, because it highly depends on the properties of the mean motion and the boundary conditions.

This situation does not improve for the smallest eddies. It is known that the dynamics at the highest wavenumbers are governed by the amount of energy received from the larger scales and viscous dissipation. Since the energy transfer rate is equal to the dissipation rate ϵ, the dominant parameters in the dissipation range are ϵ and the kinematic viscosity ν. Hence, the energy spectrum at the Kolmogorov scales is inescapably coupled with the characteristics of the fluid.

In between the energy-containing and the dissipation range lies the inertial subrange. Here, in agreement with the concept of an energy cascade, the kinetic energy is transferred to progressively smaller scales. The extent of this range depends on the flow as it becomes greater or smaller with increasing or decreasing flow Reynolds number, respectively. However, the single important parameter determining the statistics within the inertial subrange, the energy flux from large to small scales, is flow independent. Kolmogorov realised the consequences and used dimensional arguments to derive an analytical form for the energy spectrum in the inertial subrange given by

$$E(k) = C\epsilon^{2/3}k^{-5/3} \ ,$$

where C is a universal constant. This general power-law spectrum postulated by Kolmogorov has been confirmed by numerous experimental and numerical investigations and is considered a cornerstone in the analysis of turbulent flows.

The relations presented here strictly hold only for homogeneous, isotropic and statistically steady flows. However, it has been found that the estimates can still be applied even if the flow does deviate from its ideal state.

1.3 Numerical Approaches

Although many experimental and theoretical studies in the past decades have significantly increased the current physical understanding, simulations fail to accurately and reliably predict turbulent flows in many cases. The absence of a closed theory and a universal turbulence model, which are unlikely to emerge in the near future, seriously limits the technological progress of aircraft and car design, turbo-machinery and combustors as well as the prediction of environmental and biological flows. Thus, the modelling techniques and the underlying understanding of the physics of turbulent motion still have to be improved considerably. In the context of Computational Fluid Dynamics (CFD), there are generally three classic techniques: the Direct Numerical Simulation (DNS), the Reynolds-Averaged Numerical Simulation (RANS) and the Large-Eddy Simulation (LES). The applicability of these standard numerical approaches to separated, turbulent flows, as well as their general advantages and disadvantages, will be briefly discussed in this section. Additionally, the Implicit Large-Eddy Simulation (ILES) approach employed in this thesis will be introduced.

1.3.1 Direct Numerical Simulation (DNS)

The DNS approach provides a complete time-dependent solution for turbulent flows. It is conceptually the simplest of the three and provides superior accuracy because all scales of motion and time are resolved, given it is free of significant numerical or other errors. In order to represent all scales numerically, the discretisation of the governing equations has to be at least as fine as the exact solution. As a result, the step-size of the discretised problem in time and space must be smaller than the characteristic time and the characteristic length of the smallest eddies present in the flow. Additionally, the duration of the simulation and the size of the computational domain are determined by the characteristic time and the characteristic length of the largest, energy-containing eddies, which can differ substantially from the size of the time- and space-step. Since the range of scales observed in turbulent flows increases with progressively higher Reynolds number, it usually spans over several orders of magnitude — hence the resolution criterion limits the applicability of DNS to low Reynolds number, turbulent flows.

The number of points required for a numerical simulation depends on the spatial resolution and the size of the flow field. In case of DNS, every scale has to be resolved, hence the distance between the sampling points cannot exceed the Kolmogorov scale; and the computational domain should ideally have an extent of several times the characteristic length of the largest eddies present in the flow. A conservative estimate for the number of grid points in one dimension for homogeneous turbulence can therefore be deduced from Kolmogorov's hypotheses, stating that the ratio of large to small length-scale is approximately proportional to $Re^{3/4}$. Turbulent flows are inherently three-dimensional, thus the number of grid points required for a for a fully three-dimensional DNS scales with $Re^{9/4}$. Additionally, for estimating the total computa-

tional cost, the duration of the simulation must be taken into account. It should be proportional to the integral time-scale of the flow, but at the same time the step-size is limited by the need to resolve the short lifespan of the smallest eddies and numerical stability criteria. Numerical stability strongly depends on the choice of time-advancement method. For the sake of simplicity, however, the fluid is assumed to be able to move the distance of one grid spacing per time step without violating the stability constraint. It can be shown that the above conditions lead to a minimum number of time steps of the order of $Re^{3/4}$. Since the total number of operations required for a simulation is proportional to the product of number of grid points and number of time-steps, the total cost of the DNS scales as Re^3. This estimate underlines the limitations of DNS due to a very rapid increases of its computational cost with the Reynolds number .

For wall-bounded flows, the dependence of the simulation cost on the Reynolds number is even stronger because of the stricter scaling laws in the near-wall region. Moin and Kim [83] estimated that a DNS of a transport aeroplane cruising at $250\,m/s$ at an altitude of $10,000$ meters would require approximately 10^{16} grid points to adequately resolve every length-scale. Based on exclusive access to one of today's fastest supercomputers capable of 100 teraflops, it would take several decades to compute the flow for only one second of flight time, which clearly exceeds any acceptable time limit. In typical practical problems, however, engineers and designers are rather interested in the effects of turbulence on the properties of the mean flow, not so much the dynamics of the smallest eddies. Therefore, it is common practice to significantly relax the resolution requirements of numerical simulations by resolving only the larger scales and introducing the effects of the smaller scales by additional models. This approach leads to the two main techniques that are able to predict turbulent flows at higher Reynolds number: Reynolds-Averaged Numerical Simulations and Large-Eddy Simulations.

1.3.2 Reynolds-Averaged Numerical Simulation (RANS)

The most common approach to calculate a problem in engineering is the Reynolds-Averaged Numerical Simulation. Reynolds averaging is based on the idea of decomposing the exact solution of the flow into a statistical average and a fluctuating turbulent component. The averaging procedure cannot be uniquely defined because it depends on the type of problem, e.g. it could be a time average for a statistically steady flow, a spatial average for essentially two-dimensional flows, or an ensemble average for a family of similar flows.

In case of engineering applications, the controlled conditions such as inlet conditions in internal flows or free-stream conditions in external flows rarely change in time, thus time-averaging is preferred. Here, the resolved mean flow can be considered free of fluctuations and all the unsteadiness is contained in the unresolved turbulent scales that need to be modelled. Modelling is necessary because the averaging procedure introduces additional unknown terms in the governing equations that cannot be computed exactly from the mean flow variables. As a result, the averaged equations are always complemented by additional turbulence models that mimic the effects of the unsteady

motions. Since RANS requires the least possible amount of resources it gained enormous popularity in steady-state computations where the turbulence is stationary, e.g. see Leschziner [67], Mallinger and Drikakis [75].

In unsteady flows, a time-scale associated with the organised unsteady motion exists and must be well separated from the time-scale of turbulent motion. Here, the exact solution can be seen as the sum of three contributing terms: the time average, the conditional average of the coherent motion and the random fluctuation due to turbulent motion. However, very few unsteady flows are guaranteed to exhibit deterministic low-frequency motions that can, for example, be enforced externally through periodically changing inflow or free-stream conditions. If applicable, the conditional average in Unsteady Reynolds-Averaged Numerical Simulations (URANS) is therefore usually interpreted as a phase-averaged solution and the closure models are formally identical to the ones in steady-state computations.

The function of turbulence modelling in RANS is to devise approximations for the unknown correlations between mean flow and fluctuating component, the so-called Reynolds stresses, in order to close the system. The closure relations are based on combinations of known or determinable geometric parameters, flow scales and strains. However, these quantities are not able to completely represent the complex physical structures and interactions inherent to turbulent flows; hence it seems unlikely that any single model will successfully predict all types of turbulent flows with any degree of certainty. For this reason, numerous turbulence models have been developed over the past decades, all introducing a number of unknown coefficients. In order to adjust the models to particular flows, the unknowns are usually determined empirically by calibration against existing experimental and DNS data.

In recent reviews by Leschziner [67], Mallinger and Drikakis [75], the performance of several turbulence models, spanning from one- and two-equation linear eddy-viscosity models to more advanced non-linear eddy-viscosity and Reynolds-stress models, was discussed. Although the linear eddy-viscosity models often fail to adequately predict complex flows featuring separation, free shear layers and vortical flows, they are most commonly employed due to their relatively simple and robust character. More generally, despite extensive research in the area of turbulence modelling, currently available methods are still unreliable when applied without careful, problem-specific calibration prior to the simulation. Therefore, all existing turbulence models should be regarded as more or less sensible approximations of reality rather than scientific laws. The incapability of RANS to consistently produce successful simulations of turbulent flows is the reason for a reorientation of the current research focus to a more rigorous approach that became feasible with the ever-increasing computing power observed over the past years: Large-Eddy Simulations.

1.3.3 Large-Eddy Simulation (LES)

The development of Large-Eddy Simulations is motivated by the limited applicability of DNS and RANS to turbulent flows and it can be regarded as an intermediate between both approaches with respect to accuracy and computational cost. In contrast to RANS, classical Large-Eddy Simulations model only the small-scale turbulent motions whereas the larger turbulent structures are directly resolved. Since the smaller structures are only slightly affected by the boundary conditions, they exhibit a more common character for different types of flows. Thus, the models employed in LES tend to be more universal and require fewer adjustments to the specific flow compared to a similar RANS model. On the one hand, the LES strategy provides superior accuracy, on the other hand, however, higher precision also comes at a higher computational cost than RANS.

Similar to the Direct Numerical Simulations, Large-Eddy Simulations provide a fully three-dimensional, time-dependent solution. As demonstrated previously, the grid requirements for DNS strongly depend on the smallest scales present in the flow, but most of the turbulent kinetic energy is contained in the larger structures. Therefore, while computing the large-scale dynamics of the flow directly, LES significantly reduces the total computing time by modelling the less energetic, but computationally demanding, small scales. It is possible now to calculate more complex turbulent flow scenarios that are forbiddingly expensive for direct simulations without having to take a drastic accuracy penalty. Ideally, the computational cost of LES is independent of the Reynolds number, given that the reference length distinguishing the resolved, large scales from the modelled, small scales lies in the inertial sub-range and that no solid walls are present.

Formally, in classical LES the governing equations are filtered by convolving all dependent variables with a predefined filter. The filtering operation decomposes the flow field into the sum of a filtered, resolved component and a residual, subgrid-scale component. The spatial and temporal evolution of the filtered component representing the large scales is fully described by the filtered equations, and the unknown subgrid scale (SGS) stress tensor arising from the unresolved residual motions needs to be modelled. This system is commonly closed by more or less sophisticated SGS models that are primarily concerned with reflecting the dissipation of energy cascading down from the larger scales in a statistical sense.

When deriving the classical LES equations, it was implicitly assumed that differentiation commutes with the convolution, see Fureby and Tabor [38], Ghosal and Moin [41]. However, this is not valid at solid boundaries and for a variable filter kernel. The former requires reality to be modelled in a finite domain, which introduces commutation errors in the spatial derivatives. If the finite domain changes in time, additional errors in the temporal derivatives arise. A variable filter kernel could solve the problems at solid boundaries by reducing the filter width in order to resolve the small scales. This procedure violates the above commutation assumption and introduces new errors, which can be removed by correction terms. Yet, there are no available methods to tackle the

correction terms and thus previous work, e.g. by Van der Ven [117], Vasilyev et al. [121], has been aiming at filters that can eliminate these terms.

Furthermore, like in all numerical approaches, errors in classical LES arise from the approximation of the variables on a finite basis and numerical discretisation. For discretising the governing equations, the differentiation operators are substituted by numerical approximations, which lead to dissipation and dispersion terms, see truncation error analysis in Anderson [3]. The dissipation terms are responsible for the numerical diffusion, especially near discontinuities, whereas the dispersion terms produce oscillations near discontinuities. Drawbacks of conventional LES also arise from SGS modelling, the possible masking of the SGS terms by the leading order truncation error and the difficulties in devising SGS models for complex high Reynolds number wall-bounded flows.

1.3.4 Implicit Large-Eddy Simulation (ILES)

The Implicit Large-Eddy Simulation approach is based on a similar scale selection than classical LES. Here, however, it is assumed that the numerical discretisation on a computational grid implicitly separates large and small scales. Thus, no explicit filtering is necessary and the subgrid scale stress tensor found for classical Large-Eddy Simulation is absent in ILES. Yet, the unresolved motions need to be accounted for by the numerical method. This is generally achieved through adaptive, non-linear regularisation of the solution to the governing conservation laws. More details on Implicit Large-Eddy Simulation and the basic principles of the numerical methods employed here will be given in Chapter 2.

1.4 Objectives and Outline

This thesis aims at assessing the performance of high-resolution methods in predicting low-speed, separated turbulent flows in a physically realistic manner even if they are not fully resolved on the computational mesh. The numerical framework for this study is provided by the Implicit Large-Eddy Simulation approach.

Separated flows are inherently linked to the transition from well-organised flow regions to highly disorganised unsteady flow regions known as turbulence. From an engineering point of view, the accurate and efficient prediction of shear layers and jets, vortex shedding, unsteady wakes and unsteady shock/boundary layer interactions amongst others is of primary technological importance. Traditionally, experimental work dominated the research in this area because it was the only approach capable of dealing with the complexity of such flows. However, the tools for quantitative measurements are limited and until recently most of the analysis was based on qualitative arguments. Additionally, theoretical models complemented the experimental results for idealised flows.

With the advent of high performance computing facilities and the progress in microprocessor technology, computational fluid dynamics became a viable alternative to experiments. However, despite the rapid advancements made in these areas, CFD is still far from being able to fully resolve separated turbulent flows to date and this will not change in the foreseeable future. Thus, the governing equations need to be supplemented explicitly or implicitly by numerical models or mechanisms that emulate the effects of the unresolved scales. Because of the complex physics involved, no universal model has been found yet and, as with the experimental tools, the numerical tools need further improvement.

The main aspect of this thesis is to investigate different solution strategies for the governing equations based on high-resolution methods. This class of numerical schemes provides built-in subgrid scale models that may offer a better approach than explicit treatments. The success of high-resolution methods to compute turbulent flows seems to depend on a delicate balance of truncation errors due to wave-speed-dependent terms (chiefly responsible for numerical dissipation) in the case of Godunov-type methods and hyperbolic part of the flux. In the context of high-fidelity ILES, it is essential to improve the current understanding of the mechanisms that safeguard the simulation against catastrophic failure by triggering entropy production when the need arises.

The thesis is organised as follows:

Chapter 2. The concept of high-resolution methods is presented and a rationale for the Implicit Large-Eddy Simulation approach is given.

Chapter 3. The three-dimensional Navier-Stokes Equations are introduced and the numerical solution procedure is presented.

Chapter 4. In this chapter, the behaviour of different high-resolution methods is assessed in the context of transition to turbulence for the generic Taylor-Green Vortex.

Chapter 5. The capability of high-resolution methods to predict separation from gently curved surfaces are discussed in this chapter. The test case considered here is a channel with hill-type constriction, a classic case for wall-bounded flows.

Chapter 6. Results from a fully three-dimensional simulation featuring leading edge separation on a swept wing are shown and compared against experimental and available LES data.

Chapter 7. A summary of the thesis is presented, conclusions are drawn and recommendations for the future work are made.

In addition, details related to the numerical scheme, complementary material to the results presented and a list of publications to date are included in the appendices.

CHAPTER 2

High Resolution Methods and Implicit Large-Eddy Simulations

IN recent years, the focus in turbulent flow simulations has become the fidelity and the robustness of the computations. Physically meaningful results should be obtained within an adequate accuracy relative to the computational resources utilised. A further desire is the applicability of the numerical method to a broad range of problems. This implies that the method should behave smoothly even if the expected accuracy cannot be met, thus it should still produce reasonable results and not fail catastrophically. One way to achieve these goals is the use of high-resolution methods in Large-Eddy Simulations of turbulent flows.

2.1 A Glimpse into History

A previous study by Drikakis and Durst [26] shows a dependency of the numerical accuracy not only on the turbulence model employed, but also on the discretisation of the advective terms in the governing equations. In fact, the first awareness of a coupling between the numerical properties of high-resolution methods and an intrinsic subgrid turbulence model has been expressed almost two decades ago by Youngs [128] [1] and Boris [9] [2]. Since then, more evidence that the use of high-resolution methods in LES offers characteristics that mimic the effects of finite viscosity and appear to achieve many of the SGS properties has emerged.

Porter et al. [91] have been among the first to utilise this attribute of the numerical schemes in simulations of compressible isotropic turbulence. The motivation behind this investigation stems from an astrophysical background: this problem can be seen as a simplified description of the formation of stars from dense clouds of interstellar gas. Here, the performance of high-resolution methods has been compared against pseudo-spectral computations and the flow field has been interpreted in terms of the evolution

[1] "*... the method ... introduces non-linear numerical diffusion into the calculation which plays a similar role to the subgrid eddy viscosity used in large eddy simulation of turbulent flow.*"

[2] "*It is my experience that nonlinear monotone CFD algorithms really have a built-in filter, and a corresponding built-in SGS model.*"

of coherent structures. Additionally, spectral and statistical data has been extracted and analysed. More information can be found in Porter et al. [92, 93].

In a similar fashion, the classical case of incompressible decaying homogeneous turbulence has been studied, e.g. by Margolin et al. [78]. The same authors also applied this approach to geophysical flows. Margolin et al. [77] have shown comparisons between simulations with and without explicit SGS model for an atmospheric boundary layer. The results revealed that the numerical method employed is able to adapt itself to the local conditions — thereby the numerics implicitly ensure that both solutions are in agreement with benchmark simulations. These studies have been pursued further and the range of test cases has been extended by Smolarkiewicz and Margolin [106] to the convective planetary boundary layer over a hill and by Smolarkiewicz and Prusa [107] to gravity wave induced turbulence.

Early computations by Youngs [129] have demonstrated that this particular family of schemes is also applicable to the growth of instabilities and turbulent mixing observed in the Rayleigh-Taylor problem. The Rayleigh-Taylor instability occurs when the interface between two fluids of different density is subject to an increasing pressure in direction of the lighter fluid. The simulations produce excellent data when compared to experiments. This result could be confirmed later for the Richtmyer-Meshkov problem, see Youngs [130]. Here, the instability growth is triggered by a shock wave passing through the interface as opposed to the existing pressure gradient in Rayleigh-Taylor.

Further evidence has been compiled by Boris et al. [10]. This group of researchers initially focused on the transition from laminar initial conditions to turbulence and the vortex dynamics observed in free shear flows. Key papers here are concerned with the development of mixing layers, Grinstein et al. [50], coherent structures and turbulent features in free jets, Grinstein and DeVore [47], and chemically reacting flow, Grinstein and Kailasanath [49]. More recently, wall-bounded problems pertinent to practical engineering flows have been considered. The results from simulations performed by Drikakis [25], Fureby and Grinstein [37], Grinstein and Fureby [48] for an open cavity, plane channel and backward facing step, respectively, have been encouraging and the prospects for the future are promising, albeit these studies have been limited to simple geometries.

All the above investigations prove the applicability and effectiveness of high-resolution methods for a broad range of turbulent flow problems. In addition to the overwhelming computational evidence, rigorous analytical justifications of the similarity between the effects of this class of numerical schemes and the properties of explicit SGS models have been attempted, e.g. see the works of Drikakis and Rider [27], Fureby and Grinstein [36], Margolin and Rider [76].

This new insight into the numerical algorithms led to the following question: When high-resolution methods are employed for solving the governing equations of fluid dynamics, are the physical effects of subgrid scale motions in turbulent flows embedded in the numerical mechanisms involved? As a consequence, the idea to use these methods as an implicit way to numerically model complex turbulent flows, e.g. flows dom-

inated by massive separation and vorticity leading to turbulence, flows featuring shock waves and turbulence, and the mixing of materials, was born. This is an evolving area of research referred to as Implicit Large-Eddy Simulation (ILES) or Monotonically Integrated LES (MILES), for a recent review see also Grinstein et al. [51]. The success of high-resolution methods to compute such flows that are extremely difficult to practically obtain stably and accurately in spatially under-resolved conditions seems to depend on: (i) the discretisation of the governing equations in the framework of a finite volume algorithm and (ii) the fundamentally non-linear nature of the non-oscillatory approximations in high-resolution methods which are able to adapt themselves to the local solution.

In order to establish a better understanding of the physical relevance of the discretisation method and the numerical solution approach in ILES to the effects of the SGS motions and their modelling, the concepts of finite volumes and high-resolution methods will be introduced in the following sections.

2.2 The Concept of Finite Volumes

Finite volume methods are a class of discretisation schemes that have proven highly successful in approximating the solution of a wide variety of partial differential systems, especially in the area of fluid mechanics, e.g. see Ferziger and Perić [34], Lomax et al. [72]. The underlying concept is to divide the domain of interest into a finite number of control volumes and to successively solve the governing equations for each element. Faces common to two control volumes separate one from the other, thereby forming seamless connections throughout the domain. In contrast to finite difference methods, the elements can be of arbitrary shape, polyhedral in three dimensions or polygonal in two dimensions, thus finite volumes are naturally suited for unstructured grids and complex geometries.

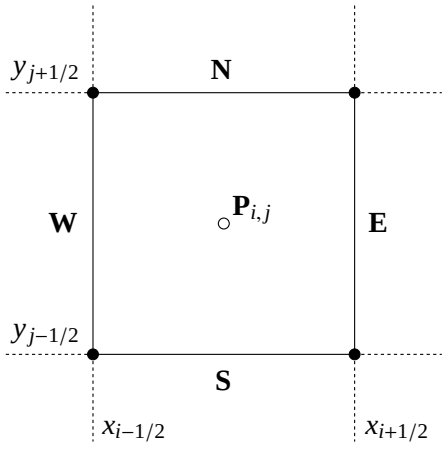

Figure 2.1: Control volume in the context of a finite volume algorithm.

Figure 2.1 illustrates a control volume in two dimensions, for the sake of simplicity a

three-dimensional schematic has been omitted. The control volume in two dimensions is bounded by the four grid lines North ($y_{j+1/2}$), South ($y_{j-1/2}$), East ($x_{i+1/2}$) and West ($x_{i-1/2}$), or, accordingly, six faces in three dimensions. The variables of interest are calculated for the computational node $\mathbf{P}_{i,j}$, located at the centre of the volume, whereas the computational grid points are stored at the intersections of two bounding lines in two dimensions, see filled circles in Figure 2.1, or the intersections of three bounding surfaces in three dimensions.

In fluid dynamics, the governing equations are applied in their conservative, integral form. This form has several advantages over a non-conservative, differential formulation. For example it allows for discontinuities within the control volumes and facilitates the numerical calculation of the variables across shock waves. Since the physical laws obey the basic principle of conservation, the rate of change of a property inside the control volume has to be equal to the net flux across the boundary of the element due to convection or dissipation and the effects of external forces such as pressure or gravitation. In order to satisfy this condition in a discrete sense, the values at the centre of the control volume represent the volumetric average of the flow properties in the element and the fluxes are numerically integrated over the bounding faces. The fluxes and force effects entering a control volume through one face are theoretically identical to those leaving the adjacent element — hence the discretisation is conservative by construction and no further conditioning is necessary.

The numerical evaluation of the fluxes requires an approximation of the variables at the boundaries of the control volume. This reconstruction step utilises the information stored at the cell-centred points $\mathbf{P}_{i,j}$ to generate a piecewise approximation of the flow properties inside the element. As a result of this approximation, the two fluxes over one face as calculated by the adjacent volumes are generally not identical and some strategy has to be applied to model this discontinuity. A straightforward procedure would be to simply take the arithmetic average of the two fluxes. However, this idea neglects the need for numerical dissipation to stabilise the solution and more models would be required. Another possible approach to this problem is to incorporate the physics of jump discontinuities into the solution process, e.g. through the use of high-resolution methods.

2.3 High-Resolution Methods

Modern high-resolution methods emerged from the search for a new family of numerical schemes that meet two seemingly contradictory targets: the desire for a highly accurate simulation and the preservation of monotonicity, a basic property of the exact solution. This predicament was summarised by Godunov [42] in his famous theorem "*There are no monotone, linear schemes of second or higher order of accuracy*". While linear higher-order methods provide superior accuracy to first-order methods in smooth regions of the flow, they produce spurious oscillations near high gradients, see Figure 2.2. Monotone, first-order methods, on the other hand, avoid spurious oscil-

lations, but they are too inaccurate for practical simulations. The key to circumvent Godunov's theorem can be found in the statement itself. In fact, a *non-linear* scheme is able to combine the high accuracy provided by a higher-order method with the non-oscillatory, monotone character of a first-order method.

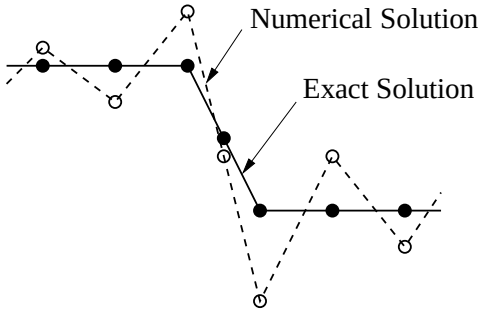

Figure 2.2: Spurious oscillations in the numerical solution in the vicinity of high gradients (after Toro [115]).

Fundamentals. In order to minimise the oscillations in the vicinity of high gradients, modern high-resolution methods employ non-linear differencing techniques, e.g. see Drikakis and Rider [27], Harten [54], Toro [115]. Here, the finite difference stencil, a function of both space and time, is based upon the behaviour of the local solution and does not produce uncontrolled oscillations. This is the distinguishing feature between a high-resolution method and other non-linear methods that are not considered high-resolution. A non-linear, non-high-resolution method can lead to an ill-behaved solution when it encounters high gradients and the result can be unpredictable. High-resolution methods, on the other hand, adaptively select a differencing operator that ensures a well-behaved solution and produces high-fidelity results. In other words, high-resolution methods provide physically meaningful results in all flow regions, even in the vicinity of high gradients which, in the absence of shocks, is usually an indication of insufficient spatial resolution typical for any LES or RANS simulation of turbulence. Harten [54] formally defined high-resolution methods as schemes satisfying the following properties:

- Provide at least second order of accuracy in smooth areas of the flow.
- Produce numerical solutions (relatively) free from spurious oscillations.
- In the case of discontinuities, the number of grid points in the transition zone containing the shock wave is smaller in comparison with that of first-order monotone methods.

Solution Procedure. The high-resolution methods employed in this thesis are all based on the pioneering work of Godunov [42]. He was the first to utilise the solution of the local Riemann problem encountered in the discretised formulation of the governing equations. The classical Godunov method is only first-order accurate, but its physical foundation attracted a great deal of interest. Consequently, the approach was

developed further in the following decades and higher-order Godunov-type methods appeared, e.g. see van Leer [120].

Figure 2.3 outlines the basic solution procedure for a Godunov-type, high-resolution algorithm employed in a finite volume framework. The concept of finite volumes introduces a piecewise constant discretisation, representing the volumetric averages of the continuous, "real" problem, see Figure 2.3(a). This would be the initial situation for the classic first-order Godunov method. However, high-resolution methods include an interpolation step, depicted in Figure 2.3(b), often referred to as high-order reconstruction or limiting. The interpolation step essentially leads to a subgrid distribution for the discretely sampled data and thus it increases the accuracy of the method. All Godunov-type methods incorporate non-linear stability constraints for minimising or eliminating the problem of spurious oscillations, whereas the order of the method varies with the order of the spatial reconstruction. More specifically, a piecewise linear or quadratic interpolation generates a second- or third-order method, respectively, while methods of arbitrary order of accuracy can be obtained by piecewise polynomial reconstructions. Because high-order interpolation is based on the assumption of smooth flow, it is reduced to a first-order piecewise constant reconstruction in areas where this condition is not met. In fact, a higher-order reconstruction rather decreases than increases the order of accuracy in the vicinity of high gradients and shocks.

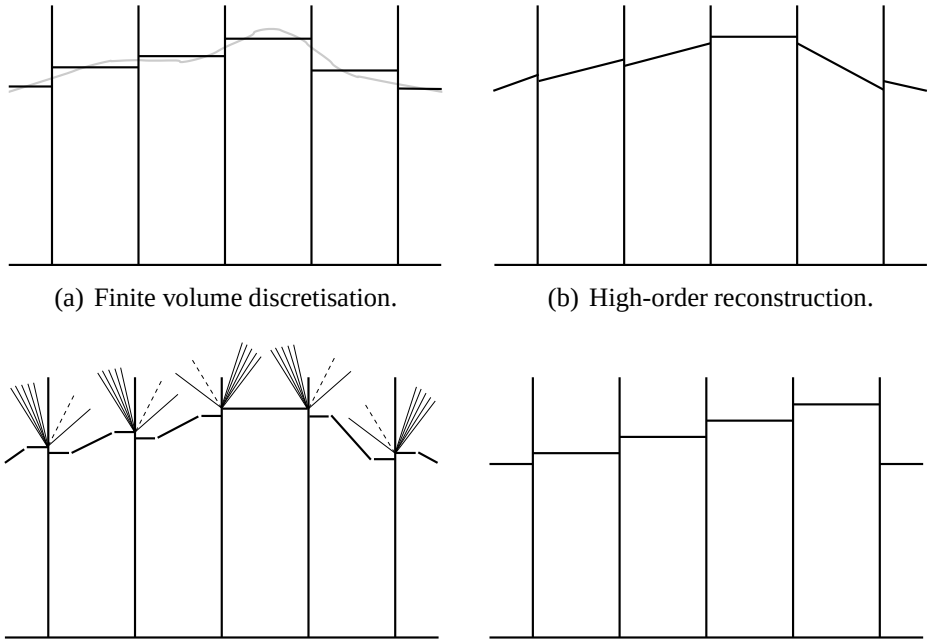

(a) Finite volume discretisation. (b) High-order reconstruction.

(c) Riemann solution. (d) Averaging.

Figure 2.3: Schematic of the basic solution procedure for a Godunov-type, high-resolution algorithm employed in a finite volume framework (after Drikakis and Rider [27]).

In practice, the reconstructed distribution still contains jump discontinuities at the cell faces. The left- and right-hand states of the discontinuity can now be regarded as two semi-infinite states similar to the initial value problem solved in shock-tube simula-

tions. Hence, this approach leads to a series of local Riemann problems at the cell faces, illustrated in Figure 2.3(c). For a perfect gas, the solution at the cell face can be determined by an elaborate exact Riemann solver. In order to reduce the computational cost of the solution and in more general cases, however, approximate Riemann solvers are usually preferred. In the final step of the procedure, the solution is averaged over the compuational cell in accordance with the concept of finite volumes, see Figure 2.3(d). This technique is philosophically appealing and owes its success to the combination of the reconstructed subgrid distribution and the physical aspects of the Riemann solver.

Monotonicity Preservation. As mentioned previously, the elimination of significant spurious oscillations is a fundamental aspect of high-resolution methods providing non-linear stability. This is generally achieved by preserving monotonicity in the numerical solution. A solution is said to be monotonicity preserving if it is monotone increasing or decreasing for all time if the initial condition is monotone increasing or decreasing, respectively. As a consequence, monotonicity preserving methods do not allow spurious oscillations if the initial conditions are monotone. In a numerical solution, however, the initial condition is not always monotone and the criterion does not address non-monotone solutions. Thus, the design of high-resolution methods sometimes relies on stronger conditions.

Total Variation Diminishing. In order to elucidate the principles of stronger non-linear stability conditions, it is useful to introduce the concept of total variation. The mathematical definition of the total variation of a discretised function in space and time, $\phi(x,t)$, at a time instant associated with a time step n is given by

$$\mathrm{TV}(\phi^n) \equiv \mathrm{TV}(\phi(t)) = \sum_{i=-\infty}^{+\infty} |\,\phi_{i+1}^n - \phi_i^n| \;.$$

In order to obtain a finite total variation, the function ϕ is assumed to be either 0 or constant as the index i, indicating the spatial discretisation on a numerical mesh, approaches infinity.

With the above definition in mind, a scheme is said to be Total Variation Diminishing (TVD) if the total variation of the solution does not increase in time. Mathematically, this can be expressed as

$$\mathrm{TV}(\phi^{n+1}) \leq \mathrm{TV}(\phi^n) \leq \ldots \leq \mathrm{TV}(\phi^0) \;,$$

where ϕ^0 is the initial condition at $t = 0$. It should be noted that the TVD constraint is not limited to non-monotone solutions. A trivial observation follows from considering a monotone initial condition: If the initial condition is monotone, the total variation remains constant and the solution is monotone for all time — hence the TVD condition implies preservation of monotonicity.

A major advantage of the Total Variation Diminishing constraint is that oscillations cannot grow indefinitely and they have to decrease in magnitude if new oscillations arise. Thus, the TVD concept imposes an upper bound on the size of the oscillations

and ensures stability of the scheme. Sometimes the TVD condition can be too weak, however, because it does not prevent the formation of new spurious oscillations. In this case, a more restrictive condition has to be applied.

Monotonicity. Figure 2.4 illustrates the strongest stability constraint using a linear reconstruction. For a monotone scheme, the piecewise profile of the solution is constrained between the cell average values of the adjacent cells. By considering a discretised scheme of the form

$$\phi_i^{n+1} = H(\phi_{i-l}^n\,,\,\phi_{i-l+1}^n\,,\,\ldots\,,\,\phi_{i+r}^n)\,,$$

the monotonicity property can be defined mathematically as

$$\frac{\partial H}{\partial \phi_j^n} \geq 0 \quad \forall \quad n\,,\; i-l \leq j \leq i+r\,,$$

where l and r are two non-negative integers and H represents an operator. The impact of the monotonicity condition on the solution can also be prescribed geometrically by the following two statements, see Drikakis and Rider [27], Toro [115]:

- No new local extrema may be created, thus spurious oscillations do not appear.
- The value of a local minimum increases, i.e. it is a non-decreasing function, and the value of a local maximum decreases, i.e. it is a non-increasing function.

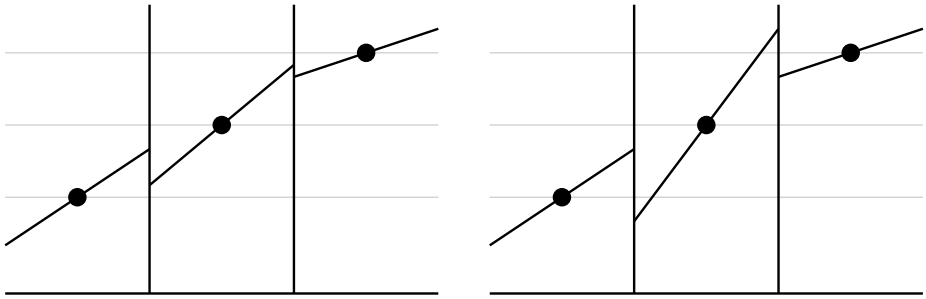

(a) Monotone scheme. (b) Non-monotone scheme.

Figure 2.4: Geometric representation of the monotonicity constraint (after Drikakis and Rider [27]).

In general, numerical methods can be classified according to the hierarchy of the nonlinear stability conditions they satisfy, see Drikakis and Rider [27]. For the constraints introduced here, the set of monotone schemes, $\mathcal{S}_{mon}$, is included in the set of TVD schemes, $\mathcal{S}_{tvd}$, and this is in turn contained in the set of monotonicity preserving schemes, $\mathcal{S}_{mpr}$, yielding

$$\mathcal{S}_{mon} \subseteq \mathcal{S}_{tvd} \subseteq \mathcal{S}_{mpr}\;.$$

2.4 The Riemann Problem

In order to retain the fundamental physical and mathematical character of the governing equations, high-resolution methods incorporate the exact or approximate solution to a local Riemann problem. Analytical solutions are available for several systems of equations and are often used as a reference for assessing the performance of numerical methods, e.g. the Euler Equations, scalar conservation laws or any linear system of equations. If the governing equations are more complex or if the computational cost of the Riemann solver is a concern, however, physical or mathematical approximations are inevitable. In practice, almost all Riemann solvers are of the approximate type and produce nearly identical results compared to the exact solution at a fraction of the cost, see Laney [65], Toro [115].

The Physics. The one-dimensional shock-tube problem consists of two regions of stationary fluid at different pressures. Initially, they are separated by a diaphragm which is considered to be removed instantaneously at $t = 0$. For $t > 0$, a wave system comprising three basic types develops: a rarefaction wave or expansion fan, a contact discontinuity and a shock wave. This physical problem can be solved by considering the Euler Equations. A generalisation of the shock-tube problem is also called the Riemann problem. Here, the fluid does not have to be stagnant at $t = 0$ and one or two of the wave types can theoretically be non-existent. However, the structure of the solution remains the same as for the shock tube problem by considering vanishing strengths for the absent waves.

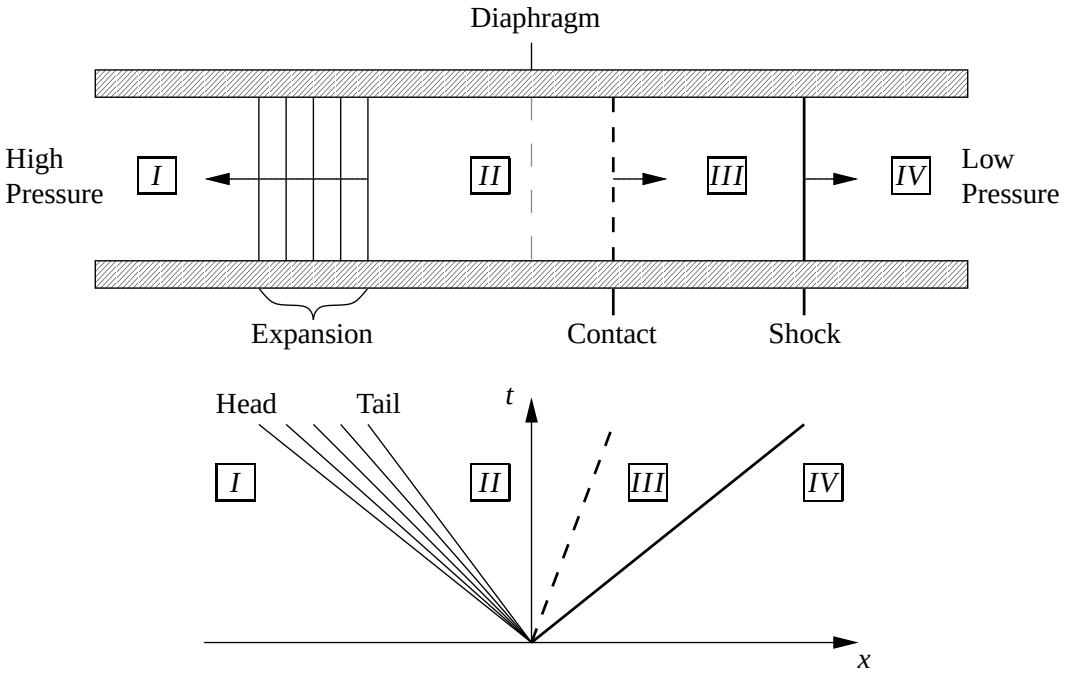

Figure 2.5: The shock-tube problem for the Euler Equations and corresponding wave diagram showing the characteristics in the *x*-*t* plane (after Laney [65]).

Figure 2.5 illustrates the shock-tube problem for the Euler Equations and the ideal gas law. In general, the solution can consist of four constant data states, I to IV, separated by the three basic wave types. It should be noted here that for the sake of clarity the waves in Figure 2.5 are sketched as straight lines which is an approximation to the non-linearity observed in reality. The states I and IV are defined by the initial condition at $t = 0$, whereas the states II and III are sought after. A left-running rarefaction wave or expansion fan, composed of diverging characteristics moving at a speed given by the difference of the local velocity and the local speed of sound $u(x,t) - a(x,t)$, decreases the pressure and the density within its bounds. The boundary on the high-pressure side, marked by the slope $u_I - a_I$, is called the head, and boundary on the low-pressure side, marked by the slope $u_{II} - a_{II}$, is called the tail. Inside the fan, the data follows a smooth, non-linear transition from state I to II, which can be determined by considering the Riemann invariants under isentropic conditions.

On the other side, a right-running shock wave can be observed. It is a non-linear wave that increases the pressure, the density, the temperature and the entropy as it passes through the fluid in state IV. Here, the shock wave is a jump discontinuity consisting of the converged characteristics given by $u(x,t) + a(x,t)$. This is a direct result of satisfying the entropy condition $u_{III} + a_{III} > s > u_{VI} + a_{VI}$, with s being the shock speed. The state III can be determined from state IV through the Rankine-Hugoniot relations.

The region between the expansion and the shock is often referred to as the star region. In the star region, the data states II and III are connected through a contact discontinuity travelling with the wave speed u^*. The characteristics in this area run parallel to each other and neither expansion nor compression can occur. Hence, both the velocity u^* and the pressure p^* are constant in the star region, but other flow properties are subject to a jump at the discontinuity. Furthermore, the Rankine-Hugoniot conditions apply across the contact wave like in shocks as well as the Riemann invariants are constant like in rarefaction waves.

An Analytical Solution. Laney [65] presented an analytical solution in terms of u, a and p to the Riemann problem for the Euler Equations and the ideal gas relations. This case corresponds to the shock-tube problem illustrated in Figure 2.5. For the Riemann problem, the relations across the rarefaction wave are given by

$$\begin{aligned} u(x,t) &= \frac{2}{\gamma-1}\left(\frac{x}{t} + \frac{\gamma-1}{2}u_I + a_I\right), \\ a(x,t) &= \frac{2}{\gamma-1}\left(\frac{x}{t} + \frac{\gamma-1}{2}u_I + a_I\right) - \frac{x}{t}, \\ p(x,t) &= p_I\left(\frac{a(x,t)}{a_I}\right)^{2\gamma/(\gamma-1)}. \end{aligned}$$

Additionally, the left and right states are connected through the Riemann invariant $u + 2a/(\gamma-1) = const$, yielding

$$u_{II} + \frac{2a_{II}}{\gamma-1} = u_I + \frac{2a_I}{\gamma-1}.$$

In the star region, the velocities and the pressures are constant across the contact wave. Thus,

$$u_{II} = u_{III} = u^*$$

and

$$p_{II} = p_{III} = p^* \ .$$

Finally, the Rankine-Hugoniot conditions across the shock wave result in

$$\begin{aligned}
\frac{a_{III}^2}{a_{IV}^2} &= \frac{p_{III}}{p_{IV}} \frac{\frac{\gamma+1}{\gamma-1} + \frac{p_{III}}{p_{IV}}}{\frac{\gamma+1}{\gamma-1}\frac{p_{III}}{p_{IV}} + 1} \ , \\
u_{III} &= u_{IV} + \frac{a_{IV}}{\gamma} \frac{\frac{p_{III}}{p_{IV}} - 1}{\sqrt{\frac{\gamma+1}{2\gamma}\left(\frac{p_{III}}{p_{IV}} - 1\right) + 1}} \ , \\
s &= u_{IV} + a_{IV}\sqrt{\frac{\gamma+1}{2\gamma}\left(\frac{p_{III}}{p_{IV}} - 1\right) + 1} \ .
\end{aligned}$$

Since the states I and IV are defined by the initial condition at $t = 0$, the only unknown in solving the above system of equations is the pressure ratio p_{III}/p_{IV}. It can be found through a combination of the conditions across the shock-tube relating p_{III}/p_{IV} to p_I/p_{IV}, namely

$$\frac{p_I}{p_{IV}} = \frac{p_{III}}{p_{IV}}\left[1 + \frac{\gamma-1}{2a_I}\left(u_I - u_{IV} - \frac{a_{IV}}{\gamma}\frac{\frac{p_{III}}{p_{IV}} - 1}{\sqrt{\frac{\gamma+1}{2\gamma}\left(\frac{p_{III}}{p_{IV}} - 1\right) + 1}}\right)\right]^{-2\gamma/(\gamma-1)} \ .$$

This non-linear implicit equation reveals the basic problem of the exact Riemann solution. Even though it is a perfectly valid analytical solution, the pressure ratio p_{III}/p_{IV} cannot be determined directly — thus a computationally expensive iterative procedure is necessary in order to calculate p_{III}/p_{IV}. In theory, the solution can be computed to any degree of precision required, but the cost increases with the order of accuracy.

Numerical Solutions. The vast majority of the computational time is spent on solving the Riemann problem. Hence, this part of the numerical code provides a high potential for reducing the cost of the simulation. Additionally, mathematical or physical approximations leading to explicit solutions rarely alter the results significantly when compared against the exact solution. For these two reasons, approximate Riemann solvers have almost entirely replaced exact Riemann solvers in practice. Further simplifications can be made by taking the self-similar character of the Riemann problem and non-moving computational grids into account. If the cell face is always at the same location $x = 0$, the wave speeds indicate the sought-after data state along the time axis in the wave diagram.

Figure 2.6 shows the schematics of wave patterns generally considered in the numerical solution to the Riemann problem. The left and the right wave can either be a rarefaction wave or a shock wave, whereas the middle wave is always a contact discontinuity.

Therefore, the unknown state in the star region can always be determined according to the type of the left and right non-linear wave. In order to encompass all possible

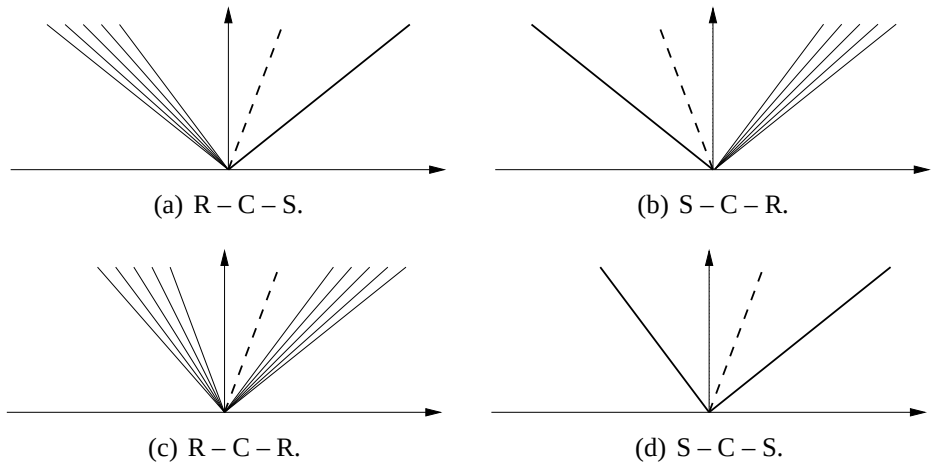

(a) R – C – S. (b) S – C – R.

(c) R – C – R. (d) S – C – S.

Figure 2.6: Possible wave patterns in the numerical solution of the Riemann problem (R denotes a rarefaction, C denotes a contact and S denotes a shock; after Toro [115]).

scenarios, however, special cases such as supersonic flow or sonic rarefaction waves are often treated separately. For supersonic flow, all waves are propagating downstream with the flow and no information can travel upstream — hence the solution simply assumes the initial left or right state depending on the flow direction. Otherwise, the state at $x = 0$ is given by the continuous solution through the expansion fan in case of a sonic rarefaction wave.

2.5 The ILES Rationale

As mentioned earlier, high resolution methods can be employed for discretising the advective fluxes in the framework of Implicit Large-Eddy Simulations of turbulent flows. This idea is based on the fact that finite volume, high resolution algorithms possess certain properties akin to the effect of subgrid-scale models used in conventional LES. On the one hand, they provide a local, non-linear numerical viscosity acting as a dynamic stabiliser for the solution which is equivalent to a purely dissipative eddy-viscosity model. On the other hand, they are also able to provide a backscatter mechanism related to scale-similarity models in classical LES. An analysis of the Modified Equation (MEA) as introduced by Warming and Hyett [124] has proven extremely useful in order to demonstrate the mathematical and physical similarities between traditional subgrid scale models and the built-in properties of finite volume, high resolution formulations. Before considering the modified equation representing the actual equation as treated by the numerical solver, however, the conventional LES equations and associated formal drawbacks will be discussed.

Conventional LES Formulation. A comprehensive account of the mathematical and the physical constraints in classical LES and approaches to model the subgrid

scales have been compiled by Fureby and Tabor [38]. They examined the full Navier-Stokes Equations, but for the purpose of illustration it suffices to consider only the incompressible Euler Equations given by

$$\frac{\partial \mathbf{u}}{\partial t} + \nabla \cdot (\mathbf{u} \otimes \mathbf{u}) + \frac{1}{\rho} \nabla p = 0 \ ,$$

where $\mathbf{u}$, t, ρ and p are the velocity vector, time, density and pressure, respectively. The velocity field is solenoidal, i.e. it satisfies $\nabla \cdot \mathbf{u} = 0$, and the scalar pressure field is determined by the continuity condition.

In conventional LES, the resolved scales are separated from the unresolved scales through a filtering operation. Thus, any variable f can be decomposed into $f = \bar{f} + f'$, where $\bar{f}$ is the grid scale and f' is the subgrid scale. The incompressible Euler Equations solved in classical LES are obtained by convolving the dependent variables with a spatial filter function $G = G(\mathbf{x}, \Delta)$ of width Δ, leading to the filtered or resolved variables $\bar{f} = G * f$. The filtered form of the Euler Equations above can now be written as

$$\frac{\partial \bar{\mathbf{u}}}{\partial t} + \nabla \cdot (\bar{\mathbf{u}} \otimes \bar{\mathbf{u}}) + \frac{1}{\bar{\rho}} \nabla \bar{p} = -\nabla \cdot \mathbf{T} - \mathbf{m} \ ,$$

where $\mathbf{T}$ is the residual or subgrid scale stress tensor and $\mathbf{m}$ is the commutation error term. It should be noted that an additional truncation error $\boldsymbol{\tau}$ arises through the discretisation of the equations. In general, the error terms are assumed to be small in comparison to the SGS stress tensor — hence they are often neglected in practice. However, this assumption is not always true. Ghosal [40] has shown that the truncation error originating from the discretisation can indeed be significant. The same holds for the commutation error, arising from the fact that the differentiation does not commute with the filtering $\overline{\partial f}/\partial x \neq \partial \bar{f}/\partial x$, in the vicinity of walls or in regions with grid stretching.

The SGS stress tensor in LES is the equivalent of the Reynolds stress tensor in RANS and needs to be modelled in order to close the system. It is defined as the difference between the filtered non-linear term in the original Euler Equations and the non-linear term in the filtered Euler equations

$$\overline{\mathbf{u} \otimes \mathbf{u}} \neq \bar{\mathbf{u}} \otimes \bar{\mathbf{u}} \ ,$$

thus $\mathbf{T}$ can be written as

$$\mathbf{T} = \overline{\mathbf{u} \otimes \mathbf{u}} - \bar{\mathbf{u}} \otimes \bar{\mathbf{u}} = \left(\overline{\bar{\mathbf{u}} \otimes \bar{\mathbf{u}}} - \bar{\mathbf{u}} \otimes \bar{\mathbf{u}} \right) + \left(\overline{\bar{\mathbf{u}} \otimes \mathbf{u}'} + \overline{\mathbf{u}' \otimes \bar{\mathbf{u}}} \right) + \left(\overline{\mathbf{u}' \otimes \mathbf{u}'} \right) = \mathbf{L} + \mathbf{C} + \mathbf{R} \ .$$

Here, $\mathbf{L}$, $\mathbf{C}$ and $\mathbf{R}$ are the Leonard stress, the Cross stress and the subgrid scale Reynolds stress representing interactions between resolved scales, between resolved and subgrid scales, and between unresolved subgrid scales, respectively. These terms are subject to the basic requirement of Galilean invariance. Fureby and Tabor [38] have shown that $\mathbf{T}$ and $\mathbf{R}$ are invariant of the frame of reference, but neither $\mathbf{L}$ nor $\mathbf{C}$ satisfy this condition independently. The added complexity in individually modelling the different physics represented by the Leonard, Cross and Reynolds terms plus the fact that

all models are only approximations in the first place defeat any attempt at precision. For this reason, it is more common to model the effect of the subgrid scale tensor as a single unit instead.

Explicit Modelling. In the book by Drikakis and Rider [27], several explicit SGS models for conventional Large-Eddy Simulation have been analysed. The modified partial differential equation emulating the inviscid, filtered LES equations considered here is given by

$$\frac{\partial \mathbf{U}}{\partial t} + \nabla \cdot \mathbf{E} = -\nabla \cdot \mathbf{T} \ ,$$

where $\mathbf{U}$ is the array of dependent variables, $\mathbf{E}$ is the inviscid flux vector and $\mathbf{T}$ is the subgrid scale stress tensor.

Smagorinsky [105] developed the most widely applied model to date. It is an eddy viscosity model similar to the Boussinesq approximation in RANS that is based on a subgrid scale dissipation according to Kolmogorov's $k^{5/3}$ law for isotropic turbulence. The form of the SGS eddy viscosity is derived from dimensional arguments balancing the production of turbulent kinetic energy with the dissipation on a subgrid level. A one dimensional analysis of the modified equation reveals that Smagorinsky's model leads to a SGS stress

$$\mathbf{T} = -C\Delta^2 \left| \frac{\partial \mathbf{U}}{\partial x} \right| \frac{\partial \mathbf{U}}{\partial x} \ ,$$

where C is a constant and Δ is the cell width. Drikakis and Rider [27] have shown that the change of global kinetic energy in the system can be calculated by

$$\bar{\mathcal{E}} = \int \frac{\partial \mathbf{U}}{\partial x} \mathbf{T} \, dx' \ ,$$

where the integral is replaced by a sum in a discrete simulation. Inserting the SGS stress for the Smagorinsky model yields

$$\bar{\mathcal{E}} = -C\Delta^2 \int \left| \frac{\partial \mathbf{U}}{\partial x} \right|^3 \, dx' \leq 0 \ .$$

Evidently, the global kinetic energy is always decreasing in time — hence the Smagorinsky model is strictly dissipative and mimics the removal of kinetic energy at a subgrid level. Although this model enjoys a great popularity, it causes problems if applied to non-homogeneous or non-isotropic flows. For example, it needs to be recalibrated for free shear-flows or additional damping functions are required to account for near-wall effects.

A significant improvement to the standard Smagorinsky model has been proposed by Germano et al. [39]. Here, the model coefficients are evaluated dynamically as the simulation pogresses. This is accomplished by applying a second, larger filter typically of width 2Δ, for which a hypothetical resolved subgrid stress is calculated. Under the assumption that the unresolved and the "resolved" SGS behave similarly, the coefficients of the underlying subgrid scale model can now be adjusted dynamically. The resulting

dynamic Smagorinsky model leads to a SGS stress of the form

$$\mathbf{T} = -C\Delta^4 \left|\frac{\partial \mathbf{U}}{\partial x}\right| \frac{\partial^3 \mathbf{U}}{\partial x^3} \quad \longrightarrow \quad \bar{\mathcal{E}} = -C\Delta^4 \int \left|\frac{\partial \mathbf{U}}{\partial x}\right| \frac{\partial \mathbf{U}}{\partial x} \frac{\partial^3 \mathbf{U}}{\partial x^3}\, dx' \ .$$

The associated change of global kinetic energy can become positive or negative, thus it also allows for backscatter and improves the predictability of transitional flows. However, the dynamic model exhibits numerical instabilities in areas of energy production and a spatial or a temporal averaging procedure is required to cure this problem. A positive aspect of the averaging is a naturally vanishing subgrid scale viscosity at solid walls, but on the other hand it defeats the purpose of a locally dynamic formulation.

It should be noted, that the double-filter approach is not limited to the Smagorinsky model. Bardina et al. [7] proposed an alternative model based on the idea that the important interactions between grid and subgrid scales occur between the smallest resolved eddies and the largest unresolved eddies. This so-called scale-similarity model produces a subgrid stress given by

$$\mathbf{T} = -C\Delta^2 \left(\frac{\partial \mathbf{U}}{\partial x}\right)^2 \quad \longrightarrow \quad \bar{\mathcal{E}} = -C\Delta^2 \int \left(\frac{\partial \mathbf{U}}{\partial x}\right)^3 \, dx' \ .$$

In theory, Bardina's model accounts for both outscatter and backscatter, but in practice it hardly dissipates any energy and it is numerically unstable. It is therefore necessary to add a dissipation mechanism in form of, e.g. the Smagorinsky model to correct for this deficiency. The resulting combination is also called mixed subgrid scale model.

Various other techniques to model the effect of the subgrid scales can be found in textbooks on conventional Large-Eddy Simulation or can be derived by adapting models found in RANS simulations. However, they will not be discussed here.

Implicit Modelling. The implicit approach to SGS modelling in LES is motivated by the fact that computational solvers are always affected by both physical as well as numerical limitations and they should not be regarded separately. It is deemed more appropriate to consider the combined effects instead. As shown previously, the numerical error has the same form as the subgrid scale term and it is therefore assumed to be capable of producing a similar subgrid stress as in the filtered LES equations. When no explicit filter is applied to the incompressible Euler Equations, the explicit SGS term and the commutation error term do not appear, yielding

$$\frac{\partial \bar{\mathbf{u}}}{\partial t} + \nabla \cdot (\bar{\mathbf{u}} \otimes \bar{\mathbf{u}}) + \frac{1}{\bar{\rho}} \nabla \bar{p} = \cancel{-\nabla \cdot \mathbf{T}} - \cancel{\mathbf{m}} \ .$$

Here, the over-bars denote an average originating from the finite volume formulation which can be seen as a form of implicit spatial filtering. As mentioned previously, the discretisation of the above equation leads to the additional truncation error term $-\nabla \cdot \boldsymbol{\tau}$ which depends on the discretisation scheme and the solution procedure. This numerical error term conveniently appears in the same divergence form as the subgrid scale stress tensor — hence it may have a similar effect on the solution.

High-resolution methods had originally been introduced with the intend to solve the advective part of the equations as accurately as possible. However, it was found that they not only provide a superior accuracy to classical linear methods, they are also equipped with a built-in subgrid scale model. In order to investigate this approach to SGS modelling analytically, Drikakis and Rider [27], Fureby and Grinstein [37], Margolin and Rider [76] employed the methodology of modified equation analysis to determine the leading order truncation errors arising from the combination of control volume differencing and inherently non-linear high-resolution approximations. Additionally, they compared the truncation error term in implicit LES against the explicit SGS term in classical Large-Eddy Simulations and identified the similarities.

Drikakis and Rider [27] considered a discrete, one-dimensional equation of the form

$$\mathbf{U}_i^{n+1} = \mathbf{U}_i^n - \frac{\Delta t}{\Delta x}\left[\mathbf{E}_{i+1/2} - \mathbf{E}_{i-1/2}\right] \ ,$$

where $\mathbf{U}$ and $\mathbf{E}$ are the array of dependent variables and the inviscid flux vector, respectively. The superscript n marks the time level, whereas the subscript i denotes the position in space. After the high-resolution reconstruction step incorporating limits based on non-linear stability criteria, the fluxes are determined from the left and right data states by a linearised Godunov-type method according to

$$\mathbf{E}_{i+1/2} = \frac{1}{2}\left[\mathbf{E}_{i+1/2,R} + \mathbf{E}_{i+1/2,L}\right] - \frac{|\mathbf{E}'|}{2}\left[\mathbf{U}_{i+1/2,R} - \mathbf{U}_{i+1/2,L}\right] \ ,$$

with $\mathbf{E}'$ being the flux Jacobian $\partial\mathbf{E}/\partial\mathbf{U}$. For this general form of the modified equation, the finite volume discretisation itself naturally produces a truncation term at second order of accuracy given by

$$\boldsymbol{\tau} = -C_1\Delta^2\mathbf{E}'\frac{\partial^2\mathbf{U}}{\partial x^2} - C_2\Delta^2\mathbf{E}''\left(\frac{\partial\mathbf{U}}{\partial x}\right)^2 \ ,$$

where C_1 and C_2 are two constants depending on the details of the numerical method and Δ is the cell width. Evidently, the first term in the truncation error as predicted by the MEA allows for backscatter while the second term is analogous to the effect of a scale-similarity subgrid model in conventional LES.

Additional error terms originate from the details of the limiting mechanism during the reconstruction step. The physical concept behind limiters is the need for entropy production in under-resolved situations, i.e. near high gradients, in order to eliminate or control spurious oscillations in the solution. Effectively, limiters can be seen as a sophisticated trigger for an "artificial viscosity" inherent to the non-linear method. The character of the numerical scheme is closely related to the form of the truncation term as analysed by Drikakis and Rider [27] for various limiters. For example, the MPDATA scheme of Smolarkiewicz and Margolin [106] yields a leading order error term of

$$\boldsymbol{\tau} = -C\Delta^2|\mathbf{E}'|\left|\frac{\partial\mathbf{U}}{\partial x}\right|\frac{\partial\mathbf{U}}{\partial x} \ ,$$

which is essentially of the same form as the SGS stress for a standard Smagorinsky model in classical Large-Eddy Simulations. Furthermore, it has been shown that the limiter of van Albada et al. [116] and the third-order WENO scheme of Liu et al. [71] produce an effective stress

$$\boldsymbol{\tau} = -C\Delta^3 |\mathbf{E}'| \left(\frac{\partial^2 \mathbf{U}}{\partial x^2} \right)^2 \left(\frac{\partial \mathbf{U}}{\partial x} \right)^{-1} ,$$

whereas the fifth-order WENO scheme of Jiang and Shu [62] leads to a truncation error of the form

$$\boldsymbol{\tau} = -C\Delta^5 |\mathbf{E}'| \left(\frac{\partial^3 \mathbf{U}}{\partial x^3} \right)^2 \left(\frac{\partial \mathbf{U}}{\partial x} \right)^{-1} .$$

All of the above methods are strictly dissipative at the leading order regarding the change of global kinetic energy, with the main difference being the scaling given by the cell width Δ. However, this does not rule out backscatter in higher order error terms or low-order dispersive terms for other high-resolution algorithms. In fact, Fureby and Grinstein [37] have shown that high-resolution discretisations are indeed able to introduce both dissipative and dispersive terms similar to a mixed SGS model in conventional LES.

In summary, an analysis of the modified equations for classical Large-Eddy Simulation and ILES implies a remarkable analogy between explicit subgrid scale models and the leading order truncation terms in Implicit Large-Eddy Simulation — hence the truncation term can be interpreted as a built-in mechanism representing the effect of the unresolved scales.

CHAPTER 3

Numerical Model

THE numerical framework for this investigation is provided by a three-dimensional, unsteady, compressible Navier-Stokes solver of the Eulerian type. Although low-speed flows are near-incompressible, it is deemed more appropriate to develop a reliable multi-purpose method that can be applied to a wide range of engineering problems. The framework is based on a block-structured finite volume approach formulated in a generalised curvilinear coordinate system and several techniques for the discretisation in time and space have been considered.

In separated turbulent flows, the flow components fluctuate rapidly and high gradients are encountered frequently, thus a simple explicit time integration method is preferred. For the discretisation in space, a central difference scheme is employed for the viscous terms and a Godunov-type method solves for the advective flux derivatives. High-resolution is achieved through the reconstruction step incorporating different variants of non-linear schemes. Furthermore, the code is fully parallelised following a domain decomposition approach. In order to provide a complete description of the numerical technique, all of the above components will be presented in this section. Additionally, a flowchart illustrating the logic of the solver can be found in Appendix B.

3.1 Governing Equations

The physics of (Newtonian) fluid flow is governed by the Navier-Stokes Equations (NSE), see Anderson [2]. These equations can be solved by considering the coupled generalised conservation laws, namely the continuity, momentum and energy equations

$$\frac{\partial \rho}{\partial t} + \nabla \cdot (\rho \mathbf{u}) = 0 \,, \tag{3.1.1}$$

$$\frac{\partial \rho \mathbf{u}}{\partial t} + \nabla \cdot (\rho \mathbf{u} \otimes \mathbf{u}) = -\nabla \cdot \mathbf{S} \,, \tag{3.1.2}$$

$$\frac{\partial e}{\partial t} + \nabla \cdot (e \mathbf{u}) = -\nabla \cdot (\mathbf{S} \cdot \mathbf{u}) - \nabla \cdot \mathbf{q} \,, \tag{3.1.3}$$

where $\mathbf{u}$, ρ, e, and $\mathbf{q}$ stand for the velocity components, the density, the total energy per unit volume, and the heat flux, respectively. The stress tensor $\mathbf{S}$ represents the effects of the thermodynamic pressure p and the viscous stresses, yielding

$$\mathbf{S} = p\mathbf{I} - \lambda_b(\nabla \cdot \mathbf{u})\mathbf{I} - \mu[(\nabla\mathbf{u}) + (\nabla\mathbf{u})^T] \,, \tag{3.1.4}$$

where $\mathbf{I}$ is the identity tensor, μ is the dynamic viscosity coefficient relating the stress to the rate of strain for a Newtonian fluid and λ_b is the bulk viscosity coefficient accounting for the dilatation of the fluid. The bulk viscosity coefficient is defined according to the Stokes hypothesis as

$$\lambda_b = -\frac{2}{3}\mu \,. \tag{3.1.5}$$

In a similar manner, the heat flux caused by temperature differences in the flow can be related to the temperature gradients following Fourier's heat conduction law

$$\mathbf{q} = -\kappa\nabla T \,, \tag{3.1.6}$$

where κ is the thermal conductivity coefficient and T is the temperature.

In order to close the above system, it is complemented by an equation of state. For a perfect gas with negligible inter-molecular forces, the equation of state is given by

$$p = \rho RT \,, \tag{3.1.7}$$

where the gas constant of air is typically $R = 287.05\,\mathrm{Nm/(kg \cdot K)}$. Furthermore, assuming the gas is also calorically perfect with constant specific heats, the following useful relations for the internal energy e_i, the specific heats c_v and c_p, and the ratio of specific heats γ can be adopted

$$e_i = c_v T \,, \quad c_p - c_v = R \,, \quad c_v = \frac{R}{\gamma - 1} \,, \quad c_p = \frac{\gamma R}{\gamma - 1} \,, \quad \gamma = \frac{c_p}{c_v} \,, \tag{3.1.8}$$

with γ typically being equal to 1.4 for air.

The perfect gas relations establish the connection between the Momentum Equation (3.1.2) and the Energy Equation (3.1.3) through the volumetric energy balance

$$e = \frac{p}{\gamma - 1} + \frac{\rho}{2}\left(u^2 + v^2 + w^2\right) \,. \tag{3.1.9}$$

Additionally, the physical properties of the fluid can now be determined. Sutherland's law for the variation of the dynamic viscosity coefficient μ with the air temperature T yields

$$\mu = \mu_0 \left(\frac{T}{T_0}\right)^{3/2} \frac{T_0 + 110.4K}{T + 110.4K} \,, \tag{3.1.10}$$

where T is in Kelvin and the reference viscosiy is $\mu_0 = 1.7894 \times 10^{-5}\,\mathrm{kg/(m \cdot s)}$ at the reference temperature $T_0 = 288.16\,\mathrm{K}$. The thermal conductivity coefficient κ is

directly proportional to μ according to molecular theory. For a calorically perfect gas, this leads to the relation

$$\kappa = \frac{c_v \gamma \mu}{Pr} \,, \tag{3.1.11}$$

where Pr is a dimensionless parameter known as the Prandtl number. In a temperature range of approximately 200K to 1000K, the Prandtl number is usually assumed to be constant and equal to 0.72.

3.1.1 Dimensionless Form

In Computational Fluid Dynamics, it is common to employ the Navier-Stokes Equations (3.1.1) to (3.1.3) in their dimensionless form. Here, the variables are re-scaled in order to reduce the the risk of numerically ill-conditioned flow states and to ensure the solution is generally well-behaved. An additional advantage is the decreasing number of parameters characterising the flow. A large set of physical and geometrical factors can be grouped into a relatively small set of dimensionless quantities that reveal similarites between seemingly different flow scenarios — hence the dimensionless formulation reduces the number of input parameters and it facilitates the comparison with experimental data.

The non-dimensionalisation is achived by relating all physical and geometrical quantities to characteristic reference values for the density (ρ_c), velocity (u_c), dynamic viscosity (μ_c) and length (l_c). This leads to the following dimensionless variables

$$\begin{aligned}
t^* &= \frac{t}{l_c/u_c} \,, & x^* &= \frac{x}{l_c} \,, & y^* &= \frac{y}{l_c} \,, & z^* &= \frac{z}{l_c} \,, \\
\rho^* &= \frac{\rho}{\rho_c} \,, & u^* &= \frac{u}{u_c} \,, & v^* &= \frac{v}{u_c} \,, & w^* &= \frac{w}{u_c} \,, \\
e^* &= \frac{e}{\rho_c u_c^2} \,, & p^* &= \frac{p}{\rho_c u_c^2} \,, & \mu^* &= \frac{\mu}{\mu_c} \,.
\end{aligned} \tag{3.1.12}$$

In order to obtain a dimensionless heat flux for the energy conservation an additional characteristic value T_c for the temperature is needed. With Equations (3.1.6) and (3.1.11), the heat flux in the non-dimensional form of Equation (3.1.3) can now be written as

$$\mathbf{q}^* = -\frac{c_v \gamma}{Re\, Pr} \frac{T_c}{u_c^2} \nabla T^* \,, \tag{3.1.13}$$

where Re is the Reynolds number given by

$$Re = \frac{\rho_c u_c l_c}{\mu_c} \,. \tag{3.1.14}$$

The reference velocity u_c and the reference Temperature T_c are chosen to satisfy

$$c_v \rho_\infty T_c = e_\infty = \rho_\infty u_c^2 \,, \tag{3.1.15}$$

where the subscript ∞ refers to the properties of the free-stream. For a perfect gas, this leads to the following definitions for u_c and T_c

$$u_c = a_\infty \sqrt{\frac{1+\frac{\gamma}{2}(\gamma-1)Ma_\infty^2}{\gamma(\gamma-1)}} , \tag{3.1.16}$$

$$T_c = \frac{a_\infty^2}{c_v}\frac{1+\frac{\gamma}{2}(\gamma-1)Ma_\infty^2}{\gamma(\gamma-1)} , \tag{3.1.17}$$

where $a_\infty = \sqrt{\gamma p_\infty/\rho_\infty}$ is the speed of sound and $Ma_\infty = u_\infty/a_\infty$ is the Mach number. Equation (3.1.13) can now be simplified to

$$\mathbf{q}^* = -\frac{\gamma}{Re\,Pr}\nabla T^* . \tag{3.1.18}$$

For the reference value l_c any length representing the characteristic dimensions of the problem at hand can be selected and the reference density is equal to the free-stream density $\rho_c = \rho_\infty$. Finally, the characteristic viscosity μ_c is chosen in order to ensure consistency between the numerical Reynolds number and the experimental Reynolds number

$$\mu_c = \frac{u_c}{u_\infty}\mu_\infty . \tag{3.1.19}$$

Inserting the above relations into the Navier-Stokes Equations (3.1.1) to (3.1.3) yields their dimensionless form

$$\frac{\partial \rho^*}{\partial t^*} + \nabla\cdot(\rho\mathbf{u}^*) = 0 , \tag{3.1.20}$$

$$\frac{\partial \rho^*\mathbf{u}^*}{\partial t^*} + \nabla\cdot(\rho^*\mathbf{u}^*\otimes\mathbf{u}^*) = -\nabla\cdot\mathbf{S}^* , \tag{3.1.21}$$

$$\frac{\partial e^*}{\partial t^*} + \nabla\cdot(e^*\mathbf{u}^*) = -\nabla\cdot(\mathbf{S}^*\cdot\mathbf{u}^*) - \nabla\cdot\mathbf{q}^* , \tag{3.1.22}$$

where $\mathbf{S}^*$ is the nondimensional stress tensor given by

$$\mathbf{S}^* = p^*\mathbf{I} + \frac{2}{3\,Re}(\nabla\cdot\mathbf{u}^*)\mathbf{I} - \frac{1}{Re}[(\nabla\mathbf{u}^*) + (\nabla\mathbf{u}^*)^T] . \tag{3.1.23}$$

Here, the nabla operator ∇ denotes the gradients and vector derivatives with respect to the dimensionless coordinates x^*, y^* and z^*. For simplicity, the superscript $*$ is omitted in the following sections.

3.1.2 Matrix Form

In order to simplify and organise the logic in a computational method, Equations (3.1.20) to (3.1.22) can be written in conservative, Cartesian matrix form, yielding a single equation representing the entire system of governing equations

$$\frac{\partial\mathbf{U}}{\partial t} + \frac{\partial\mathbf{E}}{\partial x} + \frac{\partial\mathbf{F}}{\partial y} + \frac{\partial\mathbf{G}}{\partial z} = \frac{\partial\mathbf{L}}{\partial x} + \frac{\partial\mathbf{M}}{\partial y} + \frac{\partial\mathbf{N}}{\partial z} , \tag{3.1.24}$$

where **U** is the array of the conservative variables; **E**, **F**, **G** are the inviscid and **L**, **M**, **N** are the viscous flux vectors associated with the Cartesian *x*-, *y*- and *z*-direction, respectively,

$$\mathbf{U} = \begin{pmatrix} \rho \\ \rho u \\ \rho v \\ \rho w \\ e \end{pmatrix}, \ \mathbf{E} = \begin{pmatrix} \rho u \\ \rho u^2 + p \\ \rho v u \\ \rho w u \\ (e+p)u \end{pmatrix}, \ \mathbf{F} = \begin{pmatrix} \rho v \\ \rho u v \\ \rho v^2 + p \\ \rho w v \\ (e+p)v \end{pmatrix}, \ \mathbf{G} = \begin{pmatrix} \rho w \\ \rho u w \\ \rho v w \\ \rho w^2 + p \\ (e+p)w \end{pmatrix},$$

$$\mathbf{L} = \frac{1}{Re}\begin{pmatrix} 0 \\ \tau_{xx} \\ \tau_{xy} \\ \tau_{xz} \\ u\tau_{xx} + v\tau_{xy} + w\tau_{xz} - \frac{\gamma}{Pr}q_x \end{pmatrix}, \ \mathbf{M} = \frac{1}{Re}\begin{pmatrix} 0 \\ \tau_{yx} \\ \tau_{yy} \\ \tau_{yz} \\ u\tau_{yx} + v\tau_{yy} + w\tau_{yz} - \frac{\gamma}{Pr}q_y \end{pmatrix},$$

$$\mathbf{N} = \frac{1}{Re}\begin{pmatrix} 0 \\ \tau_{zx} \\ \tau_{zy} \\ \tau_{zz} \\ u\tau_{zx} + v\tau_{zy} + w\tau_{zz} - \frac{\gamma}{Pr}q_z \end{pmatrix}.$$

In Equation (3.1.24), the heat flux has been split into the three spatial components denoted by $q_{x,y,z}$ and τ_{ij} stands for the viscous stress in the *j*-direction exerted on a plane normal to the *i*-axis. For example, on a face perpendicular to the *x*-direction, τ_{xx} is a normal stress, whereas τ_{xy} and τ_{xz} are tangential or shear stresses, further details can be found in Appendix C.

3.1.3 Generalised Curvilinear Coordinates

Most problems in engineering cannot be represented adequately in Cartesian coordinate systems but require arbitrary, body-fitted grids that naturally allow for curved geometries. It is therefore necessary to convert the Cartesian matrix form to a generalised curvilinear coordinate system given by $\xi = \xi(x, y, z, t)$, $\eta = \eta(x, y, z, t)$, $\zeta = \zeta(x, y, z, t)$ and $\tau = t$, e.g. see the book of Drikakis and Rider [27]. This is achieved by multiplying Equation (3.1.24) with the Jacobian determinant of the transformation from Cartesian (x, y, z) to curvilinear (ξ, η, ζ) coordinates

$$J = \left|\frac{\partial(x, y, z)}{\partial(\xi, \eta, \zeta)}\right| = x_\xi \left(y_\eta z_\zeta - y_\zeta z_\eta\right) + y_\xi \left(z_\eta x_\zeta - z_\zeta x_\eta\right) + z_\xi \left(x_\eta y_\zeta - x_\zeta y_\eta\right) \qquad (3.1.25)$$

and substituting the partial derivatives for non-moving grids

$$\begin{aligned}
\frac{\partial}{\partial x} &= \left(\frac{\partial}{\partial \xi}\right)\frac{\partial \xi}{\partial x} + \left(\frac{\partial}{\partial \eta}\right)\frac{\partial \eta}{\partial x} + \left(\frac{\partial}{\partial \zeta}\right)\frac{\partial \zeta}{\partial x} \,, \\
\frac{\partial}{\partial y} &= \left(\frac{\partial}{\partial \xi}\right)\frac{\partial \xi}{\partial y} + \left(\frac{\partial}{\partial \eta}\right)\frac{\partial \eta}{\partial y} + \left(\frac{\partial}{\partial \zeta}\right)\frac{\partial \zeta}{\partial y} \,, \\
\frac{\partial}{\partial z} &= \left(\frac{\partial}{\partial \xi}\right)\frac{\partial \xi}{\partial z} + \left(\frac{\partial}{\partial \eta}\right)\frac{\partial \eta}{\partial z} + \left(\frac{\partial}{\partial \zeta}\right)\frac{\partial \zeta}{\partial z} \,, \\
\frac{\partial}{\partial t} &= \frac{\partial}{\partial \tau} \,.
\end{aligned} \tag{3.1.26}$$

The compressible Navier-Stokes Equations in curvilinear coordinates now take the form

$$J\frac{\partial \mathbf{U}}{\partial \tau} + J\frac{\partial \mathbf{E}}{\partial \xi}\xi_x + J\frac{\partial \mathbf{E}}{\partial \eta}\eta_x + J\frac{\partial \mathbf{E}}{\partial \zeta}\zeta_x + \ldots = J\frac{\partial \mathbf{L}}{\partial \xi}\xi_x + J\frac{\partial \mathbf{L}}{\partial \eta}\eta_x + J\frac{\partial \mathbf{L}}{\partial \zeta}\zeta_x + \ldots \,,$$

where the subscripts indicate the partial derivatives with respect to the spatial dimensions.

Further simplification of this expression can be obtained by using the relation (in 1D)

$$J\frac{\partial \mathbf{E}}{\partial \xi}\xi_x = \frac{\partial (J\mathbf{E}\xi_x)}{\partial \xi} - \mathbf{E}\frac{\partial}{\partial \xi}(J\xi_x) \tag{3.1.27}$$

and its equivalent for the other flux derivatives, yielding

$$\frac{\partial \tilde{\mathbf{U}}}{\partial t} + \frac{\partial \tilde{\mathbf{E}}}{\partial \xi} + \frac{\partial \tilde{\mathbf{F}}}{\partial \eta} + \frac{\partial \tilde{\mathbf{G}}}{\partial \zeta} = \frac{\partial \tilde{\mathbf{L}}}{\partial \xi} + \frac{\partial \tilde{\mathbf{M}}}{\partial \eta} + \frac{\partial \tilde{\mathbf{N}}}{\partial \zeta} \,, \tag{3.1.28}$$

with

$$\begin{aligned}
\tilde{\mathbf{U}} &= J\mathbf{U} \\
\tilde{\mathbf{E}} &= J(\mathbf{E}\xi_x + \mathbf{F}\xi_y + \mathbf{G}\xi_z) \,, \\
\tilde{\mathbf{F}} &= J(\mathbf{E}\eta_x + \mathbf{F}\eta_y + \mathbf{G}\zeta_z) \,, \\
\tilde{\mathbf{G}} &= J(\mathbf{E}\zeta_x + \mathbf{F}\zeta_y + \mathbf{G}\zeta_z) \,, \\
\tilde{\mathbf{L}} &= J(\mathbf{L}\xi_x + \mathbf{M}\xi_y + \mathbf{N}\xi_z) \,, \\
\tilde{\mathbf{M}} &= J(\mathbf{L}\eta_x + \mathbf{M}\eta_y + \mathbf{N}\eta_z) \,, \\
\tilde{\mathbf{N}} &= J(\mathbf{L}\zeta_x + \mathbf{M}\zeta_y + \mathbf{N}\zeta_z) \,,
\end{aligned} \tag{3.1.29}$$

This system of equations applies to the transformed body-fitted grid, i.e. a uniform and rectangular computational grid. Hence, the numerical treatment for solving the equations in Cartesian matrix form and generalised curvilinear matrix form is identical. Please note that details on the metric relations for the coordinate transformation can be found in Appendix D. Furthermore, the superscript ˜ is omitted for the remainder of this chapter for simplicity.

3.2 Time Integration

For both steady and unsteady flows the time-dependent Navier-Stokes Equations can be considered. The solution is found by a time-marching algorithm that progressively determines the dependent variables in steps of time. In case of steady flow a constant state is approached asymptotically during the course of the simulation, whereas for unsteady flows the inherently transient solution is predicted.

In this thesis, explicit Runge Kutta time integration methods are chosen for their simplicity and their ability to temporally resolve the rapidly fluctuating velocity components encountered in unsteady separated flows. This approach constructs the solution as a linear combination of multiple stages where the number of stages is determined by the desired accuracy of the algorithm, see Drikakis and Rider [27]. Before applying a Runge Kutta method to Equation (3.1.28), however, the time derivative is isolated

$$\frac{\partial \mathbf{U}}{\partial t} = -\frac{\partial \mathbf{E}}{\partial \xi} - \frac{\partial \mathbf{F}}{\partial \eta} - \frac{\partial \mathbf{G}}{\partial \zeta} + \frac{\partial \mathbf{L}}{\partial \xi} + \frac{\partial \mathbf{M}}{\partial \eta} + \frac{\partial \mathbf{N}}{\partial \zeta} = f(\mathbf{U}, t)\,, \tag{3.2.1}$$

thus it can be considered a function of the dependent variables $\mathbf{U}$ and time t only.

3.2.1 First-Order Runge Kutta

A simple numerical approximation of the time derivative in Equation (3.2.1) is given by the single stage algorithm

$$\frac{\mathbf{U}^{n+1} - \mathbf{U}^n}{\Delta t} = f(\mathbf{U}^n, t^n)\,, \tag{3.2.2}$$

with Δt being the time step, $\mathbf{U}^{n+1} = \mathbf{U}(t + \Delta t)$ and $\mathbf{U}^n = \mathbf{U}(t)$. This is also called the forward Euler method and it is first-order accurate in time. If higher order algorithms are required multiple stages need to be computed.

3.2.2 Second-Order Runge Kutta

A straightforward modification of the forward Euler method leads to a second-order accurate two-step procedure defined by

$$\begin{aligned} \frac{\mathbf{U}^1 - \mathbf{U}^n}{\Delta t} &= \frac{1}{2} f(\mathbf{U}^n, t^n)\,, \\ \frac{\mathbf{U}^{n+1} - \mathbf{U}^n}{\Delta t} &= f(\mathbf{U}^1, t^{n+1/2})\,. \end{aligned} \tag{3.2.3}$$

There are several variants of Runge Kutta schemes that lead to the same order of accuracy and yield equivalent results if combined with a linear spatial differencing. Yet, for non-linear spatial differencing, formulations adhering to the more restrictive TVD

constraint may produce improved results at the cost of impaired stability properties. It should be noted here, however, that the TVD condition cannot be formally satisfied for non-linear equations and the expected effect can only be confirmed by numerical experiments. In the book of Drikakis and Rider [27], an example for a second-order accurate TVD Runge Kutta algorithm known as Heun's method is presented as

$$\begin{aligned} \frac{\mathbf{U}^1 - \mathbf{U}^n}{\Delta t} &= f(\mathbf{U}^n, t^n) \,, \\ \frac{\mathbf{U}^{n+1} - \mathbf{U}^n}{\Delta t} &= \frac{1}{2}\left[f(\mathbf{U}^n, t^n) + f(\mathbf{U}^1, t^{n+1/2}) \right] \,. \end{aligned} \tag{3.2.4}$$

3.2.3 Third-Order Runge Kutta

The standard third-order accurate Runge Kutta method consists of the following stages

$$\begin{aligned} \frac{\mathbf{U}^1 - \mathbf{U}^n}{\Delta t} &= \frac{1}{3} f(\mathbf{U}^n, t^n) \,, \\ \frac{\mathbf{U}^2 - \mathbf{U}^n}{\Delta t} &= \frac{2}{3} f(\mathbf{U}^1, t^{n+1/3}) \,, \\ \frac{\mathbf{U}^{n+1} - \mathbf{U}^n}{\Delta t} &= \frac{1}{4}\left[f(\mathbf{U}^n, t^n) + 3 f(\mathbf{U}^2, t^{n+2/3}) \right] \,. \end{aligned} \tag{3.2.5}$$

Similar to the two-stage algorithms, a third-order accurate TVD Runge Kutta can be formulated

$$\begin{aligned} \frac{\mathbf{U}^1 - \mathbf{U}^n}{\Delta t} &= f(\mathbf{U}^n, t^n) \,, \\ \frac{\mathbf{U}^2 - \mathbf{U}^n}{\Delta t} &= \frac{1}{4}\left[f(\mathbf{U}^n, t^n) + f(\mathbf{U}^1, t^{n+1/3}) \right] \,, \\ \frac{\mathbf{U}^{n+1} - \mathbf{U}^n}{\Delta t} &= \frac{1}{6}\left[f(\mathbf{U}^n, t^n) + 4 f(\mathbf{U}^2, t^{n+2/3}) + f(\mathbf{U}^1, t^{n+1/3}) \right] \,. \end{aligned} \tag{3.2.6}$$

Additionally, time integration schemes can be designed with extended stability properties in mind, leading to the alternative three-stage, third-order accurate algorithm given by

$$\begin{aligned} \frac{\mathbf{U}^1 - \mathbf{U}^n}{\Delta t} &= \frac{1}{2} f(\mathbf{U}^n, t^n) \,, \\ \frac{\mathbf{U}^2 - \mathbf{U}^n}{\Delta t} &= \frac{1}{2} f(\mathbf{U}^1, t^{n+1/3}) \,, \\ \frac{\mathbf{U}^{n+1} - \frac{2}{3}\mathbf{U}^2 - \frac{1}{3}\mathbf{U}^n}{\Delta t} &= \frac{1}{3}\left[f(\mathbf{U}^2, t^{n+2/3}) + f(\mathbf{U}^1, t^{n+1/3}) \right] \,. \end{aligned} \tag{3.2.7}$$

Higher than third-order methods can be constructed, but the relative improvement of the solution cannot justify the additional computational cost in most cases. Thus, they will not be discussed here.

3.2.4 CFL Condition

For time-dependent flows, time marching in all computational cells has to be performed with the same global time step Δt, which, for a given Courant-Friedrichs-Lewy (CFL) number, is defined as

$$\Delta t = min\left(J \frac{CFL}{max(|\lambda_0^\xi|, |\lambda_+^\xi|, |\lambda_-^\xi|, |\lambda_0^\eta|, |\lambda_+^\eta|, |\lambda_-^\eta|, |\lambda_0^\zeta|, |\lambda_+^\zeta|, |\lambda_-^\zeta|)} \right) , \tag{3.2.8}$$

where J denotes the Jacobian determinant and λ are the eigenvalues associated with the advective fluxes **E**, **F**, **G**, respectively.

For the forward Euler method from Equation (3.2.2), the theoretical value of $CFL \leq 1$ leads to a stable integration in time. This condition simply states that the length of the time step is equal or less than it takes for the fastest acoustic wave to travel from one grid point to the next. However, this condition is necessary but not sufficient to ensure stability of the algorithm. Time marching methods satisfying a CFL condition may still lead to instabilities in the sense of permitting large errors or they may simply blow up. In practice, this behaviour is commonly cured by lowering the CFL number until a stable solution is obtained.

This applies to all of the above Runge Kutta schemes. A characteristic of this category of time integration methods, however, is that the stability region is growing with increasing number of steps. Here, the third-order extended-stability scheme given in Equation (3.2.7) has the largest theoretical CFL limit among the methods presented in this thesis.

3.3 Spatial Discretisation

The spatial derivatives at the centre of the control volume (i, j, k) are discretised using the inter-cell flux values across the faces defined by the subscripts $(i \pm 1/2, j, k)$, $(i, j \pm 1/2, k)$ and $(i, j, k \pm 1/2)$, see Figure 3.1.

Thus, the semi-discretised form of Equation (3.2.1) can be written as

$$\begin{aligned} \frac{\partial \mathbf{U}}{\partial t} = &- \frac{\mathbf{E}_{i+1/2,j,k} - \mathbf{E}_{i-1/2,j,k}}{\Delta\xi} - \frac{\mathbf{F}_{i,j+1/2,k} - \mathbf{F}_{i,j-1/2,k}}{\Delta\eta} - \frac{\mathbf{G}_{i,j,k+1/2} - \mathbf{G}_{i,j,k-1/2}}{\Delta\zeta} \\ &+ \frac{\mathbf{L}_{i+1/2,j,k} - \mathbf{L}_{i-1/2,j,k}}{\Delta\xi} + \frac{\mathbf{M}_{i,j+1/2,k} - \mathbf{M}_{i,j-1/2,k}}{\Delta\eta} + \frac{\mathbf{N}_{i,j,k+1/2} - \mathbf{N}_{i,j,k-1/2}}{\Delta\zeta} , \end{aligned} \tag{3.3.1}$$

where each term on the right-hand side can be solved independently due to the dimensional splitting and the complete system is integrated in time after all the discretised fluxes are added up.

In case of the linear viscous fluxes **L**, **M** and **N**, the solution is simply given by a central difference scheme, whereas for the non-linear advective fluxes **E**, **F** and **G** a high-resolution Godunov-type method is developed in the following sections.

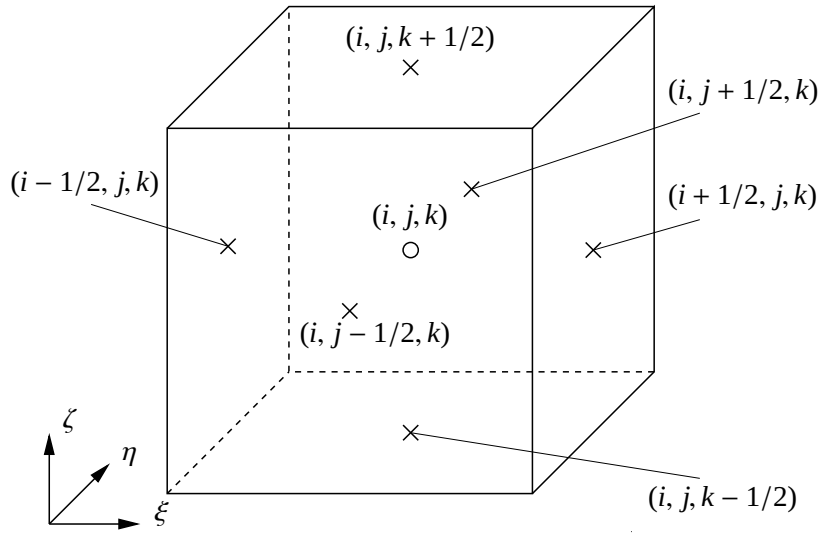

Figure 3.1: Three-dimensional notation for a finite volume cell with the centre at (i, j, k).

3.4 Characteristics-Based Scheme

The characteristics-based method employed for solving the advective part of the governing equations is a linearised Riemann solver. It is considered a high-resolution Godunov-type method when combined with a high-order reconstruction scheme for computing the left and right initial states of the Riemann problem. This method was firstly presented by Eberle [32] for the compressible Euler Equations and later extended by Drikakis [24], Drikakis et al. [28].

In order to present a new derivation of the characteristics-based scheme after Shapiro [101], it is sufficient to consider the one-dimensional inviscid counterpart of Equation (3.1.28) given by

$$\frac{\partial \mathbf{U}}{\partial t} + \frac{\partial \mathbf{E}}{\partial \xi} = 0 \; . \tag{3.4.1}$$

The solution to this one-dimensional Riemann problem is then used to calculate the sought-after inter-cell flux **E** and the remaining advective fluxes **F** and **G** can be determined accordingly.

3.4.1 Method of Characteristics

For the method of characteristics, e.g. see the book of Laney [65], the Partial Differential Equation (3.4.1) is written as

$$\frac{\partial \mathbf{U}}{\partial t} + \mathbf{A}\frac{\partial \mathbf{U}}{\partial \xi} = 0 \; , \tag{3.4.2}$$

where $\mathbf{A} = \partial \mathbf{E}/\partial \mathbf{U}$ is the flux Jacobian. In order to simplify the Riemann problem, Equation (3.4.2) is linearised, i.e. **A** is assumed to be approximately constant from one time level to the next.

Both sides of the linearised equation are now multiplied by $\mathbf{Q}^{-1}$ and the second term on the left-hand side is extended with $\mathbf{Q}$, yielding

$$\mathbf{Q}^{-1}\frac{\partial \mathbf{U}}{\partial t} + \mathbf{Q}^{-1}\mathbf{A}\mathbf{Q}\mathbf{Q}^{-1}\frac{\partial \mathbf{U}}{\partial \xi} = 0 \,, \tag{3.4.3}$$

where $\mathbf{Q}$ and $\mathbf{Q}^{-1}$ are the matrices whose columns are the right characteristic vectors and whose rows are the left characteristic vectors, respectively. The characteristic vectors are also known as eigenvectors. With the definition of the characteristic variables $\mathbf{V}$ being

$$\partial \mathbf{V} = \mathbf{Q}^{-1}\partial \mathbf{U} \tag{3.4.4}$$

and substituting

$$\mathbf{Q}^{-1}\mathbf{A}\mathbf{Q} = \mathbf{\Lambda} \,, \tag{3.4.5}$$

Equation (3.4.3) takes the characteristic form

$$\frac{\partial \mathbf{V}}{\partial t} + \mathbf{\Lambda}\frac{\partial \mathbf{V}}{\partial \xi} = 0 \,, \tag{3.4.6}$$

where $\mathbf{\Lambda}$ is the matrix whose diagonal elements are the characteristic values or eigenvalues. Thus, the Riemann problem for a linear system of five equations has been decomposed into five Riemann problems for a linear advection equation.

The characteristic variables $\mathbf{V}$ are also called signals, or the information carried by a wave travelling at a speed determined by the corresponding characteristic value λ. Analogous to Section 2.4, the wavefront or characteristic is given by $d\xi/dt = \lambda$ in the t-ξ diagram. This situation is illustrated in Figure 3.2(a) for a single wave emanating from the cell faces $i \pm 1/2$ at the current time level n. Most importantly, it can be shown that the values of $\mathbf{V}$ are constant in time along the corresponding characteristics — hence they are sometimes referred to as the Riemann invariants and they can be used to calculate the state at the next time level.

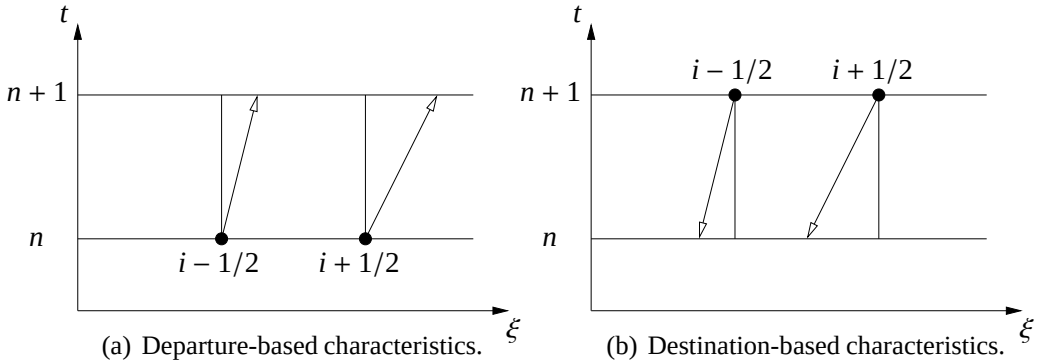

(a) Departure-based characteristics. (b) Destination-based characteristics.

Figure 3.2: Possible arrangements of the cell interfaces and a single wavefront for the method of characteristics.

Since the Riemann solution is self-similar, it is sufficient to determine the flow state at the level $n + 1$ in order to integrate the fluxes at the cell faces in time. If the characteristics start at the current time level n, shown in Figure 3.2(a), an interpolation

procedure is necessary to determine the values at the cell interface for the sought-after time step $n + 1$. Therefore, it is often more convenient to consider the case where the arrival points at $n + 1$ coincide with the cell interface as depicted in Figure 3.2(b). For the destination-based characteristics, the flow state at the next time level is fully determined because the initial states of individual characteristics at level n can be calculated through, e.g. an upwind scheme.

Upwind methods are based on the idea that information propagates at different speeds along the characteristics with different orientation. Therefore, upwind methods incorporate a sense for the direction of the incoming signal by taking the knowledge about the structure of the solution given by the eigenvalues into account. Numerically, this is expressed as

$$\mathbf{U} = (0.5 + \psi)\mathbf{U}_L + (0.5 - \psi)\mathbf{U}_R \,, \tag{3.4.7}$$

where the upwinding coefficient ψ is defined as

$$\psi = 0.5\frac{\lambda_L + \lambda_R}{|\lambda_L| + |\lambda_R| + \epsilon} \,. \tag{3.4.8}$$

The parameter ϵ averts division by zero and $\mathbf{U}_{L,R}$, $\lambda_{L,R}$ are the left and right flow states and eigenvalues at the cell face, respectively.

3.4.2 Eigenvalues of the System

As seen in the previous section, the eigenvalues of the system play a crucial role in calculating the inter-cell flux values. In order to determine the eigenvalues, Equation (3.4.1) is employed in its primitive form. This formulation based on the primitive variables $\mathbf{W} = (\rho, u, v, w, p)^T$ is often preferred for the sake of simplicity. Thus, the eigenvalues for the system of equations given by

$$\frac{\partial \mathbf{W}}{\partial t} + \mathbf{C}\frac{\partial \mathbf{W}}{\partial \xi} = 0 \,, \tag{3.4.9}$$

with

$$\mathbf{C} = \begin{pmatrix} u_\perp & \rho\xi_x & \rho\xi_y & \rho\xi_z & 0 \\ 0 & u_\perp & 0 & 0 & \frac{1}{\rho}\xi_x \\ 0 & 0 & u_\perp & 0 & \frac{1}{\rho}\xi_y \\ 0 & 0 & 0 & u_\perp & \frac{1}{\rho}\xi_z \\ 0 & \rho a^2\xi_x & \rho a^2\xi_y & \rho a^2\xi_z & u_\perp \end{pmatrix} \tag{3.4.10}$$

and

$$u_\perp = \xi_x u + \xi_y v + \xi_z w \,, \tag{3.4.11}$$

$$a^2 = \frac{\gamma p}{\rho} \tag{3.4.12}$$

can be calculated by solving

$$|\mathbf{C}-\lambda\mathbf{I}| = \begin{vmatrix} u_\perp-\lambda & \rho\xi_x & \rho\xi_y & \rho\xi_z & 0 \\ 0 & u_\perp-\lambda & 0 & 0 & \frac{1}{\rho}\xi_x \\ 0 & 0 & u_\perp-\lambda & 0 & \frac{1}{\rho}\xi_y \\ 0 & 0 & 0 & u_\perp-\lambda & \frac{1}{\rho}\xi_z \\ 0 & \rho a^2\xi_x & \rho a^2\xi_y & \rho a^2\xi_z & u_\perp-\lambda \end{vmatrix} = 0 \,. \tag{3.4.13}$$

for λ. This leads to one triple eigenvalue denoted by the subscript 0 and two single eigenvalues marked by the subscripts + and −

$$\lambda_0 = u_\perp \,, \tag{3.4.14}$$

$$\lambda_\pm = u_\perp \pm a\sqrt{\xi_x^2+\xi_y^2+\xi_z^2} \,. \tag{3.4.15}$$

The efficiency of the numerical algorithm can be improved by dividing Equation (3.4.9) with the cell face area $\sqrt{\xi_x^2+\xi_y^2+\xi_z^2}$, yielding

$$\frac{\partial\mathbf{W}}{\partial\bar{t}} + \overline{\mathbf{C}}\frac{\partial\mathbf{W}}{\partial\xi} = 0 \,, \tag{3.4.16}$$

with

$$\overline{\mathbf{C}} = \begin{pmatrix} \overline{u}_\perp & \rho\overline{x} & \rho\overline{y} & \rho\overline{z} & 0 \\ 0 & \overline{u}_\perp & 0 & 0 & \frac{1}{\rho}\overline{x} \\ 0 & 0 & \overline{u}_\perp & 0 & \frac{1}{\rho}\overline{y} \\ 0 & 0 & 0 & \overline{u}_\perp & \frac{1}{\rho}\overline{z} \\ 0 & \rho a^2\overline{x} & \rho a^2\overline{y} & \rho a^2\overline{z} & \overline{u}_\perp \end{pmatrix} \tag{3.4.17}$$

and

$$\left(\overline{x},\overline{y},\overline{z}\right)^T = \frac{\left(\xi_x,\xi_y,\xi_z\right)^T}{\sqrt{\xi_x^2+\xi_y^2+\xi_z^2}} \,, \tag{3.4.18}$$

$$\overline{u}_\perp = \overline{x}u+\overline{y}v+\overline{z}w \,, \tag{3.4.19}$$

$$\bar{t} = t\sqrt{\xi_x^2+\xi_y^2+\xi_z^2} \,, \tag{3.4.20}$$

$$1 = \overline{x}^2+\overline{y}^2+\overline{z}^2 \,. \tag{3.4.21}$$

Now, the eigenvalues take the form

$$\lambda_0 = \overline{u}_\perp \,, \tag{3.4.22}$$

$$\lambda_\pm = \overline{u}_\perp \pm a \,. \tag{3.4.23}$$

3.4.3 Characteristic Decomposition

In order to determine the Riemann invariants $\mathbf{V}$ associated with the characteristics travelling at a speed defined by the eigenvalues λ_0 and $\lambda_\pm$, the system (3.4.16) is diagonalised analogously to Equation (3.4.3). Here, the matrix of the right eigenvectors is given by

$$\mathbf{Q} = \begin{pmatrix} 0 & 0 & 1 & \frac{1}{a^2} & \frac{1}{a^2} \\ -\frac{\overline{z}}{\overline{x}} & -\frac{\overline{y}}{\overline{x}} & 0 & \frac{\overline{x}}{\rho a^2} & -\frac{\overline{x}}{\rho a^2} \\ 0 & 1 & 0 & \frac{\overline{y}}{\rho a^2} & -\frac{\overline{y}}{\rho a^2} \\ 1 & 0 & 0 & \frac{\overline{z}}{\rho a^2} & -\frac{\overline{z}}{\rho a^2} \\ 0 & 0 & 0 & 1 & 1 \end{pmatrix}, \tag{3.4.24}$$

where first three columns are the eigenvectors associated with λ_0 and the last two columns correspond to $\lambda_\pm$.

The Riemann invariants are calculated using the inverse of the eigenvector matrix

$$\mathbf{Q}^{-1} = \begin{pmatrix} 0 & -\overline{x}\,\overline{z} & -\overline{y}\,\overline{z} & 1-\overline{z}^2 & 0 \\ 0 & -\overline{x}\,\overline{y} & 1-\overline{y}^2 & -\overline{y}\,\overline{z} & 0 \\ 1 & 0 & 0 & 0 & -\frac{1}{a^2} \\ 0 & \frac{1}{2}\rho a\overline{x} & \frac{1}{2}\rho a\overline{y} & \frac{1}{2}\rho a\overline{z} & \frac{1}{2} \\ 0 & -\frac{1}{2}\rho a\overline{x} & -\frac{1}{2}\rho a\overline{y} & -\frac{1}{2}\rho a\overline{z} & \frac{1}{2} \end{pmatrix}. \tag{3.4.25}$$

Thus, the relation $\partial\mathbf{V} = \mathbf{Q}^{-1}\partial\mathbf{W}$ yields

$$\partial\mathbf{V} = \begin{pmatrix} -\overline{x}\,\overline{z}du - \overline{y}\,\overline{z}dv + \left(1-\overline{z}^2\right)dw \\ -\overline{x}\,\overline{y}du + \left(1-\overline{y}^2\right)dv - \overline{y}\,\overline{z}dw \\ d\rho - \frac{dp}{a} \\ \frac{1}{2}\left(dp + \rho a\left(\overline{x}du + \overline{y}dv + \overline{z}dw\right)\right) \\ \frac{1}{2}\left(dp - \rho a\left(\overline{x}du + \overline{y}dv + \overline{z}dw\right)\right) \end{pmatrix}, \tag{3.4.26}$$

which, after applying some linear algebra to the first two rows associated with λ_0, takes the simplified form

$$\partial\mathbf{V} = \begin{pmatrix} \overline{x}dw - \overline{z}du \\ \overline{x}dv - \overline{y}du \\ d\rho - \frac{dp}{a} \\ \frac{1}{2}\left(dp + \rho a\left(\overline{x}du + \overline{y}dv + \overline{z}dw\right)\right) \\ \frac{1}{2}\left(dp - \rho a\left(\overline{x}du + \overline{y}dv + \overline{z}dw\right)\right) \end{pmatrix}. \tag{3.4.27}$$

For solving the original system (3.4.2), however, the conservative invariants need to be recovered. If $(l, m, n)^T_{0,+,-}$ represent the conservative variables $(\rho u, \rho v, \rho w)^T_{0,+,-}$ along the characteristics associated with $(0, +, -)$, then the Riemann invariants can be written

as

$$\partial\mathbf{V} = \begin{pmatrix} \overline{x}\frac{dn_0 - wd\rho_0}{\rho} - \overline{z}\frac{dl_0 - ud\rho_0}{\rho} \\ \overline{x}\frac{dm_0 - vd\rho_0}{\rho} - \overline{y}\frac{dl_0 - ud\rho_0}{\rho} \\ d\rho_0 - P_0\frac{\gamma-1}{a} \\ \frac{1}{2}\left(P_+(\gamma-1) + \rho a\left(\overline{x}\frac{dl_+ - ud\rho_+}{\rho} + \overline{y}\frac{dm_+ - vd\rho_+}{\rho} + \overline{z}\frac{dn_+ - wd\rho_+}{\rho}\right)\right) \\ \frac{1}{2}\left(P_-(\gamma-1) - \rho a\left(\overline{x}\frac{dl_- - ud\rho_-}{\rho} + \overline{y}\frac{dm_- - vd\rho_-}{\rho} + \overline{z}\frac{dn_- - wd\rho_-}{\rho}\right)\right) \end{pmatrix}, \tag{3.4.28}$$

where the differentials of the primitive variables have been substituted according to the chain rule of differentiation

$$\begin{pmatrix} d\rho \\ du \\ dv \\ dw \\ dp \end{pmatrix}_{0,+,-} = \begin{pmatrix} d\rho \\ \frac{dl - ud\rho}{\rho} \\ \frac{dm - vd\rho}{\rho} \\ \frac{dn - wd\rho}{\rho} \\ P(\gamma-1) \end{pmatrix}_{0,+,-} \tag{3.4.29}$$

and $P_{0,+,-} = de_{0,+,-} - udl_{0,+,-} - vdm_{0,+,-} - wdn_{0,+,-} + \frac{u^2+v^2+w^2}{2}d\rho_{0,+,-}$.

Remember that the Riemann invariants are constant along the characteristics ($\partial\mathbf{V} = 0$) and the differentials can be discretised as the difference between the known initial states $(\rho, l, m, n, e)^T_{0,+,-}$ at the origin of the characteristics and the sought-after state $\left(\overline{\rho}, \overline{l}, \overline{m}, \overline{n}, \overline{e}\right)^T$ at the destination of the characteristics

$$\begin{pmatrix} d\rho \\ dl \\ dm \\ dn \\ de \end{pmatrix}_{0,+,-} \approx \begin{pmatrix} \Delta\rho \\ \Delta l \\ \Delta m \\ \Delta n \\ \Delta e \end{pmatrix}_{0,+,-} = \begin{pmatrix} \overline{\rho} \\ \overline{l} \\ \overline{m} \\ \overline{n} \\ \overline{e} \end{pmatrix} - \begin{pmatrix} \rho \\ l \\ m \\ n \\ e \end{pmatrix}_{0,+,-} . \tag{3.4.30}$$

Let $\overline{\mathbf{U}} = \left(\overline{\rho}, \overline{l}, \overline{m}, \overline{n}, \overline{e}\right)^T$, $q^2 = u^2 + v^2 + w^2$ and $\hat{\gamma} = \gamma - 1$. After setting the Equation (3.4.28) equal to zero and some more algebra the following linear system is derived

$$\mathbf{B}\overline{\mathbf{U}} = \mathbf{D} , \tag{3.4.31}$$

with

$$\mathbf{B} = \begin{pmatrix} zu - \overline{x}w & -\overline{z} & 0 & \overline{x} & 0 \\ u\overline{y} - v\overline{x} & -\overline{y} & \overline{x} & 0 & 0 \\ \frac{a}{\hat{\gamma}} - \frac{q^2}{2} & u & v & w & -1 \\ \hat{\gamma}\frac{q^2}{2} - a\overline{u}_\perp & a\overline{x} - \hat{\gamma}u & a\overline{y} - \hat{\gamma}v & a\overline{z} - \hat{\gamma}w & \hat{\gamma} \\ \hat{\gamma}\frac{q^2}{2} + a\overline{u}_\perp & -(a\overline{x} + \hat{\gamma}u) & -(a\overline{y} + \hat{\gamma}v) & -(a\overline{z} + \hat{\gamma}w) & \hat{\gamma} \end{pmatrix} \tag{3.4.32}$$

and

$$\mathbf{D} = \begin{pmatrix} (\overline{z}u - \overline{x}w)\,\rho_0 - \overline{z}l_0 + \overline{x}n_0 \\ (u\overline{y} - v\overline{x})\,\rho_0 - \overline{y}l_0 + \overline{x}m_0 \\ \left(\frac{a}{\gamma-1} - \frac{q^2}{2}\right)\rho_0 + ul_0 + vm_0 + wn_0 - e_0 \\ \rho_+\left(\hat{\gamma}\frac{q^2}{2} - a\overline{u}_\perp\right) + l_+\,(a\overline{x} - \hat{\gamma}u) + m_+\,(a\overline{y} - \hat{\gamma}v) + n_+\,(a\overline{z} - \hat{\gamma}w) + \hat{\gamma}e_+ \\ \rho_-\left(\hat{\gamma}\frac{q^2}{2} + a\overline{u}_\perp\right) - l_-\,(a\overline{x} + \hat{\gamma}u) - m_-\,(a\overline{y} + \hat{\gamma}v) - n_-\,(a\overline{z} + \hat{\gamma}w) + \hat{\gamma}e_- \end{pmatrix} \tag{3.4.33}$$

The system (3.4.31) can now be solved for the unknown vector $\overline{\mathbf{U}}$, yielding

$$\overline{\mathbf{U}} = \begin{pmatrix} \overline{\rho} \\ \overline{l} \\ \overline{m} \\ \overline{n} \\ \overline{e} \end{pmatrix} = \begin{pmatrix} \overline{\rho} \\ \overline{\rho u} \\ \overline{\rho v} \\ \overline{\rho w} \\ \overline{e} \end{pmatrix} = \begin{pmatrix} \rho_0 + R_+ + R_- \\ (\rho u)_0 + (u + a\overline{x})\,R_+ + (u - a\overline{x})\,R_- \\ (\rho v)_0 + (v + a\overline{y})\,R_+ + (v - a\overline{y})\,R_- \\ (\rho w)_0 + (w + a\overline{z})\,R_+ + (w - a\overline{z})\,R_- \\ e_0 + (H + a\overline{u}_\perp)\,R_+ + (H - a\overline{u}_\perp)\,R_+ \end{pmatrix}, \tag{3.4.34}$$

where

$$\begin{aligned} R_+ \;=\; & \frac{1}{2a^2}((\rho_0 - \rho_+)\left(a\overline{u}_\perp - \hat{\gamma}\frac{q^2}{2}\right) + (l_0 - l_+)\,(\hat{\gamma}u - a\overline{x}) + \\ & (n_0 - n_+)\,(\hat{\gamma}v - a\overline{y}) + (m_0 - m_+)\,(\hat{\gamma}w - a\overline{z}) - (e_0 - e_+)\,\hat{\gamma}\;, \end{aligned}$$

$$\begin{aligned} R_- \;=\; & \frac{1}{2a^2}((\rho_0 - \rho_-)\left(a\overline{u}_\perp + \hat{\gamma}\frac{q^2}{2}\right) + (l_0 - l_-)\,(\hat{\gamma}u + a\overline{x}) + \\ & (n_0 - n_-)\,(\hat{\gamma}v + a\overline{y}) + (m_0 - m_-)\,(\hat{\gamma}w + a\overline{z}) - (e_0 - e_-)\,\hat{\gamma} \end{aligned}$$

and the total enthalpy H is given by

$$H = \frac{a^2}{\gamma - 1} + 0.5q^2\;.$$

The velocities u, v, w and the speed of sound a are the average values of their left and right states. Finally, the advective flux $\mathbf{E}$ at the cell face as required for solving equation (3.4.1) can be calculated using the characteristics-based variables $\overline{\mathbf{U}}$, i.e.

$$\mathbf{E} = \mathbf{E}(\overline{\mathbf{U}})\;. \tag{3.4.35}$$

3.5 High-Resolution Algorithms

High-resolution of the numerical solver is achieved by extrapolating the variables as linear, quadratic or higher-order functions in a cell, whereas first-order algorithms follow a piecewise constant approach. This is the general basis of the non-linear mechanism that distinguishes modern methods from classical linear schemes. Additionally, high-resolution methods are able to adapt to the behaviour of the local solution instead

of treating every part of the solution the same — hence they also exhibit a sensitivity to the state of the flow.

Two classes of reconstruction methods are presented in this section: different variants of the *Monotonic Upwind Scheme for Scalar Conservation Laws* (MUSCL) as originally introduced by van Leer [119] and a *Weighted Essentially Non-Oscillatory* (WENO) scheme following the ideas of Liu et al. [71].

3.5.1 MUSCL Schemes

For the family of MUSCL schemes, the left and right states of the conservative variables $\mathbf{U}$ at the cell interface $(i+1/2)$ are computed according to Toro [115] as

$$\begin{aligned}\mathbf{U}_{L,i+1/2} =& \mathbf{U}_i \quad + \frac{1}{4}\left[(1-k)\,\phi\,(r_L)\,(\mathbf{U}_i - \mathbf{U}_{i-1}) + (1+k)\,\phi\left(\frac{1}{r_L}\right)(\mathbf{U}_{i+1} - \mathbf{U}_i)\right] ,\\ \mathbf{U}_{R,i+1/2} =& \mathbf{U}_{i+1} - \frac{1}{4}\left[(1-k)\,\phi\,(r_R)\,(\mathbf{U}_{i+2} - \mathbf{U}_{i+1}) + (1+k)\,\phi\left(\frac{1}{r_R}\right)(\mathbf{U}_{i+1} - \mathbf{U}_i)\right] ,\end{aligned} \tag{3.5.1}$$

where k is a free parameter in the interval $[-1, 1]$ and ϕ is a limiter function based on the slopes of the conserved variables within, for the second- and third-order accurate schemes, the four-point stencil given by the cell averaged values at positions $(i-1)$, (i), $(i+1)$ and $(i+2)$. For $k = -1$ or $k = 0$ the MUSCL extrapolation in Equations (3.5.1) is essentially a full upwind scheme or a central difference scheme, respectively, and third-order of accuracy can be obtained for $k = 1/3$ if the limiter is not entirely symmetric. It should be noted that the second-order limiters considered here do not satisfy this criteria, thus their order of accuracy cannot be increased.

Second-order limiters. All second- and third-order accurate limiter functions use the following definitions of the left and the right ratio of the slopes

$$\begin{aligned} r_L =& \frac{\mathbf{U}_{i+1} - \mathbf{U}_i}{\mathbf{U}_i - \mathbf{U}_{i-1}} ,\\ r_R =& \frac{\mathbf{U}_{i+1} - \mathbf{U}_i}{\mathbf{U}_{i+2} - \mathbf{U}_{i+1}} .\end{aligned} \tag{3.5.2}$$

The most popular second-order limiter functions can be found in several textbooks, e.g. Laney [65], LeVeque [68], Toro [115]. Although they are not employed in this thesis, they are given here for the sake of completeness

$$\phi_{MM} = \begin{cases} 0 & \text{if } r \le 0 \\ r & \text{if } r > 0 \end{cases} , \tag{3.5.3}$$

$$\phi_{VL} = \begin{cases} 0 & \text{if } r \le 0 \\ \frac{2r}{1+r} & \text{if } r > 0 \end{cases} , \tag{3.5.4}$$

$$\phi_{VA} = \begin{cases} 0 & \text{if } r \le 0 \\ \frac{r(1+r)}{1+r^2} & \text{if } r > 0 \end{cases} , \tag{3.5.5}$$

where *MM*, *VL* and *VA* stand for the MinMod, Van Leer and Van Albada limiter, respectively. All of the above satisfy the monotonicity constraint and reduce to a piecewise linear method near local extrema.

Third-order limiter. In a similar fashion to the second-order limiters, Zóltak and Drikakis [132] developed an extension to the Van Albada function which is referred to by the subscript $M3$

$$\phi_{M3} = \begin{cases} 0 & \text{if } r \leq 0 \\ 1 - \left(1 + \frac{2Nr}{1+r^2}\right)\left(1 - \frac{2r}{1+r^2}\right)^N & \text{if } r > 0 \end{cases} . \tag{3.5.6}$$

This formulation of the third-order limiter includes a "steepening" parameter N that improves the resolution of discontinuities. For general use N is set equal to 2.

Fifth-order limiter. Kim and Kim [63] presented a fifth-order accurate MUSCL scheme using a six-point stencil as opposed to the classical four-point stencil employed previously. Here, the slope ratios are defined as

$$\begin{aligned} r_{L,i} &= \frac{\mathbf{U}_{i+1} - \mathbf{U}_i}{\mathbf{U}_i - \mathbf{U}_{i-1}} , \\ r_{R,i} &= \frac{\mathbf{U}_i - \mathbf{U}_{i-1}}{\mathbf{U}_{i+1} - \mathbf{U}_i} , \end{aligned} \tag{3.5.7}$$

and ϕ is calculated by

$$\begin{aligned} \phi^*_{L,M5} &= \frac{-2/r_{L,i-1} + 11 + 24r_{L,i} - 3r_{L,i}r_{L,i+1}}{30} , \\ \phi^*_{R,M5} &= \frac{-2/r_{R,i+2} + 11 + 24r_{R,i+1} - 3r_{R,i+1}r_{R,i}}{30} . \end{aligned} \tag{3.5.8}$$

Subsequently, this function is limited in order to maintain monotonicity and the fifth-order limiter can now be written in compact form as

$$\phi_{L/R,M5} = max(0, min(2, 2r_{L/R,i}, \phi^*_{L/R,M5})) . \tag{3.5.9}$$

3.5.2 WENO Schemes

WENO schemes are an extension of the *Essentially Non-Oscillatory* (ENO) concept originally proposed by Harten et al. [55], Shu and Osher [102]. ENO has been developed with the idea of a higher-order interpolation method in mind. Since high-degree polynomials are prone to oscillations even if the underlying data is smooth a method for controlling these oscillations has to be found. Instead of employing limiter functions like MUSCL schemes, ENO chooses the smoothest of many possible stencils to avoid disastrous overshoots or undershoots — hence it does not formally satisfy the non-linear stability criteria.

WENO methods are primarily based on the work of Balsara and Shu [6], Jiang and Shu [62], Liu et al. [71]. They combine all possible stencils rather than choosing

only a single one, where a convexly weighted average is produced according to the smoothness of the candidates. The averaging reduces the sensitivity to small changes in the samples and it also reduces the effects of the truncation errors. Thus, WENO schemes ideally reach an order of accuracy calculated by $2s-1$ with s being the number of sample points. ENO methods, on the other hand, generally achieve lower orders of accuracy because they discard most of the points.

The WENO method employed in this thesis uses a stencil of five cells to either side of the interface, yielding a ninth order accurate scheme in one dimension. In order to illustrate the basic principle, however, only a third-order WENO reconstruction derived from a linear interpolation with $s = 2$ is presented here. For the reconstruction within a cell i, two stencils $S_{0,1}$ comprising the cell-averaged values of two samples each are considered

$$\begin{aligned} S_0 &= (x_{i-1}, x_i) \ , \\ S_1 &= (x_i, x_{i+1}) \ . \end{aligned} \tag{3.5.10}$$

A standard linear interpolation using the stencils 0 and 1 leads to the following polynomials

$$\begin{aligned} \mathbf{p}_0(x) &= \mathbf{U}_i + \frac{\mathbf{U}_i - \mathbf{U}_{i-1}}{\Delta x} (x - x_i) \ , \\ \mathbf{p}_1(x) &= \mathbf{U}_i + \frac{\mathbf{U}_{i+1} - \mathbf{U}_i}{\Delta x} (x - x_i) \ , \end{aligned} \tag{3.5.11}$$

where the right interface value at $i - 1/2$ and the left interface value at $i + 1/2$ are obtained for x equal to $x_{i-1/2}$ and $x_{i+1/2}$, respectively.

Subsequently, calculation of the weighted average $\mathbf{P}$ of the above polynomials yields the reconstructed variables at the cell faces $\mathbf{U}_{R,i-1/2}$ and $\mathbf{U}_{L,i+1/2}$. The convex combination is defined by

$$\mathbf{P}(x) = \frac{\mathbf{a}_0}{\mathbf{a}_0 + \mathbf{a}_1} \mathbf{p}_0(x) + \frac{\mathbf{a}_1}{\mathbf{a}_0 + \mathbf{a}_1} \mathbf{p}_1(x) \ , \tag{3.5.12}$$

with

$$\begin{aligned} \mathbf{a}_0 &= \frac{C_0}{(\epsilon + \mathbf{IS}_0)^2} \ , \\ \mathbf{a}_1 &= \frac{C_1}{(\epsilon + \mathbf{IS}_1)^2} \ . \end{aligned} \tag{3.5.13}$$

Here, ϵ is a small positive number which is introduced to avoid a division by zero in a perfectly smooth flow and $C_{0,1}$ are the optimal weights. Furthermore, the smoothness indicators are given by

$$\begin{aligned} \mathbf{IS}_0 &= (\mathbf{U}_i - \mathbf{U}_{i-1})^2 \ , \\ \mathbf{IS}_1 &= (\mathbf{U}_{i+1} - \mathbf{U}_i)^2 \ . \end{aligned} \tag{3.5.14}$$

The derivation of a higher-order method follows the same concept. However, the complexity of the equations is rising with an increasing order of accuracy, for more details see Balsara and Shu [6], Drikakis and Rider [27], Jiang and Shu [62].

3.6 Domain Decomposition

The simulation of separated and turbulent three-dimensional flows requires a large set of data and leads to a high computational cost. In order to solve the problems in a smaller time scale, the load needs to be distributed over a set number of processes. Therefore, the global computational grid is split up into several sub-grids, which are assigned to separate processes[1]. The governing equations can now be applied in parallel as several smaller,"local" problems — thus solving the global problem in an acceptable time.

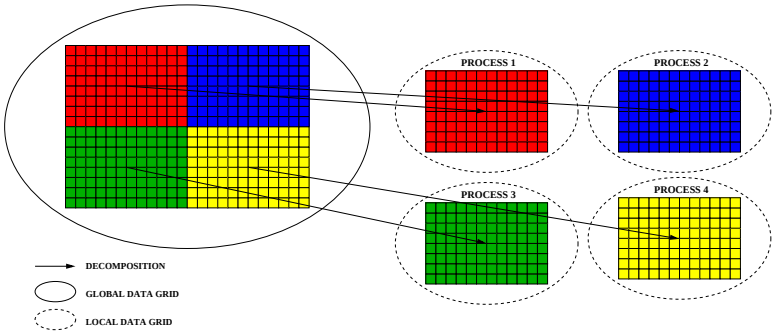

Figure 3.3: Decomposition of a two-dimensional global data domain over four processes.

The degree of domain decomposition depends on the number of processes available, see Minty et al. [81]. Figure 3.3 illustrates the decomposition of a two-dimensional global grid into four equally-sized data blocks which can be treated independently by four separate processes. The global data is split up into four sections and distributed among several processes, allowing problems that are otherwise memory bound to be calculated. Decomposing the domain as evenly as possible for a given number of processes available in each spatial direction is done automatically by a pre-processor.

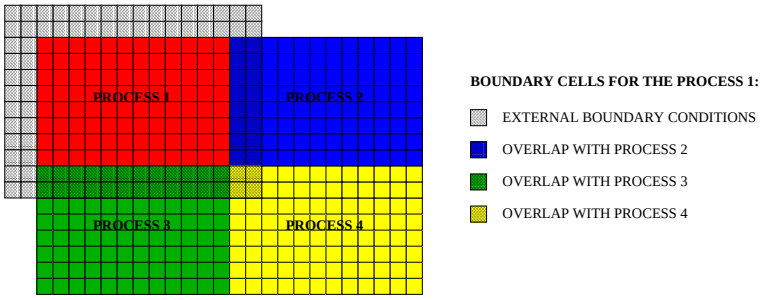

Figure 3.4: Update of local boundary cells for process 1.

At each iteration, each process requires data from its neighbours in order to calculate

[1] *In practice, each topological entity ("process") is assigned to an individual, physical central processing unit ("processor") in order to increase the performance of the simulation. In this case, the terms "process" and "processor" are interchangeable.*

the state of the local data grid. This information exchange has been implemented according to the MPI-1 standard, e.g. see MacDonald et al. [74], Pacheco [87], thus ensuring portability of the code to different computing architectures and operating systems. All processes copy the overlapping data from the local grid into buffer arrays and send it to the corresponding adjacent processes. Then they receive the buffer arrays sent by the neighbouring processes, unscramble the data and store it in the appropriate boundary cells. Swapping the boundaries involves point-to-point communication between all adjoining processes and is implemented in a similar manner to an external boundary condition. A schematic of the boundary cell update for process 1 of the above example is shown in Figure 3.4.

3.7 Summary

In this chapter, the numerical methods employed in this thesis to solve the non-dimensional, compressible Navier-Stokes Equations have been presented. For the integration in time, several options comprising second- and third-order accurate, TVD and non-TVD, explicit Runge Kutta schemes are given in Section 3.2. In combination with various variants of high-resolution, Godunov-type methods used for solving the advective fluxes (Sections 3.4 and 3.5) this allows for a rigorous investigation of different temporal and spatial discretisation techniques in the context of ILES for separated and turbulent flows. Furthermore, the solution procedure for the viscous fluxes has been explained briefly and the basic principles of parallel computing have been illustrated.

CHAPTER 4

Taylor-Green Vortex

IN simulations of separated flows, special care has to be taken to capture the transitional regime leading to a turbulent flow state as accurately as possible. In order to assess the capabilities of different numerical methods, it is preferable to isolate the problem by simplifying the conditions. Here, the vortex system introduced by Taylor and Green [109] is considered for evaluating the behaviour of the methods presented in Chapter 3 during various stages in the development of the flow.

4.1 Introduction

A grand challenge for modern methods in Computational Fluid Dynamics is the modelling and simulation of the time evolution of fully non-linear turbulent flow in and around realistic engineering applications. Moreover, for separated flows it is often necessary to capture several different stages in the development of a turbulent flow field. Here, it should be noted that the linear, non-linear and fully turbulent stages often place contradictory requirements on the numerical methods used. For example, in a fully developed turbulent flow it is desirable that the numerical method provides some kind of damping to replace the action of subgrid stresses on the resolved motions. However, in the early linear and non-linear stages it is important that the perturbations are allowed to grow without excessive damping from the numerical method.

For such flows, it is unlikely that a deterministic predictive framework based on CFD will emerge in the foreseeable future. A reason for this is the inherent difficulty in modelling and validating all the relevant physical sub-processes, and acquiring all the necessary and relevant initial and boundary conditions. Thus, the modelling challenge is to develop computational methods that will still give accurate and reliable results for at least the large energy-containing scales of motion, even if the simulation is severly under-resolved, i.e. not all dynamic eddy scales are explicitly incorporated.

In the classical picture of turbulence, the kinetic energy is transferred from large to successively smaller scales until it is transformed into internal energy, what would be the dissipation into heat. Whereas the dynamics are assumed to be essentially inviscid at the large scales, the dissipation mechanism is governed by the action of molecular

viscosity. In the absence of molecular viscosity, for example in idealistic inviscid simulations, the loss of kinetic energy can be used to assess the numerical dissipation inherent to the numerical scheme employed. The same holds for the transitional stage.

It is commonly accepted that the physical processes in transition and in fully developed turbulence are governed by the interaction of vortices. Here, a crucial mechanism described by vortex dynamics is vortex stretching. In order to investigate the straining and consequent extension of vortex lines, a complete solution of the three-dimensional governing equations is necessary — in a two-dimensional representation only vortex pairing or tearing can be observed, but the stretching mechanism is implicitly eliminated because the vortex lines are perpendicular to the domain. Therefore, a three-dimensional initial condition for a general investigation of the transition to turbulence has to provide a simple but well-defined description of the large scales and also some properties of statistically uniform isotropic turbulence. The simplest fundamental case that has been used as a prototype for vortex stretching and the consequent production of small-scale eddies is probably the vortex system introduced by Taylor and Green [109].

The dynamics of the inviscid and the viscous Taylor-Green Vortex have been discussed in detail in the 1980's by Brachet et al. [12] and later in the 1990's by the same author, see Brachet [11]. The pseudo-spectral DNS employed conserves the mass, the momentum and the energy discretely for the finite number of terms in the Fourier series expansion. Furthermore, these methods are strictly non-dissipative — hence they are often used to produce benchmark results for finite volume or finite difference solutions. In the absence of molecular viscosity, however, the pseudo-spectral method becomes inaccurate and even unstable during the course of the simulation. The reason for this behaviour is the undamped growth of an inviscid instability mechanism originating from a vortex sheet which is formed by the centrifugal forces acting on the Taylor-Green Vortex. As the vortex core twists about the vertical axis and the sheet becomes increasingly unstable the high modes can no longer be represented accurately by the underlying trigonometric polynomial. Therefore, the available data for the inviscid Taylor-Green Vortex is limited to very early times only and clues about the later behaviour of the flow have to be deduced from the viscous results and by logical reasoning. It should be noted, however, that the aim of this investigation is not the accurate reproduction of the idealistic inviscid case. In fact, the purpose of this study is to assess the performance of different high-resolution algorithms and the effects of their intrinsic numerical dissipation during the laminar, transitional and turbulent stage.

The above studies also include data for the viscous Taylor-Green Vortex at Reynolds numbers ranging from 100 to 5000. It has been found that for the highest Reynolds numbers the flow undergoes two stages. At early times, i.e. up to a non-dimensional time between 3 and 4, well-organised structures are formed and the flow remains essentially inviscid. Here, the kinetic energy spectrum behaves like a power law with the wavenumber k and the spectral exponent is of the order of -4. The k^{-4} spectrum suggests that the early flow development may be governed by quasi-two-dimensional dynamics. At later times, the effect of viscosity can no longer be neglected and highly

distorted, dissipative structures develop. When the dissipation rate reaches its maximum the kinetic energy follows a power law spectrum closer to the characteristic -5/3 law for turbulence immortalised by Kolmogorov. The flow structures as well as the dissipation rate eventually decay to zero afterwards due to the lack of an external energy source. The estimates reported by Brachet et al. [12] and Brachet [11] for the time at which the dissipation peak occurs are fairly consistent for the higher Reynolds numbers, see Figure 4.1. The almost indistinguishable results for the highest Reynolds numbers of 3000 and 5000 lead to the hypothesis that they may be close to a viscosity independent limit. Thus, the evolution of the kinetic energy and its dissipation provides a useful quantitative measure for the development of both the viscous and inviscid Taylor-Green Vortex. In the inviscid limit, the kinetic energy can only be dissipated by viscous effects introduced through the explicit or implicit subgrid-scale model of the numerical method — otherwise it should be conserved.

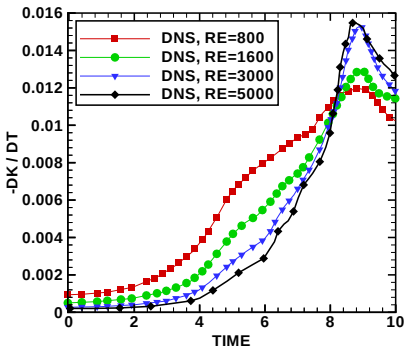

Figure 4.1: Development of the volumetrically averaged kinetic energy dissipation for different Reynolds numbers obtained by the DNS of Brachet [11], Brachet et al. [12].

Various ILES approaches, conventional LES and spectral methods have been used recently to investigate the effects of viscosity on the dynamics of the Taylor-Green Vortex. Details on the impact of both molecular viscosity in the Navier-Stokes Equations and numerical viscosity provided by the discrete approximation of the solution to the Euler Equations can be found in the works of, e.g. Bensow et al. [8], Drikakis et al. [30], Hickel et al. [57], Shu et al. [103]. The evolution of the kinetic energy and the closely related enstrophy production in time has been central to all of the above studies.

The results obtained by a diversity of numerical methods on a grid comprising 128^3 computational cells have also been compiled by Drikakis et al. [29], see Figure 4.2. The ILES methods employed to solve the inviscid problem presented here are distinguished through various limiting algorithms. They incorporate a fourth- and second-order accurate Flux Corrected Transport scheme, respectively labelled as FCT4 and FCT2; a third-order accurate Lagrange Remap method, labelled as LR3; and the third-order accurate Characteristics-Based high-resolution method presented in Chapter 3, labelled as CB3. Furthermore, a second-order accurate conventional LES using the mixed subgrid-scale model of Bardina et al. [7], labelled as MIXMOD2; and the DNS

results of Brachet [11] are plotted for comparison. In general, all the methods shown in Figure 4.2 seem to predict the global dynamics of the Taylor-Green Vortex reasonably well, but differences are apparent during the increasing stage and in the composition of the dissipation peak.

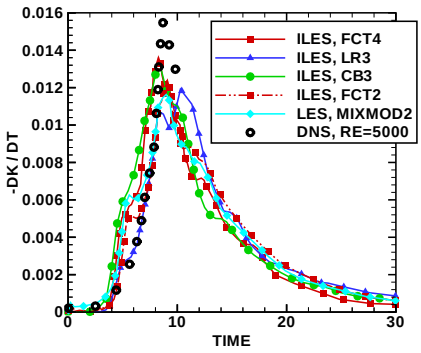

Figure 4.2: Development of volumetrically averaged kinetic energy dissipation as obtained by a range of numerical methods on a grid comprising 128^3 cells, see Drikakis et al. [29] for details.

As has been pointed out by Shu et al. [103], however, these integral measures have to be evaluated carefully. They may be misleading if not considered in combination with other parameters characterising the flow. Therefore, the performance of different numerical methods for discretising the Euler equations in time and space are thoroughly assessed in the following sections using various statistical quantities prescribing the development of the Taylor-Green Vortex.

4.2 Numerical Framework

The prototype configuration considered here for the assessment of various numerical schemes for predicting the fundamental dynamical mechanisms controlling the transitional behaviour from laminar to turbulent flow is given by the Taylor-Green Vortex. The three-dimensional, incompressible vortex field evolves from an initial, two-dimensional velocity field defined by

$$u_0 = U \sin(kx)\cos(ky)\cos(kz)\,, \tag{4.2.1}$$

$$v_0 = -U \cos(kx)\sin(ky)\cos(kz)\,, \tag{4.2.2}$$

$$w_0 = 0\,, \tag{4.2.3}$$

and the condition for the velocity components is complemented by the corresponding solution of the pressure Poisson Equation

$$p_0 = p_\infty + \frac{\rho_0 U^2}{16}\Big(2 + \cos(2kz)\Big)\Big(\cos(2kx) + \cos(2ky)\Big)\,. \tag{4.2.4}$$

As proposed by Brachet et al. [12], a single-mode initial field with $k = 1$ has been selected. In order to obtain consistent energy conditions for the compressible flow solver employed in this investigation the total energy is calculated as

$$e_0 = \frac{p_0}{\gamma - 1} + \frac{1}{2}\rho_0(u_0^2 + v_0^2 + w_0^2) \,. \tag{4.2.5}$$

Furthermore, the remaining free parameters have been chosen according to Drikakis et al. [30] for an ideal gas at near incompressible conditions characterised by a Mach number of $Ma = 0.29$, yielding

$$U = 100\frac{m}{s}\,, \quad \gamma = 1.4\,, \quad \rho_0 = 1.178\frac{kg}{m^3}\,, \quad p_\infty = 10^5\frac{N}{m^2}\,. \tag{4.2.6}$$

The resulting Taylor-Green Vortex at $t = 0$ is visualised for a cubic domain of length 2π in all three dimensions in Figure 4.3 by using iso-energy surfaces. This specific config-

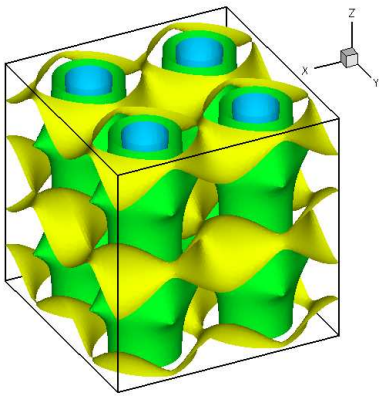

Figure 4.3: Initial condition for the Taylor-Green Vortex visualised by iso-energy surfaces.

uration allows for triply-periodic conditions at the domain boundaries. The evolution of the flow field could also be simulated in a reduced domain by taking advantage of the symmetry planes at $x = \pi$, $y = \pi$ and $z = \pi$ or additional symmetries listed by Brachet et al. [12]. However, enforcing symmetry conditions at the boundaries contradicts the aim of fully assessing a numerical method because it explicitly prevents symmetry breaking, a characteristic of discretisation schemes.

The cubic domain has been discretised on a block-structured, Cartesian mesh with evenly distributed points, see Figure 4.4. In order to study the effect of grid resolution, three different mesh sizes comprising 64^3, 128^3 and 256^3 computational cells are considered here. In addition to the grid refinement, the resolving power of three different high-resolution algorithms has been investigated in combination with the characteristics-based Riemann solver of Eberle [32]. The extrapolation methods employed are the third-order MUSCL scheme developed by Zóltak and Drikakis [132] (referred to as M3), the fifth-order MUSCL scheme presented by Kim and Kim [63] (referred to as M5) and the ninth-order WENO scheme following the ideas of Balsara

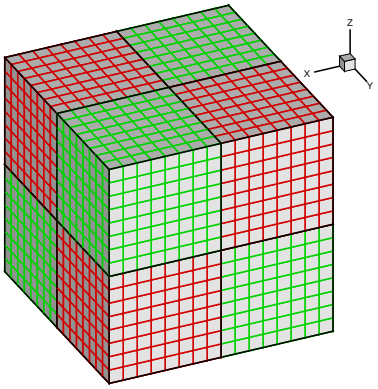

Figure 4.4: A typical block-structured grid employed in the simulations of the Taylor-Green Vortex.

and Shu [6] (referred to as W9). More details on the specific methods for the spatial discretisation of the governing equations can be found in Sections 3.4 and 3.5.

Attention has also been paid to the time-integration scheme. Although this area has attracted less interest in previous studies, it cannot be assumed in general that the flow evolution is not affected by the choice of the time-integration method. Therefore, the results obtained on a computational grid comprising 64^3 cells using the second-order scheme from Equation (3.2.3), the second-order TVD scheme given in Equation (3.2.4), the third-order TVD scheme in Equation (3.2.6) and the third-order extended stability scheme from Equation (3.2.7) are compared in Section 4.5. The methods for integrating the governing equations in time will be referred to as RK2, RK2TVD, RK3TVD and RK3HI, respectively, in the remainder of this chapter. Furthermore, all data has been non-dimensionalised with the domain length and the initial velocity magnitude U. Technical details for the simulations performed on a HP DL140 G5 server with 3.0GHz Intel Woodcrest 5160 Xeon processors can be found in Tables 4.1 and 4.2. The CFL numbers presented in Table 4.1 are the maxima for which stable simulations could be obtained and the duration of the simulations given in CPU hours in Table 4.2 are specific to the computer cluster used.

	64^3			128^3			256^3		
	M3	M5	W9	M3	M5	W9	M3	M5	W9
RK2	0.2	0.2	0.4	—	—	—	—	—	—
RK2TVD	0.2	0.2	0.4	—	—	—	—	—	—
RK3TVD	0.4	0.4	0.6	—	—	—	—	—	—
RK3HI	0.8	0.8	0.6	0.6	0.8	0.4	0.6	0.8	0.4

Table 4.1: Maximum possible CFL numbers for the simulations performed with Taylor-Green initial conditions.

	64^3			128^3			256^3		
	M3	M5	W9	M3	M5	W9	M3	M5	W9
Proc.	8	8	8	64	64	64	64	64	64
CFL	0.8	0.8	0.6	0.6	0.8	0.4	0.6	0.8	0.4
Steps	3280	3312	4485	8832	6692	13520	17947	13762	27673
CPUh	4.93	5.29	12.52	134	113	333	1161	1017	3944

Table 4.2: Numerical details for the Taylor-Green simulations using the third-order extended stability time-integration method (RK3HI).

4.3 Flow Topology

The dynamics of the Taylor-Green Vortex are discussed here qualitatively on the basis of the results obtained by the combination of ninth-order WENO (W9) scheme, third-order extended stability Runge Kutta (RK3HI) method and a computational grid consisting of 64^3 computational cells. For this purpose, the structure of the flow has been visualised in Figure 4.5 with instantaneous contour surfaces of constant Q-values. The Q-criterion as defined by Jeong and Hussain [61] is the second invariant of the velocity gradient tensor and can be written as

$$Q = \frac{1}{2}(||\mathbf{\Omega}||^2 - ||\mathbf{S}||^2) \,, \tag{4.3.1}$$

where the shear strain rate and vorticity magnitude are given by

$$||\mathbf{S}||^2 = tr(\mathbf{S}\mathbf{S}^T) \,, \quad ||\mathbf{\Omega}||^2 = tr(\mathbf{\Omega}\mathbf{\Omega}^T) \,, \tag{4.3.2}$$

and $\mathbf{S}$, $\mathbf{\Omega}$ are the symmetric and anti-symmetric components of the velocity gradient tensor, respectively. Additionally, the colour contours of total vorticity are shown in Figure 4.6 on plane cuts at the periodic boundaries of the cubic domain. Here, the colour maps are identical for all pictures and the total vorticity is defined as

$$|\omega| = |\nabla \times \mathbf{u}| \,. \tag{4.3.3}$$

The initial Taylor-Green Vortex featuring symmetry for all π-planes in the three dimensions is visualised in Figures 4.5(a) and 4.6(a). As has been described by Brachet et al. [12], the vorticity vanishes at the intersections of the symmetry planes and it reaches a maximum in the centre of the largest structures obtained by the Q-criterion. The initial, two-dimensional flow quickly becomes three-dimensional due to the action of a pressure gradient during the very early stage of the simulation.

As the flow develops, the initial vortices are driven towards the symmetry planes by centrifugal forces. The impermeability constraint pushes them along the faces until they encounter the opposing flow imposed by the symmetry. Consequently, the fluid

rushes back inwards. The result of this motion is the formation of vortex sheets, clearly visible in Figures 4.5(b) and 4.6(b), that have also been reported by Bensow et al. [8], Brachet et al. [12]. This is approximately the time where the flow starts to become under-resolved on the given grid and the kinetic energy dissipation increases.

The kinetic energy continues to decrease rapidly while the closed vortex sheets undergo an instability mechanism and tear open, shown in Figures 4.5(c) and 4.6(c). This stage in the flow development is also associated with the generation of large patches of high vorticity. Thus, a strong increase in total vorticity can be observed which peaks with the complete breakdown of the vortex sheets.

After the sheets have fully disintegrated, the evolution of the Taylor-Green flow is governed by the dynamics of the interaction between vortices. Elongated, small-scale tubes of strong vorticity appear due to vortex stretching and are subject to tearing and reconnection. However, the flow is still organised and dominated by the initial symmetries, see Figures 4.5(d) and 4.6(d).

At the late stage of the simulation, e.g. Figures 4.5(e) and 4.6(e), the symmetry can no longer be preserved. The result of several tearing and reconnection cycles is that the flow has lost all memory of the initial condition and is now fully disorganised. The characteristic, worm-like vortices simply fade away at very late times, as indicated by the low structural density in Figure 4.5(f) and the weak vorticity in Figure 4.6(f). This behaviour is extremely similar to decaying turbulent flows.

The qualitative observations made here are not unique to the specific simulation described above. The development of the Taylor-Green Vortex and the dynamics involved are similar for all numerical methods employed here. Yet, there are quantitative differences which will be identified in the following sections.

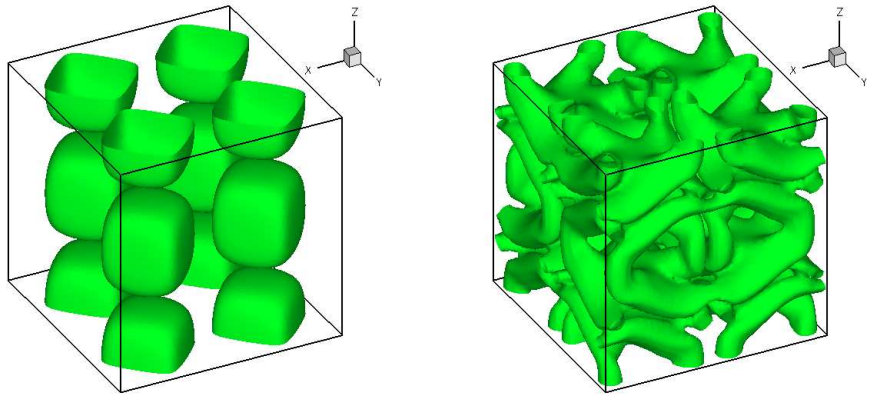

(a) T=0.0 (b) T=4.0

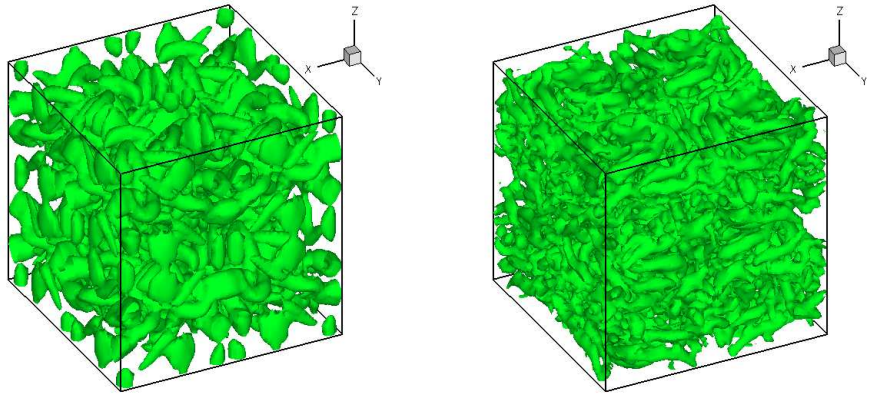

(c) T=8.0 (d) T=20.0

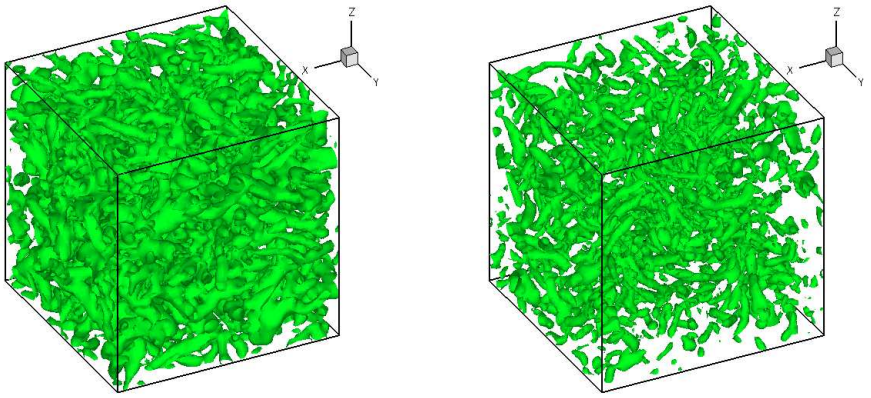

(e) T=30.0 (f) T=60.0

Figure 4.5: Instantaneous flow visualisations using iso-surfaces of the Q-criterion obtained by the combination of ninth-order WENO (W9) and third-order Runge Kutta (RK3HI) method on a 64^3 grid.

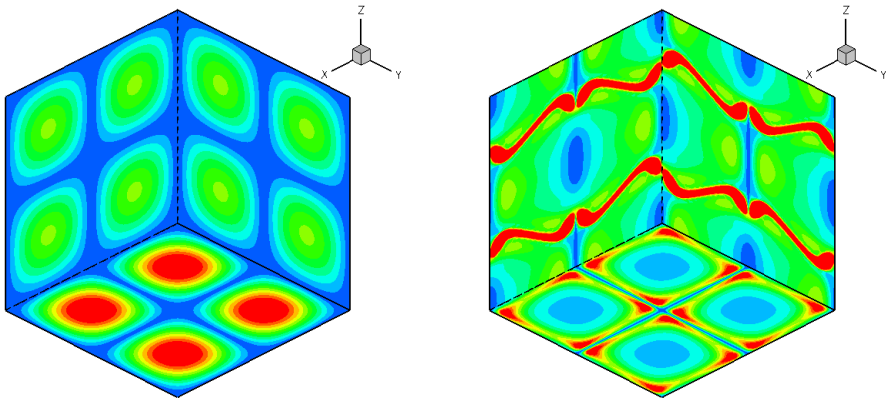

(a) T=0.0 (b) T=4.0

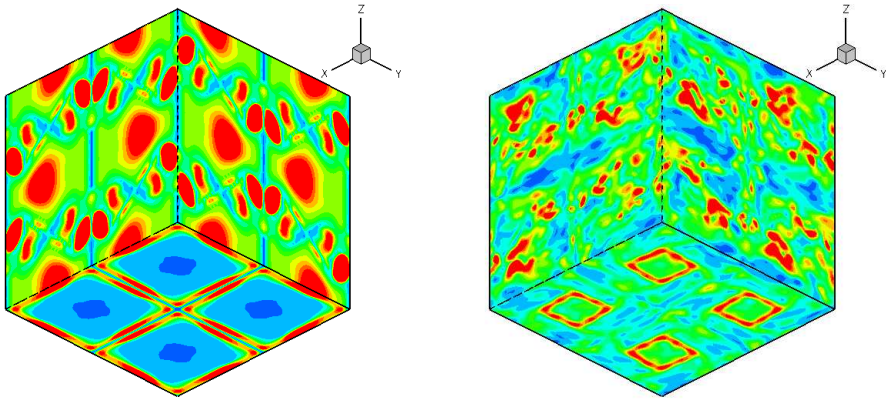

(c) T=8.0 (d) T=20.0

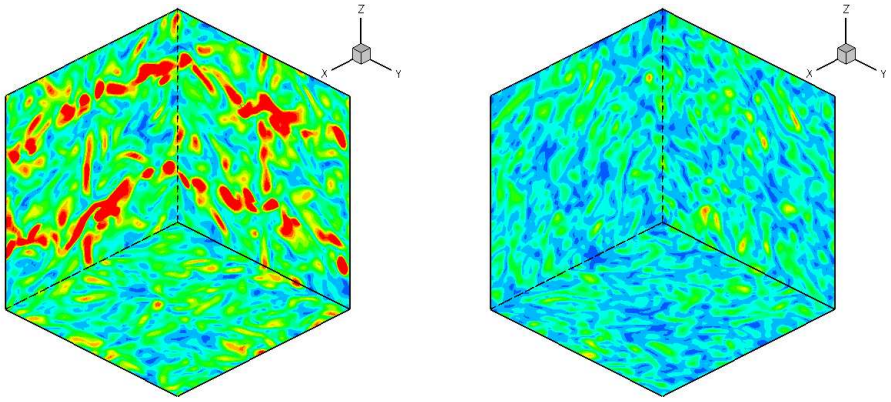

(e) T=30.0 (f) T=60.0

Figure 4.6: Instantaneous flow visualisations using vorticity contours obtained by the combination of ninth-order WENO (W9) and third-order Runge Kutta (RK3HI) method on a 64^3 grid.

4.4 Flow Diagnostics

In order to quantify the dynamics encoutered during the time-evolution of the Taylor-Green Vortex, the following quantities have been calculated. Although some of the parameters are borrowed from the classical theory of turbulence assuming homogeneity and isotropy, which does not always strictly apply to the Taylor-Green Vortex, they can be treated as indicators characterising the flow.

Kinetic Energy. The kinetic energy can be used to measure the loss of conservation due to the discrete approximation made in solving the governing equations numerically. The mean kinetic energy KE considered here is computed as

$$KE = \frac{1}{2}\left\langle |\mathbf{u}|^2 \right\rangle \ , \tag{4.4.1}$$

where <> denotes the volumetric average of the square of the velocity vector. Ideally, the kinetic energy should be constant during the course of the simulations because there is no physical dissipation in the Euler equations. Of course, this assumption only holds for a conservative numerical scheme and if the flow can be fully resolved on the given grid. Therefore, a deviation from the initial value can be used as an indicator for the onset of the under-resolved stage in the simulation.

Kinetic Energy Decay Rate. For homogeneous and isotropic turbulence, Kolmogorov [64] has shown that the time-evolution of kinetic energy should obey the power law given by the following expression that can be found in, for example, the book of Hinze [58],

$$KE \propto (t - t_0)^{-\mathcal{P}} \ . \tag{4.4.2}$$

Here, t_0 marks the onset of kinetic energy decay and $\mathcal{P}$ is a constant that has been theoretically evaluated by Kolmogorov [64] to be equal to 10/7. However, slightly lower values of $\mathcal{P}$ between 1.2 and 1.3 have been reported from wind tunnel measurements of grid-generated turbulence, e.g. see Comte-Bellot and Corrsin [18], Mohammed and LaRue [82], Skrbek and Stalp [104]. Furthermore, Skrbek and Stalp [104] have shown that the kinetic energy follows a power law with $\mathcal{P} = 2$ if the largest energy-containing scales have reached a saturated state where their length is comparable to the size of the domain and they cannot grow any further.

Kinetic Energy Dissipation. Another useful quantity to consider is the slope of the mean kinetic energy development in time. This parameter, also known as the mean kinetic energy dissipation $-dKE/dt$, can be used to quantify the loss of kinetic energy during the course of the simulation. The peak in kinetic energy dissipation also coincides with the beginning of the flow stage governed by the dynamic interaction between the vortex tubes.

Enstrophy. Closely related to the kinetic energy dissipation is the growth of enstrophy. The mean enstrophy is measured in time as the square of vorticity

$$< \omega^2 >=< |\nabla \times \mathbf{u}|^2 > \ . \tag{4.4.3}$$

The physical interpretation of the production of enstrophy during the early stage of the simulations is the stretching of the initial Taylor-Green vortex, whereas the subsequent decrease is caused by viscous damping. As the enstrophy should grow to infinity in the absence of viscosity, it is a criterion for the effective viscosity and the resolving power of a numerical method. According to Shu et al. [103], the resolving power of a numerical scheme is a measure of its ability to represent the flow physics accurately on a finite number of grid cells.

Effective Viscosity. The effective viscosity for incompressible flow can be approximated by assuming that the loss of mean kinetic energy is equal to the mean of the viscous dissipation. On the one hand, the mean viscous dissipation is determined by the mean-square of the strain-rate. On the other hand, for high Reynolds number flows, the mean-square strain-rate yields about the same value as the enstrophy, see derivation in the book of Tennekes and Lumley [113]. Thus, the effective viscosity ν_{eff} as experienced by the fluid during the course of the simulation can be calculated from the following simple expression

$$-\frac{dKE}{dt} = \nu_{eff} < \omega^2 > \ . \tag{4.4.4}$$

Kinetic Energy Spectrum. In order to obtain deeper insight into the distribution of kinetic energy among the length scales present in the flow, the three-dimensional energy spectrum $E(k)$ is employed, where k is the wavenumber. Details on the calculation of the energy spectrum can be found in the book of Hinze [58]. Through intelligent arguments based on dimensional reasoning, Kolmogorov [64] found that the kinetic energy spectrum for homogeneous and isotropic turbulence is proportional to $k^{-5/3}$ in the inertial subrange. This power law is widely used to prove the existence of a fully developed, turbulent flow. Regarding the Taylor-Green Vortex, Brachet et al. [12] found it in relatively good agreement with the energy spectrum obtained near the dissipation peak, whereas slightly lower values than $-5/3$ have been reported during the very early stages.

Integral Length-Scale. From the kinetic energy spectrum, the integral length-scale ℓ can be calculated as

$$\ell = \frac{\pi}{2\left\langle |\mathbf{u}|^2 \right\rangle} \int_0^{k_{max}} \frac{E(k)}{k} dk \ . \tag{4.4.5}$$

The integral scale is a measure of the largest distance between two points in space where the different velocities are correlated. Hence, it is a characteristic length for the largest energy-containing eddies.

Taylor Microscale. Another standard length-scale in turbulence is the Taylor microscale. Assuming isotropic flow, it can be averaged over all three spatial dimensions, yielding

$$\lambda = \frac{1}{3}(\lambda_x + \lambda_y + \lambda_z) \ , \tag{4.4.6}$$

where the individual components are given by

$$\lambda_{(x,y,z)} = \sqrt{\frac{< (u,v,w)^2_{rms} >}{< \partial(u,v,w)/\partial(x,y,z) >}} \, . \tag{4.4.7}$$

The Taylor microscale marks the transition from the inertial subrange to the dissipation range, i.e. eddies of size less than λ begin to be affected by viscous dissipation.

Velocity Structure Functions. Finally, velocity structure functions will be used here to gain insight into the dynamics of the Taylor-Green flow. These functions are also known as the higher-order velocity-derivative moments and they are written in their spatially averaged form as

$$S_n = \frac{1}{3}(S_{x,n} + S_{y,n} + S_{z,n}) \, , \tag{4.4.8}$$

with the uni-directional terms being defined as

$$S_{(x,y,z),n} = (-1)^n \frac{\left\langle \left(\partial(u,v,w)/\partial(x,y,z) \right)^n \right\rangle}{\left\langle \left(\partial(u,v,w)/\partial(x,y,z) \right)^2 \right\rangle^{n/2}} \, , \tag{4.4.9}$$

and n being the order of the function. Two common measures are the skewness and the flatness which are obtained for $n = 3$ and $n = 4$, respectively. The velocity-derivative skewness is connected to vortex stretching and the energy transfer between different scales, whereas the velocity-derivative flatness is a measure for the probability of deviations from the mean value. Thus, the skewness is an indicator for the mean dissipation in the flow and the flatness hints at the intermittent character of the velocity fluctuations. Generally, both absolute values increase with progressively higher Reynolds numbers. The typical data obtained in experimental measurements and numerical simulations of isotropic turbulence has been compiled by Sreenivasan and Antonia [108]. Here, the values listed range from -0.3 to -0.7 for the skewness and 3 to 40 for the flatness with a Reynolds numbers based on the Taylor microscale between 4 and 40000.

4.5 Effect of Temporal Discretisaton

The results presented here have been compiled in order to clarify the importance of the choice of method for integrating the governing equations in time. For this purpose, all possible combinations of the three high-resolution schemes M3, M5 and W9 and the four different second- and third-order accurate time-stepping methods RK2, RK2TVD, RK3TVD and RK3HI have been investigated, see also Table 4.1. The results obtained on a grid comprising 64^3 computational cells are compared against each other in terms of several integral quantities already presented in Section 4.4. Here, possible differences regarding the flow dynamics during the course of the simulation are of prime interest. The characteristics of the individual spatial discretisation methods employed,

however, will be discussed in Section 4.6. Their main purpose in this part is to test for possible inconsistencies with respect to combinations of discretisation methods in time and space.

Figure 4.7 shows the time-development of the integral kinetic energy and energy dissipation for all simulations. At the end of the very early, laminar stage marked by the formation of the vortex sheets, the kinetic energy starts decaying and reaches its maximum dissipation rate near the value predicted by the DNS of Brachet et al. [12]. It should be noted, that the highly under-resolved simulations are not expected to match the DNS data exactly. However, they seem to represent the physics involved within acceptable accuracy for early and medium times, i.e. the increasing loss of kinetic energy due to vortex sheet break-up and the subsequent rapid reduction of the dissipation rate during the organised flow stage. Yet, as the flow becomes more disorganised for $T \gtrsim 20$, the numerics predict an artificial increase in dissipation. Up to this point, all time-integration methods give virtually identical results, regardless of their order of accuracy or the details of the stability constraints satisfied.

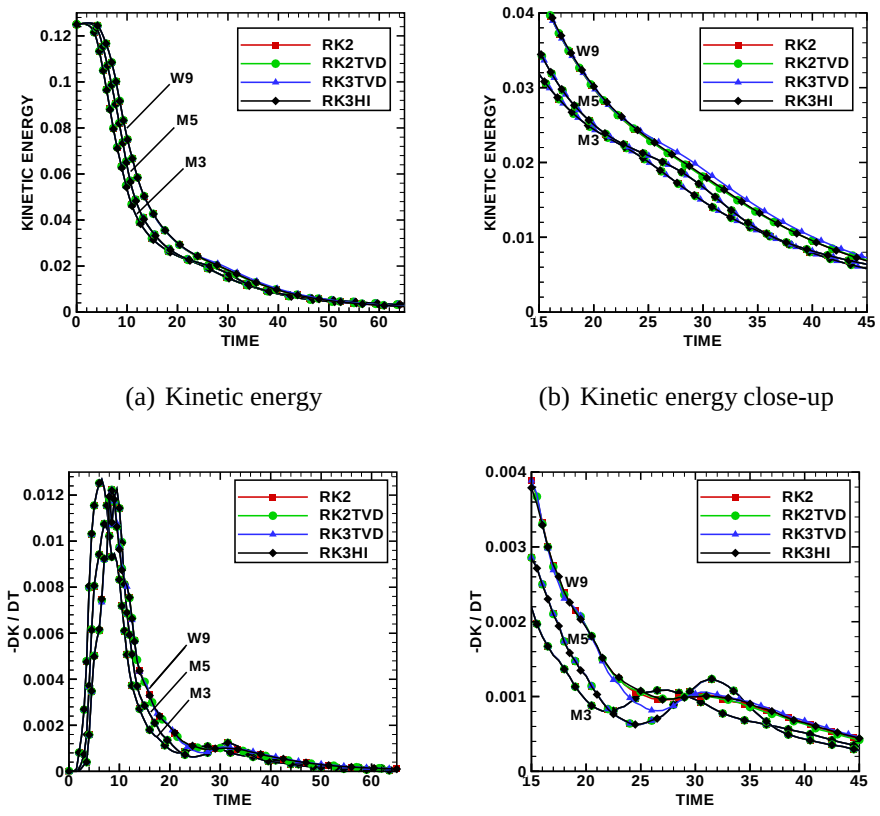

(a) Kinetic energy (b) Kinetic energy close-up

(c) Kinetic energy dissiptation (d) Kinetic energy dissiptation close-up

Figure 4.7: Development of the volumetrically averaged kinetic energy and energy dissipation obtained by different spatial and temporal discretisation techniques on a 64^3 grid.

A more clear picture of this unphysical behaviour can be obtained by also consider-

ing the length scales presented in Figure 4.8. Initially, the integral length scales are reduced due to the disintegration of the vortex sheets. As can be expected during the subsequent stage characterised by a self-similar energy decay, the largest scales are growing until they are affected by the size of the domain. The saturated state of the integral scales seems to coincide with the onset of disorganised flow. A similar effect can be observed for the Taylor microscale. The elongated vorticity-carrying tubes feature sharp velocity gradients. In under-resolved simulations, the sharp fronts are diffused by the numerics and the surrounding fluid is seemingly entrained. Since there is no clear separation between the large and the small scales due to insufficient spatial resolution, the Taylor microscales are also affected by the presence of the symmetry conditions and the vortices are re-connecting. This mechanism is akin at the backscatter observed in two-dimensional turbulence. Thus, the energy dissipation is slowed down to a rate below a physically adequate value and the Taylor microscales have grown in size. Now, the kinetic energy can be dissipated again at a higher rate — hence the artificial hump in the development of the energy dissipation. Although the impact of this numerical artifact can be reduced by using a very high-order scheme for the spatial discretisation, such as W9, the higher order methods become more and more prone to produce dissimilar results for different time-integration schemes.

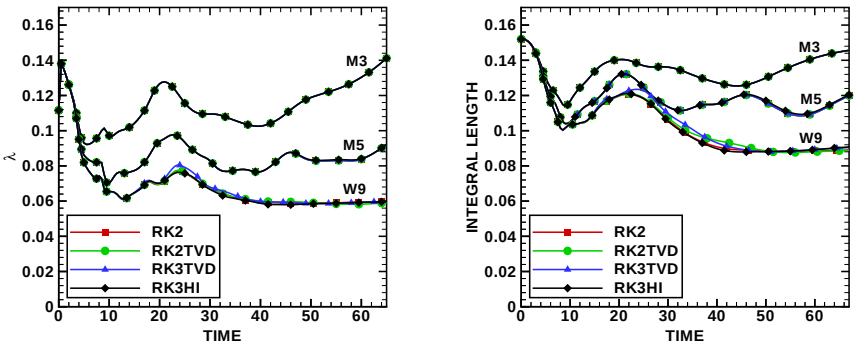

(a) Averaged Taylor microscale (b) Averaged integral length scale

Figure 4.8: Development of the Taylor microscale and the integral length scale obtained by different spatial and temporal discretisation techniques on a 64^3 grid.

The above conclusion regarding the effect of the time-integration method is also reflected in the evolution of the structure functions, see Figure 4.9. The results obtained by M3 feature large-amplitude fluctuations that are virtually identical throughout the course of the simulations. Neither the skewness nor the flatness converge to a near-constant value as would be expected for a fully developed turbulent flow. For M5, the third-order Runge Kutta methods with extended stability region (RK3HI) gives slightly different results compared to the other methods. However, the differences occur only after the unphysical hump in the development of the energy dissipation has appeared. Variations with the choice of time-integration scheme can also be observed for W9. The magnitude of the variations is particularly pronounced during the transition to a

highly disorganised state. Here, the third-order TVD Runge Kutta method seems to differ from the other three schemes. Yet, both the skewness and the flatness converge to similar values for all time-integration methods regardless of their time-history.

In summary, it has been found that the numerical integration in time has only a minor effect on the results obtained by the three different high-resolution algorithms. No method seems to offer a significant advantage over the others regarding the quality of the solution. However, because the third-order Runge Kutta method with extended stability region (RK3HI) generally allows for the highest CFL numbers, it was chosen for all simulations using finer grids .

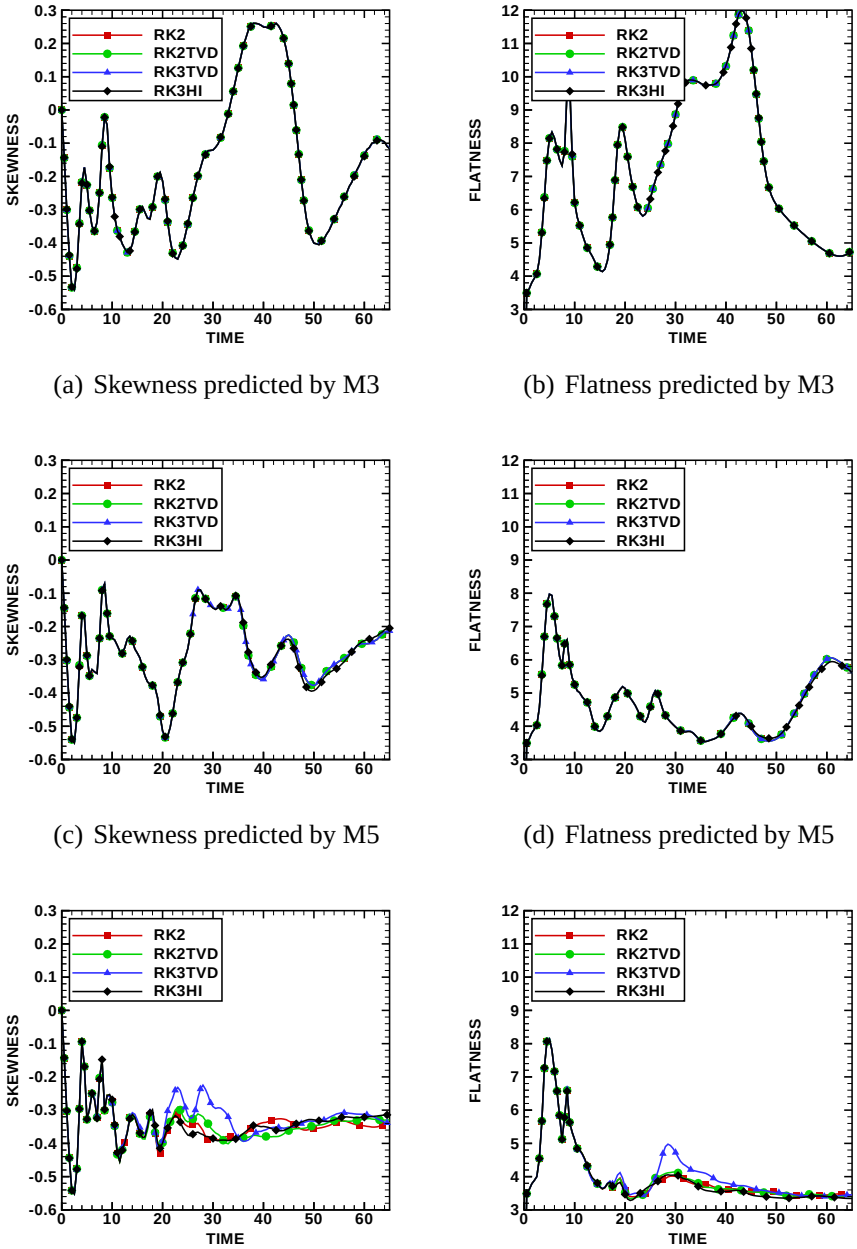

(a) Skewness predicted by M3

(b) Flatness predicted by M3

(c) Skewness predicted by M5

(d) Flatness predicted by M5

(e) Skewness predicted by W9

(f) Flatness predicted by W9

Figure 4.9: Development of the velocity structure functions obtained by different spatial and temporal discretisation techniques on a 64^3 grid.

4.6 Effect of Spatial Discretisaton

In order to assess the impact of the spatial discretisation on the results, simulations with the third- and fifth-order MUSCL schemes (M3 and M5), as well as the ninth-order WENO (W9) reconstruction method have been performed. Here, three stages of grid refinement featuring 64^3, 128^3 and 256^3 computational cells have been considered. Furthermore, all results compared in this section have been obtained with the third-order accurate, extended stability Runge Kutta algorithm (RK3HI) for the integration in time.

The evolution of kinetic energy and energy dissipation for all methods and all grids investigated is shown in Figure 4.10. Note that the kinetic energy is presented here in logarithmic scales to illustrate the existence of a power law for the decay rate. Averaged values for the decay exponent as determined by curve-fitting in a time interval between $T_0 = 11$ and $T = 60$ are given in Table 4.3. The slope of the exponential decay on the 64^3 grid seems to be within the range of values expected for homogeneous turbulence. However, this data is misleading because of the unphysical hump already discussed in the previous section. In the absence of vortex pairing, a steeper slope should be expected. This is the case indeed if the grid resolution is increased. Both M5 and W9 reach a grid-converged slope with a $\mathcal{P}$ of approximately 1.88 and 2.02, respectively, whereas M3 seems to approach a similar value only on the finest grid. This value is in close agreement with the prediction of Skrbek and Stalp [104] for turbulent flow where the largest scales are bounded by the size of the domain.

	64^3			128^3			256^3		
	M3	M5	W9	M3	M5	W9	M3	M5	W9
Decay exponent $\mathcal{P}$	1.31	1.36	1.48	1.83	1.88	2.03	2.00	1.88	2.02
Onset of decay	1.89	3.13	3.81	3.63	4.26	4.68	4.51	5.02	5.48

Table 4.3: Power law exponent for the decay rate of kinetic energy and the time marking the onset of energy decay.

Additionally, the time marking the onset of the energy decay has been documented in Table 4.3. In general, M3 loses kinetic energy before M5 and, in turn, the dissipation for M5 starts in advance of W9. This behaviour is particularly pronounced for the coarsest grid and it is diminishing with increasing grid resolution. Since the onset of decay represents the point at which the simulation becomes under-resolved, it is a good indicator for the resolving power of the numerical method — the longer the kinetic energy is conserved, the better the method for this specific case. As a consequence of the relatively large difference regarding the onset of kinetic energy dissipation on the coarsest grid, the dissipation peak predicted by M3 also appears prior to the peaks of the higher order methods, see Figure 4.10(b). However, this behaviour is less evident when the grid resolution is increased and a peak-time of $T \approx 9$ is in good agreement with the DNS of Brachet [11], Brachet et al. [12].

Moreover, additional effects of grid refinement can be observed. The hump apparent for the 64^3 grid at times near $T \approx 30$ is absent for both finer grids. Yet, another decrease in energy dissipation associated with an increasing integral length scale becomes more noticeable for the 128^3 grid near $T \approx 16$. The strength of this second hump that has also been reported by Grinstein [46] cannot be associated conclusively with the grid resolution as it is less evident for both the coarsest and the finest grid. However, flow visualisations have revealed that the particular combination of the WENO method and the 128^3 grid favours the formation of strong vortex rings which are centred around the four initial rotation axes. The presence of these strong vortex rings is the reason for a pronounced deceleration of the energy dissipation rate and it also delays the growth of the integral length scales.

Furthermore, the production of vorticity has been monitored in terms of enstrophy. In combination with the energy dissipation, this data can be used to estimate the effective viscosity during the course of the simulations. Figure 4.11 details the development of the integral enstrophy and the corresponding effective viscosity provided by the three different methods on all computational grids employed. As expected, the humps marking a decrease in kinetic energy dissipation are reflected in the values for the effective viscosity, which is most obvious for the 64^3 grid. The numerical viscosity is generally decreasing on the finer grids — hence more enstrophy is produced. Most remarkably, there are large variations in magnitude for the results obtained by the three numerical methods. W9 seems to produce an effective viscosity that is very similar to M3, but on a grid coarser by a factor of two in each spatial dimension. This observation is consistent for all levels of grid refinement. Thus, it is an indication that W9 features a resolving power twice as high as M3. M5 lies in between the two.

Similar conclusions can be drawn from the averaged Taylor microscales and the averaged integral length scales depicted in Figure 4.12. Through increasing the grid resolution or the order of the spatial discretisation method, both the integral length scale and the Taylor microscale can be reduced. Whereas the largest energy-containing scales seem to reach a converged state for the 256^3 grid, the small scales continue to decrease as could be expected in an inviscid flow problem. Again, W9 requires only half the resolution in each dimension compared to M3 in order to produce a similar Taylor microscale.

A closer look at the spatially separated microscales, shown in Figure 4.13, partly reveals another qualitative difference between the flows predicted by the three different methods. Here, only λ_x and λ_z are presented because λ_x and λ_y are nearly identical as a consequence of the initial condition. The flow obtained by M3 and M5 is highly anisotropic on the coarsest grid, but W9 reaches a more isotropic state during the late stage of the simulation. On the next level of grid refinement, the evolution of the small scales for M5 shifts closer to the one predicted by W9, especially if λ_z is considered. For the finest grid, the flow given by M5 has also reached an isotropic state and the Taylor microscales follow the shape of W9 more closely in all dimensions. M3 seems to follow this trend at the higher grid resolutions.

This behaviour may be explained by the particularities of the Taylor-Green conditions.

By design, the initial condition enforces symmetries at plane cuts through the domain at multiples of π in all directions. As has been shown in Section 4.3, W9 cannot preserve the symmetries in the flow at late times. In order to compare the performance of the two MUSCL schemes, the vorticity contours at $T = 60$ as predicted by M3 and M5 are displayed in Figure 4.14 for all grid resolutions. Clearly, the symmetries are still preserved by both methods for the coarsest grid. The results obtained on the medium grid show slight asymmetries for M5, but not for M3. In the fine-grid simulations, the symmetries are no longer preserved by M5 and M3 starts to develop small deviations. This development is not surprising because the numerical algorithms become more sensitive to small disturbances with increasing order of accuracy and grid resolution. In addition, W9 does not satisfy any stability criteria as opposed to the MUSCL schemes. The breakdown could probably be delayed if W9 is used in conjunction with a TVD method for the integration in time, but it certainly could not be prevented completely. For the Taylor-Green Vortex, symmetry-breaking is the essential mechanism that provides more isotropic and homogeneous flow conditions similar to fully developed turbulence. Thus, together with the resolving power, it is one of the main attributes for characterising the numerical methods.

With isotropy and homogeneity in mind, the seemingly erratic development of the velocity structure functions obtained with M3 for the coarsest grid is not so startling any more. As can be seen in Figure 4.15, the magnitude of the fluctuations is linked to the character of the flow. Higher-order moments are very sensitive to local changes of velocity gradients, hence they can be misleading if the flow is highly intermittent. With increasing grid resolution, the Taylor-Green Vortex leads to more isotropic, homogeneous conditions and the velocity structure fluctuations are diminishing, especially for the two MUSCL schemes. The skewness and the flatness seem to approach values of approximately -0.4 and between 4 to 5, respectively, if the flow is isotropic. This is slightly below what would be expected for fully developed turbulence.

Finally, the most common technique for characterising the flow topology has been applied to the development of the Taylor-Green Vortex. Figure 4.16 shows the kinetic energy spectra at different times as obtained by the three high-resolution methods on the three different grids. At early times $T = 4$, before the vortex sheets disintegrate, all combinations produce a k^{-4} spectrum as has been predicted by the DNS of Brachet et al. [12] and is typical for an essentially two-dimensional flow. Near the dissipation peak, the same authors have reported a $k^{-5/3}$ spectrum. Comparing the spectra in Figure 4.16(b), it can be seen that all methods are able to predict this slope more or less accurately with increasing grid resolution. In general, W9 approaches $k^{-5/3}$ faster than M5 and, in turn, M5 is in better agreement than M3. As the simulations progresses, the kinetic energy follows an almost self-similar decay. However, a slight flattening of the spectra due to a transfer of energy to the smaller scales can be observed during the organised flow regime at $T = 20$. At very late times, $T = 60$, the highly disorganised flow seems to result in a spectral decay slightly lower than $k^{-5/3}$ for M5 and W9, whereas the slope is steeper for M3.

As has been expected, an increase in grid resolution leads to a longer inertial range and

generally better statistics if compared to a fully developed turbulent flow. It should be noted that although the dynamics predicted by the three high-resolution methods can differ during the evolution of the Taylor-Green Vortex, this is not reflected in substantial slope changes of the energy spectra at lower wave-numbers.

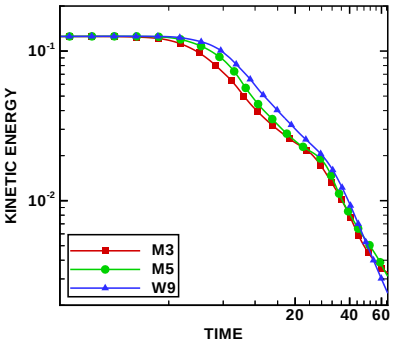

(a) Kinetic energy (64^3)

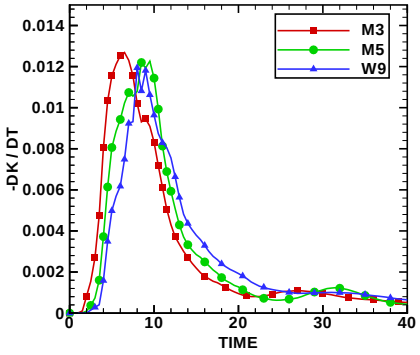

(b) Kinetic energy dissipation (64^3)

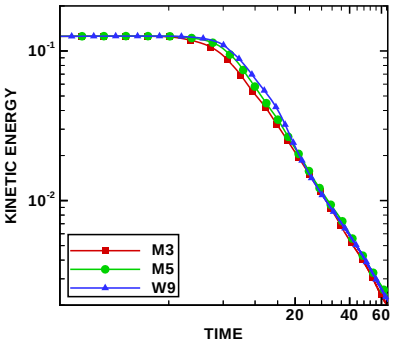

(c) Kinetic energy (128^3)

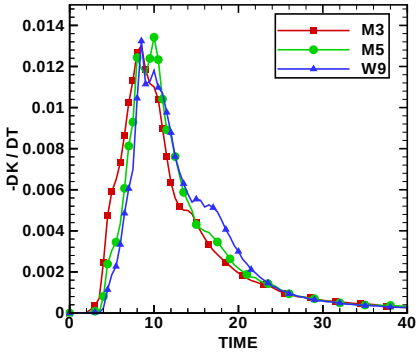

(d) Kinetic energy dissipation (128^3)

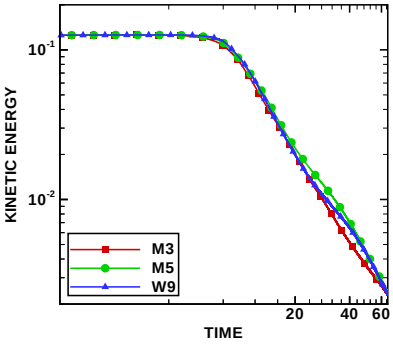

(e) Kinetic energy (256^3)

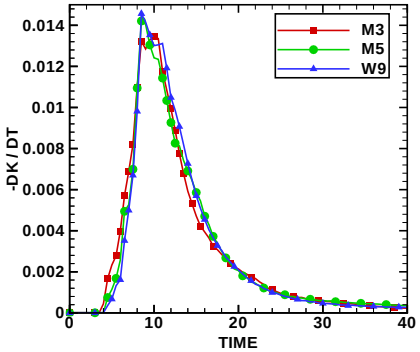

(f) Kinetic energy dissipation (256^3)

Figure 4.10: Development of the volumetrically averaged kinetic energy and kinetic energy dissipation rate obtained by different spatial discretisation techniques on a 64^3, 128^3 and 256^3 grid.

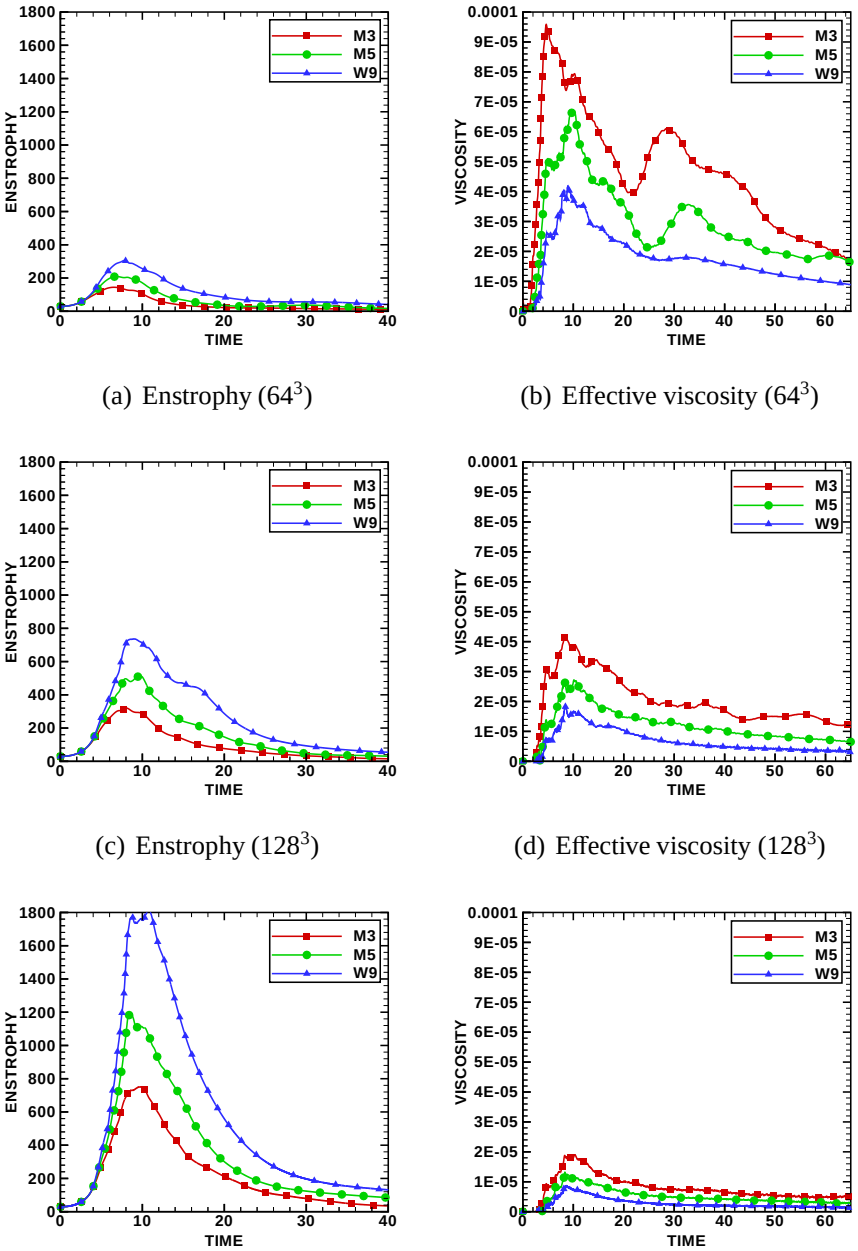

(a) Enstrophy (64^3) (b) Effective viscosity (64^3)

(c) Enstrophy (128^3) (d) Effective viscosity (128^3)

(e) Enstrophy (256^3) (f) Effective viscosity (256^3)

Figure 4.11: Development of the volumetrically averaged enstrophy and the effective viscosity obtained by different spatial discretisation techniques on a 64^3 ,128^3 and 256^3 grid.

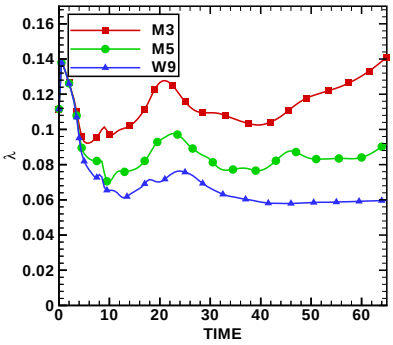

(a) Averaged Taylor microscale (64^3)

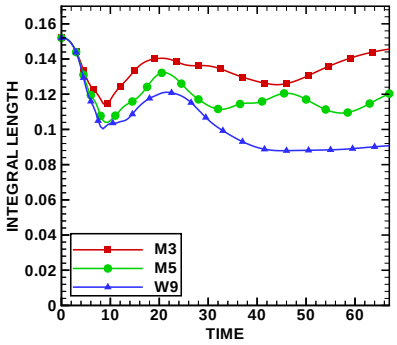

(b) Averaged integral length scale (64^3)

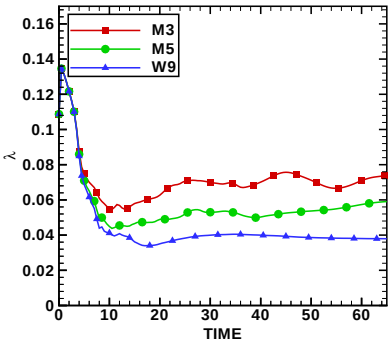

(c) Averaged Taylor microscale (128^3)

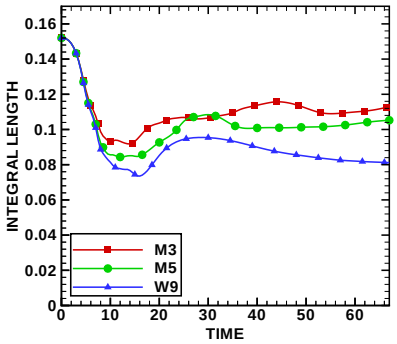

(d) Averaged integral length scale (128^3)

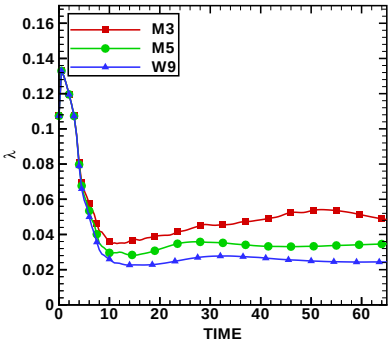

(e) Averaged Taylor microscale (256^3)

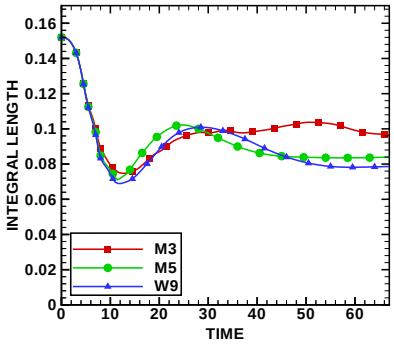

(f) Averaged integral length scale (256^3)

Figure 4.12: Development of the Taylor microscale and the integral length scale obtained by different spatial discretisation techniques on a 64^3, 128^3 and 256^3 grid.

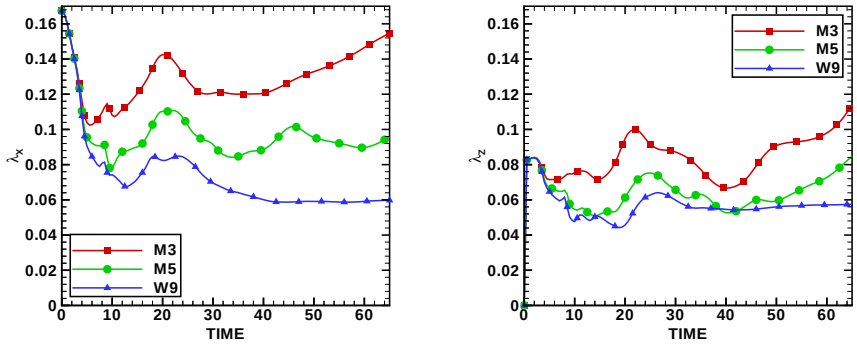

(a) Taylor microscale in x (64^3) (b) Taylor microscale in z (64^3)

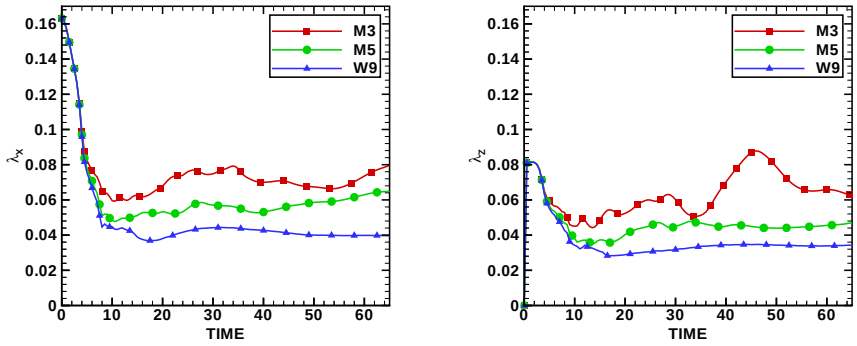

(c) Taylor microscale in x (128^3) (d) Taylor microscale in z (128^3)

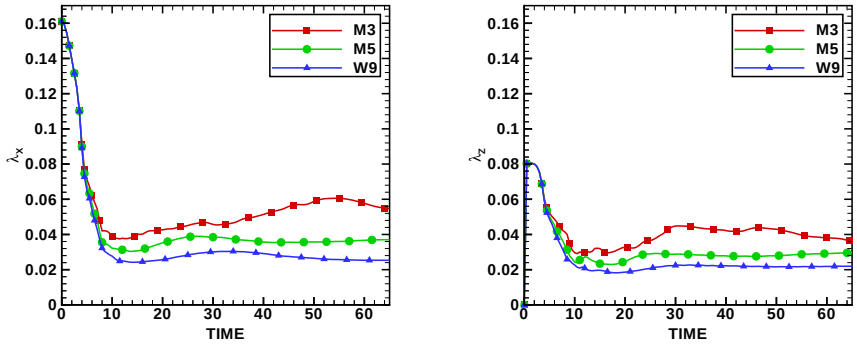

(e) Taylor microscale in x (256^3) (f) Taylor microscale in z (256^3)

Figure 4.13: Development of the Taylor microscale in x- and z-direction obtained by different spatial discretisation techniques on a 64^3, 128^3 and 256^3 grid.

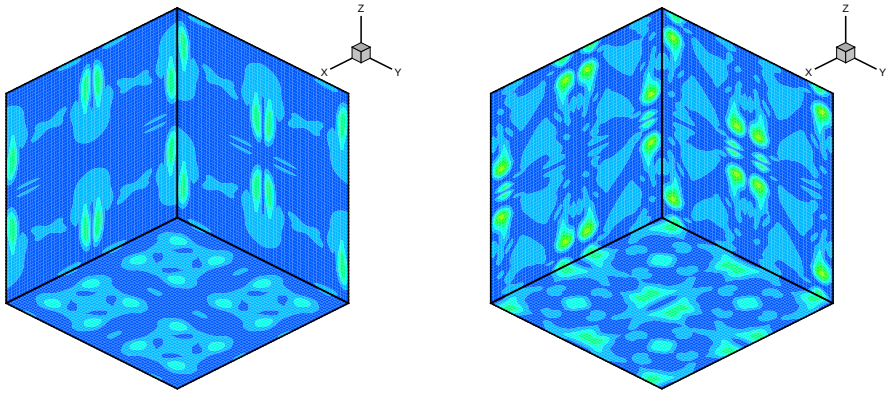

(a) M3 at T=60.0 (64^3) (b) M5 at T=60.0 (64^3)

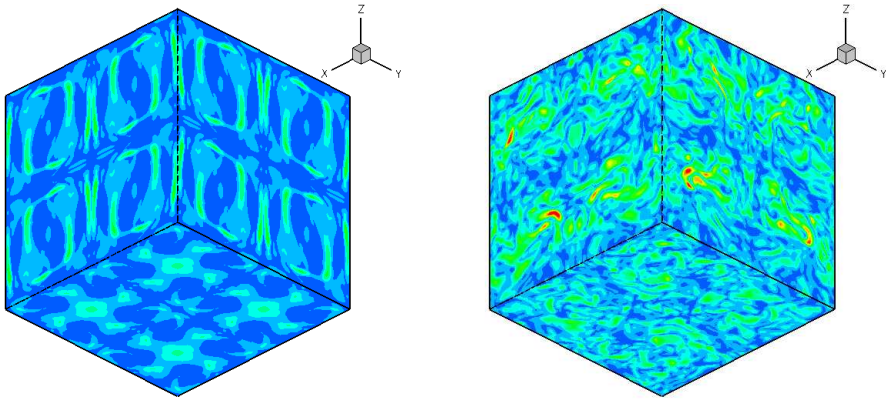

(c) M3 at T=60.0 (128^3) (d) M5 at T=60.0 (128^3)

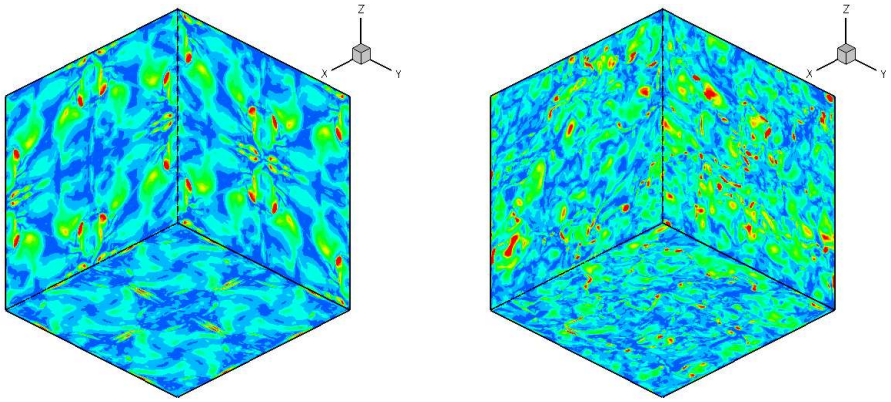

(e) M3 at T=60.0 (256^3) (f) M5 at T=60.0 (256^3)

Figure 4.14: Instantaneous flow visualisations using vorticity contours obtained by the third-order (M3) and the fifth-order MUSCL (M5) scheme on a 64^3, 128^3 and 256^3 grid.

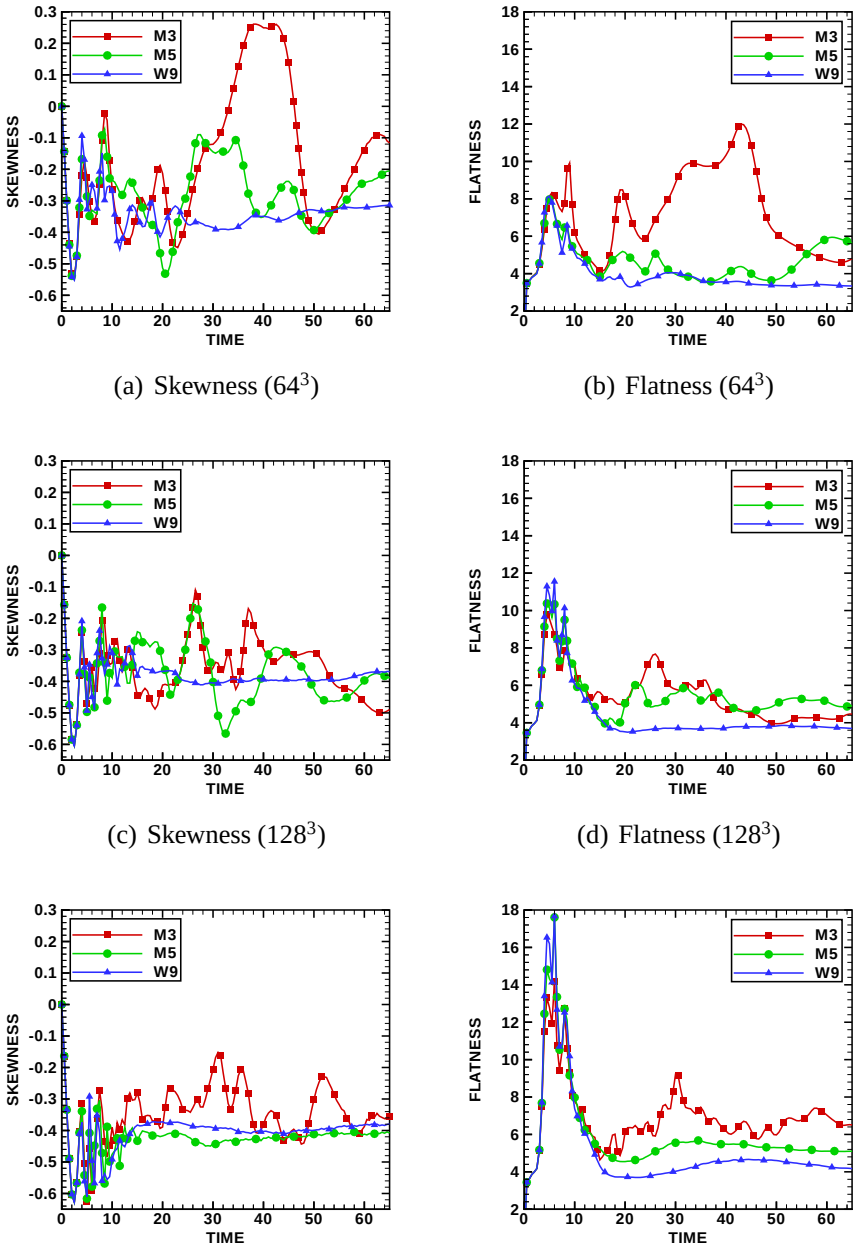

(a) Skewness (64^3) (b) Flatness (64^3)

(c) Skewness (128^3) (d) Flatness (128^3)

(e) Skewness (256^3) (f) Flatness (256^3)

Figure 4.15: Development of the velocity structure functions obtained by different spatial discretisation techniques on a 64^3, 128^3 and 256^3 grid.

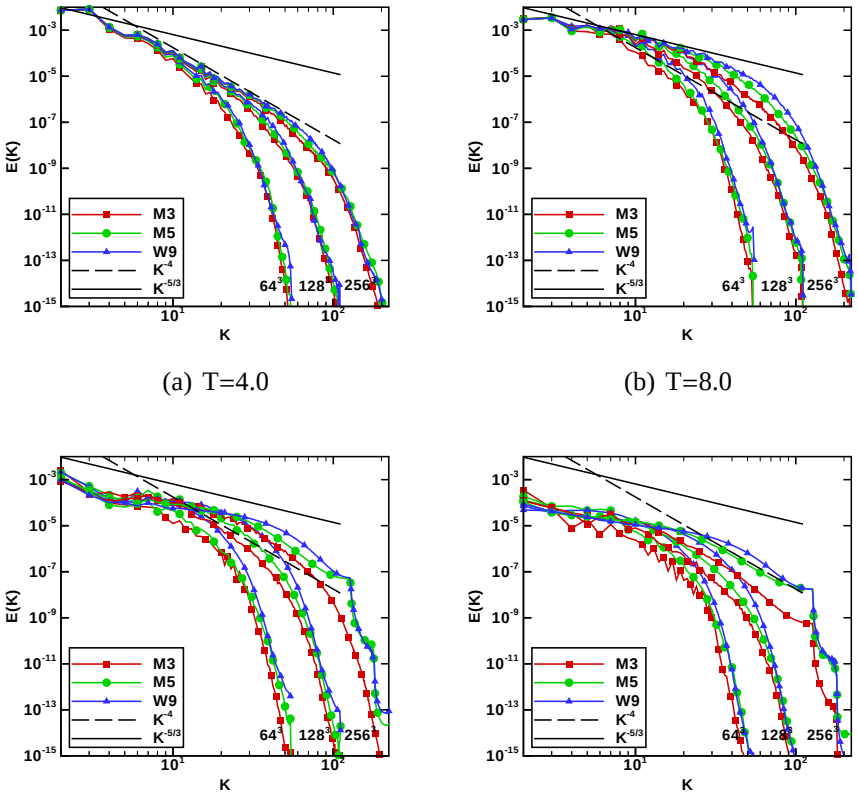

(a) T=4.0 (b) T=8.0

(c) T=20.0 (d) T=60.0

Figure 4.16: Kinetic energy spectra obtained by different spatial discretisation techniques on a 64^3, 128^3 and 256^3 grid.

4.7 Summary

In this chapter, various stages in the laminar to turbulent flow development have been investigated for the time-dependent Taylor-Green Vortex. This prototype flow is probably the simplest model for the vortex dynamics encountered during the transition from well-organised to highly disorganised coherent structures. Here, the performance of different spatial and temporal discretisation methods has been assessed.

It has been found that the choice of time-integration method plays only a minor role regarding the statistical quality of the predicted flow field. However, it may have an effect on the dynamics if the method for the spatial discretisation is prone to produce numerical instabilities.

An extensive analysis of various parameters characterising the evolution of the flow have been presented for a third-order MUSCL, a fifth-order MUSCL and a ninth-order WENO method and different grid sizes. The conservation of kinetic energy is prolonged in time when increasing the order of accuracy. This leads to the conclusion that the resolving power of a numerical model can be increased by using a higher order method. In fact, this is also supported by the less dissipative character of higher order methods if compared to lower order methods on identical grids. Likewise, the schemes produce less dissipation and more enstrophy on finer grids. This behaviour is not surprising because higher velocity gradients can be supported by increasing the grid resolution or the order of the reconstruction method. At the same time, however, the reconstruction methods become more sensitive to small disturbances.

Although the inviscid instability mechanism responsible for the disintegration of the vortex sheets is captured accurately by all schemes, the later evolution of the flow governed by vortex dynamics can exhibit substantial differences for the same grid resolution. This is mainly attributed to numerical instabilities that cause the initial symmetries to break. Symmetry-breaking is the property that allows the flow to develop into a more homogeneous and isotropic state which would be a characteristic of fully-developed turbulence. Hence, a certain level of numerical instability can be of advantage during the transitional stage. It is not clear, however, if an idealistic prototype flow should become more realistic by introducing numerical artifacts.

CHAPTER 5

Hill Flow

IN this chapter a systematic numerical investigation of different high-resolution methods in the context of Implicit Large-Eddy Simulation of massively separated flows including a local grid refinement study is presented. The three high-resolution algorithms assessed here are a third-order accurate MUSCL scheme, a fifth-order accurate MUSCL scheme and a ninth-order accurate WENO method. For a fundamental study of separation from gently curved surfaces the geometrically simple, statistically two-dimensional test case given by a channel with hill-type curvature on the lower wall has been considered and the results are compared against solutions from classical LES simulations.

5.1 Introduction

Many flows of practical importance are governed by viscous near-wall phenomena that have a major influence on the flow properties. Among those, separated flow currently poses one of the greatest challenges for numerical simulations because its characteristics covers a wide range of physical processes. Separation of the boundary layer near curved surfaces is a more common problem than it might seem. It is not confined to external flows only, e.g. flow around moving vehicles, it also occurs in internal flows such as the blades in turbo-machinery and divergent channels, nozzles or pipes.

The basic physical mechanisms leading to separation are relatively well understood and have been presented in several textbooks on boundary layer theory, e.g. see Schlichting [98]. It has been found that the separation phenomenon is intimately linked to the pressure distribution in the boundary layer. Generally, it is assumed that the pressure does not change in the direction normal to the surface and the external pressure is impressed on the boundary layer. If the flow follows a convex curvature, the external pressure in the essentially inviscid region outside the boundary layer has to rise according to Bernoulli's theorem — hence the flow experiences an adverse pressure gradient inside the boundary as it progresses further downstream. At the same time, the fluid is retarded near the wall due to the friction forces. The combination of the two effects causes the boundary layer to separate because the remaining kinetic energy

in the immediate vicinity of the solid surface is too small to overcome the pressure increase.

In general, the flow is said to be separated if the velocity in the immediate neighbourhood of a solid surface becomes reversed. Further away from the wall, however, the velocity has to take the values of the free-stream and thus the velocity profile exhibits a point of inflection that marks the existence of a shear layer. Inflection points are important for the development of the flow after separation has occurred because they are inviscidly unstable. As a consequence, the shear layer undergoes a breakdown similar to the one presented for the Taylor-Green Vortex in Section 4. Usually, this leads to strong growth of the separation zone and a highly turbulent wake region dominated by the dynamics of the generated eddies.

To date, no theoretical models have been developed that can deal with the complexity of this type of flow. The boundary-layer equations, a simplification of the Navier-Stokes equations, are only valid up to the point of separation. Downstream of this point, however, the separation zone thickens quickly and the approximations made in the boundary layer equations are no longer valid. And even if they could be applied, the turbulent fluctuations render the solutions impossible to obtain without resorting to further approximations.

Therefore, fundamental investigations of separated flows have to rely on experimental or well-established computational reference data for relatively simple geometries. Here, the quasi two-dimensional wavy terrain is a popular choice because the waves representing the curved solid surface can be prescribed analytically. Furthermore, the resulting flow field can be treated as statistically two-dimensional. Several experimental studies have been conducted under these conditions, e.g. Almeida et al. [1], Buckles et al. [16], Hudson et al. [59]. However, they often suffer from limitations imposed by the equipment, uncertainties regarding the influence of inflow conditions or possible contaminations of the flow field by three-dimensional effects arising from the finite physical scale of the experiment.

Ideally, Direct Numerical Simulations could be used to overcome these difficulties. Yet, the demanding resolution requirements for DNS to adequately represent the viscous sublayer near the wall and the long integration times needed in order to obtain reliable statistics for the complex flow pattern have to be faced. Piomelli [89] estimated that the grid size for DNS approximately scales with $Re^{2.6}$. Thus, DNS data is only available for relatively low Reynolds numbers of order 10^2 to 10^3, see DeAngelis et al. [22], Maas and Schumann [73]. For wall-resolved Large-Eddy Simulations this situation does not improve much and the grid size required is approximately proportional to $Re^{2.4}$, see Piomelli [89]. Hence, as the simulations of Armenio and Piomelli [4], Henn and Sykes [56] are limited by the same arguments, the Reynolds numbers could only be increased marginally due to the lack of computing power available at the time.

More recently, Fröhlich et al. [35] have produced reference data for a channel with hill-type constrictions from highly-resolved LES. The two simulations presented em-

ployed the dynamic Smagorinsky model of Germano et al. [39] and the wall-adapted local eddy viscosity model of Ducros et al. [31], respectively. Here, the Reynolds number of order 10^4 is approaching a level more adequate for problems of engineering interest. The flow conditions and the geometry have been chosen on the basis of the results obtained in the experiments of Almeida et al. [1], but they have been modified in order to accommodate the needs of a highly-resolved LES. The main reason that makes this case an ideal testbed is the simplicity of the geometry and boundary conditions, especially the challenging task of generating appropriate inlet conditions can be circumvented, see Veloudis et al. [122]. Therefore, it has attracted a great deal of interest and produced a wealth of data obtained by LES and RANS the current simulations can be compared against.

The Reynolds Averaged Numerical Simulations performed by Jang et al. [60], Wang et al. [123] have proven that RANS is not capable of simulating this type of flow problem correctly. This is not surprising since the spatial and temporal fluctuations in the wake region and regarding the position of the separation line, which cannot be adequately represented by the statistical closure strategies, are essential to the development of the flow. More worryingly, however, the RANS simulations lack any degree of certainty because the turbulence closures behave inconsistently and no conclusions can be drawn.

Various approaches to wall modelling and subgrid-scale modelling have been investigated in the coarse grid LES of Temmerman et al. [112] for the identical geometry. Although the predictions obtained with standard no-slip conditions at the surface could be improved, it has been found that the wall models require grid points well within the viscous sublayer in order to produce reliable results. Furthermore, Breuer et al. [15] argued that many standard wall models have no sound physical basis for predicting complex, separated flows. For example, two of the approaches used by by Temmerman et al. [112], i.e. the classical log-law first formulated by Schumann [99] and the model proposed by Werner and Wengle [126], are designed for time-averaged velocity profiles in attached flows without pressure gradients. There are several other models, usually based on the boundary layer equations, e.g. Balaras and Benocci [5], that can cope with the existence of pressure gradients. However, as noted earlier, the boundary layer equations do not apply to regions of separated flow.

Evidently, a solution to the problem of flow separation under the influence of an adverse pressure gradient has yet to emerge. The encouraging results obtained by high-resolution methods in under-resolved Large-Eddy simulations of turbulent, wall-free flows have stirred the hope that this might also transfer to the separated flow regime. Thus, the stringent grid requirements could be relaxed if the separation line can be reasonably well predicted. For this reason, several high-resolution algorithms have been employed in numerical simulations of the channel flow with hill-type constrictions and the results are benchmarked against the highly-resolved LES of Fröhlich et al. [35]. Furthermore, the following sections will also include data from the LES published by Temmerman et al. [112] for comparison.

5.2 Numerical Framework

For the systematic numerical investigation of the behaviour of different high-resolution methods employed in Large-Eddy Simulations of separated flows in a channel with hill-type constrictions three different grids have been used. The computational domain representing the constricted channel extends $9h$, $4.5h$ and between $2h$ and $3.035h$ in x-, y- and z-direction, also referred to as streamwise, cross-stream and vertical direction, respectively. Here, h is the height of the hill-type shape at the lower wall as used in the experiment of Almeida et al. [1]. The two-dimensional hill geometry can be found in the ERCOFTAC test matrix available online at ERCOFTAC [33] It is defined by a spline through the points measured in the experiment given by the coordinates

$$\begin{aligned} (x_1, z_1) &= (\ 0.0, 28.0)\ , \quad (x_2, z_2) = (\ 9.0, 27.0)\ , \\ (x_3, z_3) &= (14.0, 24.0)\ , \quad (x_4, z_4) = (20.0, 19.0)\ , \\ (x_5, z_5) &= (30.0, 11.0)\ , \quad (x_6, z_6) = (40.0,\ \ 4.0)\ , \\ (x_7, z_7) &= (54.0,\ \ 0.0)\ . \end{aligned} \tag{5.2.1}$$

The hill height determined by the spline can now be approximated by the following third order polynomials

$$\begin{aligned} &\text{for } x_1 \le x < x_2 : \\ &h(x) = min(28.00\ ,\ 28.00 + 6.78 \cdot 10^{-3} x^2 - 2.12 \cdot 10^{-3} x^3)\ , \\ &\text{for } x_2 \le x < x_3 : \\ &h(x) = 25.07 + 9.75 \cdot 10^{-1} x - 1.02 \cdot 10^{-1} x^2 + 1.63 \cdot 10^{-3} x^3\ , \\ &\text{for } x_3 \le x < x_4 : \\ &h(x) = 25.79 + 8.21 \cdot 10^{-1} x - 9.06 \cdot 10^{-2} x^2 + 1.63 \cdot 10^{-3} x^3\ , \\ &\text{for } x_4 \le x < x_5 : \\ &h(x) = 40.46 - 1.38 \cdot 10^{-0} x + 1.95 \cdot 10^{-2} x^2 - 2.07 \cdot 10^{-4} x^3\ , \\ &\text{for } x_5 \le x < x_6 : \\ &h(x) = 17.92 + 8.74 \cdot 10^{-1} x - 5.57 \cdot 10^{-2} x^2 + 6.28 \cdot 10^{-4} x^3\ , \\ &\text{for } x_6 \le x < x_7 : \\ &h(x) = max(0.0\ ,\ 56.39 - 2.01 \cdot 10^{-0} x + 1.64 \cdot 10^{-2} x^2 + 2.67 \cdot 10^{-5} x^3)\ . \end{aligned} \tag{5.2.2}$$

All of the above values are given in millimetres, leading to a maximum hill height of $h = 28mm$. For the simulations and the results presented in the following sections, however, all data has been non-dimensionalised with the bulk velocity at the hill crest and the height of the constriction.

A simple H-H-type grid topology as depicted in Figure 5.1(a) has been chosen for this case. Here, only every fourth grid point in a typical block-decompositioned computational mesh for parallel simulations is shown. No-slip boundary conditions have been applied at the top and the bottom wall of the channel, while periodicity has been assumed in the streamwise and cross-stream directions.

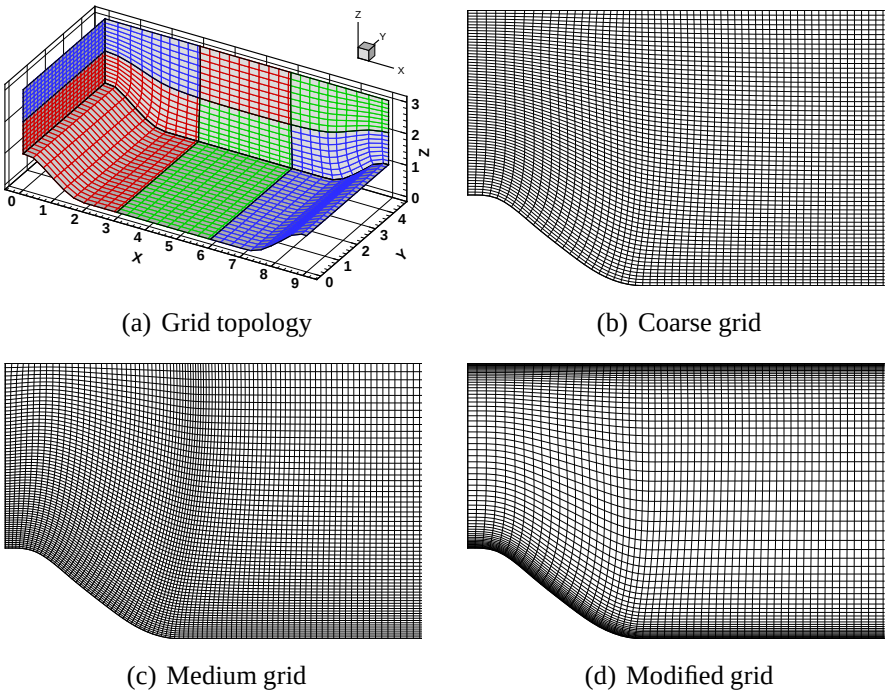

(a) Grid topology (b) Coarse grid

(c) Medium grid (d) Modified grid

Figure 5.1: The computational H-H-type grid topology and the three different grids employed in the simulations of the hill flow.

Three different grid resolutions have been investigated here: (i) a highly under-resolved grid, referred to as "coarse", comprising approximately 0.65×10^6 fairly uniformly distributed points; (ii) a modified version of the coarse grid with an identical number of points, referred to as "modified", featuring a finer clustering near the top and the bottom wall of the channel; (iii) a moderately finer grid consisting of 1.03×10^6 points, referred to as "medium", where the refinement mainly affects the distribution around the hill crest and a slightly better resolution near the bottom wall is achieved, see Figures 5.1(b) to 5.1(d). More details regarding the two-dimensional distribution of grid nodes in all three grids employed here are presented in Figure 5.2. The coarse and the medium grids are basically identical to the ones used in the wall-modelled LES of Temmerman et al. [112] and all grids are by courtesy of the same author. The characteristic parameters for all three grids including z+ values at the bottom wall, which are not sensitive to the choice of numerical discretisation method, are given in Table 5.1. Additionally, the same parameters for the highly-resolved reference simulation of Fröhlich et al. [35] are included.

For all simulations the Reynolds number based on the hill height and the bulk velocity at the hill crest is equal to $10,595$. The Mach number of $Ma = 0.2$ has been chosen for near-incompressible conditions. In order to ensure a consistent mass flow in the channel configuration it is necessary to augment the standard Navier-Stokes equations with a forcing term. This modification is required because a classic pressure-driven channel flow would violate the boundary conditions for the test case considered here, namely the periodicity in x-direction. In the absence of a pressure drop, the forcing

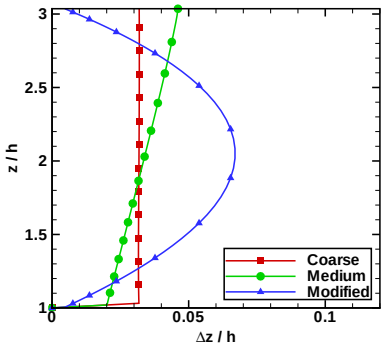

(a) Wall-normal clustering along $x/h = 0.05$

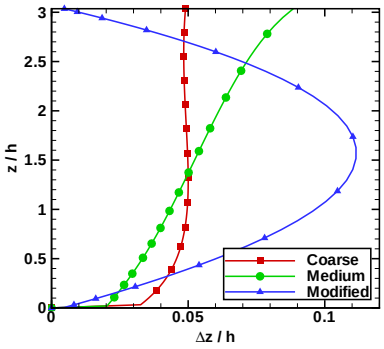

(b) Wall-normal clustering along $x/h = 2$

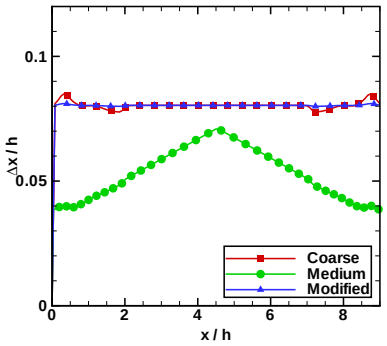

(c) Streamwise clustering along the bottom wall

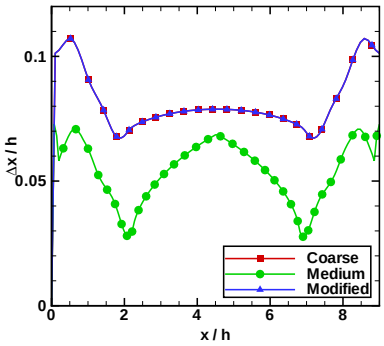

(d) Streamwise clustering along the top wall

Figure 5.2: Grid node distributions at characteristic locations for the three grids employed.

term acts as a driver for the flow and ensures a constant mass flow rate. Here, the external force has been determined in a similar fashion as outlined in the plane channel simulations of Lenormand et al. [66], more details can be found in Appendix E.

The integration in time has been performed exclusively by the third-order extended stability Runge Kutta scheme given in Equation (3.2.7) and several high-resolution methods have been considered in combination with the characteristics-based Riemann solver of Eberle [32]. This investigation includes the third-order MUSCL scheme presented by Zóltak and Drikakis [132], the fifth-order MUSCL scheme developed by Kim and Kim [63] and the ninth-order WENO scheme following the ideas of Balsara and Shu [6]. These methods are referred to as M3, M5 and W9, respectively, in the following sections. All simulations have been performed on IBM eServer326m nodes with 2.2GHz AMD 275 processors. Here, no information regarding the computing time can be presented because of hardware issues. In general, however, the size of the time step had to be reduced by a factor of approximately 2 for both M5 and W9 when compared to M3 to obtain stable solutions.

Grid	$N_x \times N_y \times N_z$	Size	$\Delta x/h$	$\Delta y/h$	$\Delta z/h$	z^+_{min}	z^+_{max}
Coarse	$112 \times 91 \times 64$	0.65×10^6	0.08	0.049	0.032	≈ 7	≈ 14
Modified	$112 \times 91 \times 64$	0.65×10^6	0.08	0.049	0.0047	≈ 1	≈ 3
Medium	$176 \times 91 \times 64$	1.03×10^6	0.04	0.049	0.02	≈ 4	≈ 9
Reference	$196 \times 186 \times 128$	4.67×10^6	0.032	0.024	0.0033	≈ 0.5	≈ 1

Table 5.1: Characteristic parameters for the three grids employed here and for the highly-resolved reference LES of Fröhlich et al. [35].

5.3 Flow Topology

In order to provide an overview of the different flow regimes encountered in the periodic hill flow, the topological features have been visualised according the Q-criterion proposed by Jeong and Hussain [61], for a definition of Q see also Section 4.3. An instantaneous snapshot of the resulting vortical structures is shown in Figure 5.3. It should be noted that, in this case, a single snapshot is not representative for the evolution of the flow at all times. However, the chosen time instant is characteristic for the general behaviour observed.

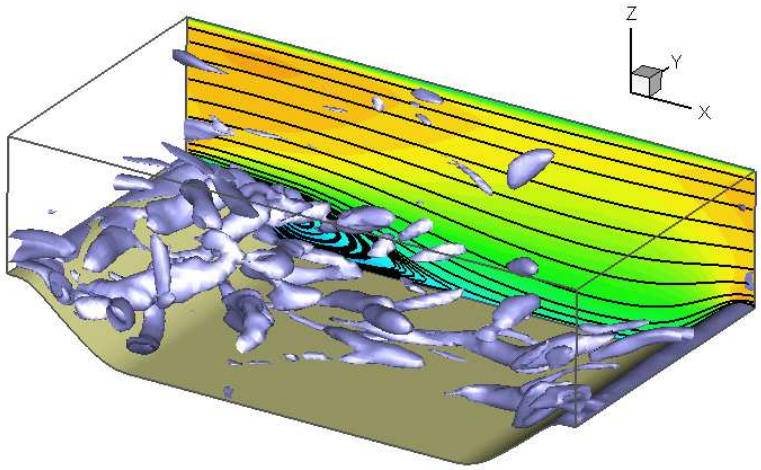

Figure 5.3: Flow features in the channel visualised by time- and space-averaged streamlines and instantaneous vortical structures defined by the Q-criterion of Jeong and Hussain [61].

In addition to the coherent vortices, colour contours of the averaged streamwise velocity and the associated streamlines are illustrated in Figure 5.3. The averaging has been performed over the cross-stream direction and over a time period of approximately 50 flow through times of the fully developed, unsteady state. It has been found that this relatively long time-window is necessary to gain good statistical data presented in the following sections.

The averaged streamlines, although partially obscured by the vortical structures, reveal

the existence of a closed recirculation area in the lee of the hill. This separation bubble originates at the convex curvature of the wall, a short distance downstream of the hill crest, and it ends after the flow has passed the region of concave curvature at the foot of the hill, i.e. in the trough between the constrictions. A highly unsteady shear layer that is emanating from the separation line marks the transitional region between recirculation and core flow. After the turbulent shear layer has reattached, a strongly agitated boundary layer is formed that subsequently experiences a slight recovery before it approaches the hill. As has been pointed out by Castro and Epik [17], the boundary layer downstream of a separation bubble is not of standard form because the influence of the shear layer goes well beyond the line of reattachment. At the windward slope, the flow is quickly accelerated and thus the boundary layer becomes thinner. The acceleration is clearly indicated by the colour contours of the streamwise velocity. As this particular case generates its own inlet conditions due to the periodicity in x-direction, the incoming boundary layer is also very thin and contains a certain level of turbulence. Consequently, both the line of separation and reattachment exhibit significant fluctuations around their averaged positions. This behaviour has been observed as well by Na and Moin [85] for the detachment and subsequent attachment of a turbulent boundary layer.

In the separated flow region, a Kelvin-Helmholtz-type roll up of the shear layer leading to the generation of span-wise vortices can be observed. The unsteadiness of the separation line enhances the irregular character of the vortex formation in space and time. As a result, the flow field in the lee of the constriction is highly intermittent and it exhibits the highest levels of turbulence, especially within the shear layer. The vortices are subject to secondary instabilities as they progress in x-direction and eventually impinge on the bottom wall of the channel. Since the reattachment location is fluctuating, the vortices are either drawn back into the separation bubble or they are convected downstream. Hence, information is allowed to travel back to the crest of the hill at irregular intervals. This feedback mechanism adds to the unsteadiness of the flow detachment and the unpredictability of the shear layer roll-up.

Downstream of the reattachment, the coherent structures near the bottom wall are predominantly aligned with the flow. The reason for this is a slight vertical inclination of the structures. One end of the vortices is exposed to a faster flow regime than the other end and thus the principal axis gets aligned with the main flow direction. As the flow evolves, the velocity gradient normal to the wall leads to an elongation of the structures and vortex stretching becomes more pronounced as the flow is accelerated along the windward side of the hill. Additionally, the strong acceleration can lead to overshoots at the hill crest and subsequent contamination of the core flow by areas of high vorticity.

The instantaneous flow field discussed here underlines the complex character of the separated hill flow. Several features and the physics associated with them will be revisited during the interpretation of the results in the following sections.

5.4 The Separation Bubble

The most evident phenomenon in the averaged flow field for the hill geometry is the separation bubble. In order to compare the results of different simulations the point of separation, marking the beginning of the bubble, and the reattachment location, defining the end of the bubble, have been deduced from the averaged, two-dimensional flow field. This is commonly achieved by identifying the minima in the z+ distribution along the wall, where z+ is the distance of the centre of the first grid cell above the wall measured in wall units. According to Pope [90], z+ is calculated as

$$z+ = \frac{u_\tau \Delta n}{\nu} \quad \text{with} \quad u_\tau = \sqrt{\frac{\tau_w}{\rho}} \tag{5.4.1}$$

being the friction velocity and τ_w is the wall shear-stress given by

$$\tau_w = \rho\nu \left. \frac{d < u_\parallel >}{dn} \right|_{WALL} . \tag{5.4.2}$$

Here, Δn is the wall-normal distance of the cell centre and $< u_\parallel >$ is the averaged velocity component parallel to the wall, its gradient is calculated with respect to the wall-normal direction.

The resulting normalised wall distance along the bottom wall of the modified grid is shown in Figure 5.4 for the three different high-resolution methods. The plot also includes the corresponding data from the fine grid reference LES of Fröhlich et al. [35]. Although variations regarding the wall distance as well as the position and the

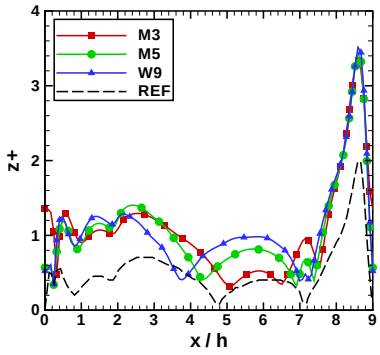

Figure 5.4: Average of the normalised distance between the bottom wall and the centres of the adjacent cells for the three different methods and the modified grid. The corresponding data from the fine-grid reference LES of Fröhlich et al. [35] has also been included.

length of the separation bubble can be observed, all distributions appear to follow a similar shape — hence the underlying physics is similar in all cases. Most remarkably, the high-resolution methods predict a small separation zone at the foot of the windward slope of the hill, i.e. $x/h \approx 7.2$, which is not noticeable in the reference LES. Fröhlich

	Coarse		Medium		Modified	
Method	x_{sep}/h	x_{att}/h	x_{sep}/h	x_{att}/h	x_{sep}/h	x_{att}/h
M3	0.98	2.89	0.55	3.62	0.32	5.06
M5	1.06	2.57	0.63	3.00	0.24	4.35
W9	0.74	2.33	0.47	3.40	0.24	3.77
LL3	0.53	2.98	0.34	4.32	-	-
WW	0.46	4.00	0.32	4.56	-	-
NS	1.12	2.17	0.38	3.45	-	-
Reference	x_{sep}/h=0.22			x_{att}/h=4.72		

Table 5.2: Averaged locations of separation and re-attachment obtained by M3, M5 and W9 on the coarse, the medium and the modified grid. The published data from Temmerman et al. [112] has also been included for comparison.

et al. [35] have pointed out, however, that the flow in this region is indeed at the brink of separation in the highly-resolved LES. In the wall-modelled LES of Temmerman et al. [112], as well as for the coarse and the medium grid, no reversed flow can be seen at the foot of the windward slope of the hill. For the modified grid, the separation is barely visible for W9, whereas M3 predicts a boundary layer lift-off well in advance of the slope. Consequently, the destabilising effect of the concave curvature appears to be become less pronounced with increasing order of the method. This already hints at a different character of the upstream boundary layer.

All separation and reattachment points obtained with M3, M5 and W9 for the coarse, the medium and the modified grid are listed in Table 5.2. Additionally, the data published by Temmerman et al. [112] has been included for comparison. The results in rows labelled “LL3”, “WW” and “NS” are from the classical, wall-modelled LES using the WALE subgrid-scale model proposed by Ducros et al. [31] on grids identical to the coarse and the medium mesh. LL3 and WW refer to simulations with a three-layer logarithmic wall model and the wall approximation of Werner and Wengle [126], respectively, whereas NS refers to a simulation with no-slip boundary conditions, i.e. no wall model, at the top and the bottom wall of the channel.

From the data presented here, it is already clear that all simulations using high-resolution methods outperform the classical LES without a wall model for the highly under-resolved, coarse grid. Applying the log-law model improves the classical LES result regarding the prediction of the separation point. However, the effect on the reattachment is only minor because it is not valid for separated flows. Strictly speaking, neither is the WW model, but it still yields the best result for the coarse grid. This can mainly be attributed to the specific implementation in cell-integrated form that leads to a higher wall shear-stress and thus favours separation. Temmerman et al. [112] has also shown a declining dependence of the results on the near-wall approximation for the medium grid. This effect is reflected in the relatively close proximity of the separation and reattachment predicted by LL3 and WW. The local grid refinement also enhances the performance of the classical LES with no-slip condition, although the

separation bubble remains too short.

Among the high-resolution methods, W9 gives the best result for all grids regarding the location of the separation. Yet, it highly under-predicts the length of the separation bubble. On the other hand, the bubble length obtained by M3 is closest to the reference length from the simulations of Fröhlich et al. [35] on all grids. Most remarkably, the drastic improvement of the results for the medium grid as seen in all classical LES is not reproduced. As expected, however, a grid refinement in the wall normal direction has the desired effect and both detachment and reattachment are in better agreement with the reference LES. It should be noted that, for a correct interpretation of the results, the different behaviour of M3, M5 and W9 has to be assessed in combination with other parameters presented in the following sections. The position of the separation bubble alone is not very meaningful because it is strongly influenced by several factors, e.g. the grid resolution near the separation point and in the shear layer and above all the characteristics of the incoming boundary layer.

5.5 Length Scales

The scales of the coherent structures as predicted by the third-order MUSCL (M3), the fifth-order MUSCL (M5) and the ninth-order WENO (W9) scheme can be compared visually by applying the Q-criterion of Jeong and Hussain [61] to an instantaneous realisation of the fully developed flow field. It has been found that more and finer structures are resolved by all methods with increasing grid resolution, but the relative difference between them appear to be similar irrespective of the grid size. Therefore, only the flow fields obtained on the modified grid have been visualised in Figure 5.5 by using the same levels of Q for all methods.

In accordance with the results presented in Chapter 4, M5 is able to resolve smaller scales than M3 on identical grids and, in turn, W9 provides a higher resolution power than M5. However, the basic character of the structures does not seem to change. In the free shear layer emanating from the separation line near the crest of the hill, the preferred axis of orientation is in cross-stream direction for all methods because of the Kelvin-Helmholtz type instability. It should be noted that this behaviour is largely obscured by the vortices in the upper portion of the channel in case of W9. When the shear layer develops further downstream, the vortices break into smaller scales more rapidly with increasing order of the method. As a result, the turbulence mixing is enhanced and more unsteady activity in the core region and the recirculation zone can be observed for M5 and, most significantly, for W9. This is also the main reason for the premature reattachment of the flow predicted by M5 and in particular W9. For all methods, predominantly elongated structures aligned in streamwise direction can be observed in the trough of the channel after the shear layer has disintegrated and in the core flow over the whole domain.

The coherent structures in the flow field can also be characterised by exploiting the statistical information obtained from the two-point correlations of the fluctuating velocity

components. Here, the correlations between pairs of points with identical streamwise and vertical coordinates are averaged in time and in space. For the spatial average, equidistant points in cross-stream direction are considered. The auto-correlation function in one-dimensional form is defined by

$$R_{\delta\delta}(d_y) = \frac{< \delta\, \delta(d_y) >}{\sqrt{< \delta\, \delta > < \delta(d_y)\, \delta(d_y) >}} \,, \tag{5.5.1}$$

where δ stands for the three fluctuating velocity components u', v', w'; <> are the averages in time and in space; and d_y indicates the distance separating the point pair.

Figure 5.6 shows the fluctuating velocity correlations in the boundary layer of the recirculation zone at $(x/h\,,\, z/h) = (1.93, 0.03)$ and in the free shear layer at location $(x/h\,,\, z/h) = (2.02, 0.79)$. Since the results reveal similar features for all grids only the correlations obtained on the modified mesh are presented here. In the boundary layer, the correlation function of the streamwise component $R_{u'u'}$ merely converges to a value close to zero for M3, whereas they vanish completely for both M5 and W9, see Figure 5.6(a). This behaviour indicates less coherent behaviour of the streamwise velocity fluctuations predicted by the two higher-order methods which is most likely also the reason for the earlier separation from the hill surface in case of M5 and W9. Moreover, differences can be noticed regarding the shape of the correlations functions. M3 predicts the smoothest shape. W9, on the other hand, decays faster initially and the curvature seems to change at a correlation length of approximately half a hill height. M5 lies in between the two and the change in decay rate seems to be shifted slightly towards a larger separation distance when compared with W9. This is indicative for more abrupt local changes in the simulations using W9 which can be observed in general for all components and all positions investigated.

The presence of the wall can be noticed when comparing the smallest, uncorrelated lengths for the cross-stream component $R_{v'v'}$ and the vertical component $R_{w'w'}$ presented in Figures 5.6(c) and 5.6(e). At this location, the cross-stream components are less impaired by the wall blockage than the vertical components — hence the uncorrelated length scales are smaller and the level of coherence is generally lower for $R_{v'v'}$. In the free shear layer, however, the velocity fluctuations have a more isotropic character than in the boundary layer, as can be seen in Figures 5.6(b) to 5.6(f). Furthermore, the differences between the high-resolution methods become more pronounced away from the wall.

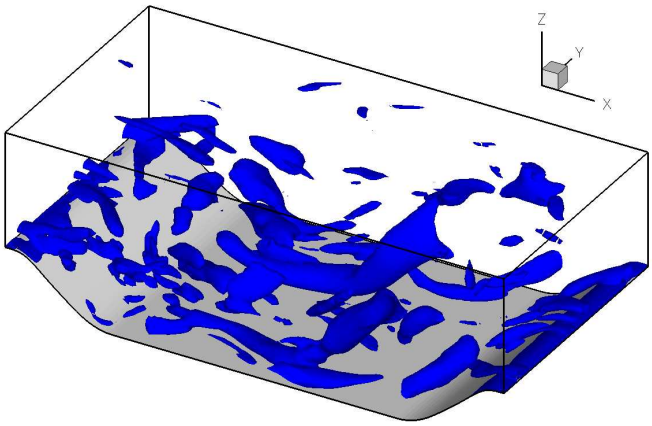

(a) Third-order MUSCL method (M3)

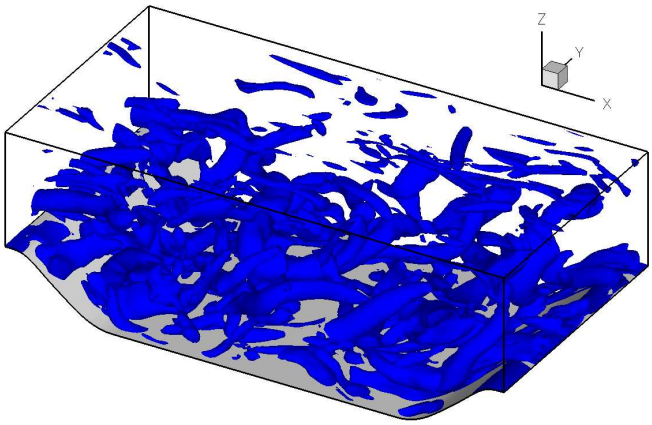

(b) Fifth-order MUSCL method (M5)

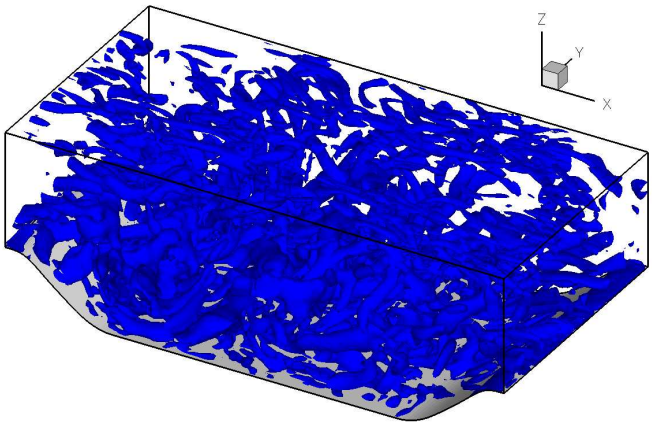

(c) Ninth-order WENO method (W9)

Figure 5.5: Vortical structures in the instantaneous flow field as obtained by three different high-resolution methods on the modified grid visualised by the Q-criterion of Jeong and Hussain [61].

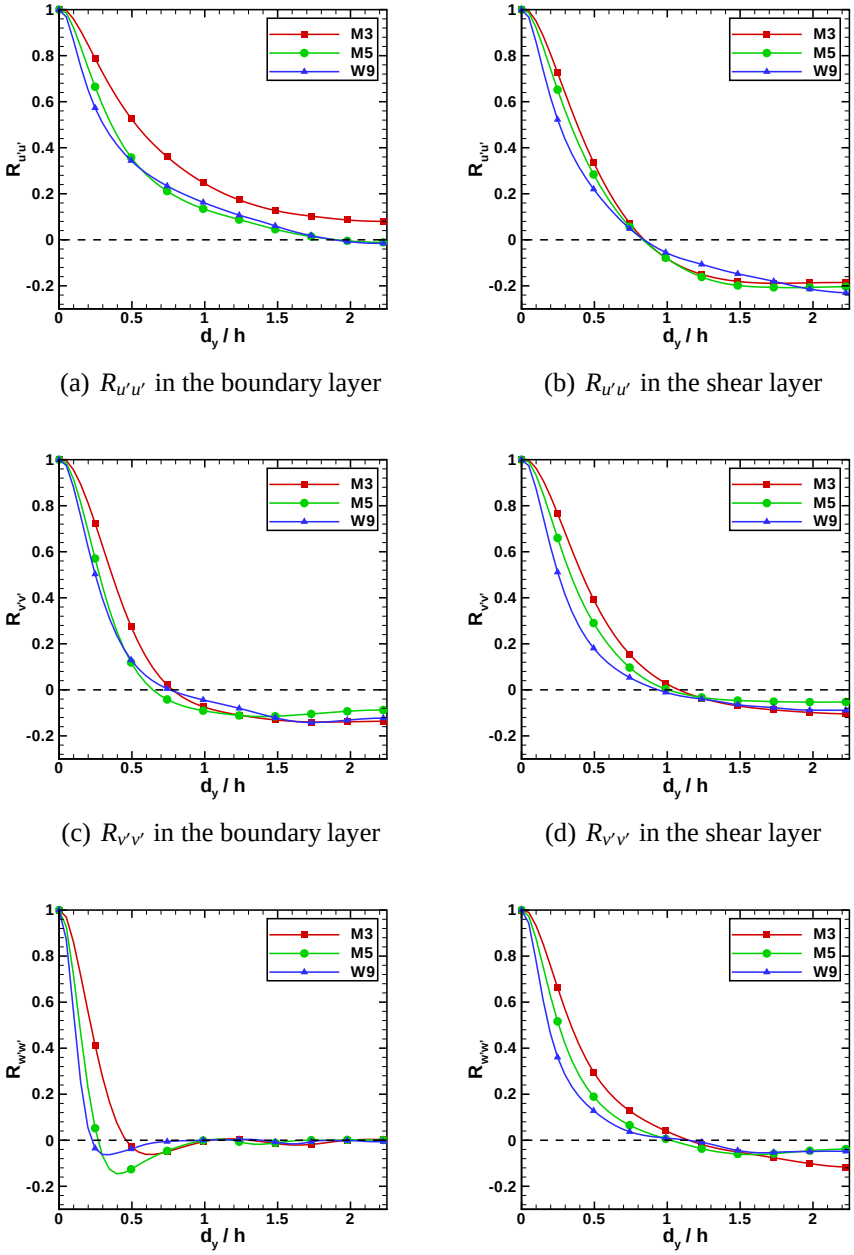

(a) $R_{u'u'}$ in the boundary layer

(b) $R_{u'u'}$ in the shear layer

(c) $R_{v'v'}$ in the boundary layer

(d) $R_{v'v'}$ in the shear layer

(e) $R_{w'w'}$ in the boundary layer

(f) $R_{w'w'}$ in the shear layer

Figure 5.6: Fluctuating velocity correlations in the boundary layer of the recirculation zone and in the shear layer obtained by different high-resolution methods on the modified grid.

5.6 Comparison with Classical Wall-Resolved LES

In order to assess the performance of the three high-resolution methods employed quantitatively, the results have been compared against the highly resolved classical LES of Fröhlich et al. [35]. It should be noted that only the boundary layer at the bottom wall of the channel was fully resolved in the reference case. Along the top wall, the approximations proposed by Werner and Wengle [126] had been applied. In this section, the profiles of the mean streamwise velocity, the normal and the shear stress are investigated. All quantities have been averaged over approximately 50 flow through times in time and across the span-wise extent of the domain in space. Furthermore, the turbulent stresses have been calculated according to the standard Reynolds decomposition of the flow field into mean and fluctuating components. The data has been extracted for the coarse, the medium and the modified grid at four characteristic locations along the streamwise direction which are representative of different behaviours of the flow field.

5.6.1 Incoming Flow

The profiles as obtained by M3, M5 and W9 shortly after the crest of the hill at a streamwise location of $x/h = 0.05$ are shown in Figure 5.7. The results for the three grids employed in this study are compared one at a time against the reference data from the fully wall-resolved reference LES. As a result of the turbulent reattachment and the subsequent strong acceleration along the windward slope of the hill, the flow at this position features a thin, but excited boundary layer near the hill surface. As suggested by Fröhlich et al. [35], however, the sharp peak observed for the normal stress in the bottom boundary layer is mainly due to the influence of the fluctuating separation line and not a characteristic of the incoming flow. The boundary layer at the upper wall on the other hand is relatively thick and more gentle. For the coarse grid, Figure 5.7(a), all high-resolution methods largely over-predict the velocity maximum near the hill and under-predict the second peak near the top wall. Since this specific configuration generates its own inlet conditions, the effects of all phenomena are able to propagate through the whole flow field and thus influence each other. Therefore, this behaviour will be explained in the following paragraphs. The shear stress shown in Figure 5.7(b) is nearly zero for all methods and the maximum normal stresses in the boundary layer are approximately one order of magnitude too low which can be attributed to the delayed separation at the lee side of the hill. In general, both Reynolds stresses are almost uniformly distributed across the channel and the level of turbulence is very low.

Although the resolution near the wall is increased only marginally for the medium grid, approximately 3 points in the boundary layer as opposed to about 2 points for the coarse grid at this position, a drastic improvement in the results can be seen. This already indicates substantial differences in the oncoming flow field. The characteristic shape of the velocity profile featuring two narrow maxima near the top and the bottom

wall is approached, albeit the effect in Figure 5.7(c) is only faint. Additionally, the peak velocity is much closer to the fully resolved LES with W9 yielding the best result, followed by M3 and then M5. Again, this is associated with the characteristics of the upstream flow. The shear stress in Figure 5.7(d) exhibits a similar shape and magnitude as the reference solution where W9 follows it almost exactly, except in the boundary layer. Here, the peak is less pronounced. The same holds for the maximum normal stress. W9 predicts about half the amount of normal stress in the boundary layer as observed in the reference LES and it is further decreasing for the lower order schemes. Furthermore, the shape of the normal stress appears more flat for all high-resolution methods when compared with the classical LES in the lower half of the channel and the level of turbulence is generally lower.

The results for the modified grid featuring a higher clustering of grid points near the walls are presented in Figures 5.7(e) and 5.7(f). For this particular mesh, approximately 11 points lie within the boundary layer at the hill surface and the z+ distribution along the bottom wall indicates nearly resolved conditions throughout the domain, see Figure 5.4. The averaged velocity profiles from the reference LES and the simulations performed here are virtually identical near the surface of the hill. The local minimum near the half-height of the channel at this position is slightly more pronounced for all high-resolution methods. Minor differences can also be observed at the top wall where the reference solution yields a very thick boundary layer as opposed to a much thinner boundary layer predicted by the current simulations. This can mainly be attributed to the fact that the grid employed in the reference LES was relatively coarse in this area and a wall function had been used. Additionally, the wall treatment introduces an unrealistic kink in the velocity profile which appears at all locations along the channel. Fröhlich et al. [35] reported that the near-wall approximation at the top surface is not relevant to the solution in the rest of the flow field. However, this claim will be revisited for the reattached flow region.

In Figure 5.7(f), a significant improvement can also be observed for the Reynolds stresses on the modified grid. The shape and magnitude of the shear stresses as predicted in all simulations are in very good agreement with the reference solution. Although the minimum shear stress in the bottom boundary layer is slightly less distinct, the peak normal stresses at the same location are very close to the reference. Both are strongly related to the movement of the separation line. With increasing grid resolution in the wall normal direction, the high-resolution methods are able to tap their full potential. This is indicated clearly by the upstream shift of the averaged separation points. Small disturbances start to develop normal to the wall and are propagated along the surface even though the grid resolution in the streamwise direction is fairly coarse. Because the higher order methods are more sensitive to small fluctuations, they predict a separation prior to M3. This is reflected by the peak normal stresses shown in Figure 5.7(f). Here, W9 results in the strongest maximum, followed by M5 and then M3. It should be noted that the averaged points of separation are identical for W9 and M5, but the influence of the fluctuations on the stress profiles are probably stronger for W9 due to its higher order of accuracy. Further away from the hill surface, less turbulence is

predicted by all high-resolution methods when compared against the LES of Fröhlich et al. [35] in the lower half of the channel, but increased levels of normal stress are observed for M5 and especially M3 in the upper half.

5.6.2 Separated Flow

The maximum turbulent intensities are reached after separation has occurred. Here, several phenomena are interacting with each other: the two boundary layers at the top and the bottom wall of the channel; the recirculation zone which can be seen as a shear layer; the highly unsteady free shear layer emanating from the separation line and the core flow can be distinguished at the streamwise location $x/h = 2$. Averaged velocity and stress profiles for this position are shown in Figure 5.8.

A substantial difference between the velocity profiles from the reference LES and the current simulations on the coarse grid is illustrated in Figure 5.8(a). The size of the separation bubble is heavily under-predicted by all high-resolution methods due to the delayed separation and the subsequent early reattachment. Hence, the separation region covers only approximately half a hill-height in the wall normal direction and the reversed flow is less developed. Since the same mass flow rate has to be achieved in all simulations, the core velocity is under-predicted accordingly when compared to the reference solution. This is the main reason for the relatively uniform velocity distribution above the hill crest in Figure 5.7(a). Surprisingly, however, the stress magnitudes shown in Figure 5.8(b) are of approximately the same order. Differences between the high-resolution methods can be observed regarding the location of the shear layer, marked by the peak stresses, and the shape of the profiles. M5 yields the lowest shear layer as late separation favours this behaviour. Although M3 separates downstream of W9, the position of the shear layer is slightly higher which is associated with the early reattachment of W9. Additionally, the peak normal stresses and the spreading of the shear layer appear to be dominated by the separation location. For the coarse grid, higher normal stresses are observed for delayed separation and the width of the shear layer grows with the distance from its origin.

Figures 5.8(c) and 5.8(d) present the results for the medium grid at the same streamwise location. In accordance with the above, early separation and late reattachment lead to a better prediction of the separation bubble height. Thus, all methods approach the reference velocity profile in Figure 5.8(c), albeit the reversed flow in the lower portion of the channel is still slightly under-predicted. Regarding the Reynolds stresses, more turbulence can be supported due to the grid refinement and consequently higher levels of shear stress and normal stress are observed, both exceeding the predictions of Fröhlich et al. [35] in the trough where the turbulence is produced. This behaviour is worrying because it indicates that the solution is not grid converged. Large variations of the peak stresses have also been observed by Temmerman et al. [112] who associated them with the differences regarding the separation point. Yet, this conclusion was not consistent since different turbulence intensities had been found in simulations with similar separation points. Hence, the effect of grid clustering in the free shear

layer cannot be disregarded. However, no information about the grid resolution in this region is available for the reference LES of Fröhlich et al. [35]. It should be noted that the peak stresses for the medium grid are less dependent on the exact location of detachment and reattachment at this position because the free shear layer had more time to develop and it is still well ahead of the impingement at the bottom wall.

For the modified grid, the velocity profiles in Figure 5.8(e) follow the reference solution more closely, with minor differences in the boundary layers at the top and the bottom wall. Additionally, all high-resolution methods predict a smoother transition between the free shear layer and the core flow. M5 appears to predict a stronger recirculation than W9 although separating at identical locations. This leads to later reattachment of the separation bubble. A strong dependence of the upper boundary layer on the grid resolution and the core flow can be observed. As expected, the boundary layer becomes thinner for higher velocities in the core of the channel. The classical LES, despite predicting slightly stronger velocities, results in a considerably thicker boundary layer than the high-resolution methods. This can mainly be attributed to the combined effect of the relatively coarse grid and the wall approximations employed in the reference solution. Good agreement for the stresses is revealed in Figure 5.8(f). In the upper portion of the channel, both the shear and the normal stress are very close to the reference profile. Again, a slight discrepancy does exist near the boundary layer at the top wall due to the inadequate treatment in the classical LES. In the recirculation region, more turbulent energy is produced by M3, M5 and W9 when compared to the results of Fröhlich et al. [35]. Here, all high-resolution methods yield similar Reynolds stresses. Minor differences, however, appear in the shear layer where the maximum intensities occur. The behaviour of the stresses, especially near the peaks, is influenced by a number of parameters, e.g. the location of separation and reattachment or the specifics of the numerical method, but no consistent pattern seems to emerge in the massively separated flow region.

5.6.3 Reattached Flow

The next position along the channel that has been investigated is the post-reattachment region at $x/h = 6$, see Figure 5.9. Here, the flow is recovering to a state more typical for a plane channel geometry. Not surprising, the results obtained by the high-resolution methods on the coarse grid exhibit large discrepancies to the reference solution as the time history of the flows differ substantially. The constriction felt by the flow, i.e. the combination of the hill geometry and the separation bubble, is much smaller for the former. Hence, the velocity profiles predicted in the current simulations, shown in Figure 5.9(a), are already closer to the state of equilibrium. Most remarkably, however, is the qualitative difference of the normal stress profile obtained by W9 when compared to the lower order methods. The pronounced maximum in Figure 5.9(b) indicates more transport of turbulence initially generated in the free shear layer. This effect is intensified on the coarse grid because W9 also yields the strongest fluctuations further upstream.

The velocity profiles obtained on the medium grid, see Figure 5.9(c), are in better agreement with the reference solution than for the coarse grid as could be expected. In general, earlier reattachment leads to higher velocities in the trough at the same streamwise locations. This is the case indeed for all methods if applied on the modified grid, but does not hold for combinations of W9 and the medium or the coarse grid. Here, W9 reattaches prior to M3 and exhibits smaller velocities in the lower portion of the channel. The Reynolds stresses obtained on the medium grid are displayed in Figure 5.9(d). Apart from the normal stresses in the vicinity of the top wall, they are relatively close to the reference profiles. Especially the shear stresses are in very good agreement over the whole height of the channel. At about the height or the hill crest, the distinctive peak due to turbulence transport can be observed for all methods. It is most pronounced for W9, however, which leads to higher levels of turbulence in the lower half of the attached flow field throughout the channel.

The results for the modified grid are presented in Figures 5.9(e) and 5.9(f). Regarding the averaged streamwise velocities, they are approaching the reference profiles in the main flow field. Near the bottom wall, however, the velocity is over-predicted because of the earlier reattachment. Consequently, the transition between the flow in the core of the channel and the trough is smoother. The boundary layer at the top wall thickens similar to the prediction from the classical LES of Fröhlich et al. [35] due to the deceleration of the core flow. However, major differences can be observed for the normal stresses along the top wall, see Figure 5.9(f). The normal stress seems to vanish in the reference solution, whereas all current simulations predict considerable turbulent activity. According to the fully wall-resolved simulations from Breuer [14], the normal stress should reach a minimum of approximately 0.015 in the vicinity of the top wall and then increase again as the solid surface is approached. Thus, all high-resolution methods appear to reproduce the correct behaviour. In general, the level of turbulence across the channel also reflects the location of the reattachment point because they are relatively close on the medium grid. The reattachment is delayed for the lower order methods and thus the turbulent intensity at the current location is higher for M3 than M5, and, in turn, M5 than W9. All methods lead to virtually identical results as the reference LES regarding the shear stress.

5.6.4 Accelerated Flow

The flow in the channel is subject to strong acceleration as it passes over the windward side of the hill. This region is represented by the averaged velocity and stress profiles at $x/h = 8$. It should be noted the slope of the geometry has not been accounted for during the extraction of the data presented in Figure 5.10. Hence, in accordance with the reference solution of Fröhlich et al. [35], the components do not represent the normal and the tangential directions at the surface.

As the flow recovers and a more uniform state is achieved, the velocity profiles as predicted by the high-resolution methods are nearly indistinguishable irrespective of the grid employed. The data confirms the observations made prior to this position and

no new insight can be gained. For the coarse grid, the velocity profiles are less full because of the severely under-predicted size of the separation bubble. This behaviour can be improved gradually with increasing the grid resolution near the walls as shown for the medium grid in Figure 5.10(c) and for the modified grid in Figure 5.10(e). Additionally, the boundary layers at the top and the bottom wall become thinner as the flow is accelerated in the streamwise direction. In the vicinity of the hill surface, the velocity is decreased due to the positive pressure gradient acting on the flow field.

Although less pronounced, the Reynolds stresses presented in Figures 5.10(b) to 5.10(d) bear similar features to the ones already discussed for the reattached flow at $x/h = 6$. Interestingly, even at this location the wall approximations made in the reference LES still have a significant effect on the boundary layer profile and the normal stresses near the top wall. Attention should be paid to the shear stresses at the hill surface since they appear to reverse sign. However, this is only an artifact of the misalignment between the hill slope and the velocity components which also has to be considered when interpreting the velocity profiles at this specific location.

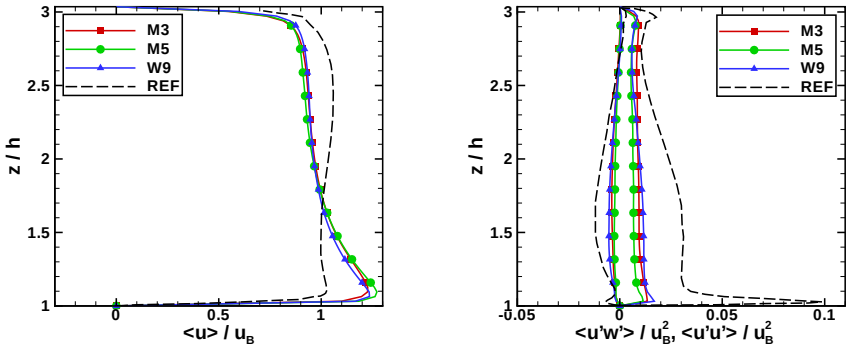

(a) Streamwise velocity for the coarse grid (b) Reynolds stresses for the coarse grid

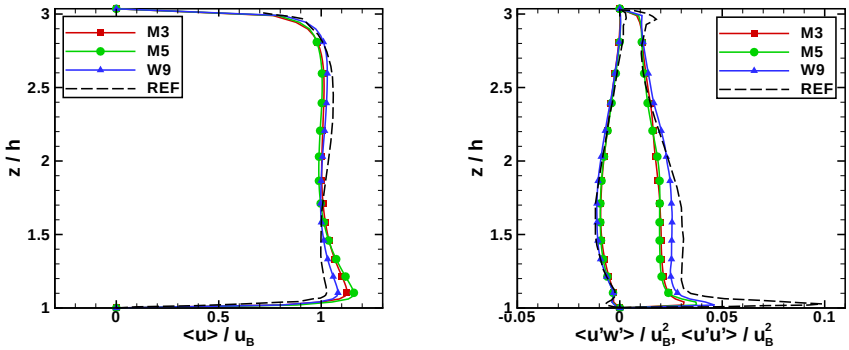

(c) Streamwise velocity for the medium grid (d) Reynolds stresses for the medium grid

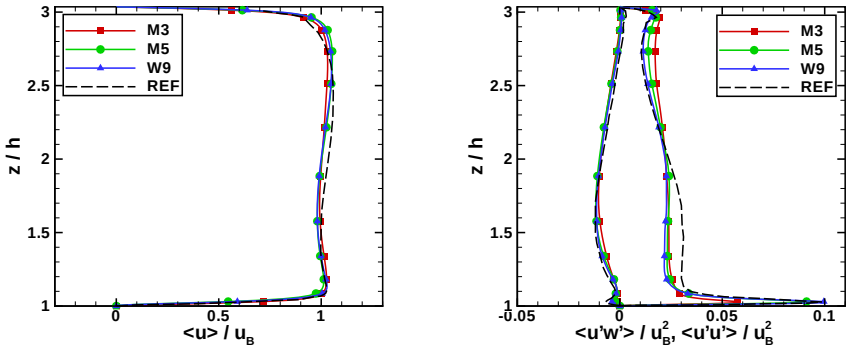

(e) Streamwise velocity for the modified grid (f) Reynolds stresses for the modified grid

Figure 5.7: Comparison of the averaged streamwise velocity and Reynolds stresses near the hill crest at $x/h = 0.05$ as obtained by different high-resolution methods on the coarse, the medium and the modified grid with the reference LES of Fröhlich et al. [35].

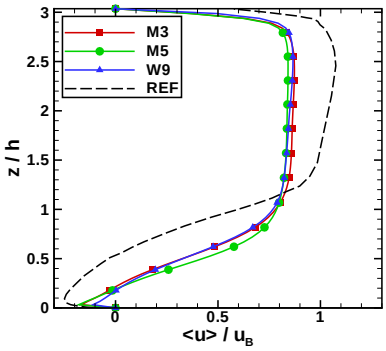

(a) Streamwise velocity for the coarse grid

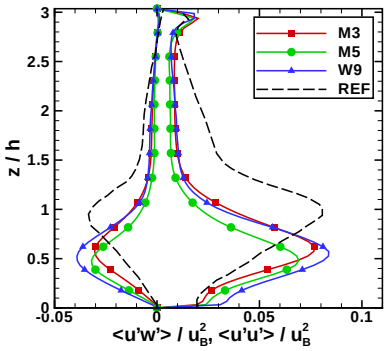

(b) Reynolds stresses for the coarse grid

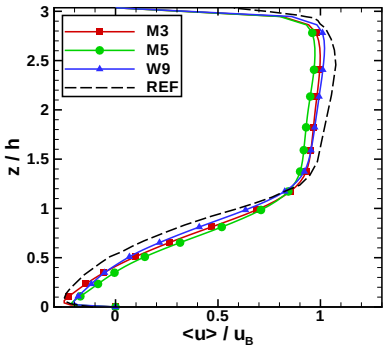

(c) Streamwise velocity for the medium grid

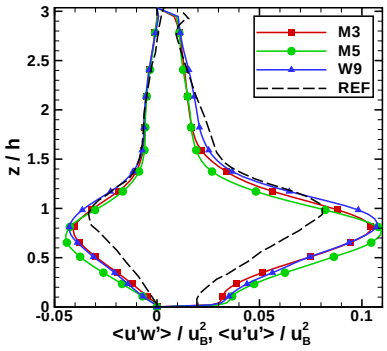

(d) Reynolds stresses for the medium grid

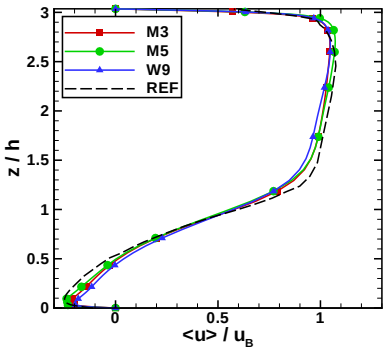

(e) Streamwise velocity for the modified grid

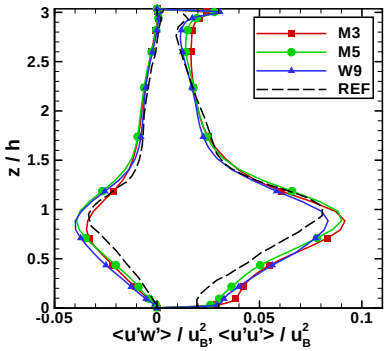

(f) Reynolds stresses for the modified grid

Figure 5.8: Comparison of the averaged streamwise velocity and Reynolds stresses across the recirculation zone at $x/h = 2$ as obtained by different high-resolution methods on the coarse, the medium and the modified grid with the reference LES of Fröhlich et al. [35].

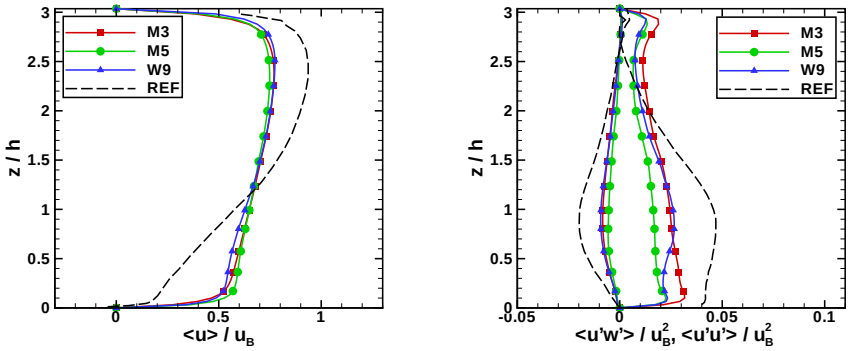

(a) Streamwise velocity for the coarse grid (b) Reynolds stresses for the coarse grid

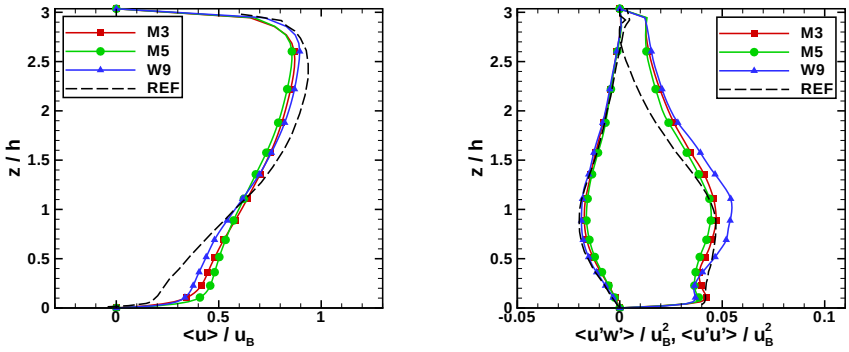

(c) Streamwise velocity for the medium grid (d) Reynolds stresses for the medium grid

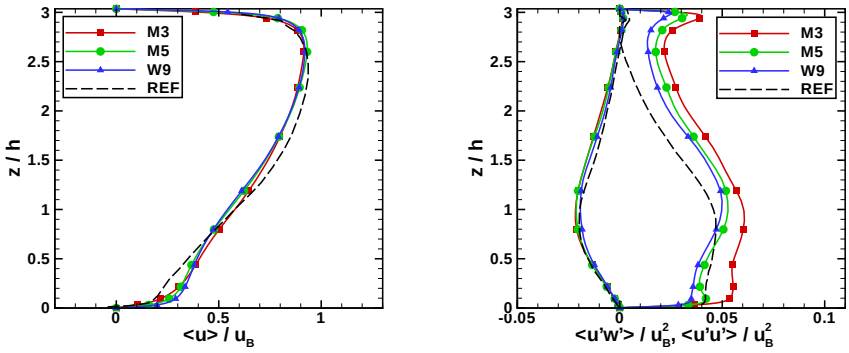

(e) Streamwise velocity for the modified grid (f) Reynolds stresses for the modified grid

Figure 5.9: Comparison of the averaged streamwise velocity and Reynolds stresses after reattachment at $x/h = 6$ as obtained by different high-resolution methods on the coarse, the medium and the modified grid with the reference LES of Fröhlich et al. [35].

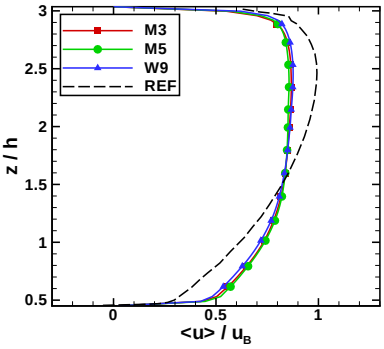

(a) Streamwise velocity for the coarse grid

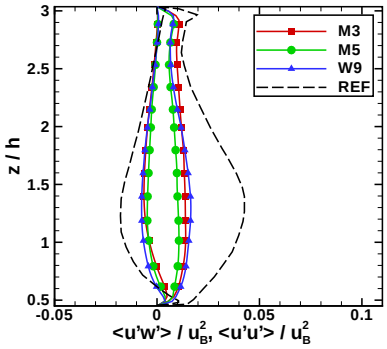

(b) Reynolds stresses for the coarse grid

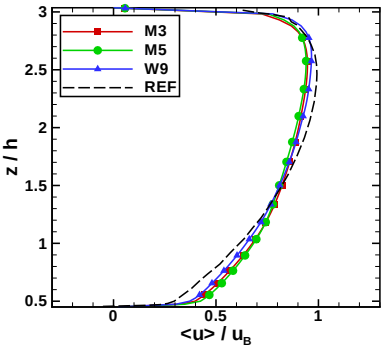

(c) Streamwise velocity for the medium grid

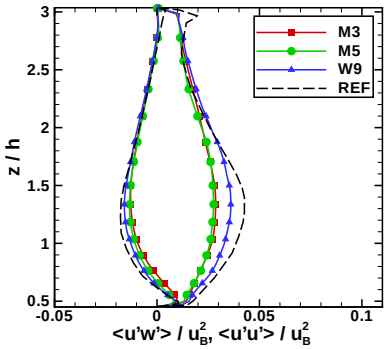

(d) Reynolds stresses for the medium grid

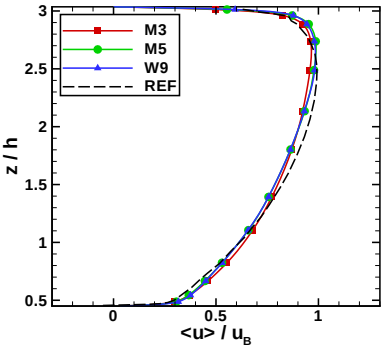

(e) Streamwise velocity for the modified grid

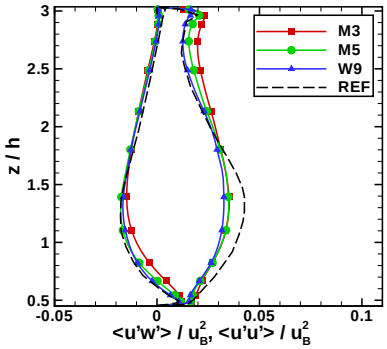

(f) Reynolds stresses for the modified grid

Figure 5.10: Comparison of the averaged streamwise velocity and Reynolds stresses above the windward slope at $x/h = 8$ as obtained by different high-resolution methods on the coarse, the medium and the modified grid with the reference LES of Fröhlich et al. [35].

5.7 Comparison with Classical Under-Resolved LES

It has been found that a fine grid resolution normal to the solid surfaces is essential for accurately predicting the flow features in the constricted channel using high-resolution methods. However, the performance can also be assessed with regard to classical LES for highly under-resolved conditions. Temmerman et al. [112] have investigated this scenario and tested several wall approximations in conjunction with the massively separated hill flow.

From Section 5.4, it is already known that the prediction of the separation point and the location of reattachment can be improved by using high-resolution methods. However, if this also transfers to the rest of the flow field and to what extent wall functions affect the statistical data still needs to be clarified. Therefore, the averaged streamwise velocity and the Reynolds stress profiles as obtained by M3, M5 and W9 on the coarse grid are compared against the available data from the wall-modelled LES of Temmerman et al. [112] which has been produced on an identical grid, see Figure 5.11. In accordance with Section 5.4, the profiles referred to as "LL3", "WW" and "NS" are the results from classical LES using the WALE subgrid-scale model of Ducros et al. [31] in combination with a three-layer logarithmic wall model, the wall function proposed by Werner and Wengle [126] and no wall approximation, i.e. no-slip condition, respectively. Additionally, the reference data from Fröhlich et al. [35] has been included for comparison.

Figures 5.11(a) and 5.11(b) show the averaged velocity profiles in the separation region at $x/h = 2$ and after reattachment occurred at $x/h = 6$. Although the point of separation is further upstream than for the classical LES with no-slip condition, the velocity profiles as obtained by the high-resolution methods are very close to the classical LES without wall-treatment at both locations. Applying a logarithmic model near the wall does not improve the situation significantly in the recirculation zone or the reattached region. On the other hand, WW appears to be much closer to the reference solution, especially after reattachment. However, this is not due to the power-law assumption made in the model of Werner and Wengle [126]. As has been pointed out by Temmerman et al. [112], the difference can mainly be attributed to the specific implementation of the approximation which results in earlier detachment of the flow from the hill surface.

For the normal stresses in the recirculation zone presented in Figure 5.11(c), a strong relationship between separation location and both position and strength of the free shear layer can be observed for the classical LES. The same applies to the shear stresses shown in Figure 5.11(e). This is not the case for the high-resolution methods. However, this behaviour can be expected because all classical LES simulations used essentially the same numerical method and the wall model does not affect the shear layer. The peak stresses predicted by the high-resolution methods generally appear to be in better agreement with the reference solution than the classical LES with no-slip condition. Yet, it should be noted that concerns have been raised regarding the grid-converged representation of the shear layer. After reattachment, see Figure 5.11(d), all normal

stress profiles obtained without wall approximations seriously under-predict the level of turbulence. With wall functions, the normal stress in the attached boundary layer is more accurately represented. Here, the log-law assumption seems to give better results than the power-law. Away from the wall, however, the reattachment location and the strength of the shear layer appear to be the two factors dominating the shape and the peak of the normal stress. This also holds for the shear stresses presented in Figure 5.11(f).

In general, the semi-empirical wall models used in the classical LES of Temmerman et al. [112] only affect the point of separation in under-resolved conditions. However, the effectiveness depends strongly on the size of the wall adjacent cells. In order to yield an improvement in the attached flow region, the first grid point has to be in the viscous sublayer as has been pointed out by Breuer et al. [15]. Additionally, their influence declines with higher clustering near the solid surface. No direct improvement could be observed in the massively separated flow region in the lee of the hill which could be expected because they are not designed for this condition. A better prediction of the flow detachment can also be achieved by using high-resolution methods. However, the subsequent development of the free shear layer and the point of reattachment are more sensitive to the specifics of the numerical method than the location of the separation point.

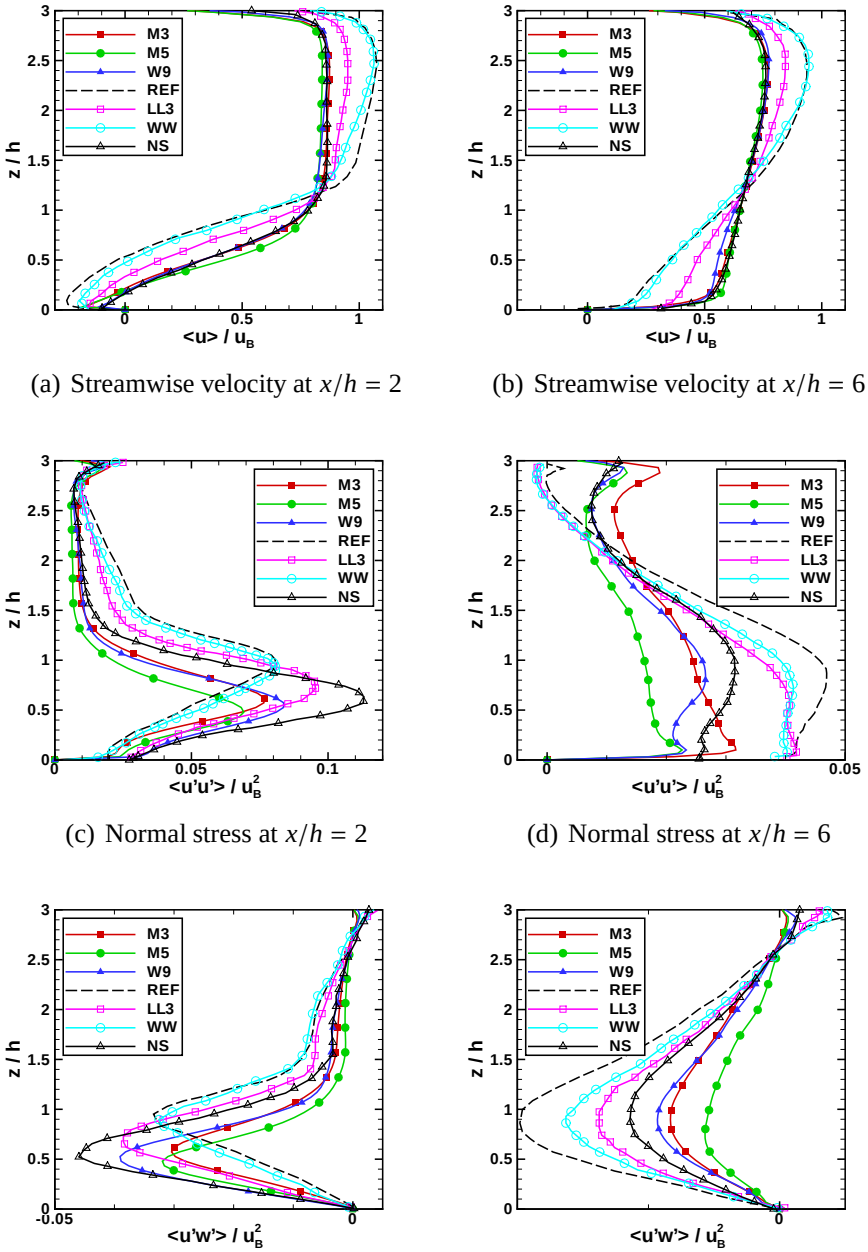

(a) Streamwise velocity at $x/h = 2$

(b) Streamwise velocity at $x/h = 6$

(c) Normal stress at $x/h = 2$

(d) Normal stress at $x/h = 6$

(e) Shear stress at $x/h = 2$

(f) Shear stress at $x/h = 6$

Figure 5.11: Comparison of the averaged streamwise velocity and Reynolds stresses across the recirculation zone at $x/h = 2$ and after reattachment at $x/h = 6$ as obtained by different high-resolution methods with the classical LES of Temmerman et al. [112] on identical grids.

5.8 Summary

The performance of three high-resolution methods has been assessed with respect to the massively separated flow in the lee of a hill geometry. The complex flow field encountered in this test case comprises various regions where different requirements have to be met. Near the crest of the hill, the accurate prediction of the thin boundary layer detachment from the gently curved surface is paramount to the downstream development of the flow field. After separation has occurred, the highly unsteady free shear layer emanating from the hill challenges the turbulence modelling capabilities of the numerical method. The reattachment location at the bottom wall of the channel is strongly influenced by the representation of the free shear layer. Reattachment itself, on the other hand, is an unsteady process and the coherent structures originating in the shear layer alternate between being propagated downstream or being swept back into the recirculation bubble. Thus, a feedback loop is generated that adds to the fluctuation of the separation line. In the post-reattachment region, the recovery process towards a plane channel flow has to be captured. Here, the boundary layer in the trough causes additional difficulties because it is of non-standard form and it undergoes several evolution steps before it reaches the next hill crest. Initially, it is very thick and highly turbulent. As it approaches the windward side of the following hill, it is accelerated and undergoes a less pronounced separated state at the bottom of the slope. During the acceleration stage, it becomes thinner and thus it poses even more stringent requirements regarding the grid resolution.

All of the above phenomena are intimately connected to each other because the hill flow generates its own inlet condition through the periodicity constraint in streamwise direction. Therefore, it is almost impossible to isolate the effects of the numerical method on individual regions. However, it can certainly be claimed that the higher order methods yield an improvement in predicting the averaged separation point even if the boundary layer is under-resolved. It has also been found that a clustering of grid points in the wall normal direction is more beneficial than a streamwise clustering. This can be explained by the reduced influence of wall blockage on the fluid movement near the surface. Since the higher order methods are more sensitive to small disturbances, they are able to propagate along the wall and increase the likelihood of separation.

In the free shear layer, the increased sensitivity of the higher order methods M5 and W9 leads to a more rapid breakdown of the layer when compared to M3. Consequently, the predicted separation length becomes shorter with increasing order of the method. This is also associated with more turbulence mixing and the formation of small scale structures whose size depends on the resolution power of the numerical scheme. No conclusive prediction can be made for the post-reattachment region, however, because the history of the flow strongly influences the results obtained here.

CHAPTER 6

Swept Wing

IN this chapter, the Implicit Large-Eddy Simulation approach based on the third-order accurate MUSCL reconstruction method is applied to the investigation of the highly complex flow around a fully three-dimensional swept wing geometry combining the importance of transition, free shear layers, detached and attached regions. As this case has been designed to test and challenge numerical methods, qualitative and quantitative data from experiments and hybrid RANS/LES simulations are available for comparison. No attempt to incorporate a wall-approximation has been made in the current simulation. Instead, the boundary layer is nearly resolved over the majority of the wing.

6.1 Introduction

One of the greatest challenges for current Large-Eddy Simulations is the application to flow problems of practical engineering interest. In an aeronautical context, curved three-dimensional geometries such as swept and delta wings are among the most difficult scenarios encountered because they are prone to separation. Swept and delta wings can be found in all modern aircrafts travelling at transonic or supersonic speeds. However, it is not only cruise conditions that are of aerodynamical interest. Most of these vehicles also fly a considerable amount of time at subsonic speeds and moderate to high angles of attack, e.g. takeoff and landing or air combat. In fact, as has been pointed out by Cummings et al. [19], the non-linear effects associated with separation at these flow conditions are more interesting from the modeller's point of view and much more difficult to simulate accurately. Computational challenges include the prediction of transition leading to turbulence and separation, control of numerical viscosity, and generation of adequate grids.

Although sharp-edged delta wings ignore the curvature of the leading edge, the large-scale flow structures are similar to those observed in three-dimensional swept wings. A brief summary of the flow around delta wings at high angles of incidence is given in the book of Anderson [2]. It is shown that a pair of leading edge vortices arises from the pressure difference between the top and bottom surface of the wing. The flow

tries to curl around the swept leading edge from the bottom (pressure side) to the top (suction side) and eventually separates. A free shear layer emanates from the leading edge and a span-wise pressure gradient forces the shear layer to roll up, yielding a closed leading edge vortex (LEV).

On closer examination, however, the flow structure is far more complex. For slender wings in particular, the LEV induces outflow of the attached fluid on the suction side of the wing which encounters an adverse pressure gradient towards the leading edge. The result is a secondary separation zone underneath the LEV featuring smaller, counter-rotating vortices, displacing the LEV farther inboard and above the surface. Secondary separation strongly depends on the character of the boundary layer. A laminar boundary layer favours separation, whereas separation occurs later and the secondary vortices are smaller for turbulent boundary layers.

As the sweep and angle of attack are modified, the vortex structure, interaction and near-surface phenomena change dramatically as has been shown by Gursul [52] and Gursul et al. [53]. For non-slender delta wings at low angles of incidence, LEVs emanate from the apex of the wing only and flow separation at the leading edge may occur even at low Reynolds numbers, e.g. see Ol and Gharib [86], Taylor and Gursul [110], Taylor et al. [111] and Yavuz et al. [127]. Separation strongly depends on the shape of the leading edge and the flow conditions. With increasing angle of incidence, the LEV becomes unstable and eventually breaks down. For wings with lower sweep angle, breakdown occurs at lower angles of attack compared to wings with higher sweep. Two distinctive types of vortex breakdown have been reported by Delery [23], Gordnier [43] and Payne et al. [88]: the bubble breakdown characterised by a stagnation point, at the head of the breakdown region, and rapid diffusion; and the spiral breakdown marked by deceleration of the vortex core and large scale turbulence. Furthermore, other phenomena like vortex shedding at very high angles of attack or the Kelvin-Helmholtz roll up of the free shear layer have been studied experimentally by Rediniotis et al. [94] and Riley and Lowson [96], respectively.

Computational studies of separated swept wing flows have traditionally been focused on sharp-edged delta geometries because the detachment process is greatly simplified. Various combinations of slender and non-slender delta wings at different angles of attack between 5° and 30° have been investigated for Reynolds numbers ranging from the order 10^4 to 10^6, e.g. see the RANS, LES, and hybrid simulations performed by Brandsma et al. [13], Gordnier [43], Gordnier and Visbal [44, 45], Rizzetta [97]. When transition and separation from curved wing surfaces is a prime concern, on the other hand, all previous studies have been limited to quasi-infinite aerofoil sections. For example, Mellen et al. [80] have summarised the findings from the European LESFOIL project on Large-Eddy Simulations around an Aerospatiale A-aerofoil near stall conditions at an angle of incidence of 13.3°. It has been shown that near-wall resolution is of paramount importance for accurately predicting this type of flow. This impression has been confirmed by the ILES simulation of Morgan and Visbal [84] and the local 2D/3D coupling approach for LES employed to the identical configuration by Dahlström and Davidson [20], Mary and Sagaut [79] . These investigations have been conducted at

high Reynolds numbers of order 10^6. In order to obtain a fully resolved solution of a similar flow field, however, the Reynolds number has to be decreased by one order or magnitude because of the current hardware limitations, e.g. see the direct numerical simulation for a NACA 0012 aerofoil performed by Shan et al. [100].

Although a great deal of attention has been paid to complex separated flow structures for wings at relatively high angles of incidence, in particular, a theoretical or computational model for predicting the flow behaviour with any degree of certainty has not emerged yet. In fact, no attempt at combining realistic conditions for the flow detachment with a leading edge sweep has been made to date. This investigation is thus concerned with a fully three-dimensional swept wing geometry featuring separation from a smoothly curved leading edge. Here, the resulting flow field is highly complex, nonlinear and characterised by transition zones, leading edge and possible trailing edge separation, vortical flow, turbulence, secondary separated zones and reattachment.

6.2 Numerical Framework

The twisted swept wing geometry considered in this investigation was specifically designed within the framework of the MSTTAR (Modelling and Simulation of Turbulence and Transition in Aerospace) initiative for the validation of CFD codes. The wind tunnel model used in the experimental campaign of Zhang and Turner [131], conducted at Manchester University, features a leading edge sweep angle of 40°, a trailing edge sweep angle of 10.56° and an effective angle of attack of 1.23°. The root chord length is $0.303m$ and the span is $0.65m$ with a taper ratio of 0.3.

In order to capture the leading edge curvature as accurately as possible and to achieve an efficient distribution of grid cells around the wing a C-O-type topology has been chosen. After preliminary computations on a very coarse grid consisting of approximately 3.5M cells and spanning a large computational domain the clustering near the wing surface has been modified and the extent of the domain has been significantly reduced. The results presented here have been obtained on a grid comprising a total of 12.5M cells in a computational domain of $6c$, $6.14c$ and $5c$ (c is the root chord length) in x-, y- and z-direction, respectively. During the mesh generation using the commercial software GRIDGEN, the structured grid has been split into eight blocks of approximately $95 \times 130 \times 127$ cells in streamwise-, span-wise- and normal-direction each, see Figure 6.1(a), and the grid quality has been improved by applying an elliptic smoothing algorithm. Subsequently, the no-slip condition on the wing surface, extrapolated outlet condition in the wake region and far-field conditions have been defined in a pre-processing step. In addition, the mesh has been decomposed for the high-performance simulation.

The characteristic parameters specifying the grid clustering near and on the surface of the swept wing as illustrated in Figures 6.1(b) and 6.1(c) are detailed in Table 6.1, for a definition of the corresponding edges see Figure 6.2. Here, the geometric growth rate does not exceed 1.05 in any direction and the resulting z+ values obtained under

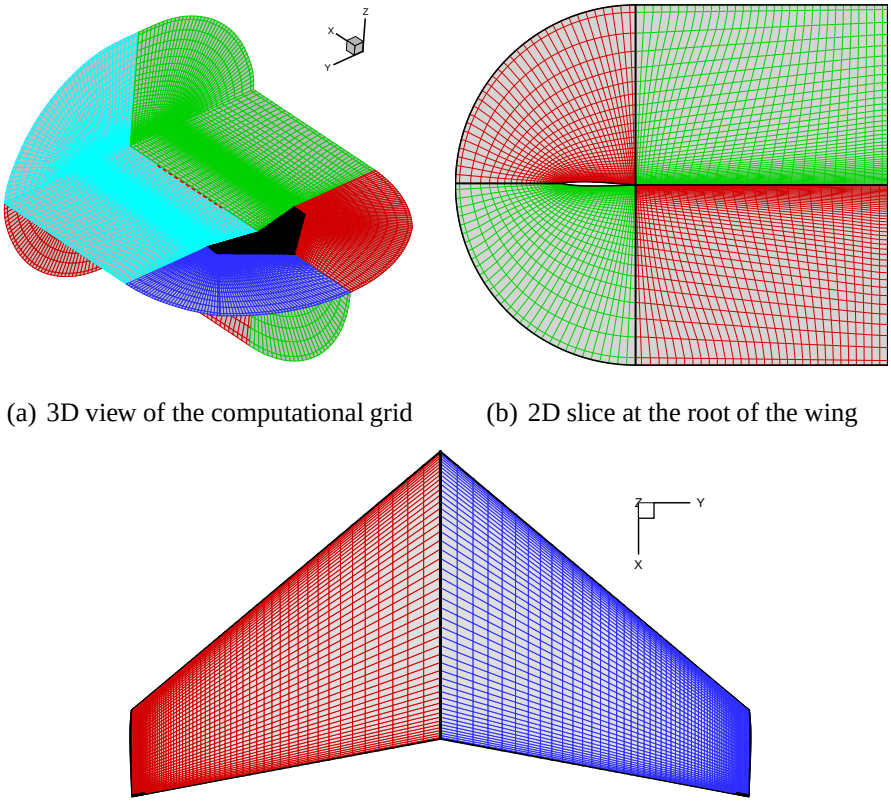

(a) 3D view of the computational grid (b) 2D slice at the root of the wing

(c) Surface grid (every second point)

Figure 6.1: C-O-type grid topology comprising 12.5M cells in a computational domain extending 6c, 6.14c and 5c (c is the root chord length) in x-, y- and z-directions, respectively (every third grid point shown here unless stated otherwise).

conditions similar to the experiment of Zhang and Turner [131] range from 1 in areas of separated flow over 3 in reattachment regions to 5 at the leading edge. Although this indicates a wall-resolved situation over the majority of the wing, the flow field is still far from being fully resolved on the computational mesh even in the areas near the wing tips where the clustering is particularly fine. In order to quantify the degree of under-resolution, the Kolmogorov length scale has been approximated for the current flow conditions to be $5 \times 10^{-5}c$, based on the relations given for isotropic turbulence and a very conservative estimate for the integral length scale of $0.5c$. Thornber et al. [114] have shown that the numerical method employed here requires about 10 grid cells for the representation of the highest wavenumbers in order to accurately describe decaying homogeneous turbulence in a statistical sense. With the data from Table 6.1, this roughly yields a 5-million-fold under-resolved flow field near the tips of the swept wing.

The simulation for the MSTTAR wing at a total angle of attack of 9° has been carried out at a Reynolds number of approximately 210, 000, based on free-stream velocity and root chord length, and a near incompressible Mach number of 0.3. These conditions

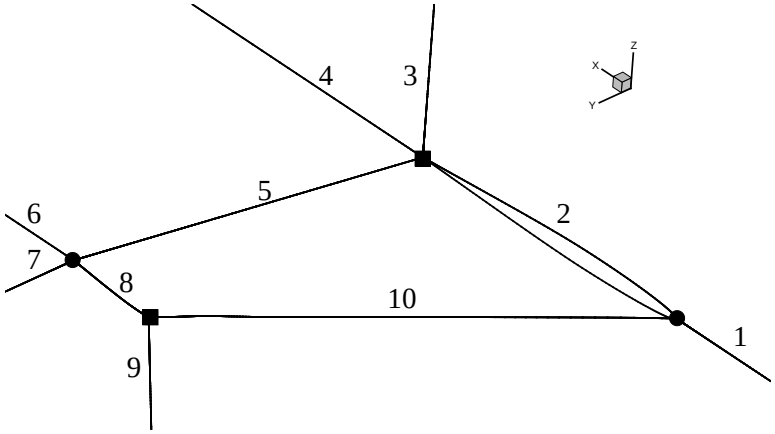

Figure 6.2: Edges employed for the grid clustering in the mirror-symmetric computational domain as specified in Table 6.1. All other edges feature an equidistant distribution of nodes.

Edge	Nodes	Distribution	Δ_{BEG}/c	Δ_{END}/c
1	128	geometric progression	—	5.0×10^{-4}
2	96	general	3.3×10^{-3}	3.3×10^{-3}
3	128	geometric progression	5.0×10^{-4}	—
4	96	monotonic rational quadratic spline	3.3×10^{-3}	3.8×10^{-2}
5	131	general	3.0×10^{-2}	1.0×10^{-3}
6	96	monotonic rational quadratic spline	—	1.0×10^{-3}
7	128	geometric progression	—	1.0×10^{-3}
8	96	general	1.0×10^{-3}	1.0×10^{-3}
9	128	geometric progression	1.0×10^{-3}	—
10	131	general	1.0×10^{-3}	3.0×10^{-2}

Table 6.1: Characteristic parameters specifying the point clustering in the immediate vicinity of the three-dimensional wing surface. A definition of the corresponding edges can be found in Figure 6.2, where the beginning and end of the edges are marked by ■ and •, respectively.

have been chosen according to the experiments conducted by Zhang and Turner [131] at Manchester University. Since the computational cost of the near-wall resolved LES is immense and the resources are limited, the third-order Runge Kutta time-integration method from Equation (3.2.7) and the third-order MUSCL extrapolation in space proposed by Zóltak and Drikakis [132] have been chosen for their superior stability characteristics when compared to the performance of other schemes in wall-bounded flows. Although higher order methods may lead to general improvements of the results, this is not self-evident in the near-wall region. The third-order MUSCL scheme therefore seems to be a good compromise between the accuracy and computational cost of the simulation. Furthermore, the characteristics-based Riemann solver of Eberle [32] has been employed. All results presented in the following sections have been non-dimensionalised with the free-stream velocity and the root chord length. In order to obtain converged statistical averages, it was sufficient to consider a time-window

equivalent to two flow-through cycles. Although the length of the time-window is not formally correlated to the extend of the computational domain, this information is presented here to put it into perspective. The total runtime including the flow development from an initial condition based on the coarse grid solution was 60,000 CPUh on IBM eServer p5 575 nodes with POWER5 1.5Ghz processors.

6.3 Flow Topology

The general topology of the flow around the swept wing geometry is illustrated in Figure 6.3 by instantaneous streamlines, slices of iso-vorticity contours and pressure coefficient distribution on the suction side of the wing. Similar to sharp-edged delta wings, the shear-layer emanating from the leading edges rolls up into a distinctive leading edge vortex system which grows and becomes less stable as it progresses towards the trailing edge. After about 50% of the root chord the LEVs start bending inboard and lift off the wing surface at an increasing rate. The main vortex cores are associated with the large regions of vorticity still visible near the trailing edge. However, as they are less coherent than near the leading edge and are influenced by the fully turbulent flow near the wing tips, they exhibit strong fluctuations and are not symmetrical anymore.

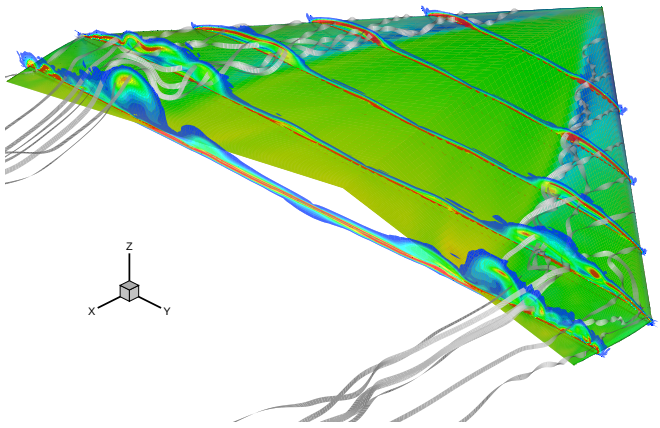

Figure 6.3: Instantaneous streamlines, slices of iso-vorticity contours and pressure coefficient distribution on the suction side of the wing.

The effect of the leading edge vortex system can also be felt on the wing surface as revealed by the pressure coefficient profiles taken at different locations along the half-wing span s, see Figure 6.4. A suction peak due to strong flow acceleration can be observed at the leading edge for all stations. As the LEV is close to the surface inboard of 50%s a second peak appears near the vortex core and the lift is enhanced. Because the vortex moves away from the wing surface its influence decreases further outboard and only a flat pressure profile remains on the suction side.

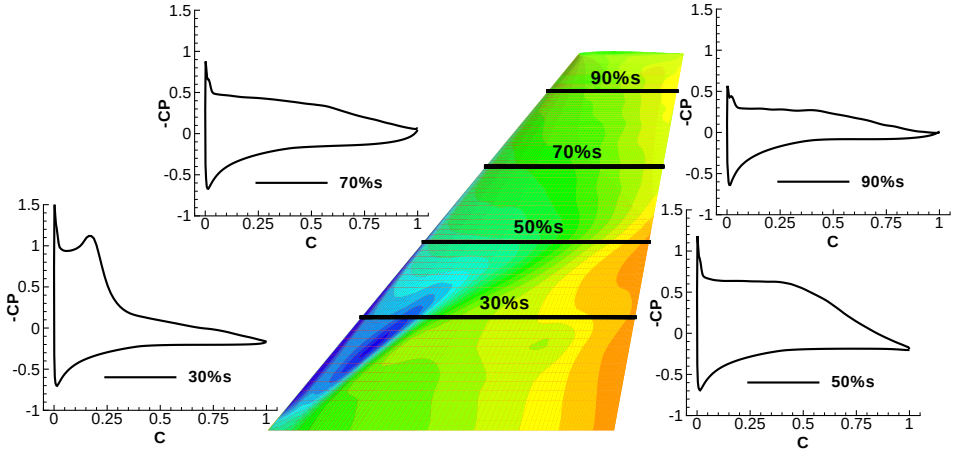

Figure 6.4: Colour contours of the pressure coefficient on the top surface and corresponding distributions on the suction and pressure side of the wing at different span-wise locations.

A comparison between time-averaged streamlines just above the wing surface obtained by the current simulation and the experimental oil-film visualisation of Zhang and Turner [131] is shown in Figure 6.5. The computational results in the right-hand half of the picture also include contours of the pressure coefficient on the suction side of the wing. Several common flow features, marked by dashed lines for the experimental data, can be observed in both parts of the picture. First, the reattachment of the leading edge vortex (VR) is well-defined in the computations inboard of approximately 30%s, but it starts to diffuse and bend towards the trailing edge as the LEV becomes less coherent. Close to the wing root, the reattachment line exhibits a similar angle for both the experiment and the simulation. However, the deviation from a straight line on the right-hand side appears to begin prior to the one observed on the left-hand side. This indicates premature non-linear spreading of the leading edge vortex in the simulation and leads to a larger extent near the trailing edge. Moreover, the two saddles SA1 and SA2 identify the existence of a secondary vortical region induced by the primary vortex along the leading edge which can also be observed in the experiment of Zhang and Turner [131], albeit this behaviour is less clear in the oil-film visualisation. The secondary vortical zone does collapse, however, as the influence of the main vortex decreases towards the wing tip due to the breakdown of its core. Although the streamlines are not following the core of the leading edge vortex, as they are close to the wing surface, breakdown is clearly indicated by the stagnation point (SP) between 50%s and 60%s. This phenomenon is associated with the interaction between the relatively stable LEV coming from the inboard section and the fully turbulent flow present closer to the wing tip — hence it is not to be mistaken with the natural breakdown observed in, for example, delta wing flows. It should also be noted that a stagnation point is not visible in the experiment and thus the LEV might be still be intact. Yet another feature of the flow is apparent closer to the wing tip. In the fully turbulent region, the effect of the LEV drives the fluid towards the wing tip where it meets the opposing outer flow between 80%s and 90%s. Thus, the characteristic saddle (SA) observed in both

experiment and simulation is formed.

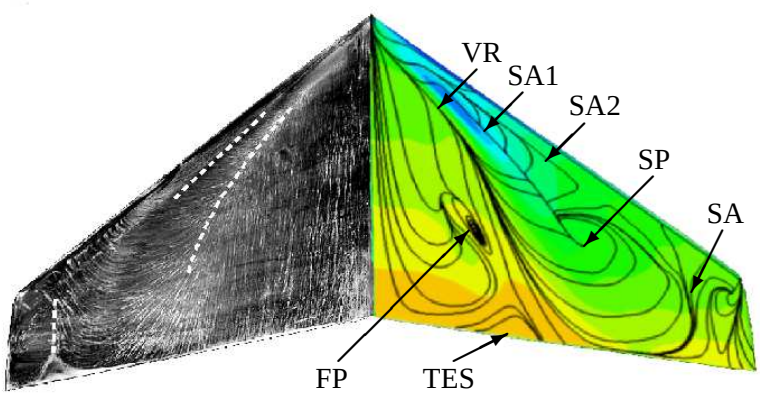

Figure 6.5: Time-averaged streamlines just above the wing surface and contours of pressure coefficient as predicted by the current simulation (right). Surface oil-film visualisation from experiment on the suction side of the wing (left).

In general, the numerically predicted streamline pattern is found to be in good agreement with the oil-film visualisation from the experiments of Zhang and Turner [131]. However, the skin friction lines inboard of the main vortex in the experimental picture are aligned in free-stream direction suggesting a simple dead-air region, whereas the simulation predicts a weakly detached region of fluid revolving around a focal point (FP). Furthermore, an incipiently separated zone near the trailing edge (TES) not existent in the experiment can be seen in the computation. This observation is not exclusive to the current results. Li and Leschziner [69] have reported a similar flow behaviour in their hybrid RANS/LES simulation of the same case.

The same authors could also confirm the LEV breakdown mechanism mentioned previously occurring at locations beyond 50% half-span. In order to illustrate the structural composition of the leading edge vortex as it progresses across the wing, colour contours of the Q-criterion as proposed by Jeong and Hussain [61] are shown in Figure 6.6. The two-dimensional slices are taken at constant span-wise positions ranging from 30%s to 90%s. A strong and coherent LEV close to the wing surface can be identified near the root at 30%s and the clearance between the vortex core and the wing surface increases further outboard, i.e. at 50%s. Additionally, the secondary vortical region is clearly visible for the first two locations. At 70% half-span, the LEV has become unstable and structural integrity can no longer be observed. Closer to the wing tip, see Figure 6.6(d), the shear layer emanating from the leading edge undergoes a roll-up similar to a Kelvin-Helmholtz mechanism and the resulting flow is akin at vortex shedding.

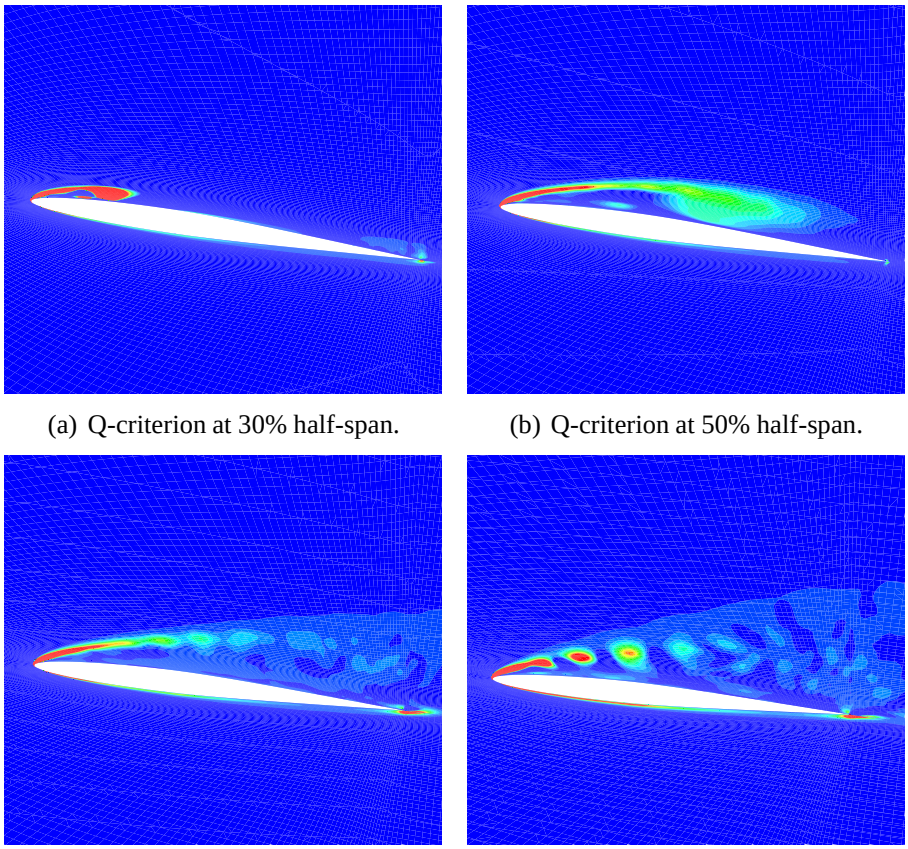

(a) Q-criterion at 30% half-span. (b) Q-criterion at 50% half-span.

(c) Q-criterion at 70% half-span. (d) Q-criterion at 90% half-span.

Figure 6.6: Contours of the Q-criterion as proposed by Jeong and Hussain [61] obtained in the current simulation at different locations along the span of the wing.

6.4 Velocity Profiles

A quantitative comparison between the flow field in the experiment of Zhang and Turner [131], the results obtained with the current ILES approach using high-resolution methods and the classical hybrid RANS/LES simulation of Li and Leschziner [69] on a large grid comprising 23.6M nodes has been performed. The time-averaged velocity and Reynolds stress profiles as a function of the distance from the wing have been calculated from the experimental data sets measured nearly normal to the surface at several positions along the half-span and the local chord by three-dimensional Laser Doppler Anemometry (LDA). This data was made available by Zhang and Turner [131], but has not been published at the time of writing. Details on the exact locations of the flow measurements and a full set of profiles can be found in Appendix F. Furthermore, it should be noted that the velocities and corresponding Reynolds stresses presented here have not been decomposed into tangential and normal directions to the wall, they rather represent the streamwise (u), span-wise (v) and azimuthal (w) portions.

Figure 6.7 shows the time-averaged velocity components for different locations along the local chord at 30% half-span. Near the leading edge, see Figure 6.7(a), all streamwise velocity profiles are in good agreement with minor differences regarding the position and magnitude of the peak. The current simulation using high-resolution methods, however, deviates from the experiment and the classical hybrid RANS/LES near the surface at 10% local chord. This behaviour is associated with the size and strength of the secondary vortical region. The span-wise component in Figure 6.7(b) features the characteristic cross-flow profile observed in swept wing aerodynamics. Close to the wing surface, the negative pressure gradient leads to an outflow towards the wing tip, whereas away from the surface the fluid tries to fill the gap opened by the higher displacement near the wing root and thus inflow occurs. Here, the magnitude of both minimum and maximum velocity are slightly under-predicted by ILES, but over-predicted by the hybrid simulation. Regarding the azimuthal component, Figure 6.7(c), the general shape of the profile dictated by the existence of the secondary vorticity and the position of the free shear layer is well captured in the current ILES simulation. However, the near-wall vortical region could not be predicted by the hybrid RANS/LES approach at this location and thus the simulation of Li and Leschziner [69] produces an entirely different result.

At 30% half-span and 50% local chord, see Figures 6.7(d) to 6.7(f), the profiles extracted from the experiment, the ILES and the hybrid RANS/LES simulations exhibit a fairly similar shape for all three velocity components. The current simulation predicts a slightly thinner boundary layer and a stronger cross-flow component near the surface than observed in the experiment and the classical RANS/LES. On the other hand, the hybrid approach under-predicts the magnitude of the azimuthal portion of the flow in Figure 6.7(f). It should be noted that this specific location is just upstream of the inboard separated zone. Hence, the influence of the detached flow on the velocity profiles here is only marginal. However, this situation does change when approaching the trailing edge as shown in Figures 6.7(g) to 6.7(i). Both simulations predict incipient flow separation at 90% local chord which is reflected clearly in the profiles of the streamwise and the azimuthal velocity. As the experimental oil-film visualisation does not suggest any detachment in this area, differences regarding the velocity profiles are expected. Yet, the cross-flow component predicted by ILES follows the experimental data surprisingly close which is most likely a coincidence.

The averaged velocity profiles for the mid-wing section at 50% half-span are presented in Figure 6.8. The secondary vortical region has developed considerably when compared to the inboard position, and the effect on the streamwise velocity component at 10% local chord is clearly visible in the experiment as well as both simulations, see Figure 6.8(a). The $< u >$ profiles near the leading edge compare well, with ILES predicting a small over-shoot near the surface, indicating stronger vorticity. The hybrid RANS/LES yields a peak velocity further from the wing than the experiment or the current simulation. The span-wise and the azimuthal velocity in Figures 6.8(b) and 6.8(b) obtained by both simulations are slightly over-predicted near the wall and they tend to peak at a lower magnitude away from the wing with respect to the experiment.

Most remarkably is the stronger displacement of fluid as reflected by a relatively high level of $< w >$ velocity in case of the ILES simulation.

The agreement is poor at the half-chord position in Figure 6.8. The velocity profiles are strongly affected by the premature non-linear growth of the leading edge vortex observed in the current simulation which manifests itself in large discrepancies between the ILES prediction and the experiment. The streamwise and the azimuthal velocities are decelerated in the vicinity of the wing, Figures 6.8(d) and 6.8(f), and the cross-stream component is amplified by the rotation of the large vortex, Figure 6.8(e). The classical RANS/LES, on the other hand, is closer to the experimental data. However, the kink in the $< u >$ profile measured in the experiment representing the influence of the leading edge vortex is not reproduced adequately. This suggests that the extent of the LEV in the streamwise direction is under-predicted in the hybrid RANS/LES, as has been confirmed by Li and Leschziner [70]. The same observations can be made for the location close to the trailing edge at 90% local chord, albeit the effect is diminished.

Further outboard, the experimental skin friction lines have revealed a non-linear spreading of the leading edge vortex similar to the current simulation. In this region of enhanced interaction with the fully separated flow regime towards the wing tip the accuracy of the ILES prediction appears to recover, see Figure 6.9. Near the leading edge, at 10% local chord, the streamwise velocity is already reversed and thus a thickening of the boundary can be observed in Figure 6.9(a). This effect is captured in the current simulation using high-resolution methods, whereas the hybrid RANS/LES approach fails. Consequently, both span-wise and azimuthal velocity profiles do not match the experimental data at this location and all components obtained by ILES are more accurate. Although the flow is not detached at positions closer to the trailing edge, it appears that the current results approach the experimental velocity profiles in Figures 6.9(d) to 6.9(f), but predictions with the classical RANS/LES are still hindered by the erroneous flow development near the leading edge. Despite being somewhat underestimated in terms of magnitude, the span-wise and, in particular, the streamwise flow component at 50% local chord from the ILES simulation follows the shape of the experimental profile closely. Only weak azimuthal motion can be observed, hence minor differences regarding the $< w >$ velocity in Figure 6.9(f) are deemed less important. At 90%s, i.e. Figures 6.9(g) to 6.9(i), the profiles exhibit a similar behaviour, except that the experimental span-wise velocity and the corresponding component obtained by ILES are in better agreement than at 50% local chord. Yet, this is not the case for $< w >$ near the wing surface.

The observations discussed previously for the span-wise location at 70%s become more pronounced in the fully separated and turbulent region close to the wing tip at 90% half-span as shown in Figure 6.10. It should be noted that the improvements are partly due to the finer grid clustering in this area, but the flow is certainly still highly under-resolved on the given computational mesh. On the one hand, the profiles of all velocity components as predicted by the current simulation are nearly identical to the experimental data at most chord-wise positions. Admittedly, small discrepancies regarding the inboard motion and the peak azimuthal velocity can be detected near

the leading edge at 10%s, see Figures 6.10(b) and 6.10(c), respectively. On the other hand, however, the classical RANS/LES approach completely suppresses separation because the RANS near-wall approximation cannot treat the massive flow detachment adequately. Thus, the results obtained in the hybrid RANS/LES simulation largely disagree with the experiment in the fully turbulent region.

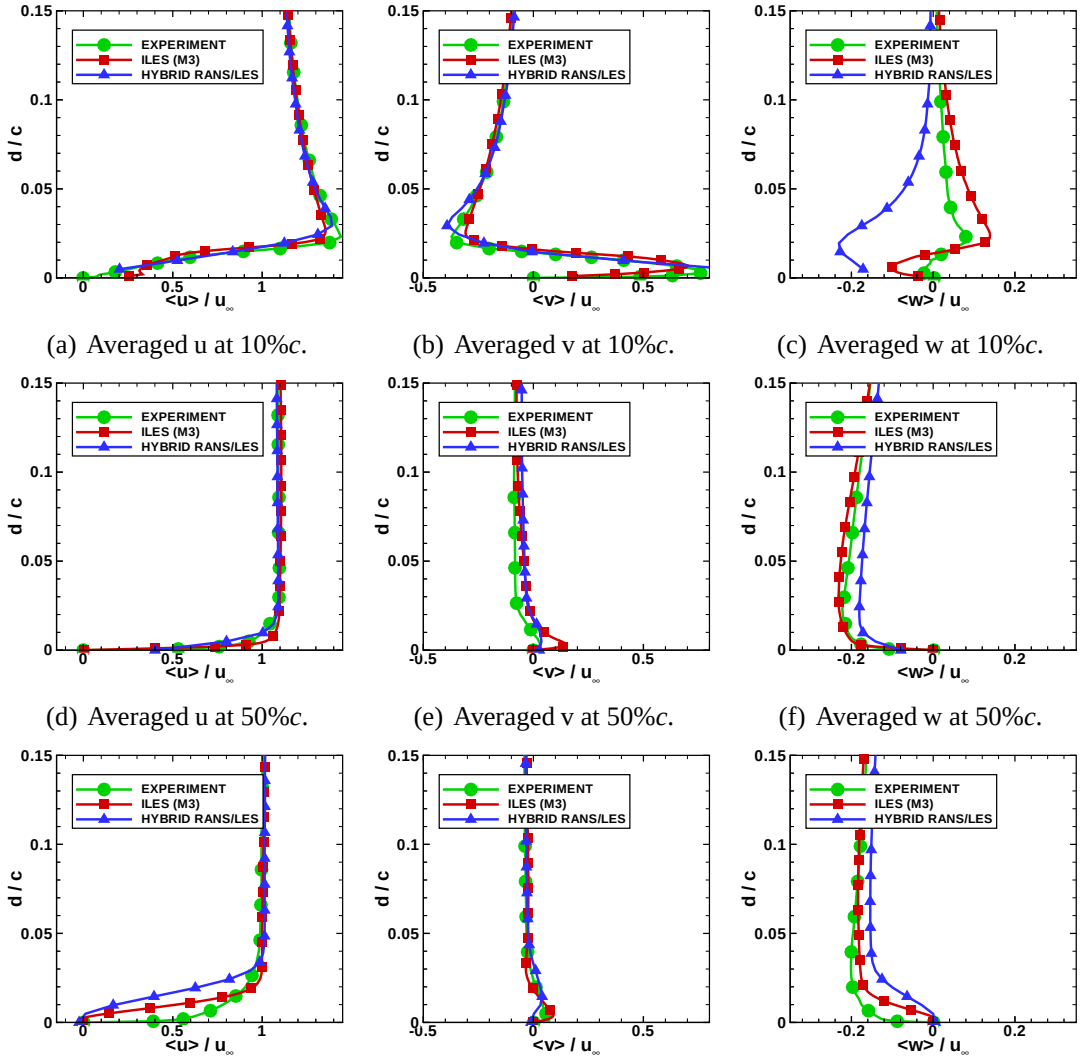

(a) Averaged u at 10%*c*. (b) Averaged v at 10%*c*. (c) Averaged w at 10%*c*.

(d) Averaged u at 50%*c*. (e) Averaged v at 50%*c*. (f) Averaged w at 50%*c*.

(g) Averaged u at 90%*c*. (h) Averaged v at 90%*c*. (i) Averaged w at 90%*c*.

Figure 6.7: Comparison between averaged velocity profiles from the experiments of Zhang and Turner [131], the results obtained with ILES and the hybrid RANS/LES of Li and Leschziner [69] for different locations along the local chord at 30% half-span.

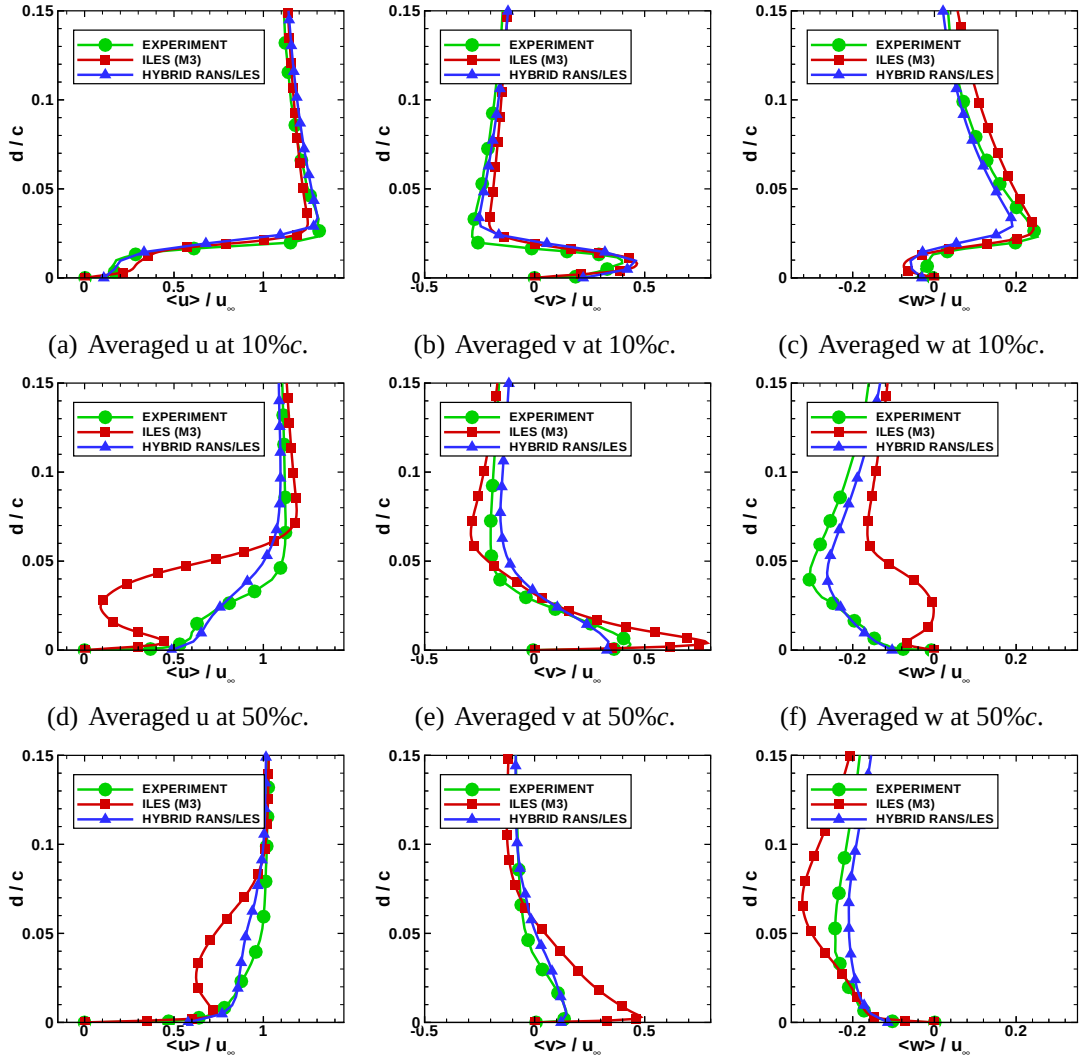

(a) Averaged u at 10%*c*. (b) Averaged v at 10%*c*. (c) Averaged w at 10%*c*.

(d) Averaged u at 50%*c*. (e) Averaged v at 50%*c*. (f) Averaged w at 50%*c*.

(g) Averaged u at 90%*c*. (h) Averaged v at 90%*c*. (i) Averaged w at 90%*c*.

Figure 6.8: Comparison between averaged velocity profiles from the experiments of Zhang and Turner [131], the results obtained with ILES and the hybrid RANS/LES of Li and Leschziner [69] for different locations along the local chord at 50% half-span.

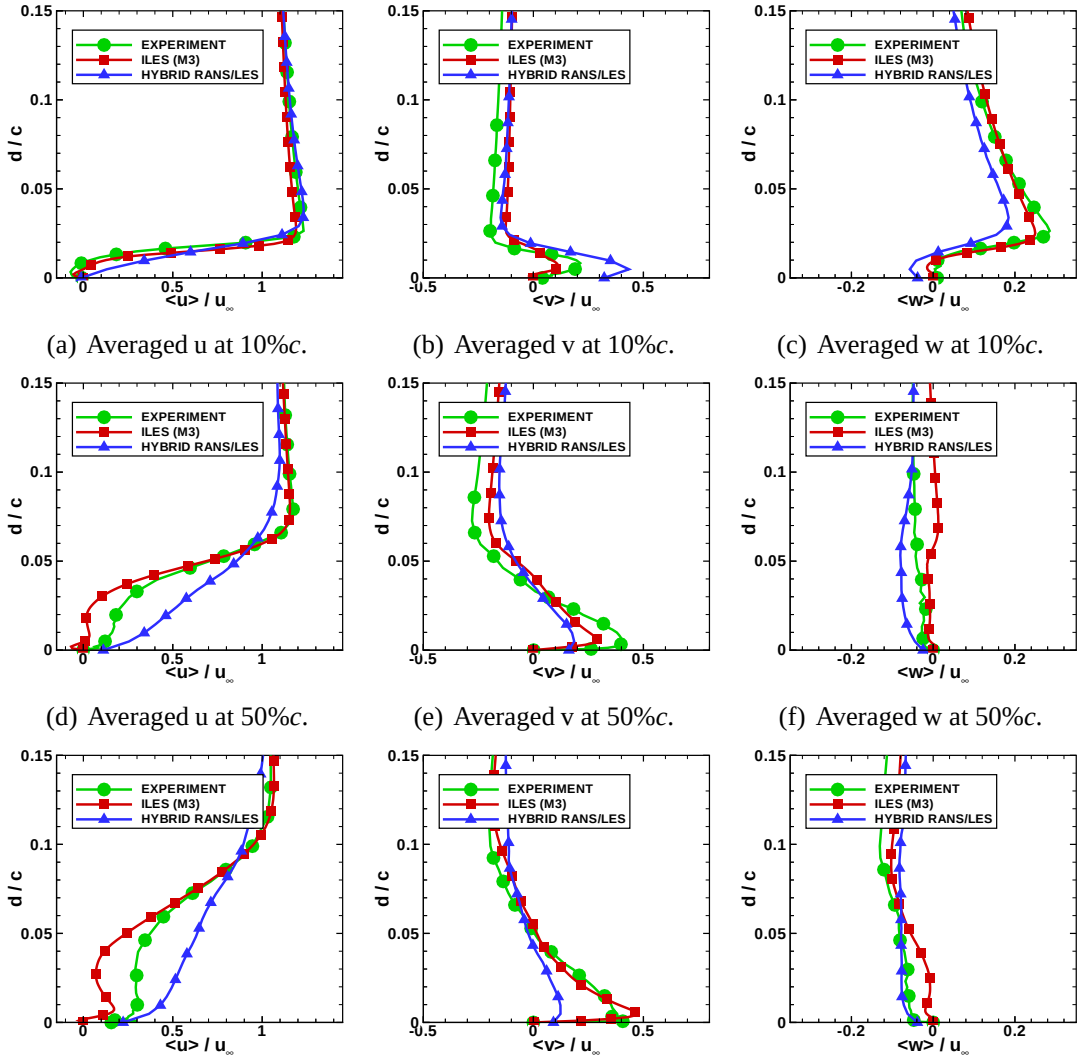

(a) Averaged u at 10%*c*. (b) Averaged v at 10%*c*. (c) Averaged w at 10%*c*.

(d) Averaged u at 50%*c*. (e) Averaged v at 50%*c*. (f) Averaged w at 50%*c*.

(g) Averaged u at 90%*c*. (h) Averaged v at 90%*c*. (i) Averaged w at 90%*c*.

Figure 6.9: Comparison between averaged velocity profiles from the experiments of Zhang and Turner [131], the results obtained with ILES and the hybrid RANS/LES of Li and Leschziner [69] for different locations along the local chord at 70% half-span.

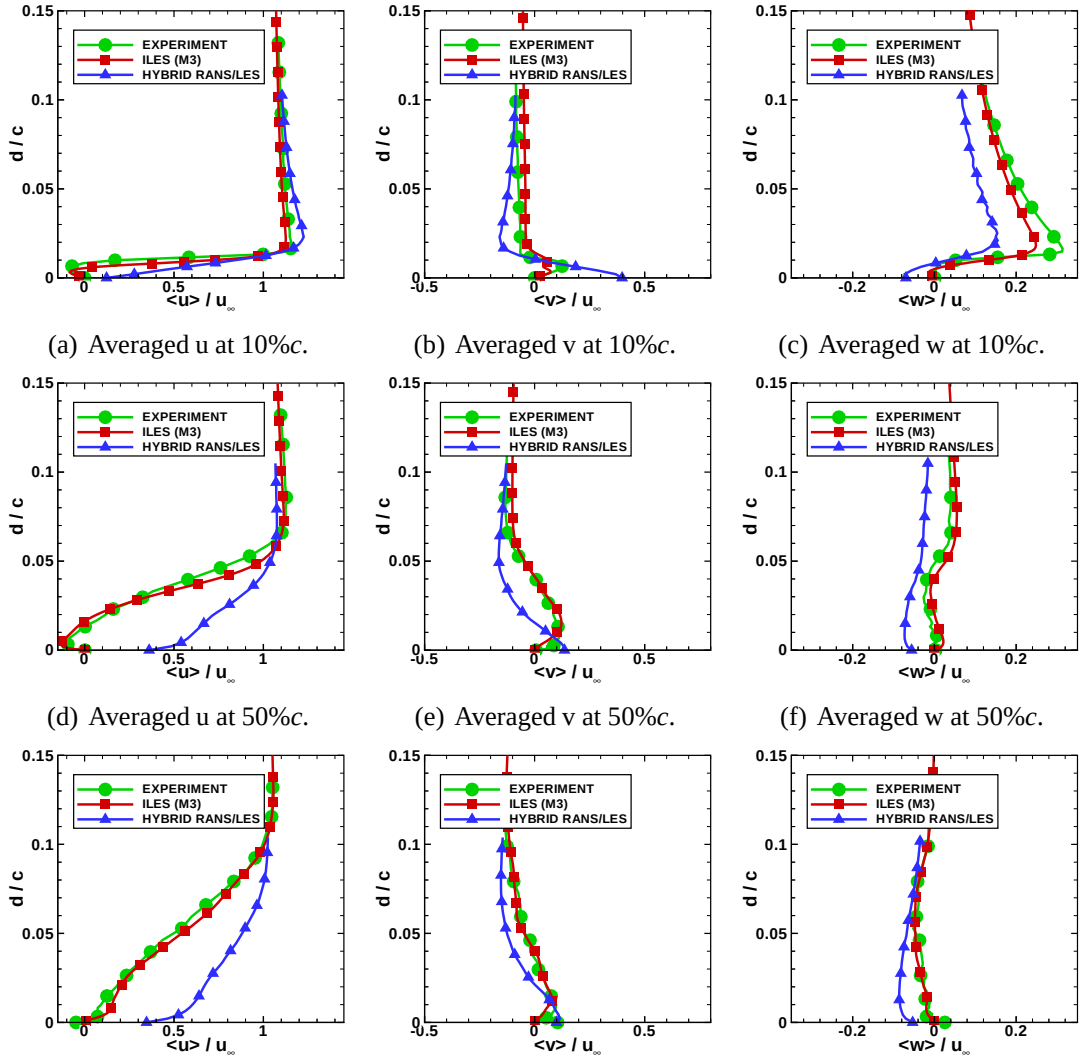

(a) Averaged u at 10%*c*. (b) Averaged v at 10%*c*. (c) Averaged w at 10%*c*.

(d) Averaged u at 50%*c*. (e) Averaged v at 50%*c*. (f) Averaged w at 50%*c*.

(g) Averaged u at 90%*c*. (h) Averaged v at 90%*c*. (i) Averaged w at 90%*c*.

Figure 6.10: Comparison between averaged velocity profiles from the experiments of Zhang and Turner [131], the results obtained with ILES and the hybrid RANS/LES of Li and Leschziner [69] for different locations along the local chord at 90% half-span.

6.5 Turbulent Energy Profiles

More insight into the flow structure can be gained by examining the turbulence levels at the characteristic positions discussed in the previous section. Here, the time-averaged total turbulent energy in normalised form defined by

$$\frac{<k>}{u_\infty^2} = \frac{0.5(\ <u'u'> + <v'v'> + <w'w'>\ )}{u_\infty^2} \tag{6.5.1}$$

is investigated. A more detailed picture presents itself when considering the individual Reynolds stress components at all locations measured in the experiment as given in Appendix F. However, it has been found that the information provided by the total turbulent energy at selected positions is sufficient to characterise the flow field.

Figure 6.11 shows the turbulent energy profiles from the experiments of Zhang and Turner [131], the results obtained in the current ILES using high-resolution methods and the hybrid RANS/LES of Li and Leschziner [69] for different locations along the local chord at 30% and 50% half-span. It can be noticed that the flow is essentially laminar at the inboard section, i.e. 30%s, over most of the chord, see Figures 6.11(c) and 6.11(e). Only the shear layer emanating from the leading edge produces a significant level of turbulence as observed in the experiment and the hybrid RANS/LES simulation at 10% local chord, Figure 6.11(a). Here, the hybrid RANS/LES overestimates the peak by about forty percent. ILES, on the other hand, strongly under-predicts the peak energy because the relatively thin layer cannot be represented adequately on the given grid with only four cells across the shear layer. Most notably, a second peak associated with the secondary vortical region can be detected closer to the wing surface in the profile predicted by the ILES approach which, in line with the previous observations, does not appear in the experimental or the classical RANS/LES data.

At the mid-span position 50%s, shown in Figures 6.11(b) to 6.11(f), a similar scenario is presented near the leading edge. The turbulence level in the ILES simulation is still too low when compared with experiment. However, the effect of the secondary vortical region is now clearly visible in all three profiles in Figure 6.11(b). A less favourable impression is left by the hybrid RANS/LES at this location. It seems that the existence of the secondary vortical zone influences the shear layer and alters its character — hence the peak energy is suddenly underestimated by a factor of approximately five. As can be seen at the mid-chord position, Figure 6.11(d), the behaviour of the free shear layer has serious consequences for the downstream development of the flow. In the current simulation using high-resolution methods, the onset of LEV roll-up can be detected just after 50%c and thus the shear layer is still intact at this location which is reflected by the peak turbulent energy away from the wing. A result of the delayed leading edge vortex formation is an increased growth rate due to the diminished influence of the wall, leading to a seemingly premature non-linear spreading of the vortex. Two additional peaks, albeit smaller, can be observed in the profile from the ILES simulation. Close to the solid surface, the strong cross-flow component, caused by the large extent of the leading edge vortex, also yields an increase in turbulent energy.

Furthermore, the influence of the LEV can be felt between the wing and the shear layer as implied by the second peak in Figure 6.11(d). Both the profiles obtained in the experiment and the hybrid RANS simulation suggest the presence of a developed leading edge vortex at 50%c and the level of turbulence decreases towards the trailing edge. Here, at 90%c, the full profile predicted by ILES indicates a stronger influence of the LEV when compared with the experiment and the classical RANS/LES in Figure 6.11(f).

Consistent with the previous comment on grid resolution in the shear layer, a slightly thicker shear layer leads to stronger velocity fluctuations as observed in the current simulation near the leading edge for the 70% half-span section, see Figure 6.12(a). However, the peak turbulent energy is still under-predicted by the ILES approach and the clearance between wing surface and the shear layer appears to low. Although the reversed flow situation close to the leading edge is not captured by the hybrid RANS/LES, the maximum turbulent energy recovers to a value closer to the experiment. It should be noted that the profile obtained by the classical RANS/LES does not start from zero at the wall which is clearly unphysical and raises doubts about the reliability of the data. At the 70% half-span station, the main vortex core has turned towards the trailing edge and undergone a breakup mechanism. Therefore, the shear layer does not roll up. In fact, it still affects the turbulent energy profiles at 50% local chord as indicated by the peaks in both the experimental and ILES observed in Figure 6.12(c), but not the hybrid RANS/LES results. However, the current simulation over-predicts the cross-flow fluctuations near the wing surface already observed at the half-chord position for 50%s. Close to the trailing edge, the level of turbulence diminishes for the classical RANS/LES, whereas it increases in the ILES simulation due to enhanced mixing caused by the large predicted vortex.

A similar picture to 70% half-span presents itself for the sections at 90%s in Figures 6.12(b) to 6.12(f). Here, the position of the free shear layer emanating from the leading edge is in better agreement with the experiment than at the inboard station, but the peak magnitude is underestimated again. Moreover, the turbulent energy profiles obtained in the current simulation using high-resolution methods match the shape of the experimental results closely further downstream and they are virtually identical in the vicinity of the trailing edge. As anticipated, however, the hybrid RANS/LES approach fails to predict the flow in this fully turbulent region dominated by massive separation.

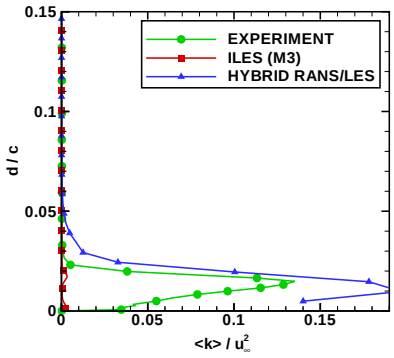

(a) Turbulent energy at 30%s and 10%c.

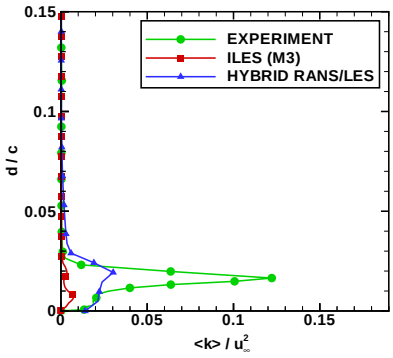

(b) Turbulent energy at 50%s and 10%c.

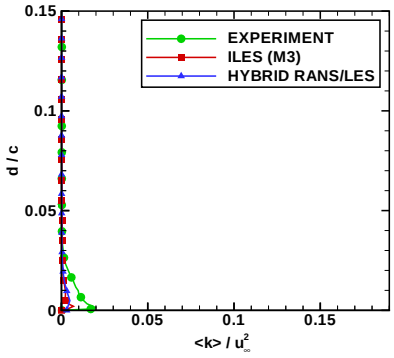

(c) Turbulent energy at 30%s and 50%c.

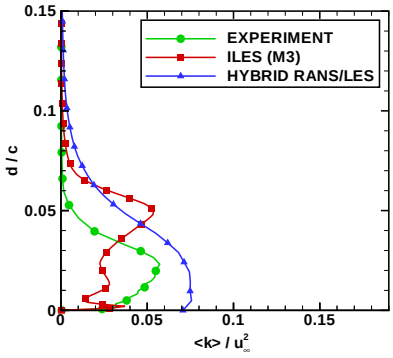

(d) Turbulent energy at 50%s and 50%c.

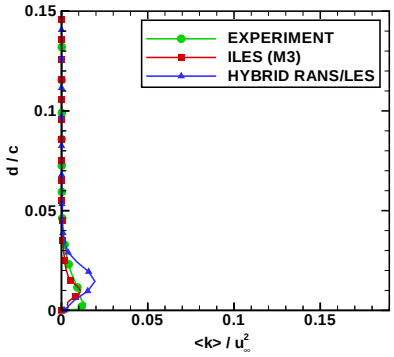

(e) Turbulent energy at 30%s and 90%c.

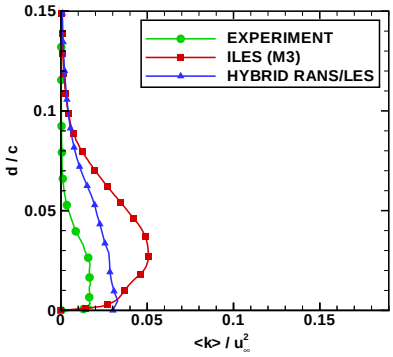

(f) Turbulent energy at 50%s and 90%c.

Figure 6.11: Comparison between averaged turbulent energy profiles from the experiments of Zhang and Turner [131], the results obtained with ILES and the hybrid RANS/LES of Li and Leschziner [69] for different locations along the local chord at 30% and 50% half-span.

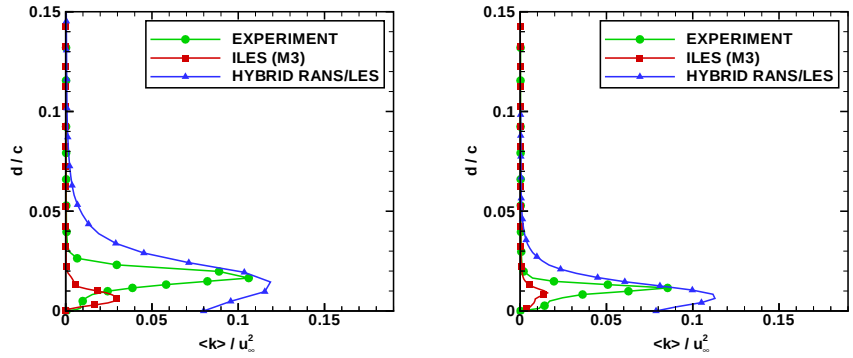

(a) Turbulent energy at 70%s and 10%c. (b) Turbulent energy at 90%s and 10%c.

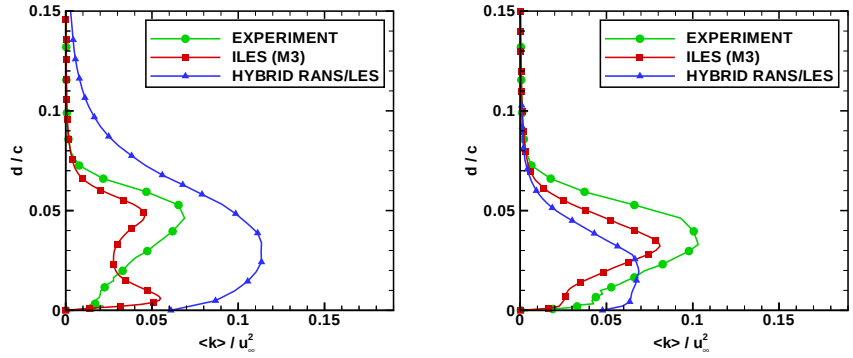

(c) Turbulent energy at 70%s and 50%c. (d) Turbulent energy at 90%s and 50%c.

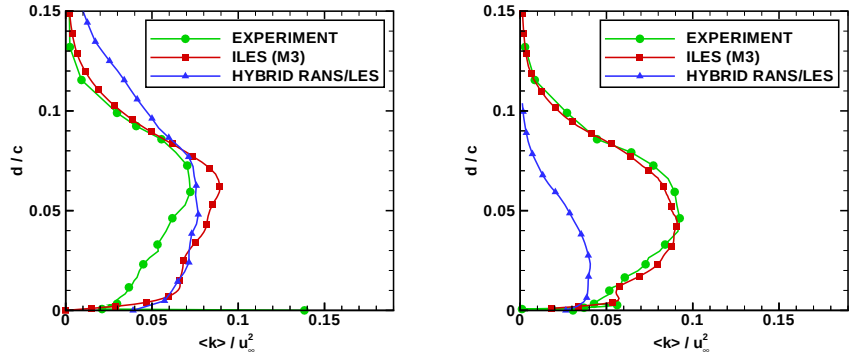

(e) Turbulent energy at 70%s and 90%c. (f) Turbulent energy at 90%s and 90%c.

Figure 6.12: Comparison between averaged turbulent energy profiles from the experiments of Zhang and Turner [131], the results obtained with ILES and the hybrid RANS/LES of Li and Leschziner [69] for different locations along the local chord at 70% and 90% half-span.

6.6 Summary

The numerical approach of Implicit Large-Eddy Simulation using high-resolution methods has been applied to the external flow around a swept wing geometry of practical aeronautical interest. This highly complex problem combines large-scale separation with substantial regions of attached flow where the realistic representation of near-wall effects are of paramount importance.

The free-stream approaching the inclined wing is quickly accelerated and detaches from the leading edge to form a free shear layer that subsequently rolls up into the characteristic leading edge vortex also observed in sharp-edged delta wing flows. Inboard of the vortex reattachment line, the conditions are essentially laminar, and beneath the LEV the flow is prone to produce secondary vorticity. As it develops in the span-wise direction, the main vortex bends towards the trailing edge and becomes more unstable. This leads to a mechanism akin to breakdown, where the vortex loses some of its coherence, and the interaction with the fully separated, turbulent flow region near the wing tip, favoured by the specifics of the twisted geometry, gains importance.

The conditions for the MSTTAR swept wing have been chosen to allow nearly wall-resolved simulations that can be assessed using the experimental LDA data and oil-film visualisations of the skin friction lines on the solid surface provided by Zhang and Turner [131]. Furthermore, the classical RANS/LES using a RANS-type approximation in the near-wall region performed by Li and Leschziner [69] are included in the comparison of flow and turbulence characteristics.

It has been found that both simulations predict an area of mildly reversed flow near the wing root and leading edge vortex breakdown beyond approximately 50% half-span whereas the experiment suggests an inboard dead-air region and vortex breakdown cannot be clearly identified. In other respects, the large-scale flow features are reasonably well represented by the two numerical approaches. Here, the hybrid RANS/LES appears to be more accurate than ILES in areas of attached flow but fails completely in the fully turbulent region closer to the wing tip because the near-wall approximation is not adequate for massively separated flow.

It should be highlighted that the computational grids employed in the two simulations differ substantially. For the hybrid approach, 23.6M nodes have been distributed using a H-H-type topology of similar extent to the C-O-type mesh presented for the current simulation which has only half the number of nodes. Furthermore, they are distinguished by the specific requirements in the vicinity of the wing surface. In the ILES simulation, the near-wall region is nearly resolved with z+ ranging from 1 to 5 whereas the node clustering in hybrid RANS/LES grid yields characteristic values between 20 and 40. Therefore, the near-wall phenomena are captured more accurately in the current simulation but the quality of the prediction in the free shear layer deteriorates. This has a severe impact on the development of the leading edge vortex as exemplified for the section at 50% half-span. However, when the LEV is not present and the flow is fully turbulent, i.e closer to the wing tip, the influence of the shear layer is diminished

and the statistical data obtained by ILES is in very good agreement with the experiment. In general, this investigation has demonstrated that high-resolution methods can be applied to complex, separated flows without any modification if the near-wall phenomena are nearly resolved on the computational grid employed.

CHAPTER 7

Conclusions and Outlook

The work in this thesis covered a range of issues pertinent to the numerical prediction of low-speed separated flows using high-resolution methods in the context of Implicit Large-Eddy Simulations. The main findings and lessons learnt will be presented in the following section. Moreover, future steps for gaining deeper insight into this complex topic are suggested that will, hopefully, aid the quest for high-fidelity simulations of reasonable computational cost in realistic engineering applications.

7.1 Conclusions

In simulations of massively separated flows, it is necessary to capture various stages in the development of the flow field after separation has occurred. Here, the behaviour of a third-order MUSCL, a fifth-order MUSCL and a ninth-order WENO algorithm have been assessed in combination with several Runge Kutta time-integration methods for predicting the evolution of the Taylor-Green Vortex. The Taylor-Green Vortex is probably the simplest model yielding an isolated representation of the linear, non-linear and fully turbulent development of an inviscid instability mechanism similar to the one observed in the characteristic free shear layer appearing in separated flows.

It has been demonstrated that the errors due to the specifics of the time-integration method can be neglected in comparison with the effects of spatial accuracy on the results. The inviscid instability mechanism is captured by all high-resolution methods and the onset of the stage dominated by vortex dynamics is in good agreement with available DNS data and other simulations. However, observations made on different grid sizes revealed that in general the computations using a lower order method become under-resolved prior to the ones with a higher order scheme. Thus, the resolving power of the numerical method is increasing with its order of accuracy. This conclusion is also supported by the fact that the higher order methods produce less numerical dissipation when compared to lower order methods on identical grids. On the other hand, it should be noted that higher order methods are more sensitive to small perturbations in the flow and thus they have to be applied with care. In case of the Taylor Green Vortex, the associated breaking of the symmetric initial condition leads to a more re-

alistic evolution of the flow field on coarser grids, but this might not hold for practical problems of engineering interest. Furthermore, a detailed comparison of the computational cost for the three high-resolution methods has shown that the savings due to the increased resolving power, i.e. reduction of grid nodes, outweighs the effect of an increasing complexity of the numerical scheme, i.e. more floating point operations, for the Taylor-Green Vortex. Hence, higher order methods are more efficient than lower order methods in wall-free, turbulent flows.

The next test case that has been considered in this thesis addressed the fundamental separation process in wall-bounded flows. Here, a statistically two-dimensional channel flow with hill-type constrictions has been employed to investigate the performance of the three high-resolution algorithms mentioned previously with respect to detachment from a gently curved surface in grid under-resolved conditions. The hill flow essentially combines the importance of near-wall phenomena leading to separation with the subsequent development of the free shear layer in a relatively simple geometry.

A comparison with classical, wall under-resolved LES uncovered that high-resolution algorithms can yield a more accurate prediction of the separation location than standard methods when both are applied in conjunction with no-slip conditions at the surface and the grid is very coarse. Different effects of local grid refinement on the results as obtained in the current simulations and the classical, second-order accurate LES have been observed. The prediction with standard LES and no-slip conditions improves considerably when the nodes are clustered in streamwise direction, whereas the high-resolution methods appear to prefer a predominantly wall-normal refinement. Because the higher order schemes are more sensitive to small disturbances they are also more likely to predict flow detachment prior to lower order methods on identical grids. Classical wall-modelled LES consistently outperforms the ILES methods regarding the separation location when taking wall-resolved classical LES as a reference. However, wall functions are also sensitive to the placement of the wall-adjacent grid nodes and still require them to lie within the viscous sublayer. In the free shear layer, higher order methods lead to seemingly premature breakdown, reflected by shorter separation bubbles, and the turbulence mixing with the core flow is increased compared to lower order methods and the reference LES. However, the quality of the reference solution in this particular region obtained by classical wall-resolved LES may be questionable. Thus, no clear conclusion can be drawn here for the behaviour of the different ILES techniques. The same holds for the reattachment location and post-reattachment zone because the flow development is highly dependent on its upstream history.

Finally, the third-order accurate MUSCL scheme has been employed in a nearly wall-resolved ILES simulation of the flow around a fully three-dimensional swept wing geometry. This case has been specifically designed to test numerical methods in an applied flow problem of practical aeronautical interest. The challenge here includes the prediction of transition leading to turbulence and separation, adaptive control of numerical viscosity, and generation of suitable grids. In order to assess the fidelity of the current simulation, experimental data and the results obtained by a classical hybrid RANS/LES simulation have been used as reference.

It has been found that the high-resolution method is able to capture the large-scale flow features such as roll-up of the free shear layer into a leading edge vortex and a fully separated, turbulent region in the vicinity of the wing tip. On closer examination, the coarseness of the current grid in the free shear layer leads to a delay of the leading edge vortex roll-up and associated increased vortex growth in the ILES simulation when compared with the hybrid RANS/LES approach and, in particular, with the experiment. Thus, the boundary layer profiles obtained by ILES and experiment differ in regions dominated by the structure of the leading edge vortex. In the massively separated and turbulent zone near the wing tip, however, the character of the boundary layer gains importance and the statistics gathered from the current simulation using a high-resolution method are virtually identical to experimental results, whereas the near-wall approximation employed in the hybrid RANS/LES computation fails completely. The particular strength of ILES is highlighted by the fact that the hybrid RANS/LES computation employed nearly twice as many grid nodes than the current simulation using a high-resolution method. On the other hand, both simulations predict an area of weakly reversed flow close the root of the wing which disagrees with the experiment.

In the past, Implicit Large-Eddy Simulations have been used to simulate a broad variety of complex flows, e.g. flows that are dominated by vorticity leading to turbulence, flows featuring shock waves and turbulence, and the mixing of materials. However, many classical test cases for these methods are not bounded by walls or feature geometrically well-defined separation lines, e.g. decaying isotropic turbulence, free jets and cavity flows. This gave cause to fervid discussions in the CFD community about the applicability of the ILES approach to complex, wall-bounded flows of practical engineering interest. With the work in this thesis, it has been clearly demonstrated that Implicit Large Eddy Simulations using high-resolution methods are indeed capable of realistically predicting just this type of flow without the need for any adjustment.

7.2 Future Work

In retrospect, several lessons have been learnt and more work needs to be done, primarily in order to control the computational cost of wall-bounded, turbulent flow simulations featuring separation from smooth surfaces. The use of higher order methods allows for significant reduction of grid nodes in the fully turbulent regime. In the near-wall region, however, they tap their full potential only if the boundary layer is nearly resolved in wall-normal direction and the grid savings in the tangential direction are scant. Therefore, the main focus in the future should be the development of a reliable wall-modelling strategy that covers both attached and detached flow conditions.

Regarding the development of free shear layers, more fundamental studies are necessary to determine the exact requirements of different numerical methods for producing realistic results. It has been shown that the break up and subsequent turbulent mixing strongly depends on the order of the scheme employed and the grid resolution available. A similar effect can be expected for the roll-up of the leading edge vortex

observed in the swept wing flow. Here, grid convergence studies and comparisons with experimental data for relatively simple geometries are desirable. In the context of internal flows, an investigation of flow over a backward facing step could offer valuable insight and, with respect to external flows, an in-depth study of sharp-edged delta wings may be proposed.

Bibliography

[1] G. P. Almeida, D. F. G. Durão, and M. V. Heitor. Wake Flows Behind Two-Dimensional Model Hills. *Experimental Thermal and Fluid Science*, 7:87–101, 1993.

[2] J. D. Anderson. *Fundamentals of Aerodynamics*. Aerospace Science. McGraw-Hill, second edition, 1991.

[3] J. D. Anderson. *Computational Fluid Dynamics: The Basics with Application*. McGraw-Hill, New York, 1995.

[4] V. Armenio and U. Piomelli. A Lagrangian Mixed Subgrid-Scale Model in Generalized Coordinates. *Flow, Turbulence and Combustion*, 65:51–81, 2000.

[5] E. Balaras and C. Benocci. Subgrid-scale models in finite-difference simulations of complex wall-bounded flows. CP 551, AGARD, 1994.

[6] D. S. Balsara and C.-W. Shu. Monotonicity preserving weighted essentially non-oscillatory schemes with increasingly high order of accuracy. *Journal of Computational Physics*, 160:405–452, 2000.

[7] J. Bardina, J. H. Ferziger, and W. C. Reynolds. Improved Subgrid Scale Models for Large Eddy Simulation. In *13th AIAA Fluid & Plasma Dynamics Conference*, number AIAA-1980-1357, July 1980.

[8] R. E. Bensow, M. G. Larson, and P. Vesterlund. Vorticity-strain residual-based turbulence modelling of the Taylor-Green vortex. *International Journal for Numerical Methods in Fluids*, 54:745–756, 2007.

[9] J. P. Boris. On large eddy simulation using subgrid turbulence models. In J. L. Lumley, editor, *Whither Turbulence? Turbulence at the Crossroads*, Lecture Notes in Physics, pages 344–353. Berlin Springer Verlag, 1990.

[10] J. P. Boris, F. F. Grinstein, E. S. Oran, and R. L. Kolbe. New insights into large eddy simulation. *Fluid Dynamics Research*, 10:199–228, 1992.

[11] M. E. Brachet. Direct simulation of three-dimensional tubulence in the Taylor-Green vortex. *Fluid Dynamics Research*, 8:1–8, 1991.

[12] M. E. Brachet, D. I. Meiron, S. A. Orszag, Nickel B. G., R. H. Morf, and U. Frisch. Small-scale structure of the Taylor-Green vortex. *Journal of Fluid Mechanics*, 130:411–452, 1983.

[13] F. J. Brandsma, J. C. Kok, H. S. Doi, and A. Elsenaar. Leading edge vortex flow computations and comparison with DNW-HST wind tunnel data. Technical Report NLR-TP-2001-238, National Aerospace Laboratory NLR, 2001.

[14] M Breuer. New reference data for the hill flow test case. online, 2005. URL `http://www.hy.bv.tum.de/DFG-CNRS/`.

[15] M. Breuer, B. Kniazev, and M. Abel. Development of wall models for LES of separated flows using statistical evaluations. *Computers & Fluids*, 36:817–837, 2007.

[16] J. Buckles, T. J. Hanratty, and R. J. Adrian. Turbulent flow over large amplitude wavy surfaces. *Journal of Fluid Mechanics*, 140:27–44, 1984.

[17] I. P. Castro and E. Epik. Boundary layer development after a separated region. *Journal of Fluid Mechanics*, 374:91–116, 1998.

[18] C. Comte-Bellot and S. Corrsin. The use of a contraction to improve the isotropy of grid generated turbulence. *Journal of Fluid Mechanics*, 25:657–682, 1966.

[19] R. M. Cummings, J. R. Forsythe, S. A. Morton, and K. D. Squires. Computational challenges in high angle of attack flow prediction. *Progress in Aerospace Sciences*, 39:369–384, 2003.

[20] S. Dahlström and L. Davidson. Large eddy simulation applied to a high-Reynolds flow around an airfoil close to stall. In *41st AIAA Aerospace Sciences Meeting and Exhibit*, number AIAA-2003-0776, January 2003.

[21] P. A. Davidson. *Turbulence – An Introduction for Scientists and Engineers*. Oxford University Press, 2004.

[22] V. DeAngelis, P. Lombardi, and S. Banerjee. Direct numerical simulation of turbulent flow over a wavy wall. *Physics of Fluids*, 9:2429–2442, 1997.

[23] J. M. Delery. Aspects of vortex breakdown. *Progress in Aerospace Sciences*, 30:1–59, 1994.

[24] D. Drikakis. *Godunov Methods: Theory and Applications*, chapter Uniformaly high-order methods for unsteady incompressible flows, pages 263–283. Kluwer Academic Publishers, 2001.

[25] D. Drikakis. Advances in turbulent flow computations using high-resolution methods. *Progress in Aerospace Sciences*, 39:405–424, 2003.

[26] D. Drikakis and F. Durst. Investigation of flux formulae in shock wave turbulent boundary layer interaction. *International Journal for Numerical Methods in Fluids*, 18:385–413, 1994.

[27] D. Drikakis and W. J. Rider. *High-Resolution Methods for Incompressible and Low-Speed Flows*. Springer, 2004.

[28] D. Drikakis, P. A. Govatsos, and D. E. Papatonis. A characteristic-based method for incompressible flows. *International Journal for Numerical Methods in Fluids*, 19:667–685, 1994.

[29] D. Drikakis, C. Fureby, F. F. Grinstein, M. Hahn, and D. Youngs. LES of Transition to Turbulence in the Taylor Green Vortex. In E. Lamballais, R. Friedrich, B. J. Geurts, and O. Métais, editors, *Direct and Large-Eddy Simulation VI*, Ercoftac, pages 159–166. Springer Netherlands, 2006.

[30] D. Drikakis, C. Fureby, F. F. Grinstein, and D. Youngs. Simulation of transition and turbulence decay in the Taylor-Green vortex. *Journal of Turbulence*, 8(20): 1–12, 2007.

[31] F. Ducros, F. Nicoud, and T. Poinsot. Wall-adapting local eddy-viscosity model for simulations in complex geometries. In M. J. Baines, editor, *Numerical Methods for Fluid Dynamics VI*, pages 293–299. Oxford University Computing Laboratory, 1998.

[32] A. Eberle. Characteristic flux averaging approach to the solution of Euler's equations. Computational fluid dynamics, VKI Lecture Series, 1987.

[33] ERCOFTAC. Periodic flow over a 2-D hill. online, 2002. URL `http://www.ercoftac.nl/workshop10/case9.2/geom9.2.html`.

[34] J. H. Ferziger and M. Perić. *Computational Methods for Fluid Dynamics*. Springer, 3rd edition, 2002.

[35] J. Fröhlich, C. P. Mellen, W. Rodi, L. Temmerman, and M. A. Leschziner. Highly resolved large-eddy simulation of separated flow in a channel with streamwise periodic constrictions. *Journal of Fluid Mechanics*, 526:19–66, 2005.

[36] C. Fureby and F. F. Grinstein. Monotonically Integrated Large Eddy Simulation of Free Shear Flows. *AIAA Journal*, 37(5):544–556, May 1999.

[37] C. Fureby and F. F. Grinstein. Large eddy simulation of high Reynolds number free and wall bounded flows. *Journal of Computational Physics*, 181:68–97, 2002.

[38] C. Fureby and G. Tabor. Mathematical and Physical Constraints on Large-Eddy Simulations. *Theoretical and Computational Fluid Dynamics*, 9:85–102, 1997.

[39] M. Germano, U. Piomelli, P. Moin, and W. H. Cabot. A dynamic subgrid-scale eddy viscosity model. *Physics of Fluids A*, 3(7):1760–1765, July 1991.

[40] S. Ghosal. An Analysis of Numerical Errors in Large-Eddy Simulations of Turbulence. *Journal of Computational Physics*, 125:187–206, 1996.

[41] S. Ghosal and P. Moin. The Basic Equations for the Large Eddy Simulation of Turbulent Flows in Complex Geometry. *Journal of Computational Physics*, 118:24–37, 1995.

[42] S. K. Godunov. Finite Difference Method for Numerical Computation of Discontinuous Solutions of the Equations of Fluid Dynamics. *Matematicheski Sbornik*, 47:271–306, 1959.

[43] R. E. Gordnier. Numerical Simulation of a 65-Degree Delta-Wing Flowfield. *Journal of Aircraft*, 34(4):492–499, July-August 1997.

[44] R. E. Gordnier and M. R. Visbal. Compact Difference Scheme Applied to Simulation of Low-Sweep Delta Wing Flow. *AIAA Journal*, 43(8):1744–1752, August 2005.

[45] R. E. Gordnier and M. R. Visbal. High-Order Simulation of Low Sweep Delta Wing Flows Using ILES and Hybrid RANS/ILES Models. In *44th AIAA Aerospace Sciences Meeting and Exhibit*, number AIAA-2006-0504, January 2006.

[46] F. F. Grinstein. private communication. Los Alamos National Laboratory, USA.

[47] F. F. Grinstein and C. R. DeVore. Dynamics of coherent structures and transition to turbulence in free square jets. *Physics of Fluids*, 8(5):1237–1251, May 1996.

[48] F. F. Grinstein and C. Fureby. Recent Progress on MILES for High Reynolds Number Flows. *Journal of Fluids Engineering*, 124:848–861, December 2002.

[49] F. F. Grinstein and K. Kailasanath. Chemical energy release and dynamics of transitional, reactive shear flows. *Physics of Fluids A*, 4(10):2207–2221, October 1992.

[50] F. F. Grinstein, E. S. Oran, and J. P. Boris. Pressure field, feedback, and global instabilities of subsonic spatially developing mixing layers. *Physics of Fluids A*, 3:2401–2409, 1991.

[51] F. F. Grinstein, L. G. Margolin, and W. J. Rider, editors. *Implicit Large Eddy-Simulation*. Cambridge University Press, 2007.

[52] I. Gursul. Review of Unsteady Vortex Flows over Slender Delta Wings. *Journal of Aircraft*, 42(2):299–319, March-April 2005.

[53] I. Gursul, R. Gordnier, and M. Visbal. Unsteady aerodynamics of nonslender delta wings. *Progress in Aerospace Sciences*, 41:515–557, 2005.

[54] A. Harten. High Resolution Schemes for Hyperbolic Conservation. *Journal of Computational Physics*, 49:357–393, 1983.

[55] A. Harten, B. Engquist, S. Osher, and S. R. Chakravarthy. Uniformly high order accurate essentially non-oscillatory schemes, III. *Journal of Computational Physics*, 71:231–303, 1987.

[56] D. S. Henn and R. I. Sykes. Large-eddy simulation of flow over wavy surfaces. *Journal of Fluid Mechanics*, 383:75–112, 1999.

[57] S. Hickel, N. A. Adams, and J. A. Domaradzki. An adaptive local deconvolution method for implicit LES. *Journal of Computational Phyics*, 213:413–436, 2006.

[58] J. O. Hinze. *Turbulence*. McGraw-Hill, 1975.

[59] J. D. Hudson, L. Dykhno, and T. J. Hanratty. Turbulence production in flow over a wavy wall. *Experiments in Fluids*, 20:257–265, 1996.

[60] Y. J. Jang, M. A. Leschziner, K. Abe, and L. Temmerman. Investigation of Anisotropy-Resolving Turbulence Models by Reference to Highly-Resolved LES Data for Separated Flows. *Flow, Turbulence and Combustion*, 69:161–203, 2002.

[61] J. Jeong and F. Hussain. On the identification of a vortex. *Journal of Fluid Mechanics*, 285:69–94, 1995.

[62] G.-S. Jiang and C.-W. Shu. Efficient Implementation of Weighted ENO Schemes. *Journal of Computational Physics*, 126:202–228, 1996.

[63] K. H. Kim and C. Kim. Accurate, efficient and monotonic numerical methods for multi-dimensional compressible flows. Part II: Multi-dimensional limiting process. *Journal of Computational Physics*, 208:570–615, 2005.

[64] A. N. Kolmogorov. The local structure of turbulence in incompressible viscous fluid for very large Reynolds number. *Doklady Akademii Nauka SSSR*, 30:299–303, 1941.

[65] C. B. Laney. *Computational Gasdynamics*. Cambridge University Press, 1998.

[66] E. Lenormand, P. Sagaut, L. Ta Phuoc, and P. Comte. Subgrid-Scale Models for Large-Eddy Simulations of Compressible Wall Bounded Flows. *AIAA Journal*, 38(8):1340–1350, August 2000.

[67] M. A. Leschziner. Turbulence modelling for separated flows with anisotropy-resolving closures. *Philosophical Transactions of the Royal Society of London, Series A*, 358:3247–3277, 2000.

[68] R. J. LeVeque. *Finite Volume Methods for Hyperbolic Problems*. Cambridge University Press, 2002.

[69] N. Li and M. A. Leschziner. Large-eddy simulation of separated flow over a swept wing with approximate near-wall modelling. *The Aeronautical Journal*, 111(1125):689–697, November 2007.

[70] N. Li and M. A. Leschziner. private communication. Imperial College, London, UK.

[71] X.-D. Liu, S. Osher, and T. Chan. Weighted Essentially Non-oscillatory Schemes. *Journal of Computational Phyics*, 115:200–212, 1994.

[72] H. Lomax, T. H. Pulliam, and D. W. Zingg. *Fundamentals of Computational Fluid Dynamics*. Springer Verlag, 2003.

[73] C. Maas and U. Schumann. Direct numerical simulation of separated turbulent flow over wavy boundary. In E. H. Hirschel, editor, *Flow Simulation with High Performance Computers*, volume 52, pages 227–241. Notes on Numerical Fluid Dynamics, 1996.

[74] N. MacDonald, E. Minty, J. Malard, T. Harding, S. Brown, and M. Antonioletti. Wrinting Message Passing Parallel Programs with MPI. Edinburgh Parallel Computing Centre, University of Edinburgh.

[75] F. Mallinger and D. Drikakis. Laminar-to-turbulent transition in pulsatile flow through a stenosis. *Biorheology*, 39:437–441, 2002.

[76] L. G. Margolin and W. J. Rider. A rationale for implicit turbulence modeling. *International Journal for Numerical Methods in Fluids*, 39:821–841, 2001.

[77] L. G. Margolin, P. K. Smolarkiewicz, and Z. Sorbjan. Large eddy simulations of convective boundary layers using nonoscillatory differencing. *Physica D*, 133: 390–97, 1998.

[78] L. G. Margolin, P. K. Smolarkiewicz, and A. A. Wyszogrodzki. Implicit turbulence modeling for high Reynolds number flows. *Journal of Fluids Engineering*, 124:862–867, 2002.

[79] I. Mary and P. Sagaut. Large Eddy Simulation of Flow Around an Airfoil Near Stall. *AIAA Journal*, 40(6):1139–1145, June 2002.

[80] C. P. Mellen, J. Fröhlich, and W. Rodi. Lessons from the European LESFOIL project on LES of flow around an airfoil. In *40th AIAA Aerospace Sciences Meeting and Exhibit*, number AIAA-2002-0111, January 2002.

[81] E. Minty, R. Davey, A. Simpson, and D. Henty. Decomposing the Potentially Parallel – A one day course. Edinburgh Parallel Computing Centre, University of Edinburgh.

[82] M. S. Mohammed and J. C. LaRue. The decay power law in grid-generated turbulence. *Journal of Fluid Mechanics*, 219:195–215, 1990.

[83] P. Moin and J. Kim. Tackling turbulence with supercomputers. *Scientific American*, 276(1):62–68, January 1997.

[84] P. E. Morgan and M. R. Visbal. Large-Eddy Simulation Modeling Issues for Flow Around Wing Sections. In *33rd AIAA Fluid Dynamics Conference and Exhibit*, number AIAA-2003-4152, June 2003.

[85] Y. Na and P. Moin. Direct numerical simulation of a separated turbulent boundary layer. *Journal of Fluid Mechanics*, 374:379–405, 1998.

[86] M. V. Ol and M. Gharib. Leading-Edge Vortex Structure of Nonslender Delta Wings at Low Reynolds Number. *AIAA Journal*, 41(1):16–26, January 2003.

[87] P. S. Pacheco. *Parallel Programming with MPI*. Morgan Kaufmann Publishers, San Francisco, 1997.

[88] F. M. Payne, T. T. Ng, and R. C. Nelson. Experimental Study of the Velocity Field on a Delta Wing. In *19th AIAA Fluid Dynamics, Plasma Dynamics, and Lasers Conference*, number AIAA-1987-1231, June 1987.

[89] U. Piomelli. Large-eddy simulation of turbulent flows. In *Large-Eddy Simulation and Related Techniques: Theory and Application*. VKI Lecture Series, 2006.

[90] S. B. Pope. *Turbulent Flows*. Cambridge University Press, 2000.

[91] D. H. Porter, A. Pouquet, and P. R. Woodward. A Numerical Study of Supersonic Turbulence. *Theoretical and Computational Fluid Dynamics*, 4(1):13–49, November 1992.

[92] D. H. Porter, A. Pouquet, and P. R. Woodward. Kolmogorov-like spectra in decaying three-dimensional supersonic flows. *Physics of Fluids*, 6(6):2133–2142, June 1994.

[93] D. H. Porter, P. R. Woodward, and A. Pouquet. Inertial range structures in decaying compressible turbulent flows. *Physics of Fluids*, 10(1):237–245, January 1998.

[94] O. K. Rediniotis, H. Stapountzis, and D. P. Telionis. Periodic Vortex Shedding ofer Delta Wings. *AIAA Journal*, 9:1555–1562, 1993.

[95] L. F. Richardson. *Weather Prediction by Numerical Process*. Cambridge University Press, 1922.

[96] A. J. Riley and M. V. Lowson. Development of a three-dimensional free shear layer. *Journal of Fluid Mechanics*, 369:49–89, 1998.

[97] D. P. Rizzetta. Numerical Simulation of the Interaction between a Leading-Edge Vortex and a Vertical Tail. In *27th AIAA Fluid Dynamics Conference*, number AIAA-1996-2012, June 1996.

[98] H. Schlichting. *Boundary-Layer Theory*. McGraw-Hill, 1979.

[99] U. Schumann. Subgrid scale models for finite difference simulations of turbulent flows in plane channels and annuli. *Journal of Computational Physics*, 18:376–404, 1975.

[100] H. Shan, L. Jiang, and C. Liu. Direct numerical simulation of flow separation around a NACA 0012 airfoil. *Computers & Fluids*, 34:1096–1114, 2005.

[101] E. Shapiro. Step-by-Step Eberle's scheme derivation. Technical report, Cranfield University, October 2006.

[102] C.-W. Shu and S. Osher. Efficient Implementation of Essentially Non-Oscillating Shock-Capturing Schemes. *Journal of Computational Physics*, 77: 439–471, 1988.

[103] C.-W. Shu, W.-S. Don, D. Gottlieb, O. Schilling, and L. Jameson. Numerical Convergence Study of Nearly Incompressible, Inviscid Taylor-Green Vortex Flow. *Journal of Scientific Computing*, 24(1):1–27, 2005.

[104] L. Skrbek and S. R. Stalp. On the decay of homogeneous isotropic turbulence. *Physics of Fluids*, 12(8):1997–2019, August 2000.

[105] J. Smagorinsky. General circulation experiments with the primitive equations: I. The basic experiment. *Monthly Weather Review*, 91(3):99–164, March 1963.

[106] P. K. Smolarkiewicz and L. G. Margolin. MPDATA: A Finite-Difference Solver for Geophysical Flows. *Journal of Computational Physics*, 140:459–480, 1998.

[107] P. K. Smolarkiewicz and J. M. Prusa. VLES modeling of geophysical fluids with nonoscillatory forward-in-time schemes. *International Journal for Numerical Methods in Fluids*, 39:799–819, 2002.

[108] K. R. Sreenivasan and R. A. Antonia. The Phenomenology of Small-Scale Turbulence. *Annual Review of Fluid Mechanics*, 29:435–472, 1997.

[109] G. I. Taylor and A. E. Green. Mechanism of the Production of Small Eddies from Large Ones. *Proceedings of the Royal Society of London A*, 158:499–521, 1937.

[110] G. S. Taylor and I. Gursul. Buffeting Flows over a Low-Sweep Delta Wing. *AIAA Journal*, 42(9):1737–1745, September 2004.

[111] G. S. Taylor, T. Schnorbus, and I. Gursul. An investigaton of vortex flows over low sweep delta wings. In *33rd AIAA Fluid Dynamics Conference and Exhibit*, number AIAA-2003-4021, June 2003.

[112] L. Temmerman, M. A. Leschziner, C. P. Mellen, and J. Fröhlich. Investigation of wall-function approximations and subgrid-scale models in large eddy simulation of separated flow in a channel with streamwise periodic constrictions. *International Journal of Heat and Fluid Flow*, 24:157–180, 2003.

[113] H. Tennekes and J. L. Lumley. *A First Course in Turbulence*. The MIT Press, 1972.

[114] B. Thornber, A. Mosedale, and D. Drikakis. On the implicit large eddy simulations of homogeneous decaying turbulence. *Journal of Computational Physics*, 226:1902–1929, 2007.

[115] E. F. Toro. *Riemann Solvers and Numerical Methods for Fluid Dynamics – A Practical Introduction*. Springer Verlag, Heidelberg, 1997.

[116] G. D. van Albada, B. Van Leer, and W. W. Roberts. A Comparative Study of Computational Methods in Cosmic Gas Dynamics. *Astronomy & Astrophysics*, 108:76–84, 1982.

[117] H. Van der Ven. A family of large eddy simulation filters with nonuniform filter widths. *Physics of Fluids*, 7(5):1171–1172, 1995.

[118] M. van Dyke. *An Album of Fluid Motion*. The Parabolic Press, 1982.

[119] B. van Leer. Towards the ultimate conservative difference scheme. Part II: Monotonicity and conservation combined in a second order scheme. *Journal of Computational Physics*, 14:361–370, 1974.

[120] B. van Leer. Towards the ultimate conservative difference scheme. Part V: A Second-Order Sequel to Godunov's Method. *Journal of Computational Physics*, 32:101–136, 1979. Reprinted in Volume 135 Number 2, pp. 229–248, August 1997.

[121] O. V. Vasilyev, T. S. Lund, and P. Moin. A general class of commutative filters for LES in complex geometries. *Journal of Computational Physics*, 146(1): 82–104, 1998.

[122] I. Veloudis, Z. Yang, J. J. McGuirk, G. J. Page, and A. Spencer. Novel Implementation and Assessment of a Digital Filter Based Approach for the Generation of LES Inlet Conditions. *Flow, Turbulence and Combustion*, 79:1–24, 2007.

[123] C. Wang, Y. J. Jang, and M. A. Leschziner. Modelling of two- and three-dimensional separation from curved surfaces with anisotropy-resolving turbulence closures. *International Journal of Heat and Fluid Flow*, 25:499–512, 2004.

[124] R. F. Warming and B. J. Hyett. The Modified Equation Approach to the Stability and Accuracy Analysis of Finite-Difference Methods. *Journal of Computational Physics*, 14:159–179, 1974.

[125] H. Werle. Le tunnel hydrodynamique au service de l'industrie. Technical Report 191, ONERA, 1970.

[126] H. Werner and H. Wengle. Large eddy simulation of turbulent flow over and around a cube in a plate channel. In *8th Symposium on Turbulent Shear Flows*. Technical University of Munich, 1991.

[127] M. M. Yavuz, M. Elkhoury, and D. Rockwell. Near-Surface Topology and Flow Structure on a Delta Wing. *AIAA Journal*, 42(2):332–340, February 2004.

[128] D. L. Youngs. Modelling turbulent mixing by Rayleigh-Taylor Instability. *Physica D*, 37:270–287, 1989.

[129] D. L. Youngs. Three-dimensional numerical simulation of turbulent mixing by Rayleigh-Taylor instability. *Physics of Fluids A*, 3(5):1312–1320, 1991.

[130] D. L. Youngs. Application of MILES to Rayleigh-Taylor and Richtmyer-Meshkov mixing. In *16th AIAA Computational Fluid Dynamics Conference*, number AIAA-2003-4102, June 2003.

[131] S. Zhang and J. T. Turner. private communication. Manchester University, UK.

[132] J. Zóltak and D. Drikakis. Hybrid upwind methods for the simulation of unsteady shock-wave diffraction over a cylinder. *Computer Methods in Applied Mechanics and Engineering*, 162:165–185, 1998.

APPENDIX **A**

Notation

In this thesis, the following notation exemplified for two vectors $\mathbf{a} = [a_1, a_2, a_3]^T$ and $\mathbf{b} = [b_1, b_2, b_3]^T$ has been used. The dot product of two vectors is given by

$$\mathbf{a} \cdot \mathbf{b} = a_1 b_1 + a_2 b_2 + a_3 b_3 \ ,$$

the cross product of two vectors is defined as

$$\mathbf{a} \times \mathbf{b} = \begin{vmatrix} \mathbf{i} & \mathbf{j} & \mathbf{k} \\ a_1 & a_2 & a_3 \\ b_1 & b_2 & b_3 \end{vmatrix} \ ,$$

the tensor product of two vectors is written as

$$\mathbf{a} \otimes \mathbf{b} = \begin{bmatrix} a_1 \\ a_2 \\ a_3 \end{bmatrix} \begin{bmatrix} b_1 & b_2 & b_3 \end{bmatrix} = \begin{bmatrix} a_1 b_1 & a_1 b_2 & a_1 b_3 \\ a_2 b_1 & a_2 b_2 & a_2 b_3 \\ a_3 b_1 & a_3 b_2 & a_3 b_3 \end{bmatrix} \ ,$$

the gradient (nabla) operator yields

$$\nabla = \mathbf{i}\frac{\partial}{\partial x} + \mathbf{j}\frac{\partial}{\partial y} + \mathbf{k}\frac{\partial}{\partial z} \ ,$$

the gadient of a scalar is defined as

$$\nabla a = \mathbf{i}\frac{\partial a}{\partial x} + \mathbf{j}\frac{\partial a}{\partial y} + \mathbf{k}\frac{\partial a}{\partial z} \ ,$$

the gadient of a vector is given by

$$\nabla \mathbf{a} = \begin{bmatrix} \frac{\partial}{\partial x} & \frac{\partial}{\partial y} & \frac{\partial}{\partial z} \end{bmatrix} \begin{bmatrix} a_1 \\ a_2 \\ a_3 \end{bmatrix} = \frac{\partial a_1}{\partial x} + \frac{\partial a_2}{\partial y} + \frac{\partial a_3}{\partial z} \ ,$$

the divergence of a vector is written as

$$\nabla \cdot \mathbf{a} = \begin{bmatrix} a_1 \\ a_2 \\ a_3 \end{bmatrix} \begin{bmatrix} \frac{\partial}{\partial x} & \frac{\partial}{\partial y} & \frac{\partial}{\partial z} \end{bmatrix} = \begin{bmatrix} \frac{\partial a_1}{\partial x} & \frac{\partial a_1}{\partial y} & \frac{\partial a_1}{\partial z} \\ \frac{\partial a_2}{\partial x} & \frac{\partial a_2}{\partial y} & \frac{\partial a_2}{\partial z} \\ \frac{\partial a_3}{\partial x} & \frac{\partial a_3}{\partial y} & \frac{\partial a_3}{\partial z} \end{bmatrix} \ ,$$

and the divergence of a tensor yields

$$\nabla \cdot \mathbf{A} = \begin{bmatrix} a_{11} & a_{12} & a_{13} \\ a_{21} & a_{22} & a_{23} \\ a_{31} & a_{32} & a_{33} \end{bmatrix} \begin{bmatrix} \frac{\partial}{\partial x} \\ \frac{\partial}{\partial y} \\ \frac{\partial}{\partial z} \end{bmatrix} = \begin{bmatrix} \frac{\partial a_{11}}{\partial x} + \frac{\partial a_{12}}{\partial y} + \frac{\partial a_{13}}{\partial z} \\ \frac{\partial a_{21}}{\partial x} + \frac{\partial a_{22}}{\partial y} + \frac{\partial a_{23}}{\partial z} \\ \frac{\partial a_{31}}{\partial x} + \frac{\partial a_{32}}{\partial y} + \frac{\partial a_{33}}{\partial z} \end{bmatrix}.$$

APPENDIX **B**

Flowchart

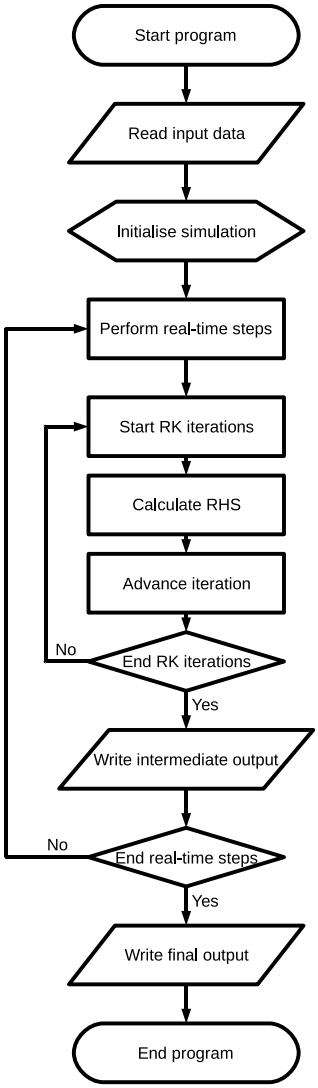

Figure B.1: Flowchart of the solver for unsteady problems including explicit multi-stage Runge-Kutta time integration schemes.

APPENDIX **C**

Viscous Stresses

The individual components of the viscous stress tensor in non-dimensional form as used in Chapter 3 can be written as follows

$$
\begin{aligned}
\tau_{xx} &= \frac{1}{Re}\left(\frac{4}{3}\frac{\partial u}{\partial x} - \frac{2}{3}\frac{\partial v}{\partial y} - \frac{2}{3}\frac{\partial w}{\partial z}\right), \\
\tau_{yy} &= \frac{1}{Re}\left(-\frac{2}{3}\frac{\partial u}{\partial x} + \frac{4}{3}\frac{\partial v}{\partial y} - \frac{2}{3}\frac{\partial w}{\partial z}\right), \\
\tau_{zz} &= \frac{1}{Re}\left(-\frac{2}{3}\frac{\partial u}{\partial x} - \frac{2}{3}\frac{\partial v}{\partial y} + \frac{4}{3}\frac{\partial w}{\partial z}\right), \\
\tau_{xy} &= \tau_{yx} = \frac{1}{Re}\left(\frac{\partial u}{\partial y} + \frac{\partial v}{\partial x}\right), \\
\tau_{xz} &= \tau_{zx} = \frac{1}{Re}\left(\frac{\partial u}{\partial z} + \frac{\partial w}{\partial x}\right), \\
\tau_{yz} &= \tau_{zy} = \frac{1}{Re}\left(\frac{\partial v}{\partial z} + \frac{\partial w}{\partial y}\right).
\end{aligned}
$$

Please note that the Reynolds number has been included here as opposed to the notation in Equation (3.1.24).

APPENDIX **D**

Discretisation

For the sake of completeness, the metric relations and their discretisation as used in Chapter 3, also found in the book of Drikakis and Rider [27], are presented here. In a three-dimensional context, the metrics for the coordinate transformation is given by

$$\xi_x = \frac{y_\eta z_\zeta - y_\zeta z_\eta}{J}\ ,\ \xi_y = \frac{-x_\eta z_\zeta + x_\zeta z_\eta}{J}\ ,\ \xi_z = \frac{x_\eta y_\zeta - x_\zeta y_\eta}{J}\ ,$$
$$\eta_x = \frac{-y_\xi z_\zeta + y_\zeta z_\xi}{J}\ ,\ \eta_y = \frac{x_\xi z_\zeta - x_\zeta z_\xi}{J}\ ,\ \eta_z = \frac{-x_\xi y_\zeta + x_\zeta y_\xi}{J}\ ,$$
$$\zeta_x = \frac{y_\xi z_\eta - y_\eta z_\xi}{J}\ ,\ \zeta_y = \frac{-x_\xi z_\eta + x_\eta z_\xi}{J}\ ,\ \zeta_z = \frac{x_\xi y_\eta - x_\eta y_\xi}{J}$$

and the derivatives across a cell face, e.g. defined by the subscript $(i-1/2,\, j, k)$, can be discretised as

$$\begin{aligned}
x_\eta|_{i-1/2,j,k} &= 0.5(x_{i,j+1,k} + x_{i,j+1,k+1} - x_{i,j,k} - x_{i,j,k+1})\ ,\\
y_\eta|_{i-1/2,j,k} &= 0.5(y_{i,j+1,k} + y_{i,j+1,k+1} - y_{i,j,k} - y_{i,j,k+1})\ ,\\
z_\eta|_{i-1/2,j,k} &= 0.5(z_{i,j+1,k} + z_{i,j+1,k+1} - z_{i,j,k} - z_{i,j,k+1})\ ,
\end{aligned}$$

$$\begin{aligned}
x_\xi|_{i-1/2,j,k} &= 0.125(x_{i+1,j,k} + x_{i+1,j+1,k} + x_{i+1,j+1,k+1} + x_{i+1,j,k}\\
&\quad - x_{i-1,j,k} - x_{i-1,j+1,k+1} - x_{i-1,j+1,k+1} - x_{i-1,j,k+1})\ ,\\
y_\xi|_{i-1/2,j,k} &= 0.125(y_{i+1,j,k} + y_{i+1,j+1,k} + y_{i+1,j+1,k+1} + y_{i+1,j,k}\\
&\quad - y_{i-1,j,k} - y_{i-1,j+1,k+1} - y_{i-1,j+1,k+1} - y_{i-1,j,k+1})\ ,\\
z_\xi|_{i-1/2,j,k} &= 0.125(z_{i+1,j,k} + z_{i+1,j+1,k} + z_{i+1,j+1,k+1} + z_{i+1,j,k}\\
&\quad - z_{i-1,j,k} - z_{i-1,j+1,k+1} - z_{i-1,j+1,k+1} - z_{i-1,j,k+1})\ ,
\end{aligned}$$

$$\begin{aligned}
x_\zeta|_{i-1/2,j,k} &= 0.5(x_{i,j+1,k} + x_{i,j+1,k+1} - x_{i,j,k} - x_{i,j,k+1})\ ,\\
y_\zeta|_{i-1/2,j,k} &= 0.5(y_{i,j+1,k} + y_{i,j+1,k+1} - y_{i,j,k} - y_{i,j,k+1})\ ,\\
z_\zeta|_{i-1/2,j,k} &= 0.5(z_{i,j+1,k} + z_{i,j+1,k+1} - z_{i,j,k} - z_{i,j,k+1})\ .
\end{aligned}$$

Furthermore, the inter-cell velocity derivatives at the same face can be calculated as

$$\begin{aligned}
u_\xi|_{i-1/2,j,k} &= u_{i+1,j,k} - u_{i,j,k}\ ,\\
v_\xi|_{i-1/2,j,k} &= v_{i+1,j,k} - v_{i,j,k}\ ,\\
w_\xi|_{i-1/2,j,k} &= w_{i+1,j,k} - w_{i,j,k}\ ,
\end{aligned}$$

$$
\begin{aligned}
u_\eta|_{i-1/2,j,k} &= 0.25(u_{i,j+1,k} + u_{i-1,j+1,k} - u_{i,j-1,k} - u_{i-1,j-1,k}) \,, \\
v_\eta|_{i-1/2,j,k} &= 0.25(v_{i,j+1,k} + v_{i-1,j+1,k} - v_{i,j-1,k} - v_{i-1,j-1,k}) \,, \\
w_\eta|_{i-1/2,j,k} &= 0.25(w_{i,j+1,k} + w_{i-1,j+1,k} - w_{i,j-1,k} - w_{i-1,j-1,k}) \,,
\end{aligned}
$$

$$
\begin{aligned}
u_\zeta|_{i-1/2,j,k} &= 0.25(u_{i,j,k+1} + u_{i-1,j,k+1} - u_{i,j,k-1} - u_{i-1,j,k-1}) \,, \\
v_\zeta|_{i-1/2,j,k} &= 0.25(v_{i,j,k+1} + v_{i-1,j,k+1} - v_{i,j,k-1} - v_{i-1,j,k-1}) \,, \\
w_\zeta|_{i-1/2,j,k} &= 0.25(w_{i,j,k+1} + w_{i-1,j,k+1} - w_{i,j,k-1} - w_{i-1,j,k-1}) \,.
\end{aligned}
$$

APPENDIX **E**

Forcing Term

For the hill flow geometry, the standard form of the Navier-Stokes equations is extended by an external forcing term f as has been proposed by Lenormand et al. [66]. This modification is necessary because pressure-driven channel flow violates the boundary conditions for the test case considered here, namely periodicity in x- direction. In the absence of a pressure drop, the forcing term acts as a driver for the flow and ensures a constant mass flow rate. Thus, the augmented Navier-Stokes equations can be written as

$$\begin{aligned}
\frac{\partial \rho}{\partial t} + \nabla \cdot (\rho \mathbf{u}) &= 0 \,, \\
\frac{\partial \rho \mathbf{u}}{\partial t} + \nabla \cdot (\rho \mathbf{u}\mathbf{u}) &= -\nabla \cdot \mathbf{P} - f \cdot \hat{\mathbf{x}} \,, \\
\frac{\partial e}{\partial t} + \nabla \cdot (e \mathbf{u}) &= -\nabla \cdot (\mathbf{P} \cdot \mathbf{u}) - \nabla \cdot \mathbf{q} - f \cdot \mathbf{u} \cdot \hat{\mathbf{x}} \,,
\end{aligned}$$

where $\mathbf{u}, \rho$, e, and $\mathbf{q}$ stand for the velocity components, density, total energy per unit volume, and heat flux, respectively, and $\hat{\mathbf{x}}$ is the unit basis vector in x-direction.

The forcing term is constant in space and its magnitude can be adjusted dynamically to obtain the required mass flow rate. For this purpose, the mass flow Q can be estimated by considering the momentum equation for the streamwise velocity component in dimensionless form as given by

$$\frac{\partial \rho u}{\partial t} + \frac{\partial \rho u^2}{\partial x} + \frac{\partial \rho uv}{\partial y} + \frac{\partial \rho uw}{\partial z} = -\frac{\partial p}{\partial x} + \frac{1}{Re}\frac{\partial \tau_{xx}}{\partial x} + \frac{1}{Re}\frac{\partial \tau_{yx}}{\partial y} + \frac{1}{Re}\frac{\partial \tau_{zx}}{\partial z} - f$$

Now, the individual terms as applied in the finite volume context can be simplified by taking the specific boundary conditions for the hill flow into account

$$\begin{aligned}
\int\int\int \frac{\partial \rho u}{\partial t} dx dy dz &= L_x \frac{\partial Q}{\partial t} \,, \\
\int\int\int \frac{\partial \rho u^2}{\partial x} dx dy dz &= \int\int \rho u^2 \Big|_{x_L}^{x_R} dy dz \xrightarrow{periodicity} 0 \,, \\
\int\int\int \frac{\partial \rho uv}{\partial y} dx dy dz &= \int\int \rho uv \Big|_{y_L}^{y_R} dx dz \xrightarrow{periodicity} 0 \,,
\end{aligned}$$

$$
\begin{aligned}
\int\int\int \frac{\partial \rho uw}{\partial z} dxdydz &= \int\int \rho uw\Big|_{z_L}^{z_R} dxdy \xrightarrow{no-slip} 0 \,, \\
-\int\int\int \frac{\partial p}{\partial x} dxdydz &= -\int\int p\Big|_{x_L}^{x_R} dydz \xrightarrow{periodicity} 0 \,, \\
\int\int\int \frac{\partial \tau_{xx}}{\partial x} dxdydz &= \int\int \tau_{xx}\Big|_{x_L}^{x_R} dydz \xrightarrow{periodicity} 0 \,, \\
\int\int\int \frac{\partial \tau_{yx}}{\partial y} dxdydz &= \int\int \tau_{yx}\Big|_{y_L}^{y_R} dxdz \xrightarrow{periodicity} 0 \,, \\
\int\int\int \frac{\partial \tau_{zx}}{\partial z} dxdydz &= \int\int\int \frac{\partial^2 u}{\partial z^2} dxdydz + \int\int\int \frac{\partial^2 w}{\partial x \partial z} dxdydz \\
&= \int\int \frac{\partial u}{\partial z}\Big|_{z_L}^{z_R} dxdy + \underbrace{\int\int \frac{\partial w}{\partial z}\Big|_{x_L}^{x_R} dydz}_{\xrightarrow{periodicity} 0} \\
&= \int\int \frac{\partial u}{\partial z}\Big|_{z_L}^{z_R} dxdy \,, \\
-\int\int\int f dxdydz &= -L_x L_y L_z \cdot f \,.
\end{aligned}
$$

Combining the terms again gives the estimate for the mass flow rate

$$
\frac{\partial Q}{\partial t} = -L_y L_z \cdot f + \frac{1}{L_x Re} \int\int \frac{\partial u}{\partial z}\Big|_{z_L}^{z_R} dxdy \,,
$$

where L_x, L_y and L_z mark the extent of the domain in streamwise, cross-stream and vertical direction, respectively. All assumptions made previously are strictly valid only if the governing equations are given in Cartesian form and the curvature at the bottom wall of the hill is neglected, otherwise the pressure term does not drop out. The error introduced by this simplification, however, is relatively small as is demonstrated later. The numerical evaluation of the above equation is performed in the transformed coordinate system in order to include the effect of the hill-type constriction on the term representing the shear stress contribution. Yet, for the sake of simplicity, the numerical procedure is outlined here in Cartesian form.

In the next step, the mass flow rate is replaced by its discrete counterpart, yielding

$$
Q^{n+1} = Q^n - \Delta t \, L_y L_z \cdot f + \frac{\Delta t}{L_x Re} \int\int \frac{\partial u}{\partial z}\Big|_{z_L}^{z_R} dxdy \,,
$$

where n marks the current time level and Δt is the size of the discrete time-step. Finally, the sought after expression for the forcing term at the following time instance is obtained by a predictor-corrector rule

$$
f^{n+1} = f^n + \frac{1}{L_y L_z} \left(\beta_1 (Q^{n+1} - Q) + \beta_2 (Q^n - Q) \right) \,,
$$

with $\beta_1 = 2$, $\beta_2 = -0.2$ as proposed by Lenormand et al. [66] and Q being the target mass flow. It has been found numerically that the error of this approach lies within 1% of the ideal value in case of the hill flow.

APPENDIX **F**

Profiles for the Swept Wing

The velocity and turbulent energy profiles presented in Chapter 6 have been obtained at locations according to the the experimental data provided by Zhang and Turner [131]. Here, a full set of comparisons including velocity and Reynolds stress components between the ILES simulation using high resolution methods and the experiment is provided in the following figures.

The base-points of the profiles on the wing surface are prescribed in terms of half-span s and local chord c positions as sketched in Figure F.1. In this context, the local chord is defined as the coordinate along the surface of the wing and the trajectory of the measurement in the two-dimensional cut parallel to the wing root is given by its inclination with respect to the vertical direction.

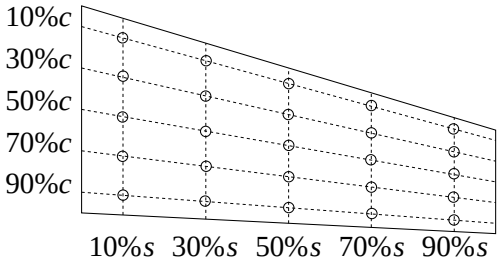

Figure F.1: Sketch of the profile base-points on the wing surface.

	30%s	40%s	50%s	60%s	70%s	80%s	90%s
10%c	-3.1230	-9.0013*	-9.0013*	-8.9999*	-8.9999*	-1.0785	-0.6679
30%c	-7.6306	-8.9999*	-9.0013*	-8.9999*	-9.0013*	-5.4307	-4.9042
50%c	-7.0443	-8.9999*	-9.0013*	-8.9999*	-9.0013*	-8.5867	-7.9587
70%c	-9.0013*	-9.0013*	-8.9904*	-9.0013*	-8.9919*	-8.2950	-8.9621
90%c	-9.0013*	-9.0013*	-9.0013*	-8.9999*	-8.9999*	-8.2254	-8.8946

Table F.1: Angles between the measurement trajectories and the vertical direction. The profiles are taken normal to the wing surface unless marked by an asterisk ($*$=trajectories normal to the root chord of the wing).

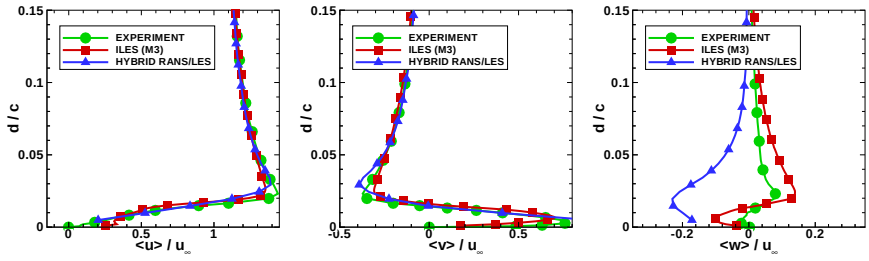

(a) Averaged u at 10%*c*. (b) Averaged v at 10%*c*. (c) Averaged w at 10%*c*.

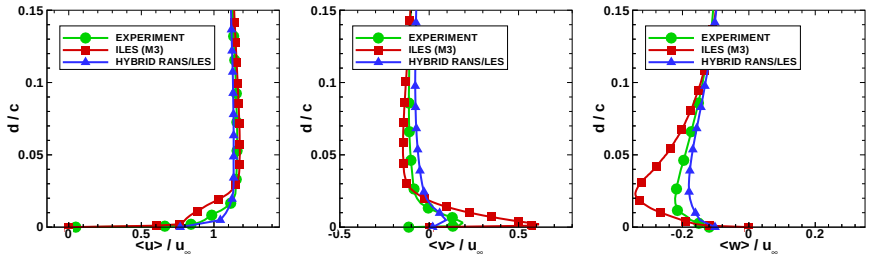

(d) Averaged u at 30%*c*. (e) Averaged v at 30%*c*. (f) Averaged w at 30%*c*.

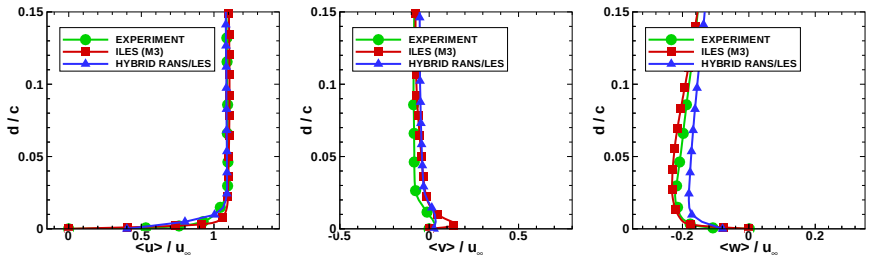

(g) Averaged u at 50%*c*. (h) Averaged v at 50%*c*. (i) Averaged w at 50%*c*.

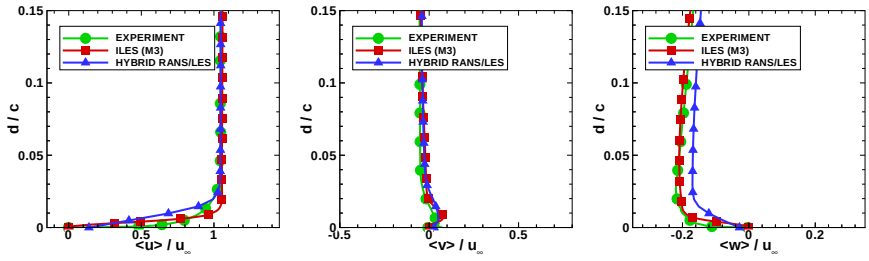

(j) Averaged u at 70%*c*. (k) Averaged v at 70%*c*. (l) Averaged w at 70%*c*.

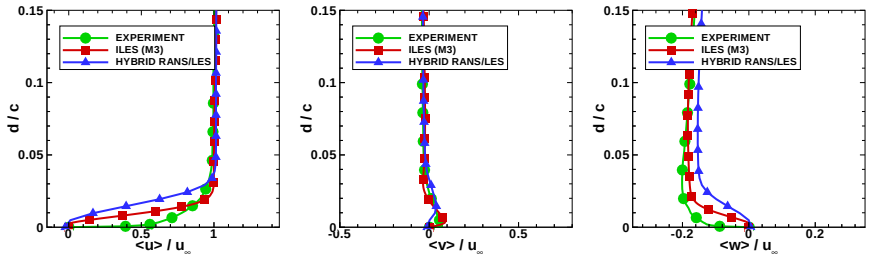

(m) Averaged u at 90%*c*. (n) Averaged v at 90%*c*. (o) Averaged w at 90%*c*.

Figure F.2: Comparison between averaged velocity profiles from the experiments of Zhang and Turner [131], the results obtained with ILES and the hybrid RANS/LES of Li and Leschziner [69] for different locations along the local chord at 30% half-span.

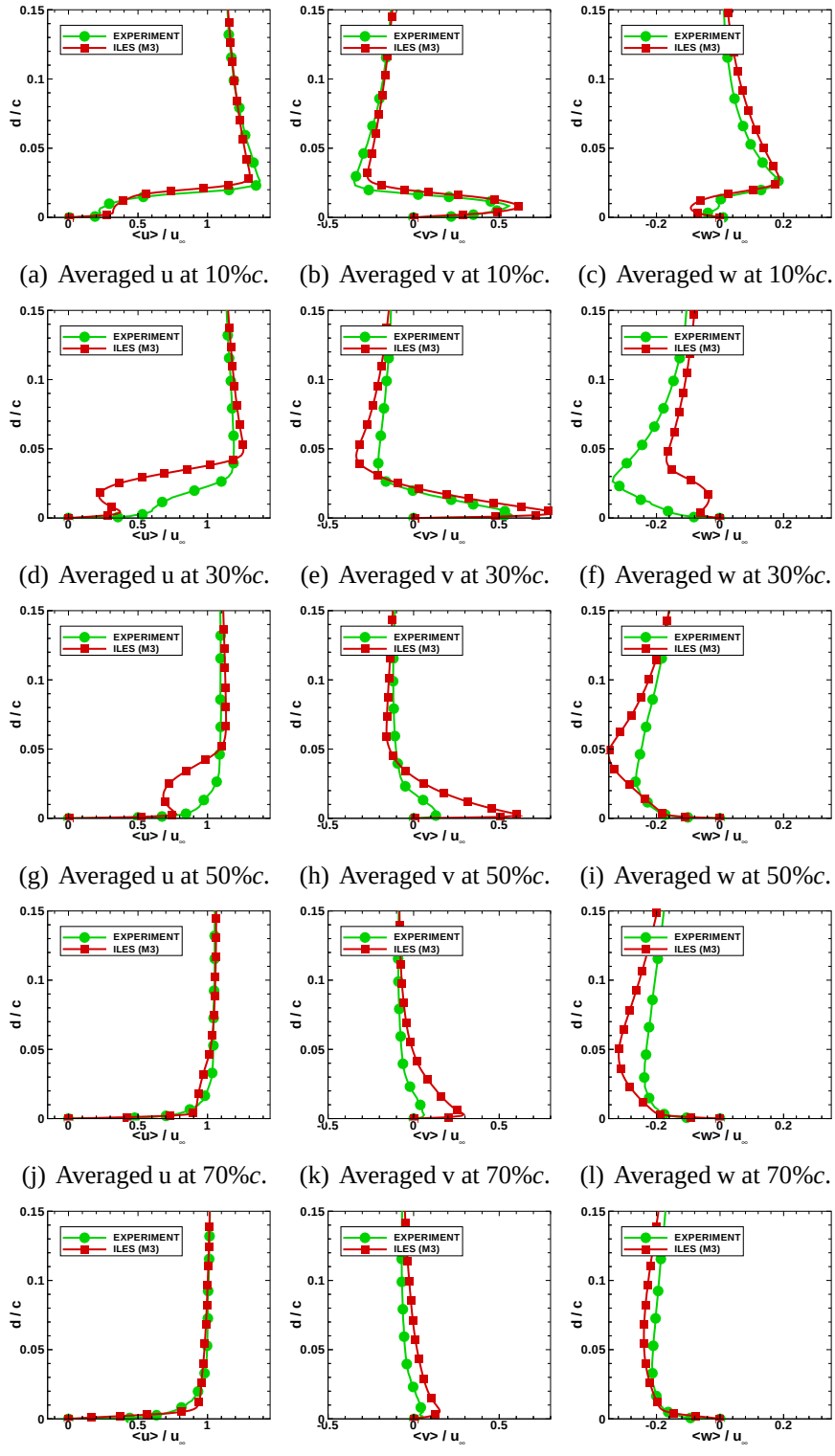

(a) Averaged u at 10%*c*. (b) Averaged v at 10%*c*. (c) Averaged w at 10%*c*.

(d) Averaged u at 30%*c*. (e) Averaged v at 30%*c*. (f) Averaged w at 30%*c*.

(g) Averaged u at 50%*c*. (h) Averaged v at 50%*c*. (i) Averaged w at 50%*c*.

(j) Averaged u at 70%*c*. (k) Averaged v at 70%*c*. (l) Averaged w at 70%*c*.

(m) Averaged u at 90%*c*. (n) Averaged v at 90%*c*. (o) Averaged w at 90%*c*.

Figure F.3: Comparison between averaged velocity profiles from the experiments of Zhang and Turner [131] and the results obtained with ILES for different locations along the local chord at 40% half-span.

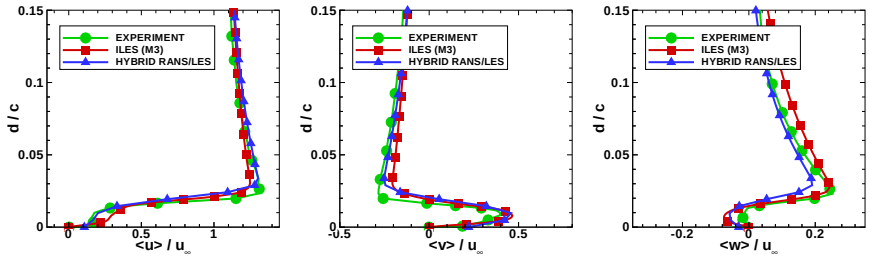

(a) Averaged u at 10%*c*. (b) Averaged v at 10%*c*. (c) Averaged w at 10%*c*.

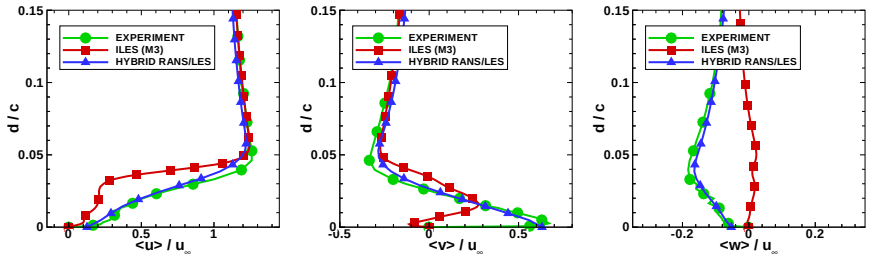

(d) Averaged u at 30%*c*. (e) Averaged v at 30%*c*. (f) Averaged w at 30%*c*.

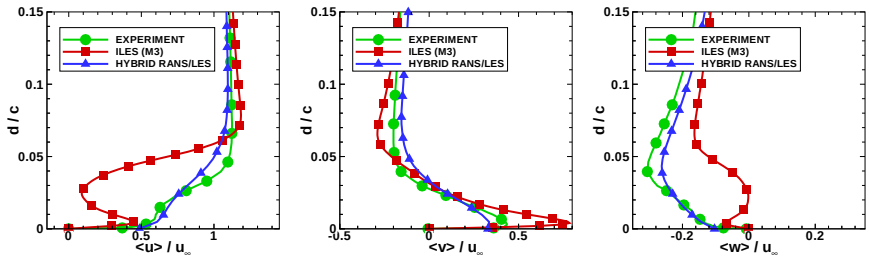

(g) Averaged u at 50%*c*. (h) Averaged v at 50%*c*. (i) Averaged w at 50%*c*.

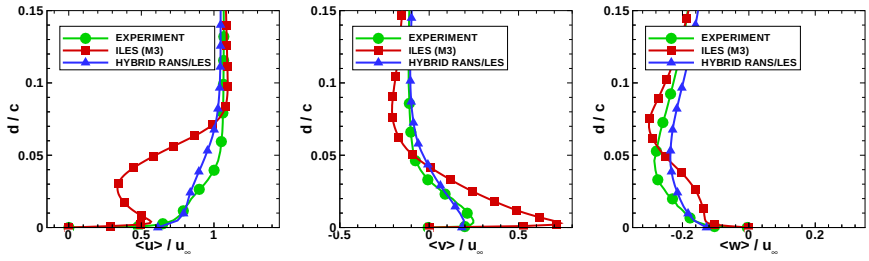

(j) Averaged u at 70%*c*. (k) Averaged v at 70%*c*. (l) Averaged w at 70%*c*.

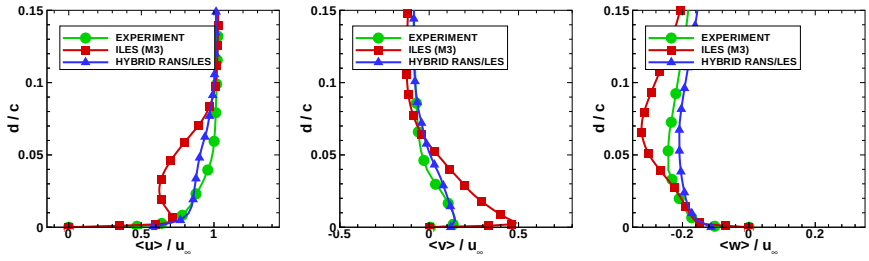

(m) Averaged u at 90%*c*. (n) Averaged v at 90%*c*. (o) Averaged w at 90%*c*.

Figure F.4: Comparison between averaged velocity profiles from the experiments of Zhang and Turner [131], the results obtained with ILES and the hybrid RANS/LES of Li and Leschziner [69] for different locations along the local chord at 50% half-span.

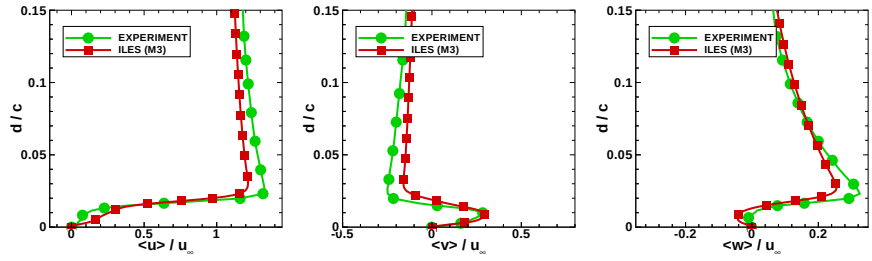

(a) Averaged u at 10%*c*. (b) Averaged v at 10%*c*. (c) Averaged w at 10%*c*.

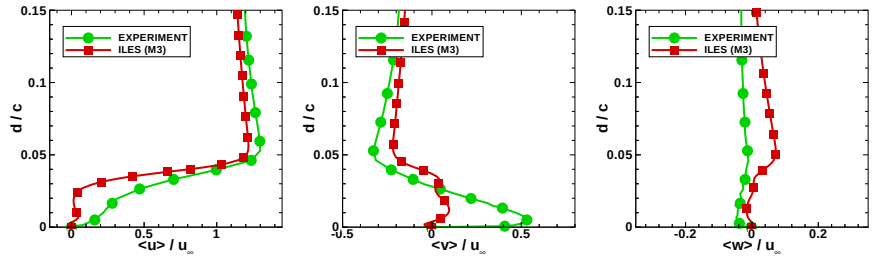

(d) Averaged u at 30%*c*. (e) Averaged v at 30%*c*. (f) Averaged w at 30%*c*.

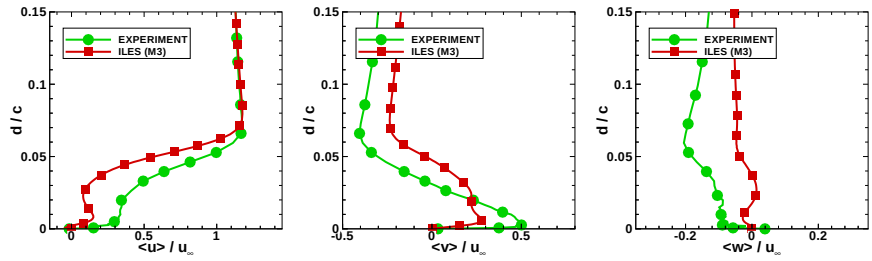

(g) Averaged u at 50%*c*. (h) Averaged v at 50%*c*. (i) Averaged w at 50%*c*.

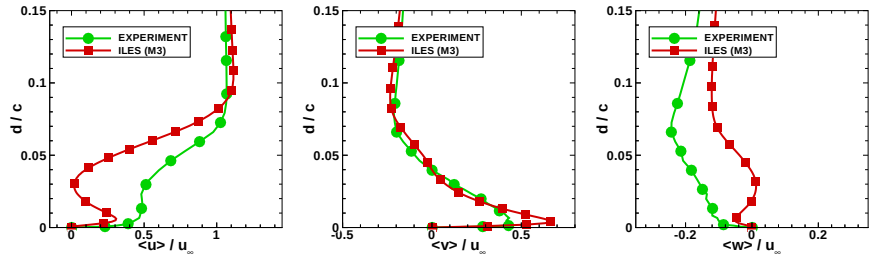

(j) Averaged u at 70%*c*. (k) Averaged v at 70%*c*. (l) Averaged w at 70%*c*.

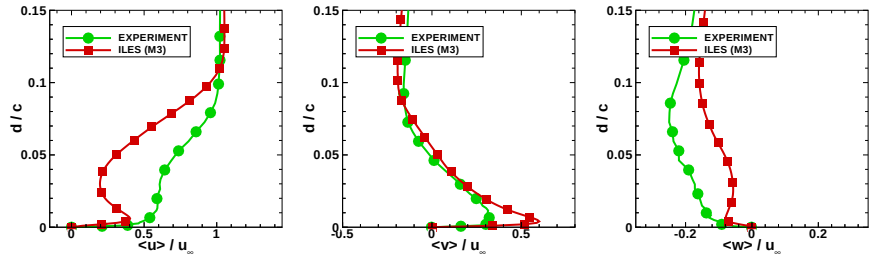

(m) Averaged u at 90%*c*. (n) Averaged v at 90%*c*. (o) Averaged w at 90%*c*.

Figure F.5: Comparison between averaged velocity profiles from the experiments of Zhang and Turner [131] and the results obtained with ILES for different locations along the local chord at 60% half-span.

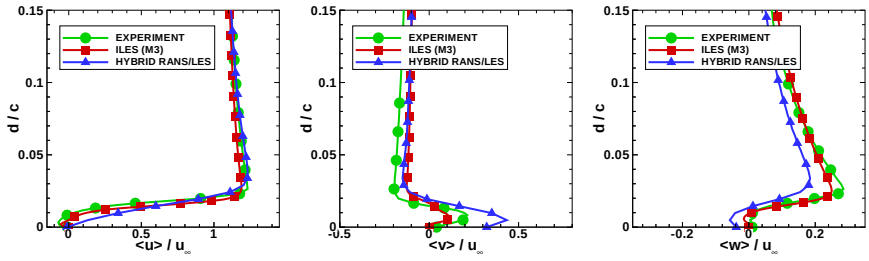

(a) Averaged u at 10%*c*. (b) Averaged v at 10%*c*. (c) Averaged w at 10%*c*.

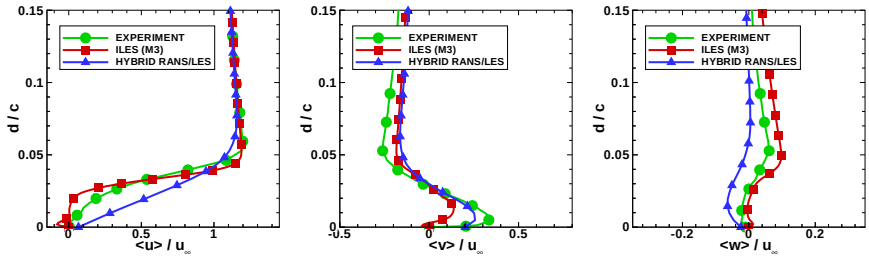

(d) Averaged u at 30%*c*. (e) Averaged v at 30%*c*. (f) Averaged w at 30%*c*.

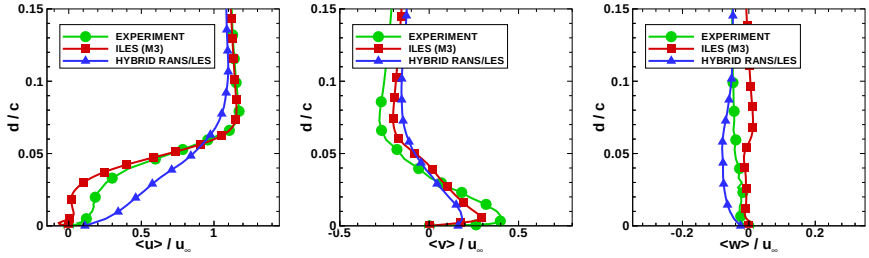

(g) Averaged u at 50%*c*. (h) Averaged v at 50%*c*. (i) Averaged w at 50%*c*.

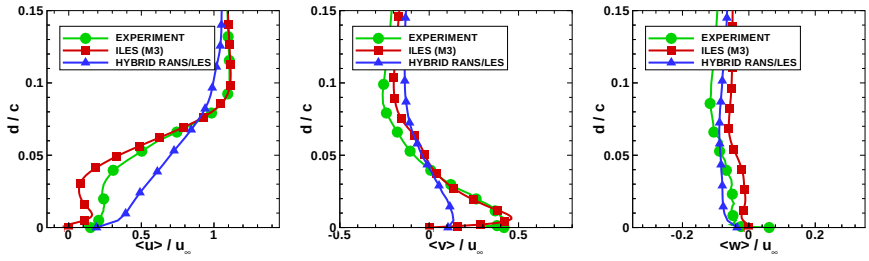

(j) Averaged u at 70%*c*. (k) Averaged v at 70%*c*. (l) Averaged w at 70%*c*.

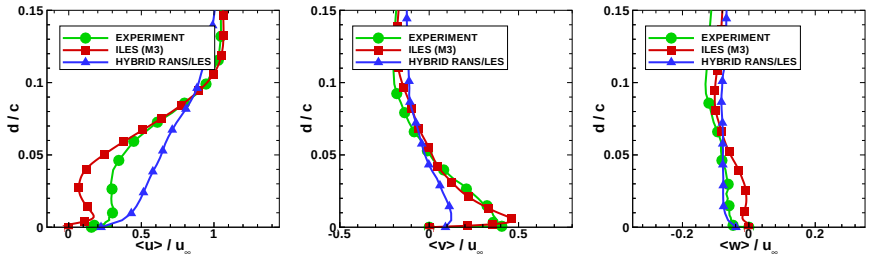

(m) Averaged u at 90%*c*. (n) Averaged v at 90%*c*. (o) Averaged w at 90%*c*.

Figure F.6: Comparison between averaged velocity profiles from the experiments of Zhang and Turner [131], the results obtained with ILES and the hybrid RANS/LES of Li and Leschziner [69] for different locations along the local chord at 70% half-span.

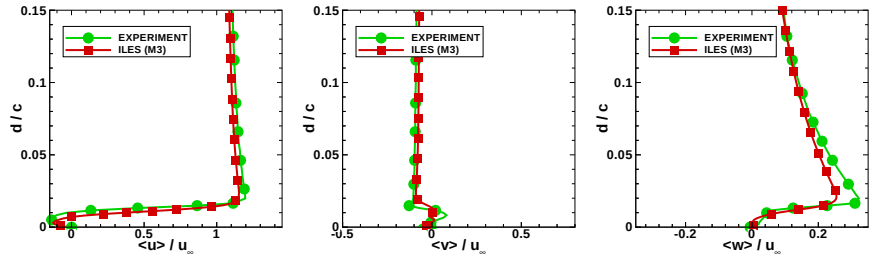

(a) Averaged u at 10%*c*. (b) Averaged v at 10%*c*. (c) Averaged w at 10%*c*.

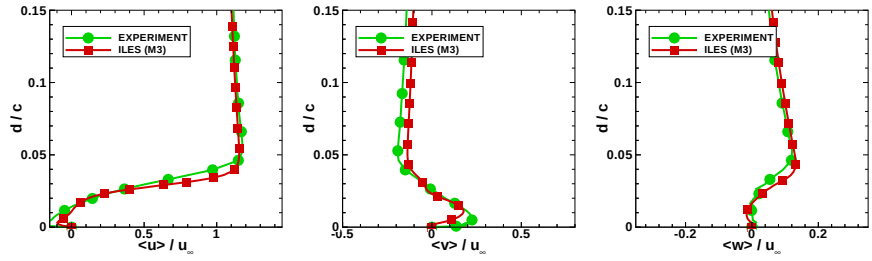

(d) Averaged u at 30%*c*. (e) Averaged v at 30%*c*. (f) Averaged w at 30%*c*.

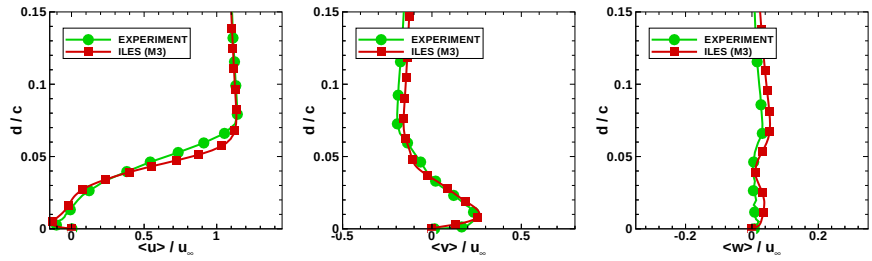

(g) Averaged u at 50%*c*. (h) Averaged v at 50%*c*. (i) Averaged w at 50%*c*.

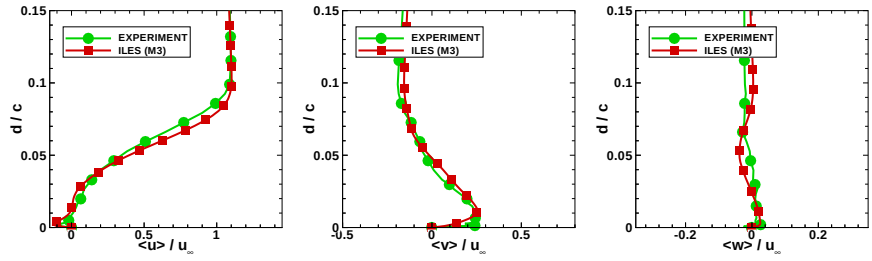

(j) Averaged u at 70%*c*. (k) Averaged v at 70%*c*. (l) Averaged w at 70%*c*.

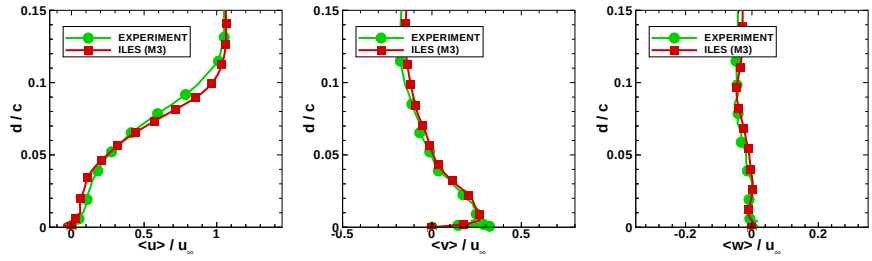

(m) Averaged u at 90%*c*. (n) Averaged v at 90%*c*. (o) Averaged w at 90%*c*.

Figure F.7: Comparison between averaged velocity profiles from the experiments of Zhang and Turner [131] and the results obtained with ILES for different locations along the local chord at 80% half-span.

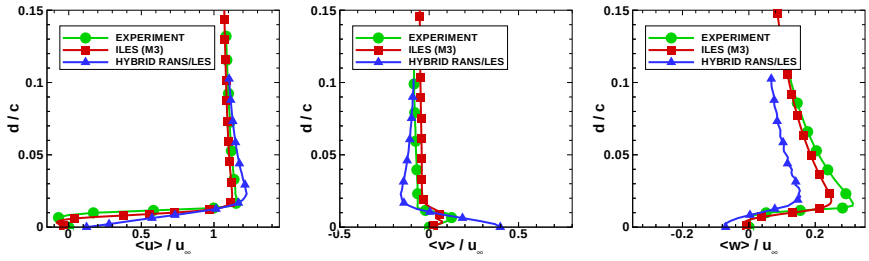

(a) Averaged u at 10%c. (b) Averaged v at 10%c. (c) Averaged w at 10%c.

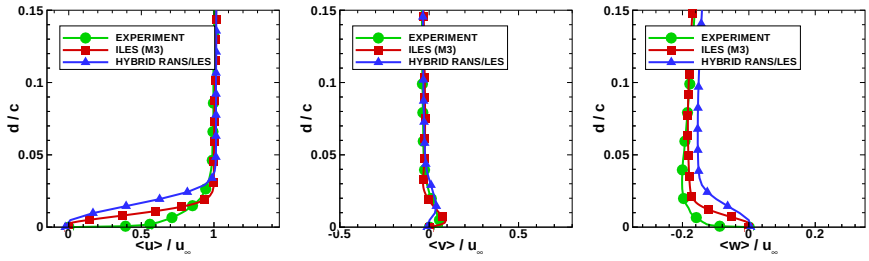

(d) Averaged u at 30%c. (e) Averaged v at 30%c. (f) Averaged w at 30%c.

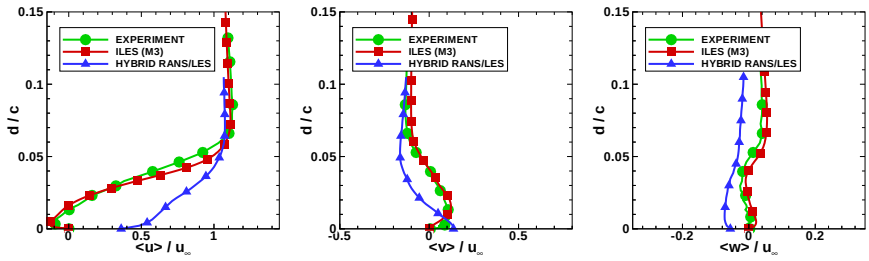

(g) Averaged u at 50%c. (h) Averaged v at 50%c. (i) Averaged w at 50%c.

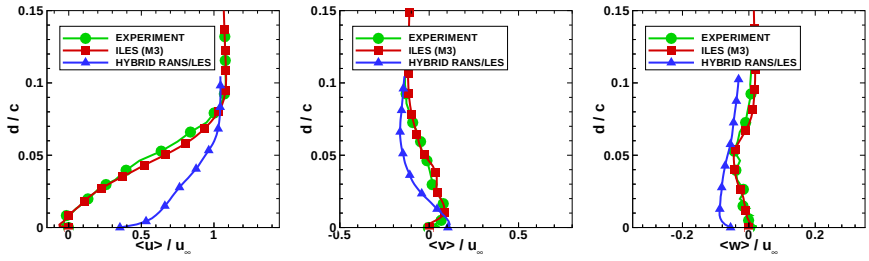

(j) Averaged u at 70%c. (k) Averaged v at 70%c. (l) Averaged w at 70%c.

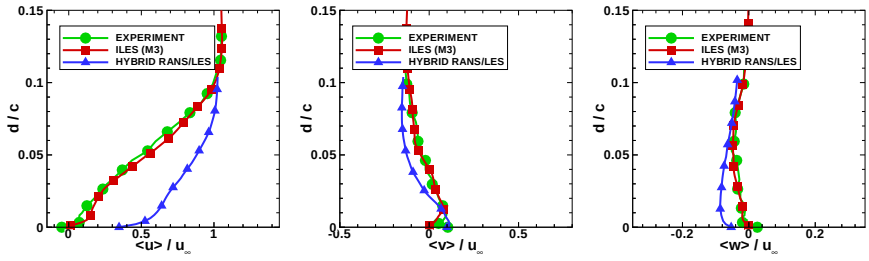

(m) Averaged u at 90%c. (n) Averaged v at 90%c. (o) Averaged w at 90%c.

Figure F.8: Comparison between averaged velocity profiles from the experiments of Zhang and Turner [131], the results obtained with ILES and the hybrid RANS/LES of Li and Leschziner [69] for different locations along the local chord at 90% half-span.

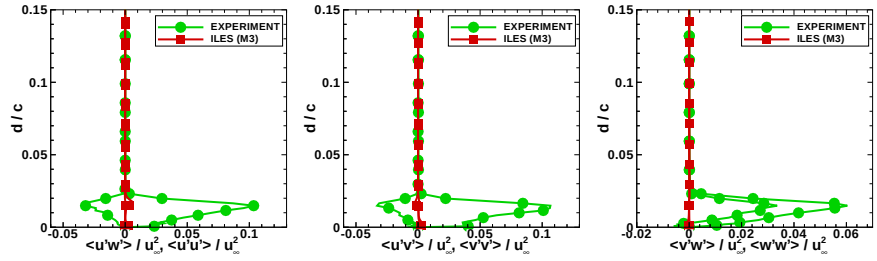

(a) Av. stresses at 10%*c*. (b) Av. stresses at 10%*c*. (c) Av. stresses at 10%*c*.

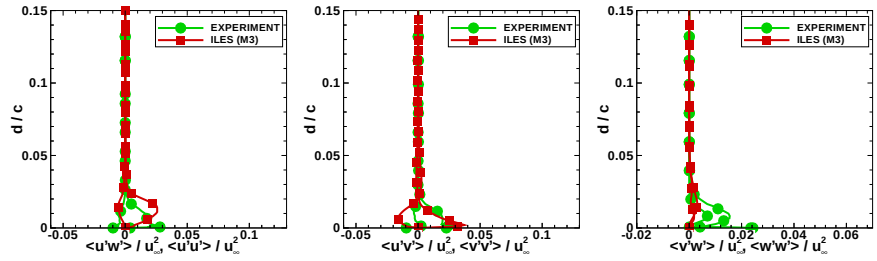

(d) Av. stresses at 30%*c*. (e) Av. stresses at 30%*c*. (f) Av. stresses at 30%*c*.

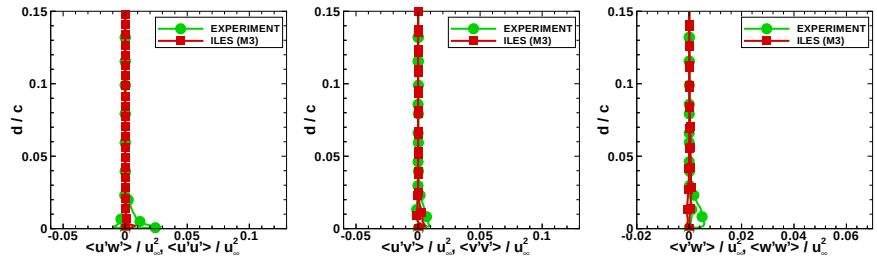

(g) Av. stresses at 50%*c*. (h) Av. stresses at 50%*c*. (i) Av. stresses at 50%*c*.

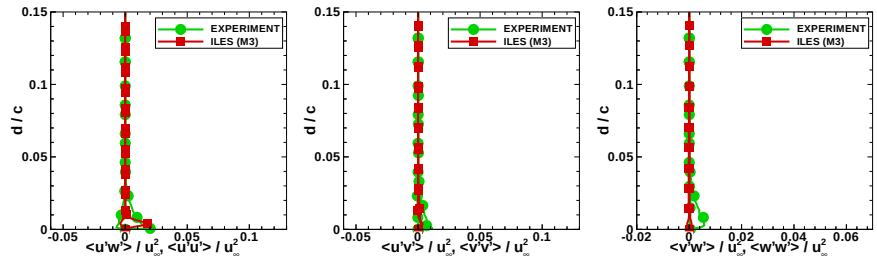

(j) Av. stresses at 70%*c*. (k) Av. stresses at 70%*c*. (l) Av. stresses at 70%*c*.

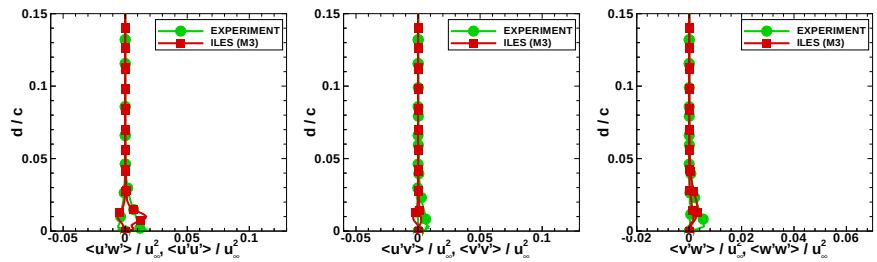

(m) Av. stresses at 90%*c*. (n) Av. stresses at 90%*c*. (o) Av. stresses at 90%*c*.

Figure F.9: Comparison between averaged stress profiles from the experiments of Zhang and Turner [131] and the results obtained with ILES for different locations along the local chord at 30% half-span.

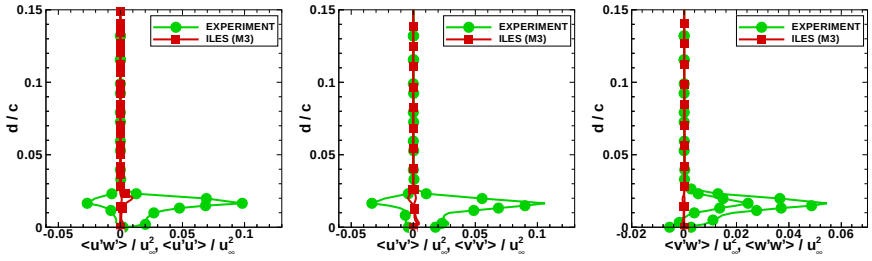

(a) Av. stresses at 10%c. (b) Av. stresses at 10%c. (c) Av. stresses at 10%c.

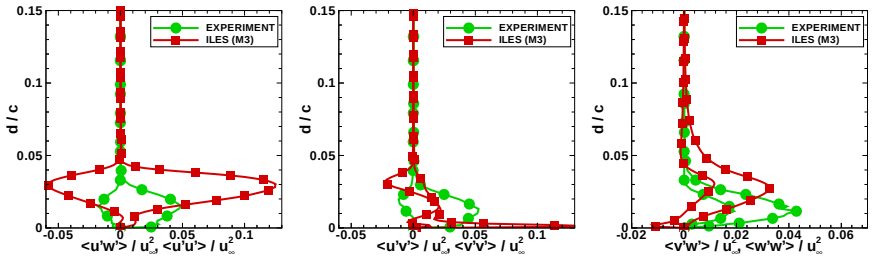

(d) Av. stresses at 30%c. (e) Av. stresses at 30%c. (f) Av. stresses at 30%c.

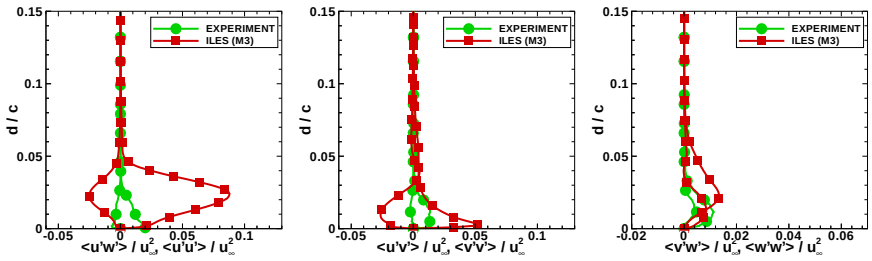

(g) Av. stresses at 50%c. (h) Av. stresses at 50%c. (i) Av. stresses at 50%c.

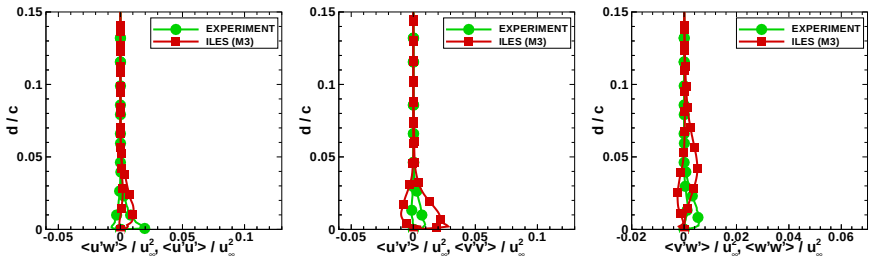

(j) Av. stresses at 70%c. (k) Av. stresses at 70%c. (l) Av. stresses at 70%c.

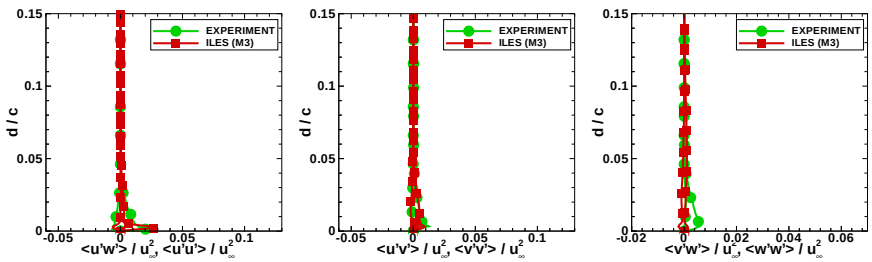

(m) Av. stresses at 90%c. (n) Av. stresses at 90%c. (o) Av. stresses at 90%c.

Figure F.10: Comparison between averaged stress profiles from the experiments of Zhang and Turner [131] and the results obtained with ILES for different locations along the local chord at 40% half-span.

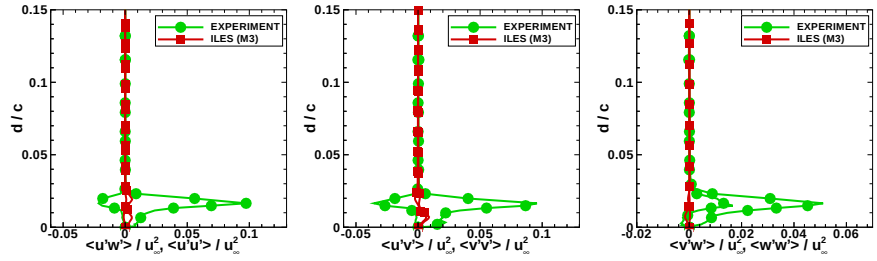

(a) Av. stresses at 10%c. (b) Av. stresses at 10%c. (c) Av. stresses at 10%c.

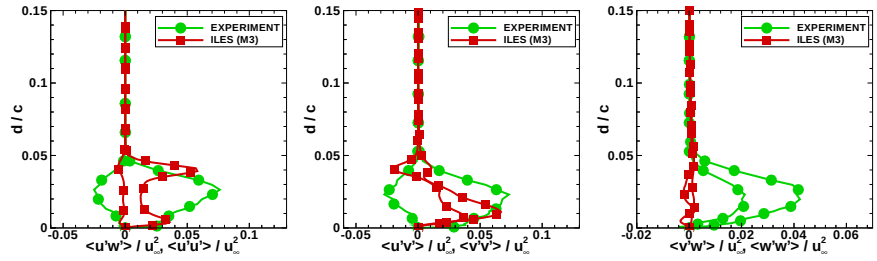

(d) Av. stresses at 30%c. (e) Av. stresses at 30%c. (f) Av. stresses at 30%c.

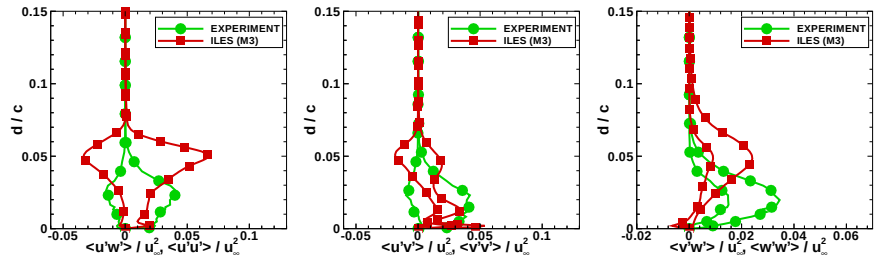

(g) Av. stresses at 50%c. (h) Av. stresses at 50%c. (i) Av. stresses at 50%c.

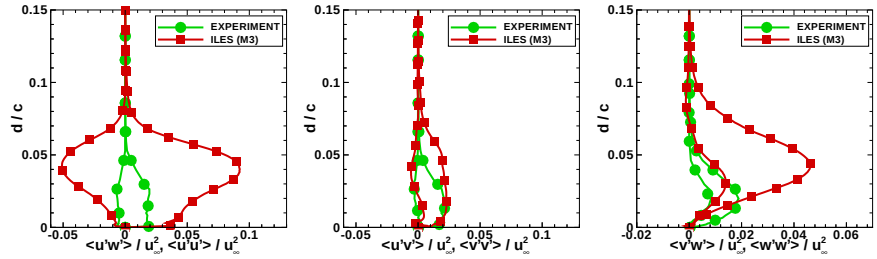

(j) Av. stresses at 70%c. (k) Av. stresses at 70%c. (l) Av. stresses at 70%c.

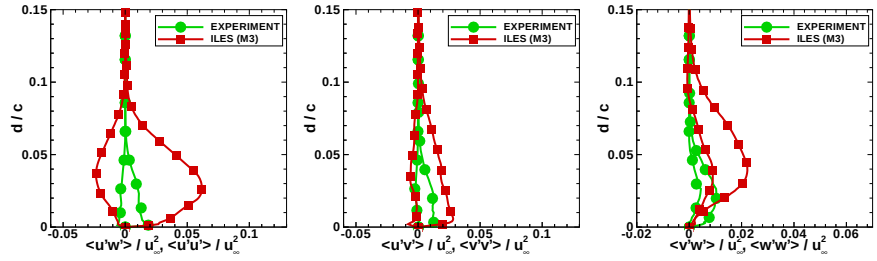

(m) Av. stresses at 90%c. (n) Av. stresses at 90%c. (o) Av. stresses at 90%c.

Figure F.11: Comparison between averaged stress profiles from the experiments of Zhang and Turner [131] and the results obtained with ILES for different locations along the local chord at 50% half-span.

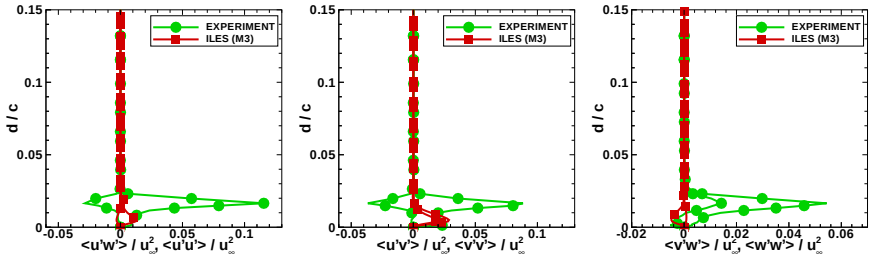

(a) Av. stresses at 10%c. (b) Av. stresses at 10%c. (c) Av. stresses at 10%c.

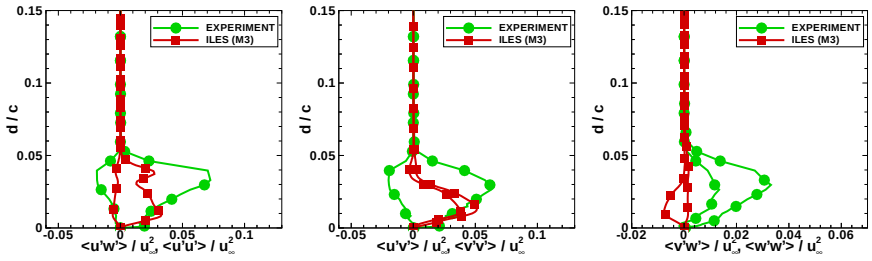

(d) Av. stresses at 30%c. (e) Av. stresses at 30%c. (f) Av. stresses at 30%c.

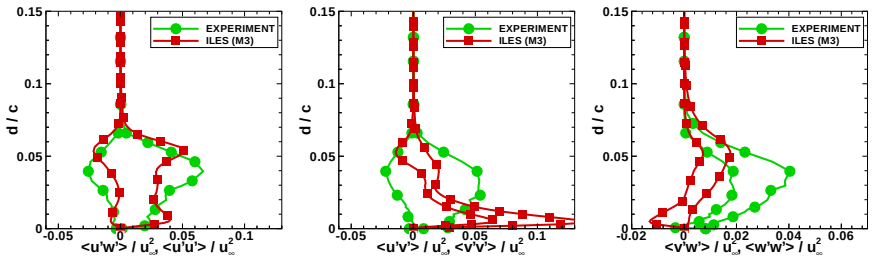

(g) Av. stresses at 50%c. (h) Av. stresses at 50%c. (i) Av. stresses at 50%c.

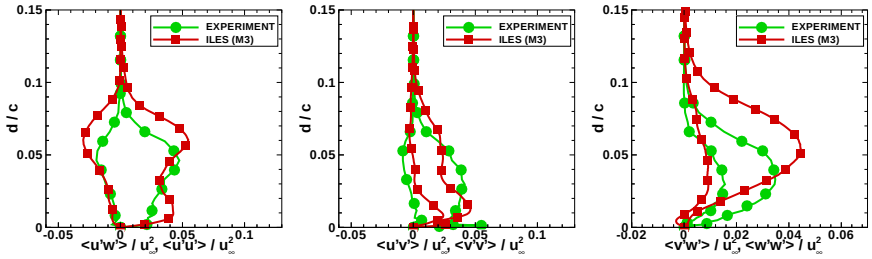

(j) Av. stresses at 70%c. (k) Av. stresses at 70%c. (l) Av. stresses at 70%c.

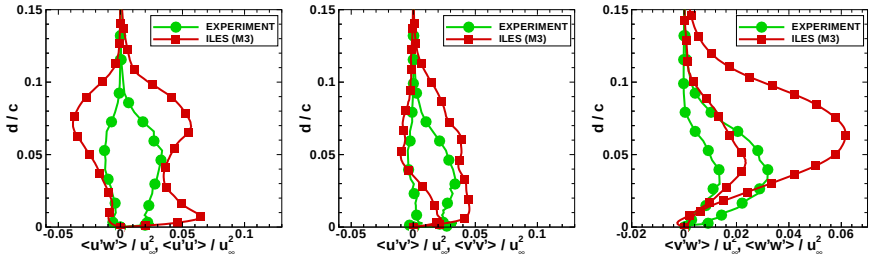

(m) Av. stresses at 90%c. (n) Av. stresses at 90%c. (o) Av. stresses at 90%c.

Figure F.12: Comparison between averaged stress profiles from the experiments of Zhang and Turner [131] and the results obtained with ILES for different locations along the local chord at 60% half-span.

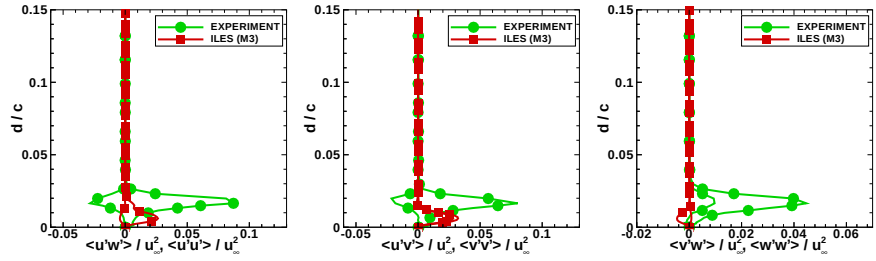

(a) Av. stresses at 10%c. (b) Av. stresses at 10%c. (c) Av. stresses at 10%c.

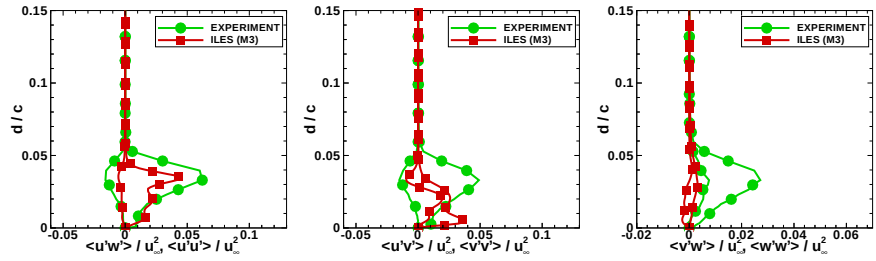

(d) Av. stresses at 30%c. (e) Av. stresses at 30%c. (f) Av. stresses at 30%c.

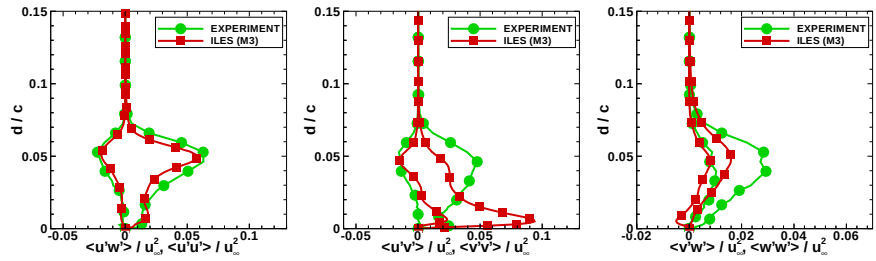

(g) Av. stresses at 50%c. (h) Av. stresses at 50%c. (i) Av. stresses at 50%c.

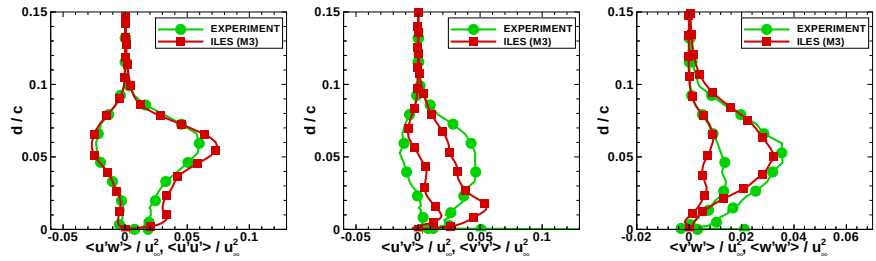

(j) Av. stresses at 70%c. (k) Av. stresses at 70%c. (l) Av. stresses at 70%c.

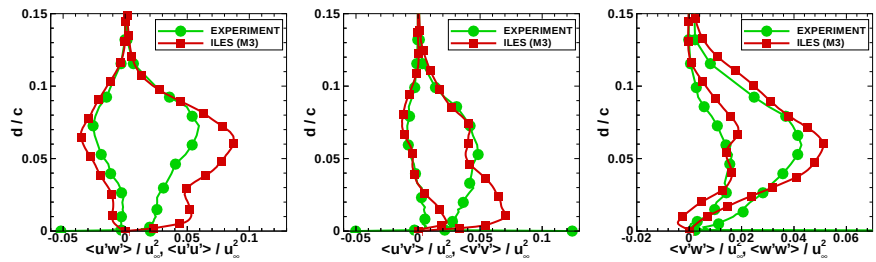

(m) Av. stresses at 90%c. (n) Av. stresses at 90%c. (o) Av. stresses at 90%c.

Figure F.13: Comparison between averaged stress profiles from the experiments of Zhang and Turner [131] and the results obtained with ILES for different locations along the local chord at 70% half-span.

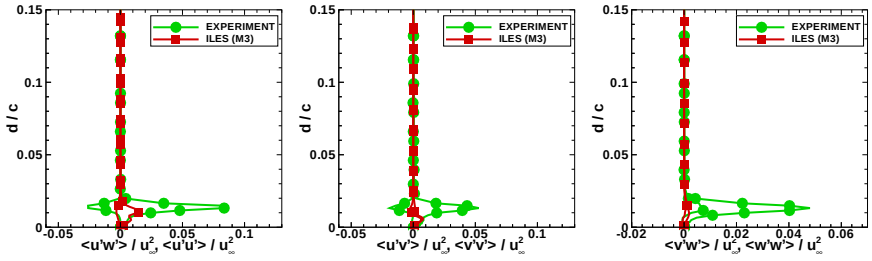

(a) Av. stresses at 10%c. (b) Av. stresses at 10%c. (c) Av. stresses at 10%c.

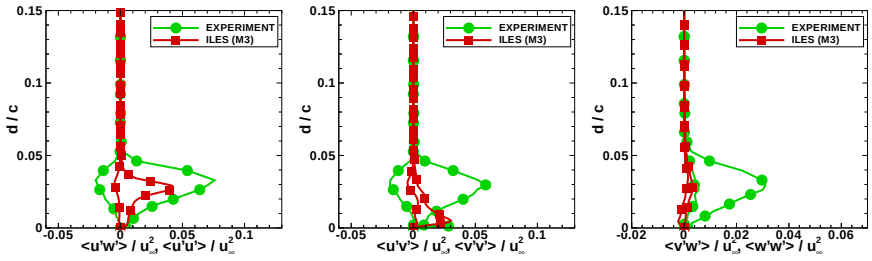

(d) Av. stresses at 30%c. (e) Av. stresses at 30%c. (f) Av. stresses at 30%c.

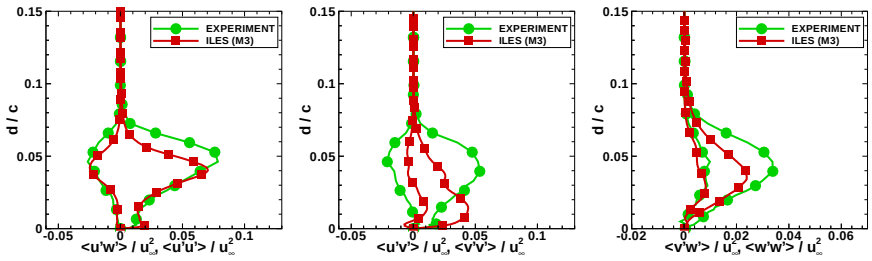

(g) Av. stresses at 50%c. (h) Av. stresses at 50%c. (i) Av. stresses at 50%c.

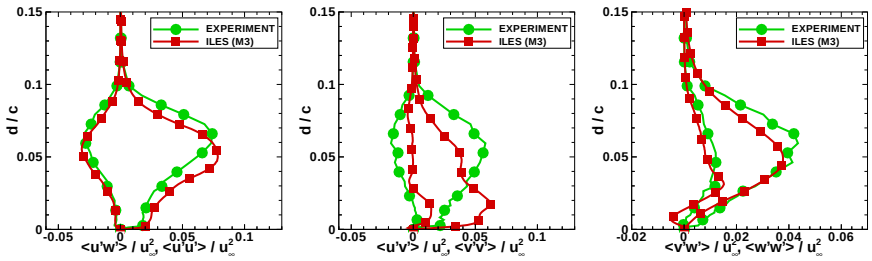

(j) Av. stresses at 70%c. (k) Av. stresses at 70%c. (l) Av. stresses at 70%c.

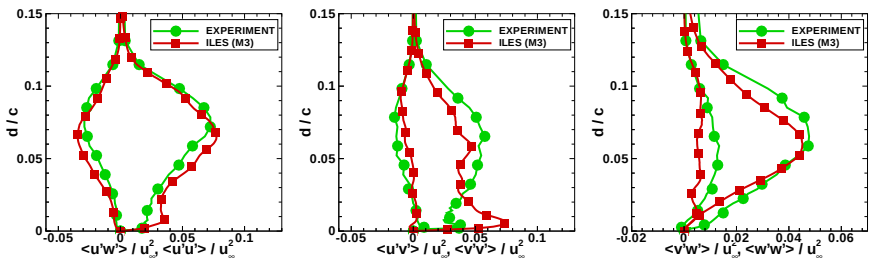

(m) Av. stresses at 90%c. (n) Av. stresses at 90%c. (o) Av. stresses at 90%c.

Figure F.14: Comparison between averaged stress profiles from the experiments of Zhang and Turner [131] and the results obtained with ILES for different locations along the local chord at 80% half-span.

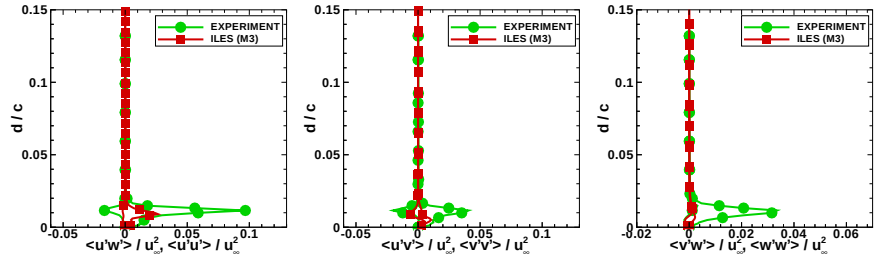

(a) Av. stresses at 10%c. (b) Av. stresses at 10%c. (c) Av. stresses at 10%c.

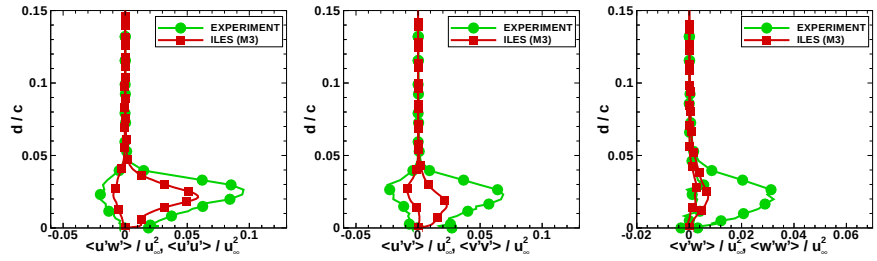

(d) Av. stresses at 30%c. (e) Av. stresses at 30%c. (f) Av. stresses at 30%c.

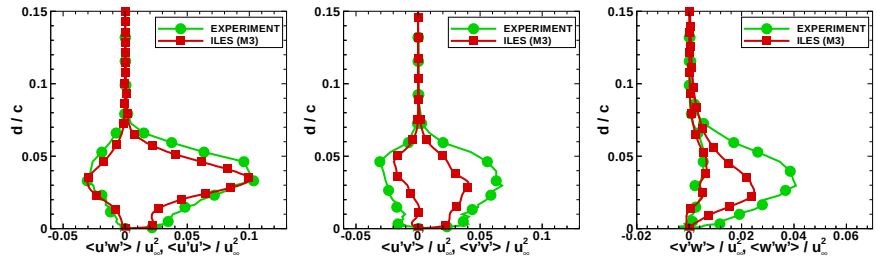

(g) Av. stresses at 50%c. (h) Av. stresses at 50%c. (i) Av. stresses at 50%c.

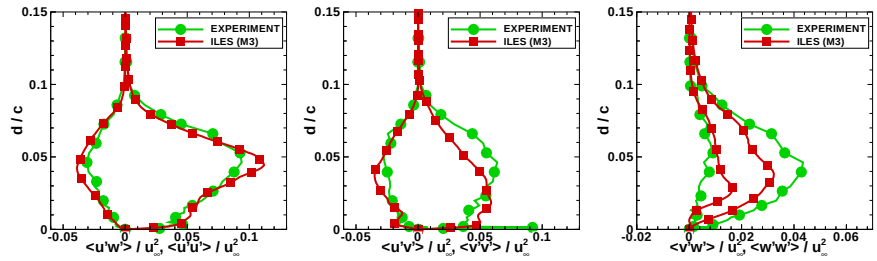

(j) Av. stresses at 70%c. (k) Av. stresses at 70%c. (l) Av. stresses at 70%c.

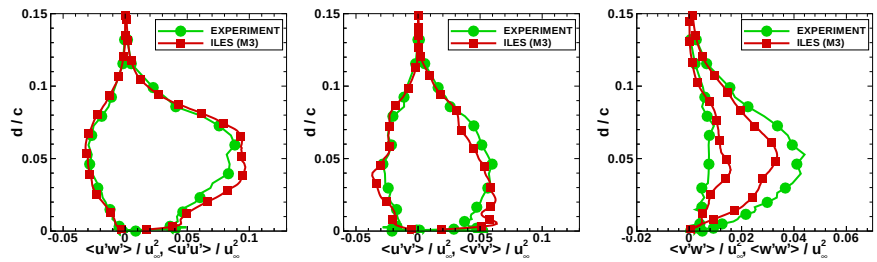

(m) Av. stresses at 90%c. (n) Av. stresses at 90%c. (o) Av. stresses at 90%c.

Figure F.15: Comparison between averaged stress profiles from the experiments of Zhang and Turner [131] and the results obtained with ILES for different locations along the local chord at 90% half-span.

APPENDIX **G**

List of Publications

Journal and conference papers:

M. Hahn and D. Drikakis. "Implicit Large-Eddy Simulation for Swept Wing Flow using High-Resolution Methods", *46th AIAA Aerospace Sciences Meeting and Exhibit*, Reno, Nevada, USA, 7 - 10 January 2008, AIAA-2008-0669.

M. Hahn and D. Drikakis. "Assessment of Large-Eddy Simulation for Separated Internal Flow", *46th AIAA Aerospace Sciences Meeting and Exhibit*, Reno, Nevada, USA, 7 - 10 January 2008, AIAA-2008-0667.

D. Drikakis, M. Hahn, A. Mosedale, E.Shapiro, B. Thornber. "Computational Uncertainty in CFD Associated with Spatial and Temporal Discretisation and Non-linear Methods Design", *AVT-147 Symposium on Computational Uncertainty in Military Vehicle Design*, Athens, Greece, 3-6 December 2007.

D. Drikakis, M. Hahn, Z. Malick, E. Shapiro. "Implicit Large-Eddy Simulations of Wall-Bounded Turbulent Flows", *ERCOFTAC Bulletin*, March 2007, 72:61–66.

D. Drikakis, C. Fureby, F.F. Grinstein, M. Hahn, D. Youngs. "LES of Transition to Turbulence in the Taylor Green Vortex", in *Direct and Large-Eddy Simulation VI*, Springer Netherlands, 2006, 159-166

M. Hahn and D. Drikakis. "Implicit Large Eddy Simulation of Turbulent Flows using High-Resolution Methods", *43rd AIAA Aerospace Sciences Meeting and Exhibit*, Reno, Nevada, USA, 10-13 January 2005, AIAA 2005–1285.

M. Hahn and D. Drikakis. "Large eddy simulation of compressible turbulence using high-resolution methods", *International Journal for Numerical Methods in Fluids*, 2005, 47:971–977.

D. Drikakis, M. Hahn, S. Patel and E. Shapiro. "High-resolution methods for compressible, constant and variable density incompressible flows", *ERCOFTAC Bulletin*, September 2004, 62:35–40.

Other presentations:

B.J.R. Thornber, M. Hahn and D. Drikakis. “Advanced Simulation Methods and High-Performance Computing for Shock Waves and Turbulence Research”, *AWE Strategic Alliance Symposia*, Shrivenham, UK, 21-22 February 2005, poster presentation.

M. Hahn and D. Drikakis. “Implicit Large Eddy Simulation for Wing Flows”, *LES-UK Colloquium*, Imperial College London, UK, 2-3 March 2005.

M. Hahn and D. Drikakis. “Implicit Large Eddy Simulation for Unsteady Turbulent Flows”, *AVT-123 Symposium on Flow-Induced Unsteady Loads and the Impact on Military Applications*, Budapest, Hungary, 25-28 April 2005.

M. Hahn and D. Drikakis. “Numerical experiments using high-resolution methods in compressible and turbulent flows”, *IWPCTM 9*, Cambridge, UK, 19-23 July 2004.